Development of an innovative ISOL system for the production of short-lived neutron-deficient ions

Venkateswarlu Kuchi

To cite this version:

Venkateswarlu Kuchi. Development of an innovative ISOL system for the production of short-lived neutron-deficient ions. Accelerator Physics [physics.acc-ph]. Normandie, Université de Caen Normandie, 2018. English. NNT : . tel-01994668v1

HAL Id: tel-01994668
https://hal.in2p3.fr/tel-01994668v1

Submitted on 25 Jan 2019 (v1), last revised 27 May 2019 (v2)

THÈSE

Pour obtenir le diplôme de doctorat

Spécialité PHYSIQUE

Préparée au sein de l'Université de Caen Normandie

Development of an innovative ISOL system for the production of short-lived neutron-deficient ions

Présentée et soutenue par
Venkateswarlu KUCHI

Thèse soutenue publiquement le 17/10/2018 devant le jury composé de		
Mme MARION MACCORMICK	Chargé de recherche HDR, INSTITUT DE PHYSIQUE NUCLEAIRE D'ORSAY	Rapporteur du jury
M. THIERRY STORA	Senior scientist, Centre Européen de Recherche Nucléaire	Rapporteur du jury
M. JEAN CLAUDE ANGELIQUE	Professeur des universités, 14 ENSI de Caen	Membre du jury
M. MAREK LEWITOWICZ	Directeur de recherche au CNRS, 14 GANIL de CAEN	Membre du jury
Mme POPESCU LUCIA	Chargé de recherche, Centre d'étude de l'énergie nucléaire	Membre du jury
M. PASCAL JARDIN	Directeur de recherche au CNRS, 14 GANIL de CAEN	Directeur de thèse

Thèse dirigée par PASCAL JARDIN, Grand accélérateur national d'ions lourds (Caen)

Title: Development of an innovative ISOL system for the production of short-lived neutron-deficient ions.

Keywords: ISOL technique, fusion-evaporation reaction, neutron-deficient alkali isotopes, diffusion, effusion, sticking process.

In the frame of GANIL/SPIRAL-1 facility, an innovative target ion source system (TISS) has been designed in order to produce new competitive radioactive ion beams, and to determine to which extent it is possible to improve the production performances by optimizing a target ion source system dedicated to the production of a specific radioactive ion beam.

The short-lived alkali isotope of ^{74}Rb ($\tau_{1/2}$ = 64.8 ms) has been chosen as a challenging case study.

By studying and improving the processes involved in the TISS designed, *i.e.* in-target production by fusion-evaporation, implantation in and release out of graphite, effusion, and ionization, an atom-to-ion transformation efficiency of 75% was predicted, leading to an ion rate of the order of 10^4 pps at the exit of the TISS.

The estimated performances would allow the GANIL / SPIRAL1 installation to deliver beams of ^{74}Rb and ^{114}Cs with competitive intensities never reached in other installations.

The production device was developed based on my work, to cope with physics objectives and with the conditions of the SPIRAL1 operation. Efficiency, reliability and thus simplicity were essential. The system meets these requirements.

The instrumentation needed for tests existed or have been specifically designed. The TISS has been built, assembled and partly tested.

In parallel, issues have been addressed to answer related questions about sticking times, resistivity, and emissivity, to get inputs for the design of the TISS.

Expected results with alkali isotopes encouraged us to apply the same principle to the production of neutron-deficient short-lived isotopes of noble gases and eventually to metals.

Titre: Développement d'un système ISOL innovant pour la production d'ions déficitaires en neutrons de courte durée.

Mots clés: Technique ISOL, réaction de fusion-évaporation, isotopes alcalins déficients en neutrons, diffusion, effusion, collage.

Dans le cadre de l'installation GANIL / SPIRAL-1, un système innovant de source d'ions cible (TISS) a été conçu pour produire des nouveaux faisceaux d'ions radioactifs compétitifs et déterminer dans quelle mesure il est possible d'améliorer les performances de production par l’optimisation de l’ensemble cible-source (ECS) d’ions dédié à la production d'un faisceau d'ions radioactifs spécifique.

L'isotope d'alcalin de courte durée de ^{74}Rb ($\tau_{1/2}$ = 64.8 ms) a été choisi comme cas d’école.

En étudiant et en améliorant l’efficacité des processus impliqués dans le fonctionnement de l’ECS, *i.e.* production dans la cible par réaction fusion-évaporation, implantation dans- et sortie du graphite, effusion et ionisation, une efficacité de transformation atome-ion de 75% est attendue, menant à un taux d'ions de l'ordre de 10^4 pps à la sortie de l’ECS.

Les performances estimées permettraient à l'installation GANIL / SPIRAL1 de délivrer des faisceaux de ^{74}Rb et ^{114}Cs avec des intensités compétitives, jamais atteintes dans d'autres installations.

Le dispositif de production a été développé sur la base de mon travail, pour répondre aux objectifs de physique et aux conditions d'opération de SPIRAL1. L'efficacité, la fiabilité et donc la simplicité étaient essentielles. Le système répond à ces exigences.

L'instrumentation nécessaire pour les tests existait ou a été spécialement conçue. L’ECS a été construit, assemblé et partiellement testé.

En parallèle, des questions ont été abordées pour répondre à des besoins connexes sur les temps de collage, la résistivité et l'émissivité, afin d'obtenir des informations pour la conception de l’ECS.

Les résultats attendus avec les isotopes d’alcalins nous encouragent à appliquer le même principe à la production d’isotopes déficients en neutrons de courte durée de gaz nobles et éventuellement de métaux.

Acknowledgement

The time has finally come to pack my bags to explore new horizons. Almost four years have passed since I arrived at GANIL and it seems to me that it was yesterday. Through these few lines, I wish to express my sincere thanks to all those who have contributed directly or indirectly to the outcome of this scientific work, exciting and user-friendly.

I wish to express my gratitude to the members of the Jury for taking their time to estimate my work. I therefore thank Thierry STORA for his expert opinion of the TISS on my work, Jean-Claude ANGELIQUE for having accepted to preside over this jury, Marion MACCORMICK and Thierry STORA for having assured the writing of the reports and meticulously reread my manuscript. Lucia POPESCU and Marek LEWITOWICZ for having examiners of this thesis. I really appreciated the insightful and constructive exchanges that we had during my defense.

I would like to express my deep gratitude to my supervisor Pascal JARDIN who gave me the opportunity to conduct this thesis work. His patience, motivation, passion and his explanations always pedagogical. His scientific and technical knowledge have made this project very rewarding and formative. I am grateful to him for his trust, his wise advice, and his availability and for all the knowledge, he has given me over the years. His guidance helped me in all the time of research and writing this report.

Following the order of the different parts of this work, I wish to thank the people who helped me to develop the fusion-evaporation TISS (source TULIP): firstly, I would like to thanks to Michel Clément for his time to design and his proposals throughout this work, during this three years.

My sincere thanks to all members of GPI with whom I worked during these three years and sharing the coffee every morning: Benoit OSMOND, Jean-Luc FLAMBARD, Frédéric LEMAGNEN, Christophe BARUE, Nicolas LECHARTIER, Mickaël DUBOIS, Olivier BAJEAT, Romain FRIGOT, Vincent METAYER, and Stéphane HORMIGOS. By sheering their skills and help along the project.

Thanks to Laurent MAUNOURY and Mamadou FAYE for their explanations and help to simulate the source, as well as for our many interactions since.

Thanks to Pierre DELAHAYE for answering my questions and his help to calculate the production rates at the beginning of the thesis.

I also wish to thank Sabrina, Virginie, and Sophie for their help during the formalities which punctuate the life of a PhD student.

I would also like to thank my fellow Ph.D. students and post-doc for the very good general mood they have contributed to GANIL, for all meals, all coffee breaks, all beer parties and fighting for ball in football field. A big thought for Arun and Trinh, Thanks also to Quentin, Benoit, Aldric, Hongjie-Li, Adrien, Simon, ville, Alexandre, Sayani, Pedja and Vivek. Congratulations to the new Ph.D. students, good luck to the following, welcome to new adventure!.

My more thanks to the Trinh sharing office as well as his knowledge. All your discussions about life are interesting and I wish that one day you will be billionaire and become a king of Vietnam.

Thanks to Eveline REIX who helps me to learn French, and enjoying my Indian food.

Grate thanks to Maëlle Maurice for her support especially during the first two years of my Ph.D. and spending her time with me. She is the one motivate me to discover the world by travel.

Finally, I apologize to those whom I have forgotten or whom I have been able to quote here but to whom I think when I write these lines. Thanks to all GANIL for helping me feels like a home during these three years.

To

My Family & Friends

Table des matières

Résumé en Français

Motivation

Une des plus fortes motivations de l'étude de la matière nucléaire est la compréhension des processus de nucléosynthèse à partir du Big-Bang. Juste après cet instant, une assemblée de particules très énergétiques commence un processus de refroidissement et d'assemblage qui va conduire aux particules que nous connaissons aujourd'hui. Des noyaux d'abord très variés se sont composés pour progressivement se transformer via différentes voies de désintégration et enfin atteindre les formes plus stables qui composent notre quotidien et la région de la carte des noyaux que l'on appelle la vallée de stabilité. Comprendre le comportement de la matière nucléaire pour nous permettre de remonter le temps jusqu'à l'origine implique de pouvoir l'étudier. Mais ayant en grande partie disparu, il est nécessaire de la reproduire sous sa forme passée.

Sur terre, nous disposons principalement de noyaux stables, qui ne se transforment pas spontanément, ou de noyaux proches de la vallée de stabilité qui possèdent des durées de vie longues. Les modèles qui décrivent le comportement de la matière nucléaire ont été en premier lieu éprouvés en les confrontant à ces noyaux. Pour les confronter à des noyaux exotiques, c'est-à-dire qui n'existent plus sur la terre à l'état naturel, il est nécessaire de produire ces noyaux à partir de ceux qui sont disponibles dans notre environnement.

Les transformations de la matière nucléaire sont souvent accompagnées d'échanges d'énergie importants. Si un noyau se sépare spontanément en deux fragments, ceux-ci peuvent s'éloigner l'un de l'autre avec une certaine énergie cinétique. Pour les rassembler de nouveau, il faudra lancer ces 2 fragments l'un vers l'autre avec une énergie cinétique équivalente. Cette seconde méthode est à l'origine du développement des accélérateurs d'ions lourds. Le but est de donner une énergie cinétique aux (à l'un des) composants de la collision pour injecter cette énergie dans le système composé. Pour réaliser cette collision, une cible est généralement fixée dans le laboratoire. Un faisceau d'ions est accéléré à une énergie suffisante pour qu'ils franchissent la barrière de répulsion coulombienne et que les noyaux des ions entrent en collision avec les noyaux de la cible fixe. Pour étudier les conséquences de la réaction, la cible est entourée d'instruments sensibles aux particules émises lors de la collision.

La probabilité que deux noyaux particuliers entrent en collision est relativement faible : elle est typiquement comparable à la probabilité qu'a une tête d'épingle, lancée au hasard dans un terrain de football, de toucher une autre tête d'épingle, placée au hasard dans ce terrain. Pour augmenter la probabilité d'observer une collision, les expérimentateurs-observateurs demandent donc logiquement d'augmenter le nombre de noyaux contenus dans le faisceau envoyé sur leur cible, et ils augmentent eux-mêmes le nombre de noyaux cibles en augmentant l'épaisseur de la cible. Hélas, les noyaux incidents sont freinés au cours de leur parcours dans la cible. Les conditions de la réaction nucléaire qu'ils souhaitaient observer peuvent donc changer et induire une imprécision dans leur étude. Ils n'ont donc pas toute latitude sur l'épaisseur de leur cible.

Au cours des 50 dernières années, pour répondre aux besoins des physiciens expérimentateurs, les installations qui délivrent des faisceaux d'ions dédiés à la physique nucléaire ont constamment augmenté l'intensité de leurs faisceaux, leur plage d'énergie ainsi que la variété des ions disponibles. Aujourd'hui, environ 50% des isotopes naturels peuvent être accélérés et utilisés comme noyaux projectiles.

Les études portent sur des phénomènes toujours plus rares et spécifiques ; parmi les événements produits, les événements d'intérêt sont donc moins nombreux. Les installations tentent donc d'augmenter l'intensité des faisceaux pour répondre au besoin de statistique des expériences, qui conditionne la précision des résultats et le temps nécessaire pour réaliser une expérience.

Processus nucléaires d'intérêt pour la production de noyaux radioactifs

Le type de réaction nucléaire est conditionné par les noyaux en jeu dans la collision et l'énergie de la collision (Chap. 1, §1). Pour des collisions dont l'énergie est proche de la limite inférieure d'énergie de réaction (barrière coulombienne), les noyaux fusionnent puis se transforment en évaporant des particules légères pour évacuer le surplus d'énergie cinétique déposée dans le système. Ce processus est appelé processus de Fusion-Evaporation. Les noyaux qui résultent de ce type de collision ont la particularité d'être situés dans la partie des isotopes déficients en neutrons, à cause de la tendance naturelle des isotopes à être plus stables lorsqu'ils sont riches en neutrons. Cette caractéristique explique la forme de la vallée de stabilité vers la zone des noyaux riches en neutrons, courbée par rapport aux noyaux qui ont un nombre Z de protons égal au nombre N de neutrons (ligne rouge Figure 1).

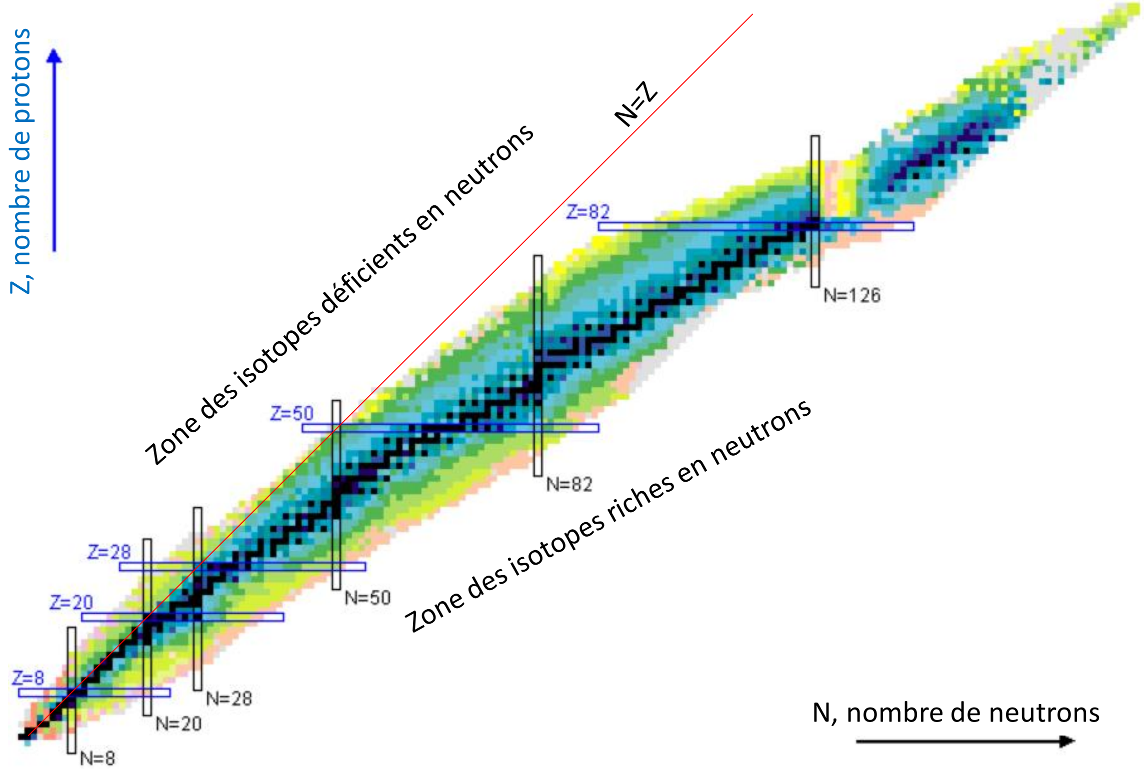

Figure 1: Carte des noyaux représentée en fonction du nombre de neutrons et de protons. Les noyaux stables correspondent aux carrés noirs. Les autres correspondent aux noyaux radioactifs. La ligne rouge indique la position des noyaux de N=Z. Les nombres Z et N indiqués correspondent à des valeurs pour lesquelles les noyaux ont une stabilité accrue.

Une fois que les deux noyaux ont fusionné, le noyau final dépend fortement de l'énergie qui reste à dissiper. Pour une énergie donnée, plusieurs noyaux peuvent être produits mais ils seront relativement peu nombreux et seront proches du noyau fusionné.

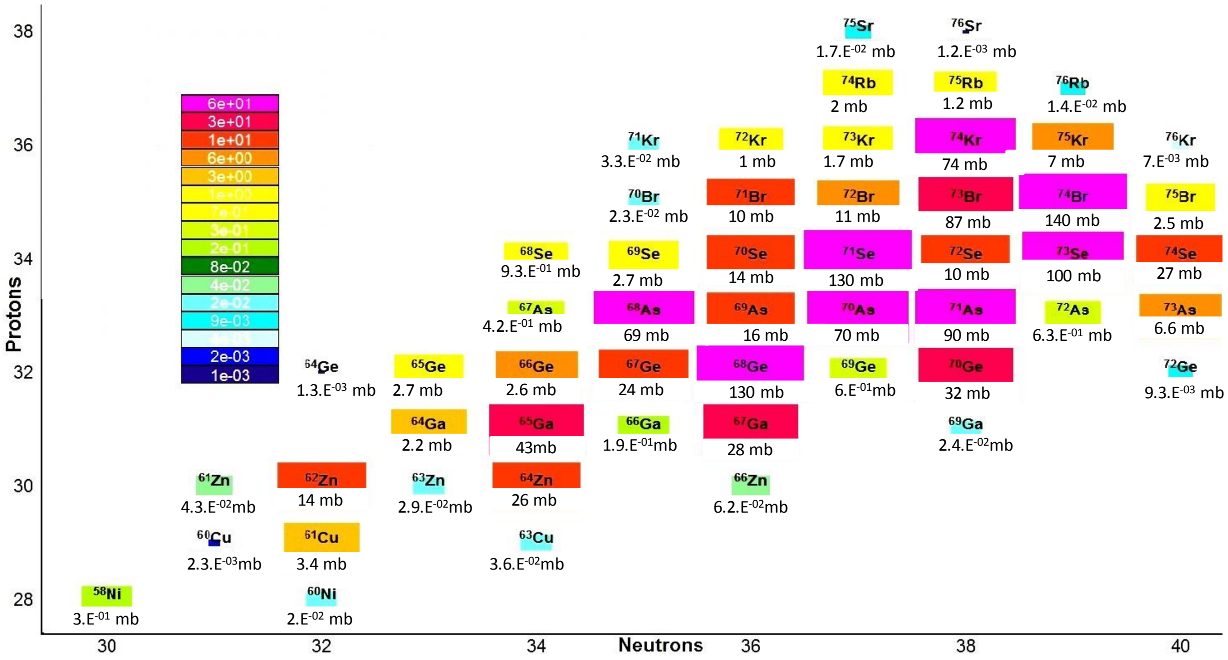

Figure 2: Production d'isotopes par processus de fusion évaporation pour la réaction ^{20}Ne + ^{58}Ni à une énergie de 5.5 MeV/n. La surface de chaque rectangle est proportionnelle à la section efficace.

L'avantage de ce processus réactionnel est donc une sélectivité de la zone de produits de réaction, qui peut être contrôlée via le choix des noyaux cible et projectile, et de l'énergie du faisceau d'ions. Techniquement, il nécessite de disposer des noyaux adaptés et d'accélérateurs qui permettent d'ajuster finement l'énergie d'accélération.

Lorsque l'énergie des ions projectiles augmente, l'énergie déposée dans la collision est plus importante et ne permet plus le processus de fusion. Les constituants de chaque noyau peuvent être directement éjectés et les produits de la réaction sont généralement plus variés.

La fragmentation de noyaux de Nb induite par des noyaux de carbone de 95 MeV/A d'énergie donne lieu à des isotopes répartis autour de la vallée de stabilité, et allant de la masse du nobium à celle de l'azote.

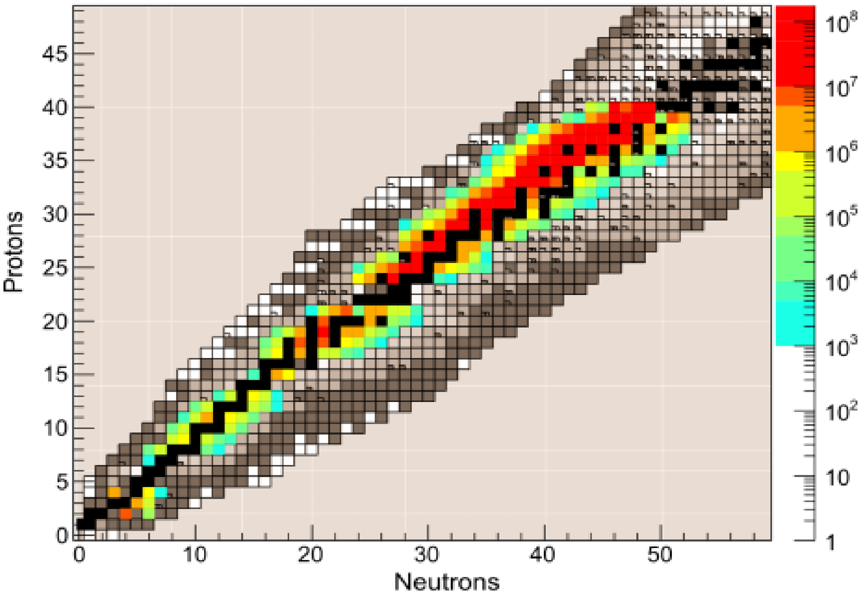

Figure 3: Production d'isotopes lors du bombardement d'une cible de niobium à l'aide d'un faisceau de C@95MeV/A. Pour une intensité relative de 5 ordres de grandeur entre les plus produits et les moins produits, la gamme de Z couverte est d'environ 32.

Dans le cas de protons de 70 MeV lancés sur une cible d'uranium, l'énergie déposée induit la fission de l'uranium, donnant lieu à la production d'isotopes radioactifs riches en neutrons et dont les masses sont centrées autour de celles du Kr et du Xe.

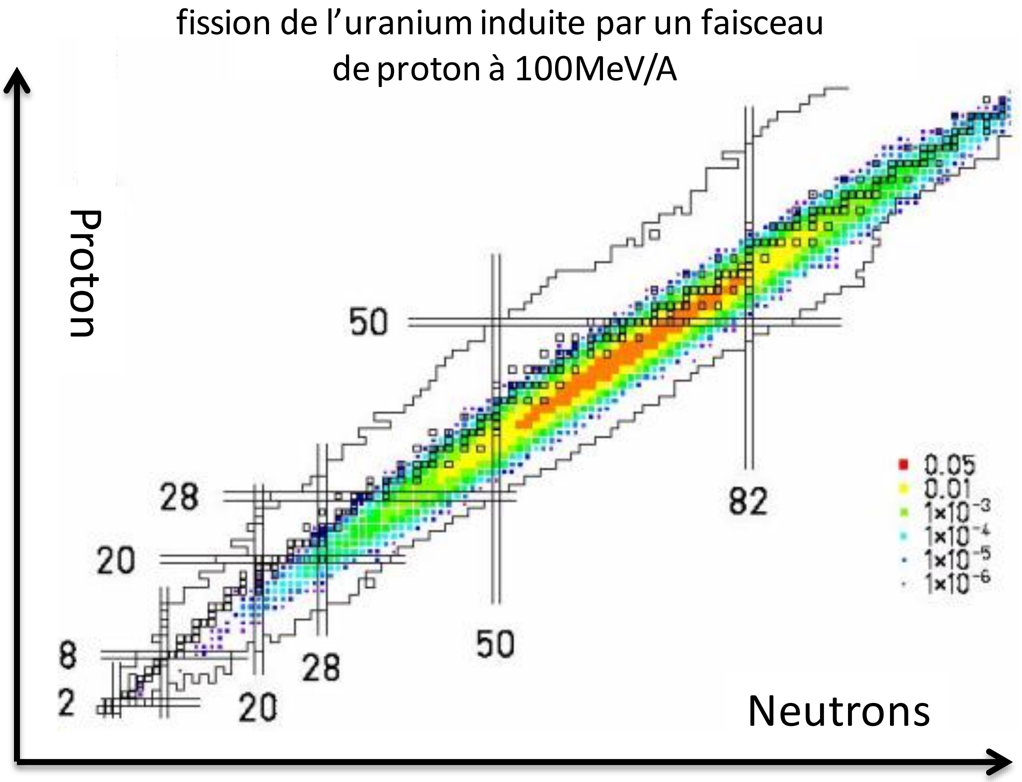

Figure 4: Production d'isotopes par fission de l'uranium induite par un faisceau de proton à une énergie de 100 MeV. Pour une intensité relative de 8 ordres de grandeur entre les plus produits et les moins produits, la gamme de Z couverte est d'environ 35 [1].

Dans le cas de protons de très haute énergie lancés sur une cible d'Uranium, le spectre d'isotopes produits couvre l'ensemble des noyaux de Z inférieurs à celui de l'uranium (Figure 5), avec une production prépondérante autour des pics de fission de l'uranium et dans la région des actinides et lanthanides déficients en neutrons. L'utilisation d'un tel faisceau de protons permet donc l'accès à une très grande variété d'isotopes, mais la sélectivité du processus de production est la plus faible parmi les processus présentés ci-avant.

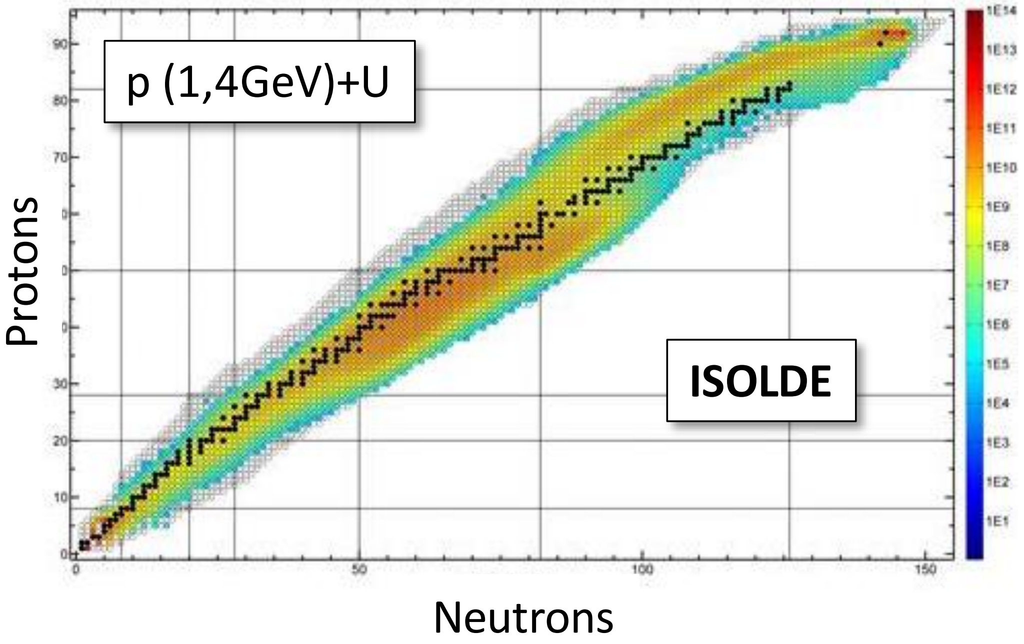

Figure 5: Production d'isotopes par spallation de l'uranium à l'aide d'un faisceau de protons de 1.4 GeV.

Pour étudier un noyau exotique donné, il est donc souvent possible d'avoir recours à plusieurs techniques de production. Chacune d'entre elles a des conséquences différentes en terme de produits de réactions (intensité, variété, énergie de recul, énergie d'excitation…). Le choix du processus réactionnel est la première étape de la production d'ions radioactifs. Il est nécessaire, au même titre que pour les étapes suivantes du processus de production, d'optimiser son choix au regard des figures de mérite des installations de production de faisceaux d'ions radioactifs qui sont entre autres l'intensité du faisceau, sa pureté et l'exoticité des ions des faisceaux.

Objectif de la thèse

Cette thèse a pour but de concevoir un dispositif destiné à la production de faisceaux d'ions radioactifs déficients en neutrons et de courte durée de vie en utilisant la méthode ISOL (Isotope Separator On Line). Cette méthode consiste à produire des isotopes radioactifs par réaction d'un faisceau d'ions avec les noyaux d'une cible, à arrêter ces isotopes, à les ioniser puis à les accélérer sous forme de faisceau.

Ma thèse a été réalisée dans le cadre d'une évolution de l'installation SPIRAL-1 (Système de Production d'Ions Radioactifs Accélérés en Ligne) située à GANIL (Grand Accélérateur National d'Ions Lourds). Le but du GANIL est de mettre à disposition des utilisateurs (physiciens expérimentateurs) des faisceaux d'ions stables et radioactifs. Les éléments stables accélérés vont du carbone à l'uranium, avec des énergies maximales qui sont respectivement de 95 MeV/A et de 8 MeV/A. Depuis son démarrage, l'installation SPIRAL-1 a délivré des ions radioactifs d'isotopes de gaz (He, Ne, Ar, Kr, O) obtenus par fragmentation de faisceaux d'ions lourds (du ^{12}C à ^{86}Kr) lancés sur une cible de graphite. Pour étendre la palette de faisceaux disponibles à la production d'isotopes d'éléments condensables, une transformation (Upgrade SPIRAL-1) a été entamée en 2013. Elle s'est achevée en avril 2018 et il est maintenant possible d'utiliser les différents couples faisceaux d'ions projectiles et cibles donnés ci-dessous pour produire des isotopes radioactifs:

- ^{12}C à ^{238}U (à énergie max.) ➔ cible graphite épaisse (qui arrête les produits de réaction)
- ^{12}C à intensité max. (2.10^{13}pps) à 95 MeV/A ➔ cible épaisse du C au Nb
- ^{12}C à ^{238}U ➔ cible mince (qui n'arrête pas les produits de réaction)

Cette variété de combinaisons offre une plage importante d'optimisation du choix de la réaction au regard de l'isotope à produire, optimisation qui était plus difficile lorsque seul un matériau cible pouvait être utilisé avec SPIRAL-1, ou qui est plus difficile lorsque que le faisceau primaire est figé.

Un des objectifs du GANIL, comme l'est celui d'autres installations, est de délivrer des faisceaux uniques, en terme de nature d'ions, d'intensité, de pureté, de disponibilité et d'offrir un environnement instrumental original. Mon travail de thèse visait la production de faisceaux originaux. Pour les identifier, j'ai commencé par comparer les faisceaux radioactifs délivrés par TRIUMF/ISAC et CERN/ISOLDE, installations ISOL majeures au niveau mondiale, à ceux attendus avec l'installation Upgrade SPIRAL-1 [2]. Ce travail m'a permis de clairement mettre en évidence deux régions où SPIRAL-1 était ou pouvait être compétitif : la région des isotopes « légers » jusqu'à M= ~50, et une région de la carte des noyaux peu explorée par les autres installations car peu accessibles à cause du processus de réaction nucléaire qu'elles utilisent (protons de haute énergie, supérieure à 500 MeV, induisant la spallation ou la fission de noyaux lourds). Cette région est celle des isotopes de masse intermédiaire (de la masse du Kr à celle du Xe) déficients en neutrons. Leur production est accessible par réaction de fusion-évaporation en utilisant les couples projectiles-cibles autorisés avec l'Upgrade de SPIRAL-1.

L'objectif de ma thèse a été d'optimiser un dispositif pour qu'il soit capable de produire un faisceau d'ions déficients en neutrons dans cette région, compétitif en intensité.

Cette région est partiellement couverte par la production des installations précitées, particulièrement à proximité de la vallée de stabilité. Lorsque l'on s'éloigne de cette vallée, les taux de production d'ions obtenus diminuent (voir Figure 4 et Figure 5) pour deux raisons : la probabilité de production des isotopes dans la cible diminue, à cause de l'évolution de la section efficace de réaction pour les isotopes plus éloignés de la vallée de stabilité, et parce que la durée de vie des isotopes diminue avec leur éloignement de la vallée de stabilité. Cette durée de vie intervient au travers de sa compétition avec le temps de transformation des isotopes en ions dans le dispositif de production. Ce processus de transformation n'est pas lié aux caractéristiques nucléaires de l'isotopes, mais à ses caractéristiques chimiques. Si ce processus est long comparé à la durée de vie de l'isotope d'intérêt, ce dernier aura une probabilité importante d'avoir disparu du dispositif de production avant d'avoir été transformé en ions. Une des caractéristiques essentielles des dispositifs de production par la méthode ISOL est donc de devoir être aussi rapide que possible par rapport à la décroissance radioactive, pour limiter les pertes.

Pour que mon dispositif soit compétitif, il fallait qu'il produise des ions aussi exotiques que possible, et donc qu'il permette de transformer des isotopes très exotiques en ions dans un temps aussi court que possible au regard de leur durée de vie.

Le taux d'ions en sortie du dispositif résulte du produit du nombre d'isotopes produits dans la cible par l'efficacité de transformation des isotopes en ions. Appelons cette transformation TAI, transformation atomes-ions. Une fois que les isotopes sont arrêtés dans la cible, leur cortège électronique se reconstitue et ils sont présents sous forme d'atomes radioactifs. Si le taux de production d'isotopes dans la cible et l'efficacité TAI étaient indépendantes, il suffirait d'augmenter l'un ou l'autre pour obtenir une augmentation du taux de production d'ions. Augmenter par exemple l'intensité des faisceaux d'ions primaire sur la cible d'un facteur X, choisir une réaction nucléaire ayant une section efficace Y fois plus grande et améliorer l'efficacité d'un facteur Z conduirait à un gain de production d'un facteur XYZ. Si tel était le cas, les intensités de faisceaux d'ions radioactifs disponibles seraient beaucoup plus importantes que ce qu'elles sont aujourd'hui. La limitation provient du couplage des techniques de production dans la cible et de transformation des isotopes en ions. La conception d'une cible adaptée à une intensité de faisceau d'ions primaire et à un processus réactionnel a un impact direct sur le temps de transformation des isotopes en ions. Par exemple, augmenter les dimensions d'une cible pour qu'elle puisse supporter le dépôt d'énergie d'un faisceau d'ions primaires plus intense, ou allonger la cible pour l'adapter à un faisceau d'ions primaire de plus haute énergie, conduiront généralement à une augmentation du temps TAI et donc, pour les isotopes de courte durée de vie, à une diminution de l'efficacité TAI.

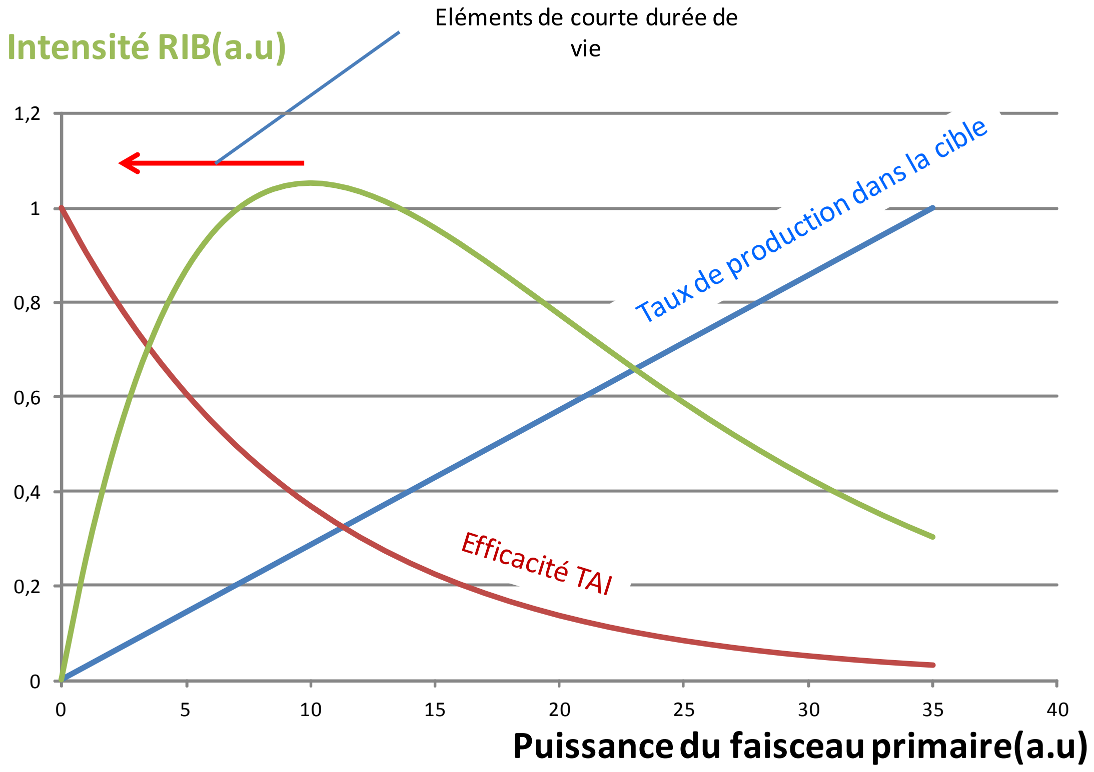

Figure 6: Illustration de principe du taux de production d'ions radioactifs par un système ISOL en fonction de la puissance du faisceau primaire et de l'efficacité TAI.

Il existe donc nécessairement une combinaison technique optimum entre les différents paramètres qui entrent en jeu dans la conception d’un dispositif ISOL qui conduit à optimiser le taux de production d’ions.

L’optimisation n’a de sens qu’au regard d’un atome radioactif donné, qui de par sa durée de vie et ses caractéristiques physico-chimiques (masse et structure électronique) conditionne les processus qui interviennent dans la TAI. C’est pour cette raison que chaque dispositif ISOL ne peut être optimisé que pour un isotope particulier. Néanmoins, compte tenu du coût de tels dispositifs, ils sont généralement conçus pour la production de plusieurs ions radioactifs, sans être optimisés pour chacun d’entre eux.

Pour montrer les performances qu’il était possible d’obtenir en optimisant un dispositif, il fallait choisir un atome radioactif qui serait le cas d’école de mon travail. Puisque ce travail avait pour ambition d’étendre la palette de faisceaux d’ions radioactifs du GANIL, il était aussi nécessaire qu’il puisse être implanté dans l’installation SPIRAL-1 et qu’il intéresse la communauté de physiciens nucléaires utilisatrice du GANIL. Parmi les lettres d’intentions d’expériences déposées par cette communauté auprès du GANIL figurait l’atome radioactif ^{74}Rb (64.8 ms). Il a été choisi comme cas d’école. Pour comprendre ce choix, il est nécessaire de décrire plus précisément le processus de production (Chap. 1, §1.5).

Optimisation d’un dispositif de production ISOL

L’ensemble du dispositif de production est placé sous vide d’air, à une pression environ égale à un milliardième de la pression atmosphérique ce qui permet en grande partie de négliger l’influence de la présence d’air sur le processus de production.

Le faisceau d’ions primaire entre en collision avec les atomes d’une cible. Des noyaux radioactifs sont produits. Une partie importante de l’énergie du faisceau est déposée dans le matériau cible, qui doit dissiper cette énergie donc avoir des caractéristiques de tenue en température, d’émissivité et de conduction thermique qui le lui permettent. Les caractéristiques de la cible et de son environnement doivent être adaptées aux caractéristiques du faisceau primaire (puissance, énergie) et à l’isotope à produire[1] (Chap.2, §2.1 et §2.2). Une fois les noyaux radioactifs arrêtés dans le matériau cible, leur cortège électronique se reconstitue et ils deviennent des atomes, dont le noyau est radioactif. Sous l’effet de la température de la cible, augmentée grâce au dépôt de puissance du faisceau primaire ou à un chauffage additionnel, les atomes se propagent en dehors du matériau cible puis sont ionisés. Les caractéristiques de l’atome et de l’environnement dans lequel il évolue conditionnent fortement ces deux processus. La structure du matériau cible conditionne le cheminement des atomes en son sein. La température, la nature du matériau cible et de l’atome conditionnent sa vitesse de propagation. Ce processus de propagation dans la matière et généralement appelé « diffusion » et nous verrons que l’entendement de ce processus doit être précisé (Chap. 2, §2.3). Une fois sorti du matériau cible, l’atome se propage dans la cavité du système de production (généralement appelé ensemble cible source (ECS) en français, ou Target Ion Source System (TISS) en anglais) qui est un environnement plus ouvert, c'est-à-dire où le

---

[1] L’environnement de la cible doit aussi être capable de supporter les conditions thermiques et de rayonnements issus de l’irradiation de la cible. Je n’ai pas traité cet aspect durant mon travail de thèse, mais ils ont été pris en compte grâce à l’expérience des personnes qui ont participé au design du dispositif de production.

libre parcours moyen entre deux collisions est plus important (Chap. 2, §2.5). Lorsque l'atome entre en collision avec une paroi de la cavité, il peut y passer un certain temps (Chap. 2, §2.4). Un système d'ionisation, connecté à- ou partie de la cavité, ionise (ou n'ionise pas) l'atome avant qu'il sorte de la cavité (chap.2, §2.6). Les ions qui émergent de la cavité sont accélérés par un champ électrique pour former un faisceau. Les ions sont alors triés en utilisant différents procédés, le tri en fonction du rapport masse sur charge dans un dipôle magnétique étant le plus répandu mais étant de plus en plus souvent associé à un système d'ionisation par laser [3]–[6].

Chacun des processus internes au dispositif de production a été étudié pour tenter de minimiser son temps dans le cas d'atomes de Rb.

Le dispositif proposé ne résulte pas simplement d'une réponse apportée aux besoins d'optimisation exposés préalablement. L'expérience de l'équipe du GPI avait permis en amont de ma thèse d'imaginer un principe, sans l'avoir étudié en détails et donc sans en avoir démontré quantitativement les possibles performances.

Mon travail a principalement consisté à démontrer les performances atteignables après optimisation.

Cette optimisation reste cependant partielle. Elle pourrait bénéficier d'une modélisation globale qui n'a pas été abordée mais qui pourrait s'inspirer de la démarche suivie dans cette thèse. Elle devra cependant s'appuyer sur des données d'entrée solides issues de résultats expérimentaux. Faute de quoi la confiance qu'il sera possible d'accorder à cette modélisation restera discutable.

Principe technique du dispositif de production

Le principe du dispositif de production d'ions ^{74}Rb est présenté Figure 17. Les choix sont justifiés après cette description.

Le dispositif est une cavité constituée de deux feuilles séparées par un anneau en graphite. Dans le sens d'écoulement du faisceau d'ions primaire (faisceau de ^{20}Ne à 110 MeV/A), la première feuille est une cible mince (feuille de ^{58}Ni de 3 µm d'épaisseur). Dans cette feuille, appelée cible de production, ont lieu les réactions nucléaires. En aval se trouve une feuille de fibre de carbone appelée « catcher » (200 µm d'épaisseur, densité 1.1 g/cm^3). L'anneau en graphite (de 50 mm de diamètre, 12 mm de long selon la direction du faisceau primaire) sert à maintenir les feuilles en regard l'une de l'autre. Un orifice de 4 mm de diamètre est réalisé sur le périmètre de l'anneau pour permettre aux ions de sortir. Un fort courant (quelques centaines d'ampères) s'écoule dans la paroi de l'anneau et dans les feuilles, à partir d'un point opposé de l'orifice, et jusqu'à l'orifice. Ce courant permet simultanément de chauffer les parois par effet Joules et de créer un champ électrique dans la cavité.

Les ions ^{20}Ne du faisceau primaire collisionnent avec les noyaux de ^{58}Ni de la cible de production. Des noyaux de ^{78}Sr sont formés par fusion. Par conservation de la quantité de mouvement du ^{20}Ne incident, les noyaux de ^{78}Sr reculent, sortent de la cible et s'implantent dans la feuille de fibres de graphite (catcher). Après formation, les noyaux de ^{78}Sr décroissent en évaporant des protons, neutron ou des particules α, et génèrent des isotopes de ^{74}Rb. Compte tenu de l'énergie de recul des noyaux de ^{78}Sr, ils sont implantés à la surface de la feuille de fibres de graphite.

La température élevée de l’ensemble permet de diminuer le temps de déroulement des différents processus physico-chimiques (diffusion, effusion, collage) qui interviennent dans la transformation atome-ion. Les noyaux diffusent à la surface de la feuille, où ils sont ionisés par ionisation de surface. Lors de leur effusion dans la cavité, ils sont entrainés par le champ électrique vers l’orifice de sortie puis sont accélérés sous forme de faisceau.

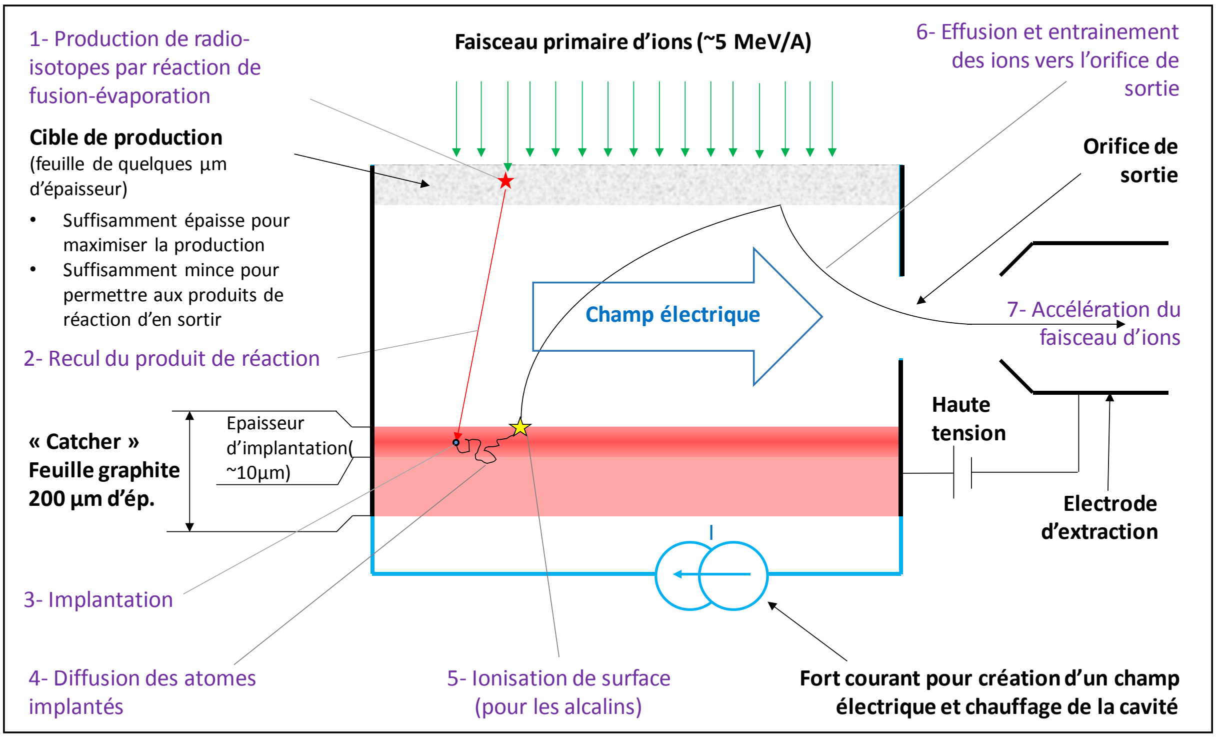

Figure 7: Principe du dispositif de production. Les étapes de la production et de la transformation sont numérotées de 1 à 7.

La simplicité du dispositif a été imposée d’emblée pour répondre à l’exigence opérationnelle de fiabilité : à part l’environnement commun à l’ensemble des ensembles cible-source de SPIRAL-1 (connectique et chambre à vide qui renferme de dispositif) le système ne comporte que 7 pièces mécaniques (hors vis) : les deux feuilles, l’anneau en graphite, deux brides de maintien des feuilles sur l’anneau et deux pièces de connexion du circuit de courant.

La compacité du système était aussi un prérequis. Le temps TAI étant dans tous les systèmes ISOL lié à la taille et à la complexité du cheminement des atomes dans le dispositif de production, il était important que le dispositif soit aussi compact et simple que possible pour minimiser ce temps et espérer produire des ions radioactifs de courte durée de vie. Les systèmes existants permettant de produire des isotopes radioactifs ayant une durée de vie de l’ordre de 100 ms avec une efficacité de l’ordre de 10%, le but visé de ce développement était de produire des ions radioactifs ayant une durée de vie proche de 10 ms avec la même efficacité. Cette approche a été initialement utilisée par R. Kirchner dans les années 70-80 [7], [8] pour concevoir un dispositif de production utilisant les réactions de fusion-évaporation dans une cible mince. La cible était associée à une source FEBIAD (Forced Electron Beam Ionization by Arc Discharge, ou système d’ionisation par impact électronique) ou à une source à ionisation de surface (qui utilise le phénomène d’échange électronique entre un atome et une surface lors de leur contact). Dans ce dispositif, les noyaux de recul étaient formés dans une cible mince et passaient au travers d'une fenêtre mince pour entrer dans une cavité où ils s'arrêtaient dans un catcher d'où ils diffusaient, effusaient avant d'être ionisés. L'ensemble était maintenu à haute température (2300 K). Malgré le volume réduit de la cavité (de l'ordre du cm^3), le temps TAI pour les atomes de Kr et de Xe était de l'ordre de 100 ms. Et dans le cas de ces gaz rares, le temps TAI n'était pas allongé par la réactivité chimique des atomes avec les constituants de la cavité, ce qui aurait été le cas pour des atomes métalliques.

Plus récemment, des catchers gazeux [9] ont été conçus pour s'affranchir, au moins partiellement, de l'impact sur le temps TAI de la réactivité chimique des atomes. Cependant, l'implantation d'un tel dispositif nécessite l'utilisation d'un système de pompage dont le volume est inenvisageable sans une modification importante du bâtiment de SPIRAL-1. Le dispositif présenté dans cette thèse poursuit donc simplement les développements menés par Kirshner, et reprend particulièrement l'idée de minimisation du volume de l'ensemble cible-source.

Principe et conception de la cavité du système de production (§1.6).
Minimiser le volume de la cavité de l'ECS minimise la puissance que le faisceau primaire pourra déposer dans l'ECS. Comme présenté.

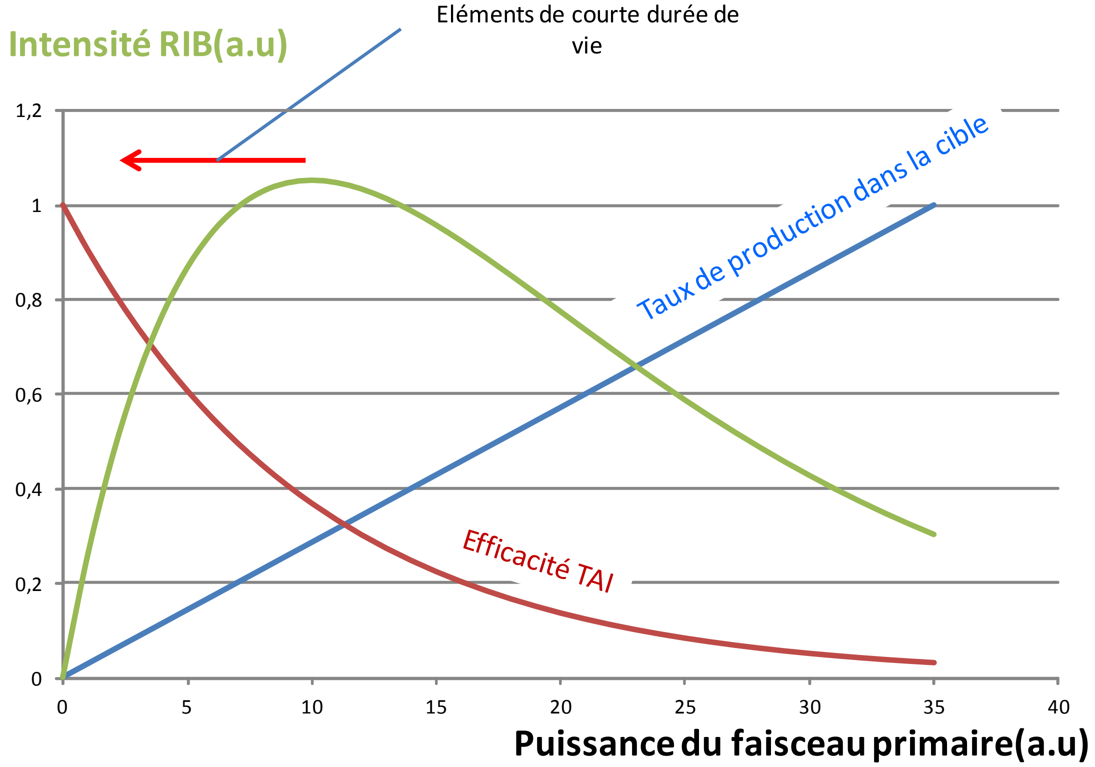

Figure 6, diminuer le volume permet d'augmenter l'efficacité de TAI, mais diminue le taux de production d'isotopes dans la cible. Dans le cas du faisceau primaire de ^{20}Ne délivré à GANIL, une puissance de 308 W est disponible. Pouvoir utiliser toute la puissance disponible tout en maximisant l'efficacité serait idéal, mais comment faire ?

Pour des raisons d'optique du faisceau primaire dans l'installation SPIRAL-1, le diamètre d'irradiation maximum de la cible est de 40 mm. La température de la cavité doit être maximum pour minimiser le temps des processus chimiques, mais doit aussi rester inférieure à la température de fusion du constituant de plus bas point de fusion de la cavité, c'est-à-dire la feuille de nickel (T_{fusion} ~1700 K). Pour minimiser l'élévation de température lors de l'envoi du faisceau primaire sur la cible de production et éviter le risque de sa destruction par sur-échauffement, la densité surfacique d'énergie déposée sur la cible doit être minimum, donc le faisceau doit être réparti sur toute la surface disponible de la cible, à savoir un disque de 40 mm de diamètre. Une cible de 50 mm de diamètre a cependant été choisie pour éviter d'implanter le faisceau dans les parties périphériques à la cible.

L'épaisseur de la cible a été déduite du calcul de sections efficaces de production effectuées à l'aide du code PACE [10]. Pour plusieurs couples faisceaux primaires/ matériaux cibles, un balayage en énergie a été effectué de façon à déterminer l'optimum de section efficace, en amplitude et en énergie (cas de la collision ^{20}Ne→^{58}Ni Figure 8).

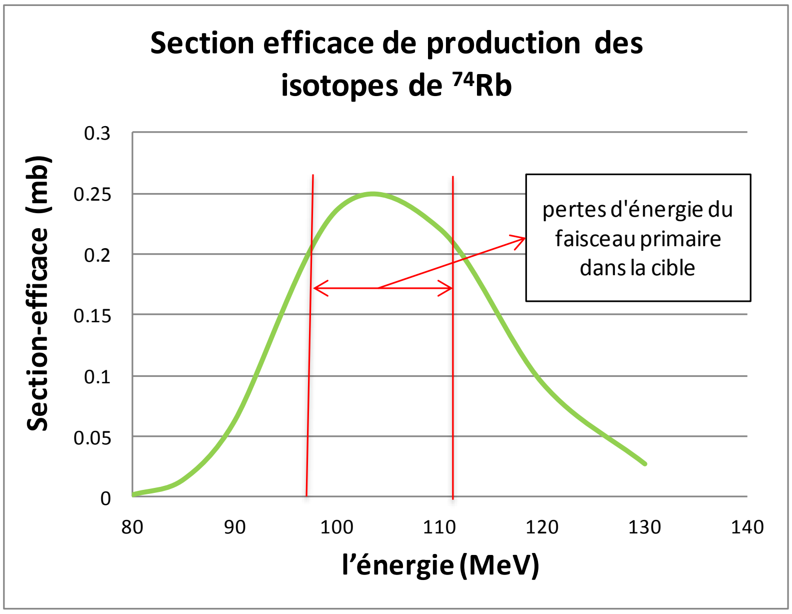

Figure 8: Section efficace de production des isotopes de ^{74}Rb en fonction de l'énergie de la collision ^{20}Ne → ^{58}Ni

Une fois le meilleur couple projectile-cible choisi pour produire des isotopes de ^{74}Rb, l'énergie de recul du ^{74}Rb a été extraite et son parcours dans la feuille de ^{58}Ni a été calculé à l'aide du code SRIM [11]. Une épaisseur de 3 µm de ^{58}Ni a été retenue. Pour maximiser le taux de réactions, l'énergie du faisceau de ^{20}Ne a été fixée à 110 MeV en entrée de la cible. La plage d'énergie couverte entre entrée et sortie (110 MeV à 98 MeV) assure théoriquement de couvrir au mieux le pic de section efficace de réaction, compris entre 80 et 130 MeV. Une démarche identique a été menée pour la production du ^{114}Cs.

Une recherche d'optimisation rigoureuse aurait imposé une étude du taux de production en fonction des dimensions et performances du dispositif. Cette démarche aurait été possible mais complexe et hasardeuse au regard du nombre de paramètres qu'elle implique et de leur dépendance mutuelle. La décision de concevoir un dispositif pouvant utiliser toute l'intensité du faisceau primaire de ^{20}Ne disponible à GANIL ne respecte pas ce souhait d'optimisation, et a conduit à une cible relativement étendue au regard de celle utilisée par Kirschner, donc à des dimensions de cavité d'ECS plus importantes. Si l'on considère que les atomes de Rb se déplacent de façon aléatoire, avec une vitesse d'effusion gouvernée par la loi de Maxwell-Boltzmann $\left(\sqrt{\frac{8k_BT}{\pi m}}\right)$, la dimension de la cavité engendre nécessairement une augmentation du temps TAI et donc une diminution d'efficacité de TAI pour le ^{74}Rb dont la durée de vie n'est que de 64.8 ms. Pour éviter cet allongement du temps TAI, la cavité a été conçue de façon à ce qu'un champ électrique de quelques volts soit présent dans la cavité. Les atomes de Rb, possédant un potentiel de première ionisation faible par rapport aux autres éléments chimiques, peuvent être très efficacement ionisés dans une cavité chaude, moyennant un choix judicieux des matériaux qui la constitue. Cette particularité des atomes de Rb a conduit à les choisir pour le cas d'école que constitue cette étude. Cela permettait d'assurer qu'ils seraient en permanence présents sous forme d'ions dans la cavité. Le champ électrique permet alors de favoriser leur déplacement vers l'orifice de sortie. Un calcul Monté-Carlo mené à l'aide du code Molflow+ [12] prenant en compte le temps de collage des atomes de Rb sur les parois de la cavité montre que l'utilisation du champ électrique pour extraire les ions diminue leur temps de présence dans la cavité d'un facteur 10 (Figure 9).

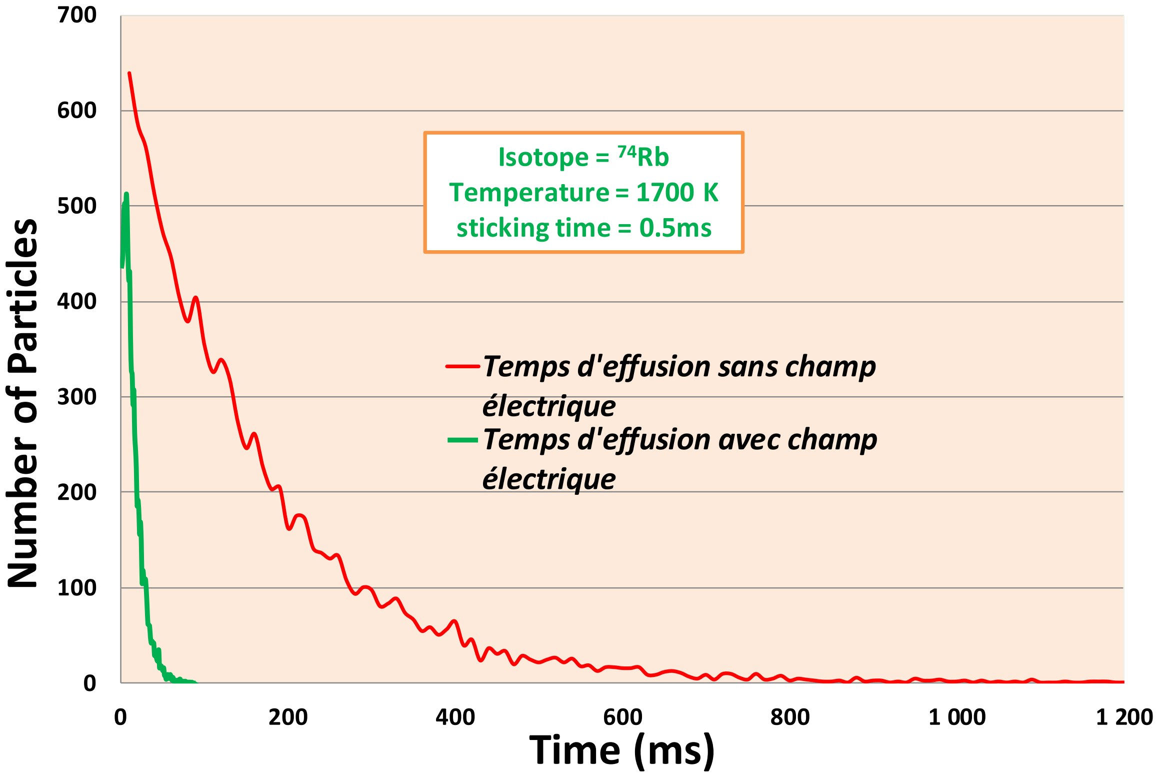

Figure 9: Calcul du temps d'effusion des ions (code Molflow) dans la cavité (50 mm de diamètre, 12 mm de long) avec (ligne verte) et sans champ électrique (ligne rouge). Temps de collage par contact : 0.5 ms. Temps d'effusion 120 ms sans champ électrique, et 12 ms avec champ électrique.

Avant d'effuser dans la cavité, les produits de la réaction de fusion émergent de la cible de production, traversent la distance qui la sépare du catcher (feuille de fibres de graphite) et arrêtent leur course dans le catcher. Leur énergie maximum d'implantation est de 28 MeV, ce qui correspond pour le ^{74}Rb à un parcours maximum de 26 µm dans les fibres de graphite (densité 1.1 g/cm^3). Pour que la probabilité de diffusion des atomes de ^{74}Rb vers l'intérieur de la cavité soit plus importante que vers l'extérieur du catcher, il était nécessaire que le catcher ait une épaisseur significativement supérieure à leur parcours. De plus, la feuille qui constitue le catcheur participe au chauffage de la cavité et à la génération du champ électrique. Enfin, il fallait que le matériau choisi pour le catcheur existe si possible commercialement pour ne pas avoir à le synthétiser.

Les feuilles de fibre de carbone (nom commercial Papyex [13]) existent en épaisseurs standard de 200 µm. Un calcul grossier, basé sur le raisonnement suivant, a permis de retenir une épaisseur de 200 µm, 1 mm, 1.5 mm, 2 mm, 3 mm ; le champ électrique désiré dans la cavité était de l'ordre de 1V/cm, champ déduit d'un travail antérieur [14] qui a quantifié l'effet d'un champ électrique appliqué dans un tube ioniseur en graphite sur l'efficacité de l'ionisation de surface d'alcalins. L'étude avait été faite pour un diamètre de tube de 4 mm de diamètre intérieur, et montrait clairement qu'une augmentation la distance entre parois conduisait à une diminution du temps TAI, donc augmentait l'efficacité dans le cas d'ions radioactifs de courte durée de vie. La distance entre feuilles a donc été fixée à 12 mm, sans tentative d'optimisation ultérieure. Pour une cavité de 5 cm de diamètre, l'ordre de grandeur de la différence de potentiel entre extrémités de la cavité devait donc être de l'ordre de 5V. Par conception de la cavité, cette différence de potentiel est simultanément appliquée aux extrémités de la feuille cible en nickel et de la feuille de Papyex. Obtenir un courant égal dans chacune d'elles nécessitait qu'elles aient des résistances proches. Connaissant la résistivité de chaque matériau (résistivités Ni : 58 µΩ.cm et Papyex : 310 µΩ.cm) et l'épaisseur de la feuille de nickel, il était possible d'en déduire l'épaisseur que devait avoir la feuille de Papyex. Mais les températures limites de ces deux matériaux sont très différentes (respectivement ~1700 K et ~2300 K). Pour que le chauffage de l'ensemble des deux feuilles en regard soit principalement dû à la puissance ohmique dissipée dans la feuille de Papyex, cette feuille a été volontairement choisie plus épaisse et donc moins résistive que la feuille de nickel (3 µm pour le nickel, 200 µm pour le Papyex). Cette évaluation, nécessairement grossière par la non prise en compte de la « structure électro-mécanique » de la cavité (présence de l'anneau entre feuille, brides de maintien, forme complexe), a été affinée par un analyse en éléments finis à l'aide du code ANSYS [15]. Ce code a simultanément permis de simuler les voies d'écoulement des courants, d'évaluer les différences de potentiel (Figure 10) et de calculer la température des différentes parties (Figure 11).

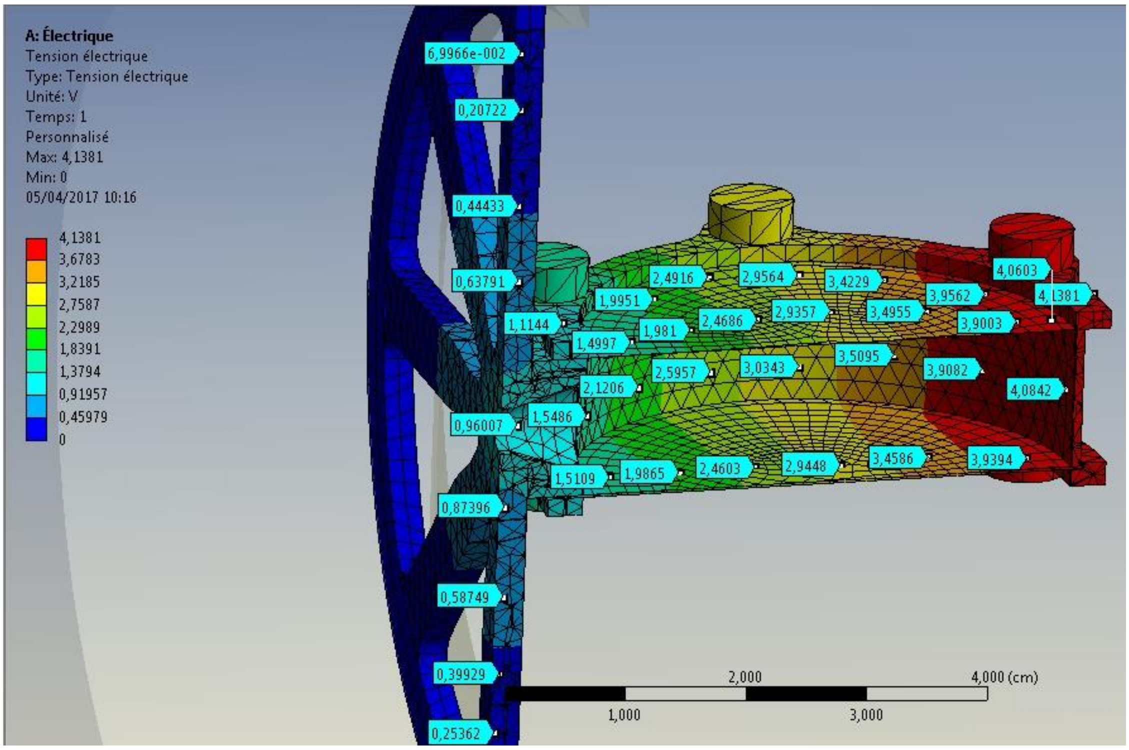

Figure 10: Potentiels en différents points du dispositif obtenus à l'aide du code ANSYS. Le courant traversant a été fixé à 300A, limite de l'installation SPIRAL-1.

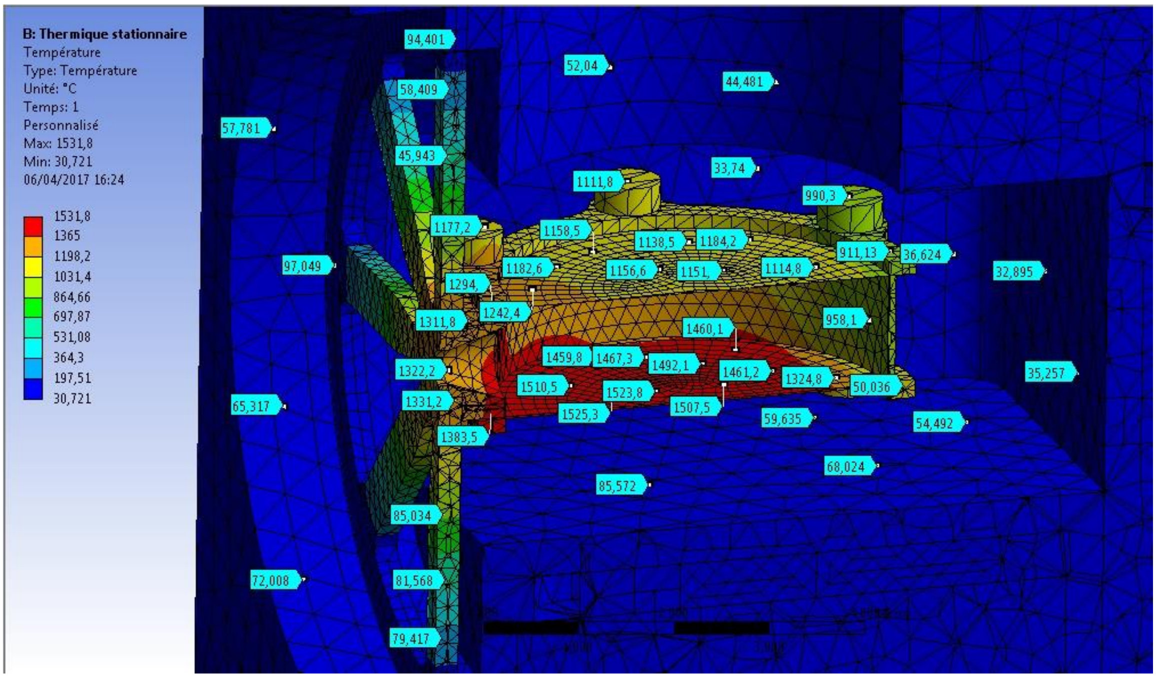

Figure 11: Simulation obtenue à l'aide du code ANSYS de la température du dispositif de production en différents points. La puissance électrique totale est de 1500 W.

Plusieurs itérations et modification du design de la cavité ont été nécessaires pour aboutir à l'obtention simultanée d'une température sur la feuille de nickel inférieure à sa limite, tout en ayant une température relativement homogène (de 958°C à 1330°C) pour le reste de la cavité, et une différence de potentiel entre extrémités de la cavité proche de 5 V.

Rq : Faute d'avoir trouvé un ensemble de données de résistivité et d'émissivité homogène en terme de protocole de mesure et de plage de température, nous avons construit un dispositif dédié à la mesure de ces deux paramètres en fonction de la température. La conception mécanique a été faite par le bureau d'étude, en partie sur la base du dimensionnement que j'ai effectué. Ce dispositif est décrit en annexe 3.2.

Le dessin en coupe de la cavité est donné Figure 12. Elle est reliée à une connexion faite d'une feuille de tantale côté injection de courant et à une roue à rayons en graphite côté sortie du courant et sortie des ions. Un calcul de contraintes thermomécaniques effectué à l'aide du code ANSYS a permis de vérifier que la dilatation des différentes pièces n'engendrait pas de risque de rupture de pièces. Les longueurs de la feuille de Ta et des rayons en graphite ont été choisies pour limiter le refroidissement de la cavité par transport de chaleur jusqu'à leurs points de fixations sur la chambre à vide refroidie dans laquelle la cavité de production est installée.

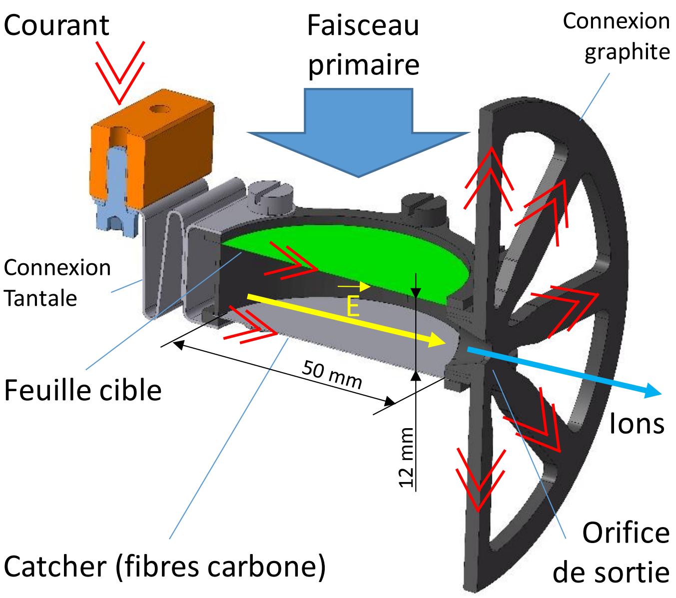

Figure 12: Dessin en coupe de l'ensemble de la cavité du dispositif de production.

Optimisation du catcher (§2.2 et 2.3).

La contribution du temps de relâchement des atomes radioactifs en dehors des matériaux cibles des systèmes ISOL est souvent importante dans le temps total de TAI. De nombreux travaux [16]–[20][21] ont donc été menés pour limiter ce temps et maximiser le taux d'ions radioactifs relâchés en trouvant un compromis entre taux de noyaux produits dans la cible et vitesse de relâchement. Avec le dispositif proposé, ce compromis n'est pas nécessaire car la cible de production (feuille de Ni) est différente du matériau dans lequel les ions radioactifs sont stoppés (catcher en fibre de graphite). Cette séparation des fonctions de production et d'arrêt simplifie leur optimisation individuelle. Du point de vue du relâchement, seul le catcher doit être optimisé.

Le catcher est ici un assemblage de fibres de graphite pressées en feuilles et recuites pour les lier. Ce choix a été fait tardivement au cours du développement de l'ECS, en partie parce que l'épaisseur de graphite requise par les raisons thermo-électriques était difficilement réalisable à l'aide d'une feuille solide de graphite.

Au début de ce travail de thèse, une étude avait donc été entamée pour optimiser le relâchement des atomes radioactifs en dehors d'une feuille de graphite. Le graphite considéré est réalisé par frittage et recuit d'une poudre de grains de carbone graphène sélectionnés en taille (typiquement du µm à quelques dizaines de µm). Il peut être décrit comme un assemblage de grains en contact et séparés par des espaces libres de matière qui constituent la porosité du matériau. La structure microscopique du matériau détermine l'ouverture entre les pores (si les pores communiquent entre eux, on parle de porosité ouverte). Dans le cadre de cette étude, et contrairement à la plupart des travaux sur le relâchement d'atomes en dehors d'un matériau dans lesquels un seul processus appelé « diffusion » est considéré, on considère ici qu'il existe deux processus correspondant à deux milieux différents dans lesquels les atomes doivent se déplacer pour sortir du matériau catcher : le milieu dense des grains, où les atomes sont arrêtés et où on emploiera le terme de diffusion pour décrire le processus de propagation, et les pores où on emploiera le terme d'effusion.

Plusieurs travaux [22], [23] confirment qu'une diminution de la taille de grain est favorable au relâchement, moyennant qu'elle s'accompagne d'une porosité ouverte importante, qui implique une densité de matériau faible. Ces résultats posent la question de savoir si à une densité de matériau donnée, il existe une taille de grain, et donc de pores, qui minimise le temps total de relâchement.

Plus précisément, pour un volume donné, le temps de relâchement en dehors d'un grain homogène de matière est proportionnel au carré de son rayon, alors qu'en dehors d'une sphère creuse, il est proportionnel au rayon. De plus, le facteur de proportionnalité entre temps et dimensions géométriques est plus important dans le cas d'un grain de matière que dans le cas d'un espace vide, ce qui augmente le temps de sortie des atomes en dehors des grains. Diminuer la taille des grains accélère donc nécessairement le relâchement des atomes en dehors des grains, ainsi que le relâchement en dehors de chaque pore (pour un rapport constant entre surface interne de pore sur ouverture du pore). Mais à densité macroscopique constante du matériau et pour une épaisseur de matériau fixe, diminuer la taille des grains conduit à une diminution de la taille des pores et à l'augmentation du nombre de pores au travers desquels les atomes devront se propager pour sortir du matériau. Ces deux processus, relâchement en dehors des grains et effusion au travers des pores ayant des effets opposés sur le temps lorsque la taille des grains évolue, une taille de grain optimum doit exister, qui minimise le temps de relâchement des atomes en dehors du matériau.

Pour la déterminer de façon grossière, la structure d'une cible frittée a été décrite de façon simplifiée. Une feuille de matériau de grains frittés, d'épaisseur macroscopique, est assimilée à un ensemble de sphères alignées Figure 13.

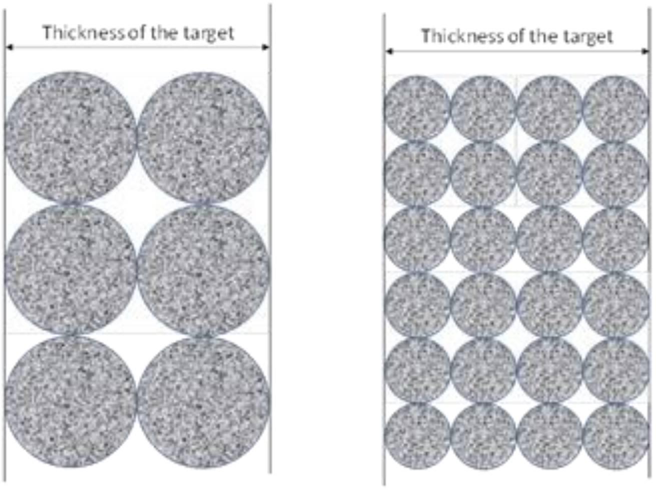

Figure 13: Arrangement géométrique des sphères, correspondant aux grains de matière à l'intérieur d'une feuille de matière

Les sphères représentent les grains où la densité de matériau est maximum. Elles sont en contact ponctuels (densité 1.1 g/cm^3 pour le carbone) ou présentent un recouvrement, selon la densité macroscopique choisie. Une densité maximum de 2.2 g/cm^3 pour le carbone correspond à un recouvrement total, donc à un matériau sans pores.

Les processus de diffusion et d'effusion interviennent dans des régions identiques à une échelle macroscopique, mais différentes à l'échelle microscopique des grains et des pores. Les atomes sont d'abord libérés des grains, et le taux d'atomes relâchés en dehors des grains donné par une expression établie par Fujioka [24], alimente le processus d'effusion dans les pores jusqu'à ce que les atomes atteignent la surface du catcher (on suppose que la forme du catcheur est une feuille). Certains coefficients de diffusion peuvent être extraits de la littérature. Le coefficient d'effusion et de diffusion n'ayant jamais été clairement séparé, la détermination du coefficient d'effusion a nécessité une approche nouvelle donnée au paragraphe 2.3. Il a été calculé au niveau microscopique pour un pore. Le pore élémentaire est assimilé à l'espace situé entre 8 sphères accolées. Le coefficient d'effusion étant par définition intensif, c'est-à-dire indépendant des dimensions macroscopiques du catcher, le coefficient d'effusion déterminé au niveau microscopique a été utilisé au niveau macroscopique pour évaluer le taux d'effusion des atomes en dehors du catcher. Pour se faire, il a été introduit dans l'expression elle-aussi établie par Fujioka pour calculer le flux d'atomes qui se propagent en dehors d'une feuille. La combinaison des processus consécutifs de diffusion et d'effusion a permis d'obtenir l'expression suivante du flux $F(t)$ d'atomes relâchés à l'instant t. $t = 0$ correspond à l'instant de l'apparition de N_0 atomes dans les grains du catcher. Dans le cas présent, il s'agit de l'implantation des noyaux radioactifs:

$$\boldsymbol{F(t) = 48.\lambda_D.\lambda_E.N_0.e^{-\lambda t} \sum_{n=0}^{\infty} \sum_{m=1}^{\infty} \frac{1}{\lambda_{En} - \lambda_{Dm}} \left[e^{-\lambda_{Dm}t} - e^{-\lambda_{En}t}\right]}$$

λ_D(s^{-1}) est le taux de diffusion, lié au coefficient de diffusion D (cm^2/s) par la relation $\lambda_D = D/4R^2$, où R est le rayon des grains,

λ_E (s^{-1}) est le taux d'effusion, lié au coefficient d'effusion D_E par la relation $\lambda_E = D_E/d^2$, où d est l'épaisseur du matériau catcher.

λ (s^{-1}) est le taux de décroissance radioactive de l'atome considéré

λ_{Dm} et λ_{En} sont des taux de diffusion et d'effusion liés aux taux λ_D et λ_E et définis par le formalisme mathématique proposé par Fujioka.

Il est possible de déduire de cette expression celle du temps moyen de relâchement, qui a été représenté Figure 14 dans le cas de la propagation d'atomes d'^{35}Ar ($T_{1/2}$=1.79 s) dans une feuille de matériau faite de grains de graphène, d'une épaisseur de 3 mm et d'une densité égale à 1.8 g/cm^3. Le coefficient de diffusion a été extrait de mesures antérieures [25].

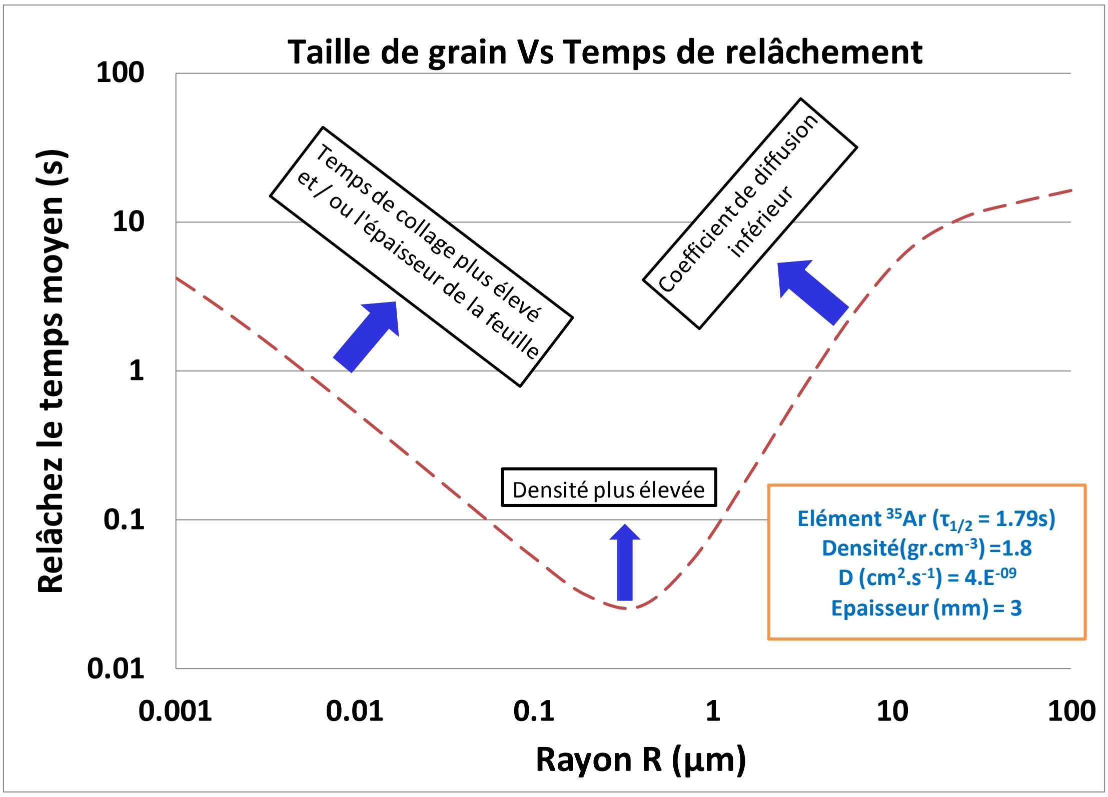

Figure 14: Temps de relâchement moyen des atomes en dehors du matériau en fonction de la taille des grains dans le cas de l'isotope ^{35}Ar ($T_{1/2}$=1.79 s).

Ce calcul, bien que grossier, présente l'avantage d'être analytique, de ne pas avoir recours à des paramètres d'ajustement et de donner la tendance qu'auront les paramètres physiques sur le temps moyen de relâchement. Il montre que dans les conditions de l'exemple, il existe un temps de relâchement minimum pour une taille de grains de l'ordre de 0.3 µm, taille qu'il est techniquement possible d'atteindre. Mais de façon plus générale, il montre comment il est possible de faire évoluer le choix de la taille des grains en fonction des autres paramètres du matériau. Les flèches reportées sur la figure indiquent le sens de déplacement de la courbe dans différents cas, cas qui conduisent à augmenter le temps moyen de relâchement : introduction d'un temps de collage des atomes lors de leur effusion dans les pores, augmentation de l'épaisseur de la feuille, augmentation de la densité et diminution du coefficient de diffusion dans les grains.

Faute de temps, ce calcul n'a pas été mené spécifiquement pour le relâchement de du ^{74}Rb en dehors de fibres de carbone. Il pourra être adapté en suivant la même démarche et en remplaçant la matrice de sphères par une matrice de fibres et en adaptant en conséquence les formules analytiques. L'introduction du temps de collage des atomes de Rb sur le carbone sera aussi nécessaire.

Une estimation du temps de sortie du Rb en dehors d'une matrice de graphite a cependant été faite. Compte tenu de la très faible épaisseur d'implantation du Rb dans le graphite (12 µm max. pour une densité de 1.1 g/cm^{3}), son temps caractéristique de sortie est de ~7 ms.

Optimisation du processus d'effusion.

Le processus d'effusion correspond au déplacement d'atomes ou d'ions dans un espace relativement libre, où le libre parcours moyen entre deux collisions est significativement plus grand (plusieurs diamètres atomiques) que dans la matière dense, où les atomes sont en « contact » quasi permanent avec un atome de la matière. L'effusion procède donc par vols libres successifs, entrecoupés de contacts avec la matière. Le temps d'effusion est la somme du temps de vol libre et du temps de contact.

Le temps de vol libre dans une cavité de volumes simples et ouverts munie d'un orifice de forme géométrique simple peut être estimé en première approche en divisant le volume de la cavité par la conductance de l'orifice (voir §2.5). Cette conductance dépend des caractéristiques de l'orifice, de la masse de l'atome considéré et de l'énergie cinétique des atomes. Cette méthode est aisément utilisable dans le cas des gaz rares dont le temps de contact sur les parois peut être négligé pour les températures typiques des systèmes ISOL (toujours supérieures à la température ambiante).

Optimisation du temps de collage.

Dans le cas des atomes chimiquement réactifs, le temps de contact des atomes avec les parois du système de production (voir étude §2.4) peut être plus long que de la durée de vie des atomes radioactifs visés dans cette thèse (quelques dizaines de ms). Une fois collés sur une paroi, les atomes seront possiblement perdus. Il est donc essentiel de minimiser ce temps de collage. De nombreuses données existent sur les temps de collage mais elles ont été obtenues en utilisant des protocoles et des dispositifs différents. Elles sont donc difficilement comparables. Et le nombre de combinaisons possibles atomes/surface/température étant très important, il est souvent difficile de trouver des résultats correspondant au cas d'intérêt. Concevoir un dispositif, le qualifier et mener une campagne de mesures systématiques de temps de collage avec différents matériaux et différents atomes aurait nécessité beaucoup plus que trois années de thèse. En plus d'être chronophage, la détermination des valeurs absolues de temps de collage est-elle utile à l'optimisation d'un système ISOL, sachant que les conditions rigoureuses de mesure (état de surface, propreté, température…) ne seront pas rassemblées dans un système ISOL ?
Au regard du temps TAI, optimiser le choix des matériaux de l'ECS consiste à minimiser le temps de collage. Dans un premier temps, la connaissance globale de l'évolution du temps de collage en fonction des couples atomes-matériaux semble donc suffisante. Mais je n'ai pas trouvé de représentation simple de cette évolution dans la littérature. Ma démarche a donc consisté à tenter une représentation du temps de collage déduit des énergies de désorption ($\mathrm{E_{des}}$) calculées par B. Eichler et al. [26] en fonction de deux paramètres qu'il m'a semblé relativement évident de considérer comme fortement impliqués dans la liaison chimique entre atome et surface, à savoir le potentiel de première ionisation de l'atome et le travail de sortie des électrons de la surface du matériau.

Le temps de collage est calculé à partir de l'énergie de désorption et de la température T en utilisant la formule de Frenkel [27]:

$$\mathrm{t = t_o . e^{-\left(\frac{E_{des}}{k_B . T}\right)}}$$

Où k_B est la constante de Boltzman et t_o est le temps vibratoire minimum induit par l'énergie thermique.Rq : $E_{des} < 0$.

Les données de Eichler ont été divisées en trois groupes :

- Atomes alcalins (Cs, Rb, K, Na) sur Nb, Zr, Al*, Ta, W, Cu*, Re, Ir
- Atomes alcalino-terreux (Ba, Sr, Ca, Mg) sur Nb, Zr, Ti, Ta, W et Re
- Atomes de métaux (La, In, Ti, Bi, Pb, Ag, Cu, Po, Cd, Hg) sur Mo, Fe* et W

Les calculs faits pour les surfaces marquées d'un astérisque sont hypothétiques, la température de fusion de ces matériaux étant inférieure à 1600 K.

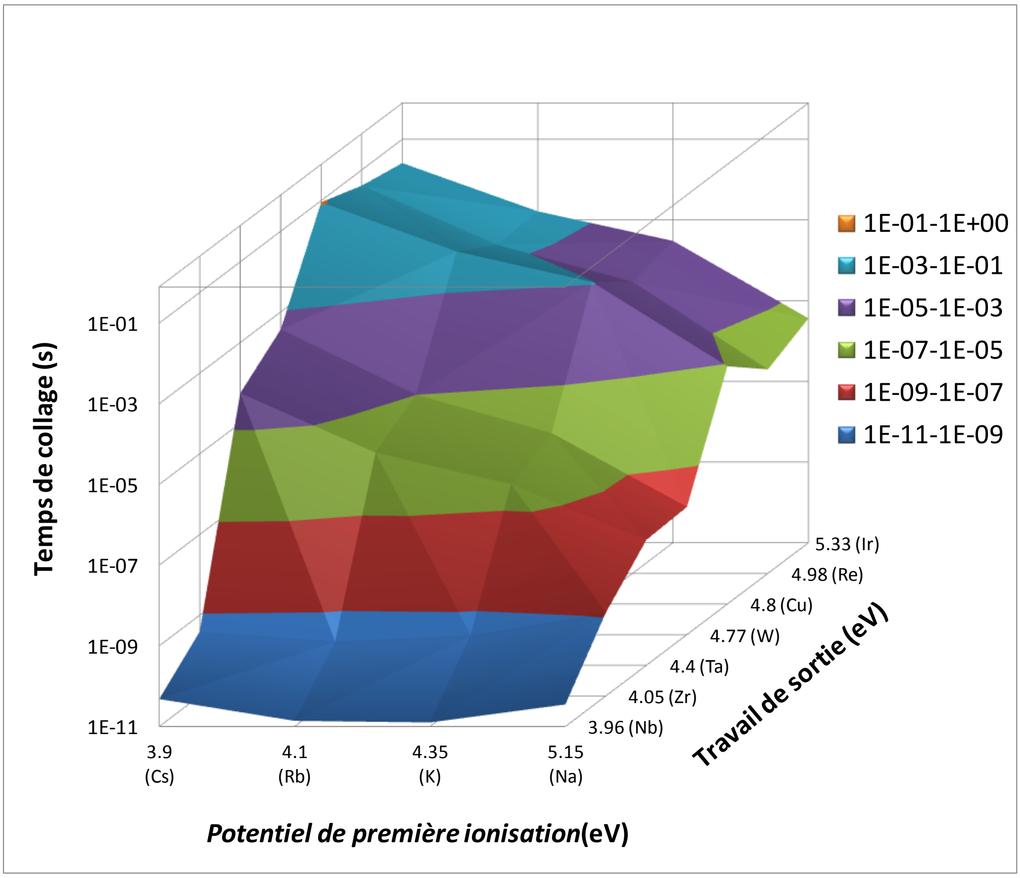

Figure 15: Temps de collage d'atomes alcalins (Na, K, Rb et Cs) sur différentes surface métalliques calculés à une température de 1600 K. Représentation en fonction de potentiel d'ionisation des atomes et du travail de sortie des surfaces de métaux.

Pour ces trois groupes de couples atomes/matériaux, une tendance très claire apparait sur l'évolution du temps de collage en fonction du potentiel de première ionisation des atomes et du travail de sortie du matériau : le temps de collage augmente si le potentiel de première ionisation diminue ou si le travail de sortie de la surface augmente. Le temps de collage est donc minimum pour des atomes de fort potentiel de première ionisation qui entrent en contact avec des surfaces métalliques de faible travail de sortie. Cette conclusion est issue d'un nombre de couples atomes/surface relativement restreint (86) au regard du nombre de possibilité mais elle concerne des éléments couvrant de larges domaines de potentiel de première ionisation (3.9 eV à 10.5 eV) et de travail de sortie (3.96 eV à 5.33 eV), et qui contiennent plusieurs des matériaux fréquemment utilisés dans la conception des systèmes de production ISOL.

La détermination par interpolation d'un temps de collage pour un couple atome/matériau qui ne fait pas partie des couples précédents mais dont les potentiels d'ionisation et travail de sortie appartiennent à ces domaines est tentant. Une étude plus poussée, basée sur un nombre de couple atomes/matériau plus large, permettrait de confirmer, infirmer ou nuancer la tendance extraite de cette étude.

En interpolant au cas de ce travail de thèse, on trouve qu'un atome de Rb restera sur une surface de Ni portée à 1600 K pendant un temps d'environ 0.5 ms. Ce temps a été pris en compte dans le temps d'effusion présenté Figure 9.

Estimation du taux de production d'ions de ^{74}Rb et de ^{114}Cs.
Finalement, on déduit des considérations précédentes de diffusion, d'effusion, de collage et d'ionisation que 50% des atomes de Rb produits devraient être transformés en ions et être sortis de la cavité au bout d'un temps de diffusion de 7 ms et d'un temps d'effusion de 12 ms (temps de collage inclus), à comparer à la demi-vie du ^{74}Rb qui est de 64.8 ms. Ces temps de TAI conduisent à une efficacité de TAI égale à 77%. Une telle efficacité pour un élément généralement considéré comme de courte de durée de vie par les experts de la méthode ISOL est remarquable. Elle permettrait, si la mise en œuvre du dispositif la confirme, de transformer la plupart des noyaux radioactifs de ^{74}Rb produits en ions. Cette efficacité, proche de 1, peut être comparée à celles obtenues dans les installations ISOLDE/CERN et ISAC/TRIUMF qui sont respectivement de l'ordre de 10^{-4} et 6.10^{-4}. Dans ces installations, les taux de production d'isotopes de ^{74}Rb dans la cible sont plus importants (respectivement 3.10^{6} pps avec un faisceau de protons de 1.2kW, 600 MeV sur une cible de Nb, et $1.2.10^{8}$ pps avec un faisceau de protons de 50 kW, 500 MeV sur Nb) que ceux attendus par fusion-évaporation avec un faisceau de 20Ne@110 MeV de 308 W sur une cible de Ni. Mais au final, le produit des productions dans la cible par l'efficacité TAI (2.10^{3} Rb/s pour ISOLDE, $1.7.10^{4}$ Rb/s pour ISAC et $2.5.10^{4}$ Rb/s pour SPIRAL-1, avec une efficacité TAI de 77%) pourrait donner la faveur à un système basé sur l'optimisation de l'efficacité. Cette comparaison est motivante mais optimiste : les valeurs des installations ISOLDE et ISAC sont des taux d'ions mesurés en sortie des systèmes de production, alors que la valeur pour SPIRAL-1 doit encore être démontrée expérimentalement.

J'ai mené une démarche identique pour la production de ^{114}Cs (0.57 s). Les résultats donnent dans ce cas une faveur très nette à l'installation SPIRAL-1, avec un taux de production (~$2.1.10^{4}$ pps) de plusieurs ordres de grandeur supérieur à celui obtenu à ISOLDE (5 pps de ^{114}Cs).

Caractérisation du dispositif (chap. 4).
La conception mécanique du dispositif a été faite en tentant de respecter au mieux les conclusions des études que j'ai menées (étude du collage, calculs d'épaisseur de cible, de profondeur d'implantation dans le catcheur, simulation de répartition du champ électrique, calcul de gain sur le temps d'effusion lié au champ électrique, recherches bibliographique) ou auxquelles j'ai participé (étude de propagation dans les matériaux, d'effusion, simulations thermiques). Une fois les parties du dispositif réalisées, j'ai participé à son montage, qui nécessite une attention soutenue compte tenu de la

fragilité des pièces (feuille de 3 µm en Ni, anneau en graphite de 0.8 mm d'épaisseur…).

Le dispositif a ensuite été installé sur un banc qui reproduit l'environnement des dispositifs de production dans la casemate de production.

La validation du fonctionnement d'un ECS peut être divisée en quatre étapes :

1. Dans un premier temps, les circuits de refroidissement, l'étanchéité au vide, la conformité mécanique et électrique sont vérifiés.
2. Vient ensuite un test de tenue thermique, qui consiste à porter les différentes parties chaudes à leur température nominale de fonctionnement sous faisceau en appliquant une puissance de chauffage adéquate. La température des parties visibles au travers de hublots à l'aide de pyromètres optiques est vérifiée. La durée de tenue en température requise lors du test sur banc par l'exploitation de l'installation SPIRAL-1 est de 3 semaines.
3. Le troisième test consiste à injecter des atomes ou des ions dans le dispositif pour mesurer son efficacité de TAI
4. Le dernier test est effectué en installant l'ECS dans la casemate de production, en irradiant la cible à l'aide du faisceau d'ions primaires et en mesurant le taux de production d'ions d'intérêt en sortie de l'ECS.

Après avoir passé avec succès le premier test, le dispositif a été chauffé jusqu'à sa température nominale de fonctionnement (1600 K) en 6 heures. La résistance de l'ensemble du circuit de l'ECS, déduite du rapport tension d'alimentation sur courant, est supérieure à celle déduite des simulations, malgré l'utilisation des données de résistivités et d'émissivités mesurées dans le cadre de ce travail pour la fenêtre en nickel et le catcher. Cette différence pourrait être expliquée par l'utilisation d'autres matériaux, dont les paramètres sont moins bien maitrisés, et pas les résistances de contact dont la résistance est difficile à évaluer.

La mesure de l'efficacité et du temps de réponse de TAI a été préparée dès le début de mon travail de thèse en remettant en fonctionnement et en adaptant un canon à ions et sa plateforme haute tension à sa future utilisation (voir §4.3). Son principe consiste à produire un faisceau d'ions alcalins (de Rb en l'occurrence) de faible énergie (typiquement 1 keV) et à l'envoyer dans la cavité du dispositif au travers d'un orifice réalisé préalablement dans la feuille de Ni. Une fois dans la cavité, la probabilité qu'ont les ions de ressortir par cet orifice est limitée par des considérations géométriques et par la présence du champ électrique dans la cavité. Le faisceau d'ions peut être continu ou pulsé, ce qui permet en plus de déterminer le temps de TAI caractéristique de la cavité, et ainsi de calculer a priori l'efficacité de TAI qu'aura le dispositif dans le cas d'ions radioactifs.

Ce dispositif est fonctionnel. Il est en mesure de délivrer une intensité de l'ordre de 1 µA d'ions alcalins (K^+) en continu ou sous forme de pulses d'une durée de 1 ms. Il n'a malheureusement pas pu être utilisé dans le cadre de ma thèse, faute de temps, mais sera disponible pour mon successeur.

Conclusions et perspectives

Un dispositif de production d'ions radioactifs de ^{74}Rb a conçu dans le but d'optimiser ses performances, en étudiant les différents mécanismes impliqués dans le processus de transformation des atomes en ions, et en cherchant un compromis technique entre production d'isotopes dans la cible et efficacité de transformation des atomes en ions.

Les performances estimées sont prometteuses : elles permettraient à l'installation GANIL/SPIRAL-1 de délivrer des faisceaux de ^{74}Rb et de ^{114}Cs avec des intensités compétitives voir jamais atteintes dans d'autres installations.

Le dispositif de production a été réalisé sur la base de mon travail. Sa compatibilité avec l'installation SPIRAL-1, en terme de servitudes, a été testée et validée.

Conformément au souhait initial de simplicité, motivé par le besoin opérationnel de fiabilité, le dispositif construit est simple, ce qui limite a priori les difficultés que sa mise au point générera.

Sa caractérisation a seulement pu être entamée au cours du travail de thèse. A ce jour, la tenue thermique de la cavité et du catcher est de 18 jours, sans aucune modification visible de la résistance. L'origine de la défaillance de la cible a été diagnostiquée et devrait aisément pouvoir être évitée.

Tous les instruments nécessaires sont disponibles pour poursuivre les tests thermiques, les mesures d'efficacité et les mesures de temps de réponse. Une fois qualifié, le dispositif devrait être testé en ligne avec faisceau primaire sur cible en collaboration avec l'IPN d'Orsay (2019), puis utilisé dans SPIRAL-1

La transposition de son principe à la production des isotopes déficients en neutrons de la chaine des Xe semble simple par association de la cavité à une source ECR. La possibilité de produire des éléments métalliques dans la région de l'^{100}Sn, déficients en neutrons et de courte durée de vie, est en cours d'étude et fera l'objet du travail de mon successeur.

English version

Context

An element and its properties are defined by its number of protons and electrons, the number of neutrons in the nuclei can vary. Nuclei with the same number of protons but a varying number of neutrons are called isotopes of an element. Certain combinations of protons and neutrons are known as the stable elements surrounding us. Other combinations where the number of neutrons is higher or lower than the stable elements are unstable with half-lives reaching up to billions of years. All known nuclei are listed in the nuclear chart (Figure 16) where the stable isotopes form the so called valley of stability (black dots). Isotopes on the left or right side of the valley of stability decay via a variety of possible channels towards the valley of stability and eventually end up as stable nuclei. Those unstable nuclei are called as radioactive isotopes.

The goal of this PhD is to study a technique for the short-lived radioactive ion beam production. To optimize the technique, the characteristics of the primary production mechanism must be well understood.

All nuclei, stable or radioactive, can be put on a “nuclide chart”, whose axes represent the number of neutrons and the number of protons they contain Figure 16.

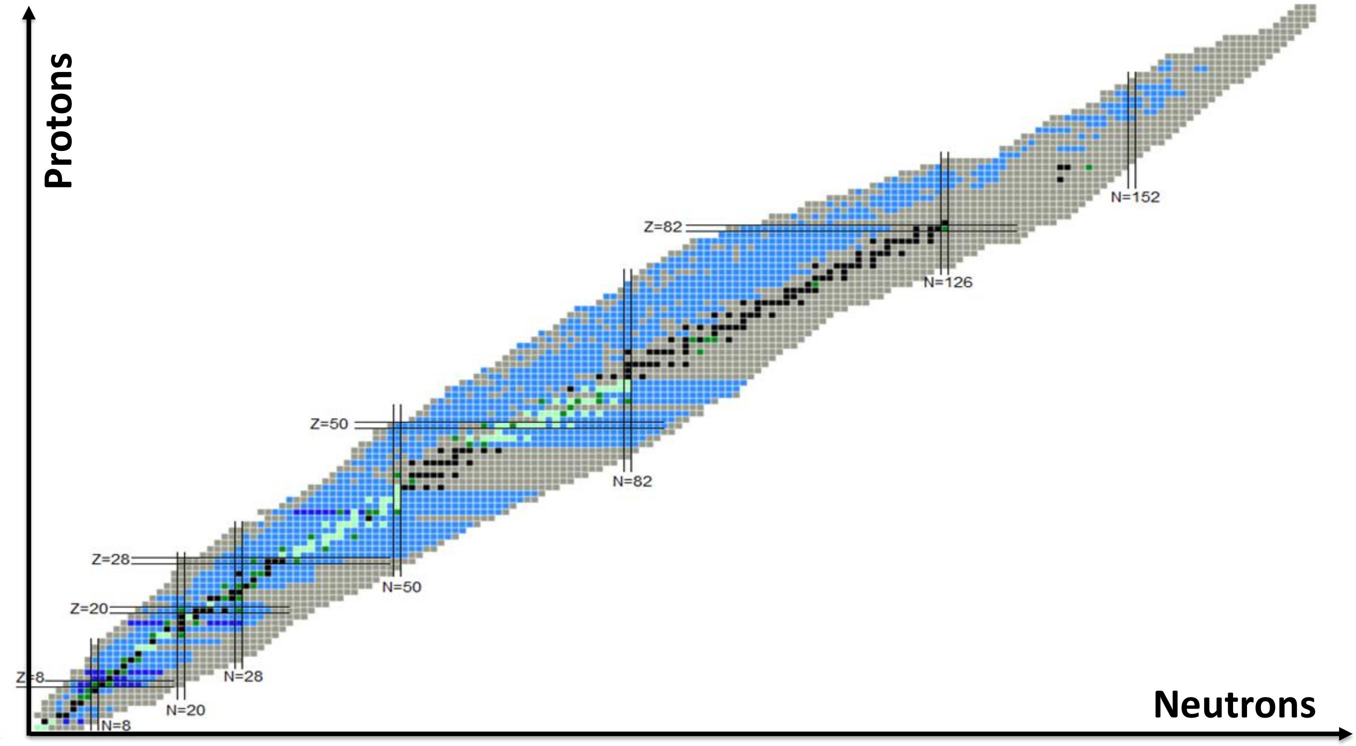

Figure 16: The presently known nuclei displayed according to proton number Z on the vertical scale, and neutron number N on the horizontal scale. The black squares denote the stable nuclei, and also the extremely long-lived nuclei like ^{238}U that exist on Earth. The blue and gray squares indicate radioactive nuclei.

We presently consider that the total number of “bound” nuclei is of some thousands [28]. However, the major part of the initial nuclei has disappeared from the earth and are therefore called exotic nucleus. To produce them, stable elements or neutrons or protons or electrons are ionized and accelerated at energy close enough to undergo a nuclear reaction and hit stable nuclei of a target. Nuclear reaction processes between the two nuclei are diverse that an important variety of nuclei can be produced using the same projectile-target combination at the same energy. The secondary radioactive nuclei productions are depend on the probability of interaction between the projectile and a target nucleus. In that, the fraction of particular nucleus is then reduced. Nuclei close to the valley of stability are relatively easy to produce as slightly different from the stable ones. In the case of more exotic nuclei, harder collisions are required in terms of energy or particle exchanges. The probability to get such reaction products is lower and their half-lives generally shorter. The quest of these distant ancestors is thus particularly hard owing to these two reasons: the decrease of their production rate and of their half-life when farther from the valley of stability. To explore these exotic territories, the instrument efficiency must be sufficiently rapid to observe it before it decays.

This Ph.D. work proposes a design of a system able to deliver short-lived isotopes of given elements.

To answer the beams requested for physics experiments, the high number of nuclei and fast observation systems are required. Generally, the ions must be first manipulated to be transported up to the experimental rooms where detectors are situated, the manipulation time must also be as short as possible regarding the half-life of the nuclei. To limit the losses and post-accelerate them, the nuclei must be part of ions, which can be accelerated and deflected using simple magnetic and electric fields.

They are many facilities for the production of radioactive ions across the world: ISOLDE at CERN (Switzerland) working from 1964, ISAC at TRIUMF (Canada) which has started in 1968, SPIRAL-1 (2001) and SPIRAL-2/S^3 (2023) at GANIL (France), GSI/FAIR (1969, Germany), RIKEN (1931, Japan), NSCL at MSU (1963), JINR at FLNR (1956, Dubna). These major installations use different combinations of ion beams, targets, different energies, intensities and different production methods (In-flight/ ISOL) which are presented in paragraph 1.2, pg.46 to 1.3, pg.48.

All the facilities generally try to produce beams as intense as possible to answer the physics requirements and to explore new regions of the nuclide chart. After a comparison of the beams produced in two of the other Radioactive Ion Beam (RIB) facilities see paragraph 1.3, pg.48, two main regions of the nuclide chart have been identified as accessible with an upgrade to the current SPIRAL-1 facility, as complementary regions to the other facilities and where SPIRAL-1 intensities can be competitive: the region of light elements up to masses of 50, and the region of neutron-deficient isotopes, from ~Kr to ~Xe.

The system designed within this Ph.D. aims to produce isotopes in the region of neutron-deficient isotopes, using fusion-evaporation reactions.

Nuclear reaction cross-sections effects the number of radioactive nuclei produced during the collision of the primary beam with the target atoms. Once the nuclear reaction is chosen, there are two main ways, which can be combined to increase the radioactive ion production yields: the first one consists of increasing the intensity of the primary ion beam. The second solution consists in optimizing the radioactive atom-to-ion (ATI) transformation efficiency and target thickness.

My aim is to optimize the parameters in the Target Ion Source System (TISS) to increase the final intensity of the ion beam combination see paragraphs 1.5, pg.56 and 1.6, pg.57.

The technical framework of this Ph.D. is the SPIRAL-1 facility. It uses the Isotope Separator On-Line (ISOL) technique, which consists in producing radioactive isotopes in a target thick enough to stop the produced nuclear reaction products. They then propagate through the target material, through the vacuum chamber and are ionized before being accelerated by an electric field to form an ion beam. The production system is generally called TISS.

As the nuclei have a limited half-life, the time of the process between the instant they are produced and the instant they exit the TISS must be as short as possible compared to their half-live. In this work, we consider that the shortest half-lives are of the order of 10 ms, which is roughly the lower limit determined by the amount of time taken by the ISOL production systems [8].

Several processes are present in most of the ISOL systems. Elements release out of the target material is presented in paragraph 2.3, pg.64, sticking with the different materials present in the TISS In paragraph 2.4, pg.74, and effusion within the chamber of the TISS is presented in paragraph 2.5, pg.80. Each process has been studied to be optimized or to minimize its impact on the global response time and try to reach the limit of 10 ms.

The goal of this work was to develop a system above to deliver ion beams having of the order of 10 ms.

Two important parameters limiting the production efficiency of short-lived isotopes are the size and the difficulty of the system. Both increase the AIT time and thus the losses owing due to the radioactive decay of the element during the AIT process. To balance these losses, one can imagine producing more radioactive nucleus by sending higher primary ion beam on the target. To sustain the higher power deposited in the TISS, the target must be thick enough, to avoid the overheating of the target materials. That leads to a reduction of the AIT efficiency. Once the nuclear reaction process fixed, there is compromise between intensity of the beam and AIT efficiency.

The neutron-deficient isotope region is technically interesting as the required primary beam energy can be closer to the reaction threshold energy, leading to a low energy deposition in the TISS and allowing a compact TISS geometry.

GANIL is a platform for users and it aims to provide beams requested for physics experiments. The development of the system had to be justified for the production of short-lived elements requested by physicists. In response to a call for experiments with the upgraded SPIRAL-1 facility, several letters of intent were submitted to GANIL by the physics community at the beginning of this Ph.D.

Among the radioactive isotopes request, ^{74}Rb has been chosen as a case study. The goal was to demonstrate how it is possible to improve yields, despite an in-target production lower than at other facilities. This is achieved by optimizing the AIT efficiency. The principle of the production system, specifically designed for ^{74}Rb production, is summarized in chapter3, pg.84.

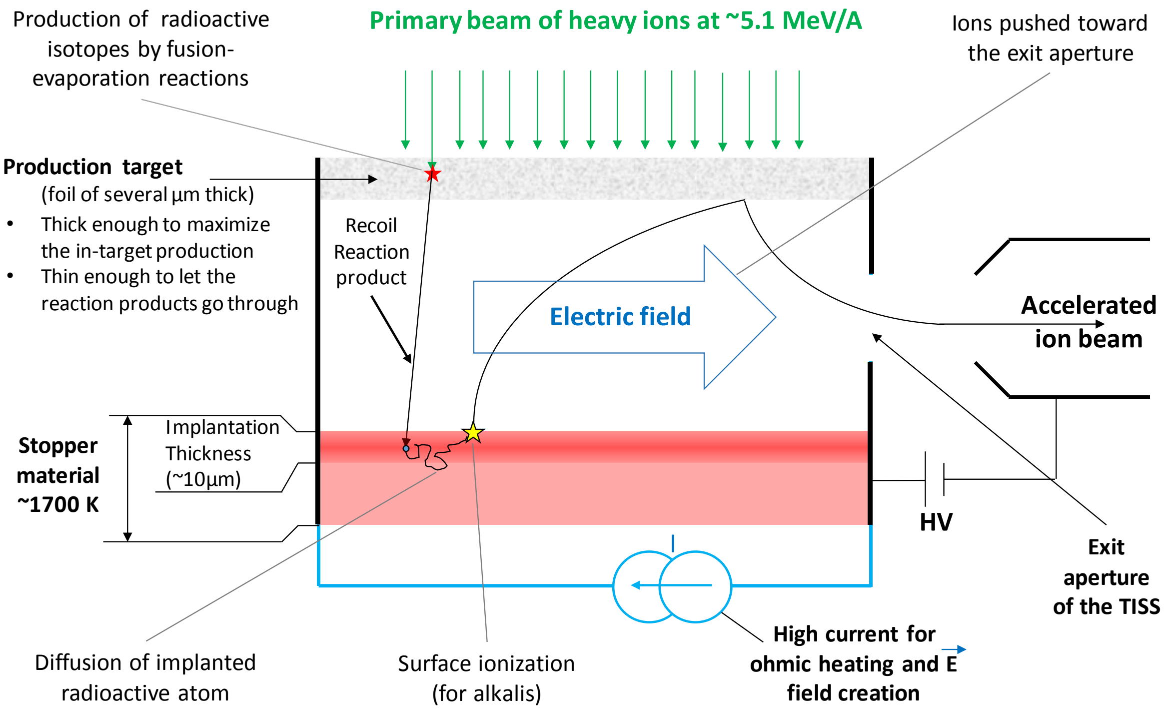

Figure 17: Principle of the TISS. Radioactive ion production follows steps # 1 to # 6.

A primary beam of stable heavy ions hits a thin target at an incident energy just above the Coulomb barrier to favor nuclear fusion reactions. The beam energy and target thickness are optimized for the highest in-target production rates in paragraph 2.2, pg.64, with end products (heavy evaporated residuals at tens of MeV speeds) being sufficiently energetic to be implanted, or "stopped" in a solid catcher material placed behind the target see in paragraph 2.3, pg.64. The ions are neutralized in the catcher, and undergo temperature-driven diffusion back up to the catcher surface see in paragraph 2.4, pg.74 and effuse into the TISS vacuum cavity see in paragraph 2.5, pg.80. Atom speeds by this point are of the order of a few hundreds of meV (thermal energy). In the case of alkalis (Rb in the present case), the atoms are ionized by contact with the metallic surface forming the cavity in paragraph 2.6, pg.74. The whole cavity is heated at “high temperature” to improve the efficiencies of the different processes involved in the atom-to-ion (AIT) transformation. Moreover, an electric field, parallel to the target and catcher foils, pushes the ions towards the exit aperture, beyond which they are strongly accelerated to form a radioactive ion beam (RIB). They are than mass-separated and magnetically selected for experiments.

The main aim of radioactive ion production techniques is to minimize the (AIT) time, and so accessing more exotic isotopes. The main concern in ISOL systems is chemistry and the complex techniques to avoid, or greatly reduce, these effects are primordial.

This approach was first implemented by R.Kirchner and colleagues in the '70s and '80s [7], [29] with a target ion source system (TISS) exploiting fusion-evaporation reactions in a thin production target within a FEBIAD ion source. In the original design, energetic nuclei produced in the target passed through a window were stopped in a solid catcher, diffused and effused up to an ionizing zone, and then they level the source. The cavity was maintained at a high temperature (up to 2300 K) to speed up the release of radioactive atoms from the catcher and to reduce absorption/desorption time on the TISS walls. Despite the very small cavity volume (of the order of 1 cm^3), the AIT time for Kr and Xe was of the order of 100 ms. This precursor did not include "sticking" (effusion) or diffusion times, and had it done so would have predicted longer extraction times for chemically reactive elements and low AIT efficiencies for metallic elements with half-lives shorter than 100 ms.

In more recent years, gaseous catchers have been designed and improved [9] to get rid of the sticking time issue. Implementing a similar setup at GANIL would require accommodating a voluminous vacuum system and this imposes non-negligible technical modifications to the building infrastructure. The only system that could be envisaged at GANIL is therefore inspired by the one developed by Kirchner at the UNILAC accelerator at GSI [29] in Germany**.**

The innovative solution investigated in this Ph.D. aims to limit the chemical issues by mixing three techniques: the use of an optimized stopper material, the immediate ionization of the atoms within the TISS cavity and the generation of an internal electric field within the cavity.

After the study of processes to be optimized and the results are described in chapter 2, pg.60, the technical design of the TISS is presented in chapter 3, pg.84. Main technical objectives were the creation of an electric field within the cavity and the heating of the cavity while taking into account the studies presented in chapter 2.

In the TISS, temperature is an essential parameter in most of the AIT processes: the release of the atoms out of the catcher material, effusion in the TISS cavity, sticking on the materials and ionization. It can improve the process efficiencies because the atoms gain energy and the speed increases. It also limited to preserve the TISS materials of premature damage, regarding the lifespan expected for the operation (15 days).

Emissivity and resistivity of the materials at TISS working temperature must be known to simulate the thermal behavior of the TISS and help to its design is described in paragraph 3.1, pg.81. As data available in the literature were not satisfying, a specific experimental setup has been realized to get comparable data given in paragraph 3.2, pg.82. It will provide reliable inputs for the design of this TISS and future designs see in chapter 6.

In the ISOL systems, material must cope with several constraints: sustain the primary beam power deposition, be convenient regarding the nuclear reaction chosen to produce the radioactive nucleus of interest, release efficiently the radioactive atoms. Compromises must be found to optimize the yields. In the present TISS design, production target and catcher are made of different materials. It allows to introduce the application of electric field. Thus increases the efficiency of the system.

The influence of the electric field on the effusion efficiency is presented in paragraph 3.6, pg.94. The overall AIT efficiency is estimated and finally, yields estimations are given for ^{74}Rb production is given in paragraph 3.7, pg.95, and for ^{114}Cs which can be produced using the same TISS.

Chapter 4 is dedicated to the TISS characterization. It has to conform to all the operational requirements, before installation in the production cavern. It is set up on a test bench, identical to the one in the production cavern of SPIRAL-1. After first technical verifications, the heating system is calibrated (temperature versus electrical power is given in paragraph 4.2, pg.101).

Given the promising yields of the system, the principles exploited here could be applied to the production of neutron-deficient isotopes of other chemical species (ex: metallic elements).

Chapter 1: Basic processes involved in RIB production

1.1 Nuclear reaction mechanisms for RIB production

Nuclear reactions are the fundamental process governing the production of radioactive isotopes. Basic parameters used to describe nuclear reactions can vary, depending on the energy regime and nature of the interaction. Here, four commonly used RIB production mechanisms will be introduced, in order of increasing collision energy.

1.1.1 The reaction mechanism

When the projectile nucleus interacts with target nucleus, various events possible to occur such as the two nuclei can diffuse elastically (or) in-elastically, exchange few nucleons (or) fuse to form a compound nucleus. The type of reaction mechanism depends on nature and the energy of the primary beam (projectile nuclei) used, on the nature of the target nuclei used and on the impact parameter (see Figure 18).

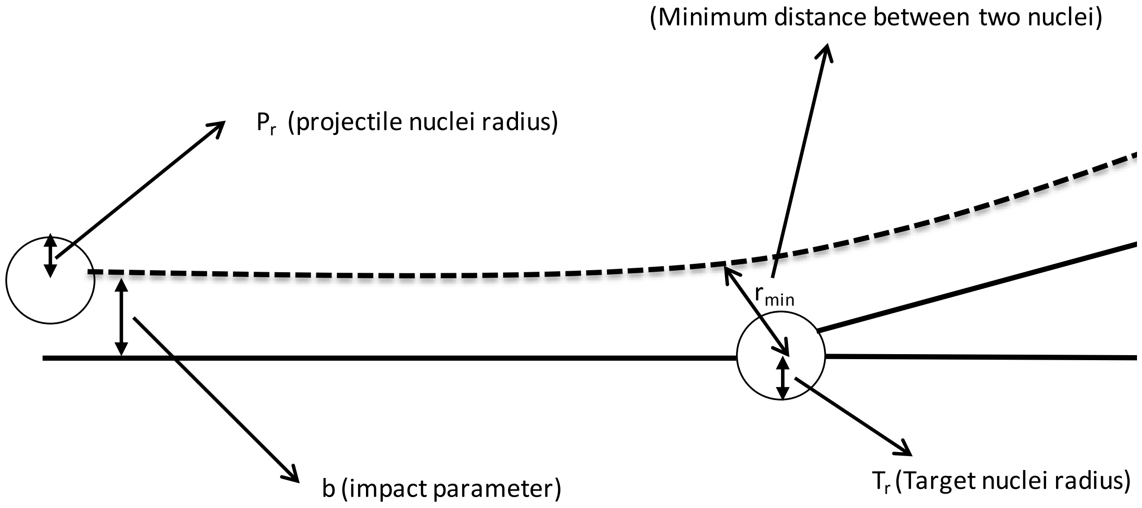

Figure 18: Impact parameter in the laboratory frame.

Following the semi-classical approach [30], there is a value of the impact parameter, bmax, corresponding to the minimum approach distance between the projectile nucleus and the target nucleus, which is equal to Pr (radius of the projectile nucleus) + Tr (radius of the target nucleus). For all values of b ≤ bmax, there will be a nuclear collision between the projectile nucleus and the target nucleus (D ≤ Pr + Tr). The nucleus undergoes internal excitation and transfer of particles which can affect the cross-section of the particular isotope.

Reaction cross-section

The probability of reaction to occur is related to cross-section. The total cross-section as σ_R is defined as the efficient area of interaction between the target and the projectile. In this simple approach, the cross-section is given by the geometric area shared by the nuclei in interaction. For example, a point like projectile and a spherical target nucleus have a radius R.

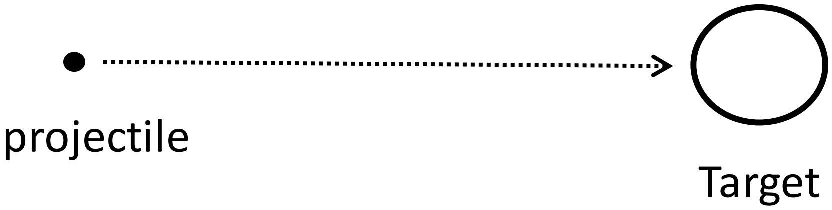

The total reaction cross-section is equal to:

$$\sigma_R = \pi R^2$$

The geometrical representation of the impact parameter Figure 18 makes it possible to deduce that the total reaction cross-section represents the area of a disk of radius bmax.

$$\sigma_R = \pi(b_{max})^2$$

The reaction cross-section mainly depends on the nuclear reaction process. It relates to the nature and the energy of the primary beam used, the nature of the target used and the impact parameter. The cross-section unit is barns, with 1 barn = 10^{-24} cm^{-2}.

1.1.2 Fusion-evaporation reactions: collision energy <10 MeV/A

Fusion-evaporation reactions describe a particular mechanism for low-energy RIB production. This multi-step process implies partial, or total, fusion of the incoming projectile with the target nucleus, to form a merged, short-lived compound nucleus. This unstable object, will then get rid of its excess energy in a succession of nuclear transformations: evaporating off excess particles (protons, neutrons, deuterons, and alphas), emitting gamma radiation in internal re-adjustments, and beta-decaying to reach more stable nuclear configurations. As a result, one same repeated collision does not lead to one single final produced nuclide, but instead may lead to several tens of possible end heavy residual products. Each residual production rate depends on the angular momentum and energy of the initial merged compound nucleus. The decay path probabilities are seen to follow a statistical dependence.

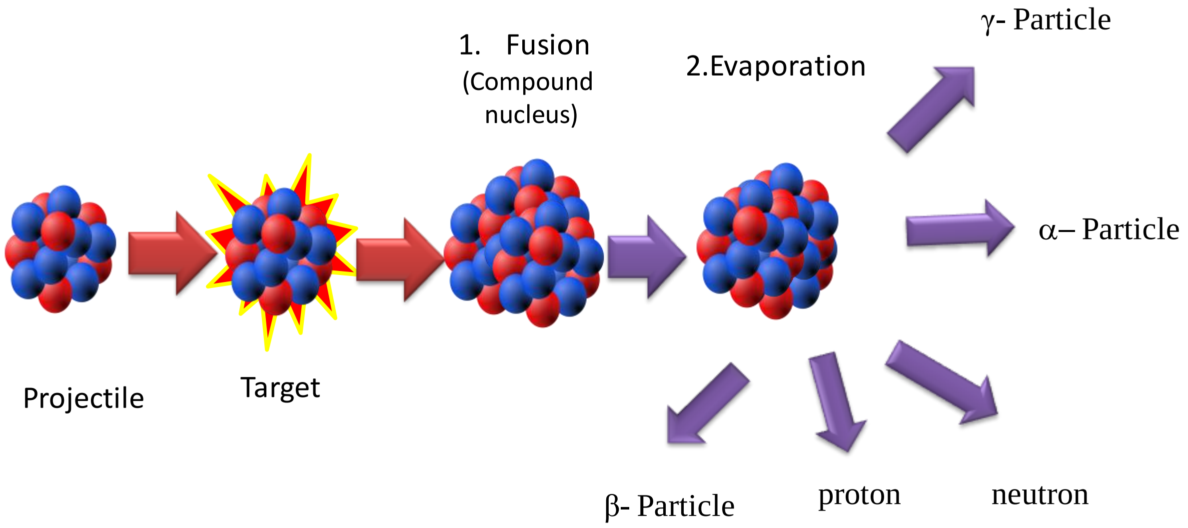

Figure 19: Fusion – evaporation reaction: first step leading to the formation of compound nucleus and the evaporation of one or several lightweight nuclei leads to the formation of interested nucleus.

In this case, the energy of the projectile must be sufficient to overcome the Coulomb barrier so that the nucleus is captured and form a compound nucleus. As the projectile and target nuclei fuse to form a compound nucleus, the combination of those nuclei leads to the formation of heavy elements. In the second step, light particles evaporate from the compound nucleus due to the internal excitation thus leads to the formation of other elements near to it. This reaction gives the opportunity to study the neutron-deficient nucleus as well as super-heavy elements. To generate this reaction, the projectile must have an energy large enough to overcome the coulomb barrier (E_{CB}) [31]:

$$\mathrm{E_{CB}} = \left(\frac{A_{CN}}{A_T}\right) \frac{0.90\, Z_P\, Z_T}{\left(A_P^{1/3} + A_T^{1/3}\right)} \; MeV$$

Where Z_P and A_P are the atomic number and mass number of the projectile respectively and Z_T and A_T are the corresponding values for the target nucleus. A_{CN} is the atomic number of the compound nucleus.

The production process of fusion-evaporation requires a well-defined projectile and target couple based on the required beam as the cross-sections are very sensitive to the target-projectile couple and the energy of the incident beam. The two-step fusion-evaporation process has been the single most productive mechanism for creating new neutron-deficient isotopes and to produce the nuclei far from the stability valley on the neutron-deficient side.

1.1.3 Fission reactions

Fission is a promising source for discovering, producing and investigating exotic nuclei with high neutron excess. Reliable predictions of fission product yields are available as this process has been extensively studied in the context of nuclear energy production.

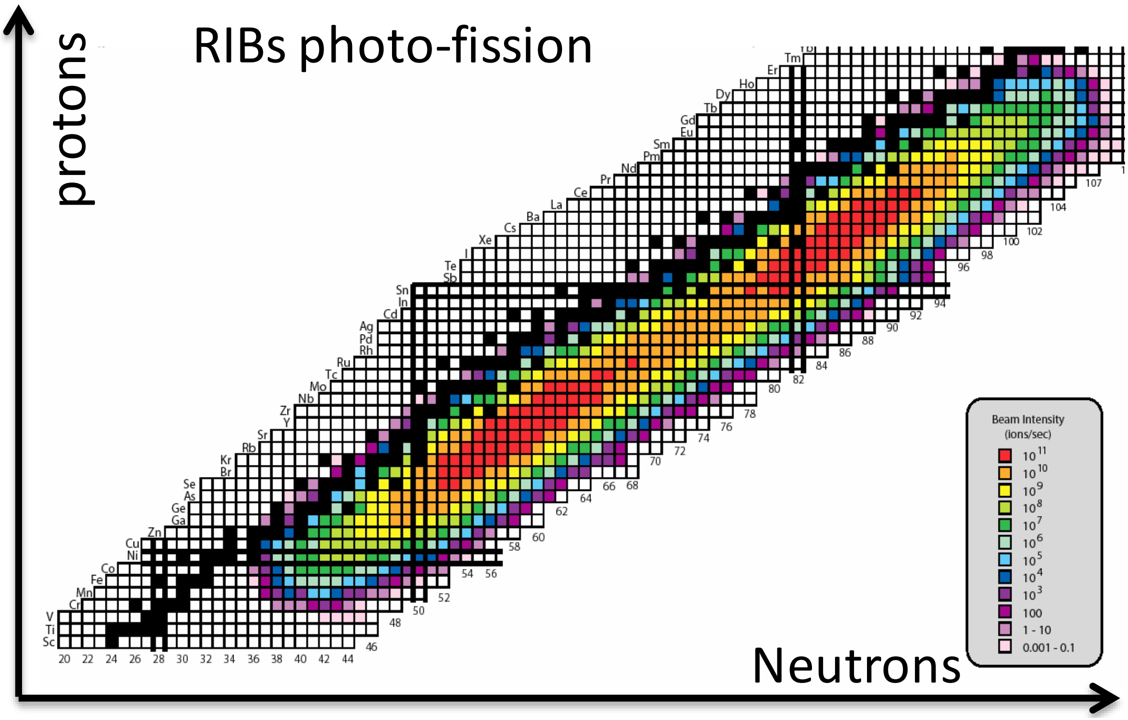

Figure 20: Reaction products of the photon-induced fission reactions.

The fission of actinides can be caused by thermal neutrons (energy = 0.025 eV), neutron converters and fast neutrons (several MeV) in the nuclear reactors and charged particles or light ions in the accelerators. Two asymmetric fragments are generally produced at reactor energies, the masses peaked around Kr and Xe ones. Initial core having a large excess of neutrons relative to the right Z = N, the fragments produced are rich in neutrons.

1.1.4 Fragmentation reactions: collision energy of 10 MeV/A to 100 MeV/A

The projectile fragmentation reaction is a very important tool to produce and study the isotopes on either side of the stability valley. The projectile fragmentation reaction takes place when a heavy ion at energies above the Fermi energy and up to hundreds of MeV per nucleons undergoes peripheral or mid-peripheral collisions with the target nuclei. These reactions produce a wide variety of isotopes of elements with masses smaller than the projectile. The fragments emerge in the forward direction with velocities near that of the projectile.

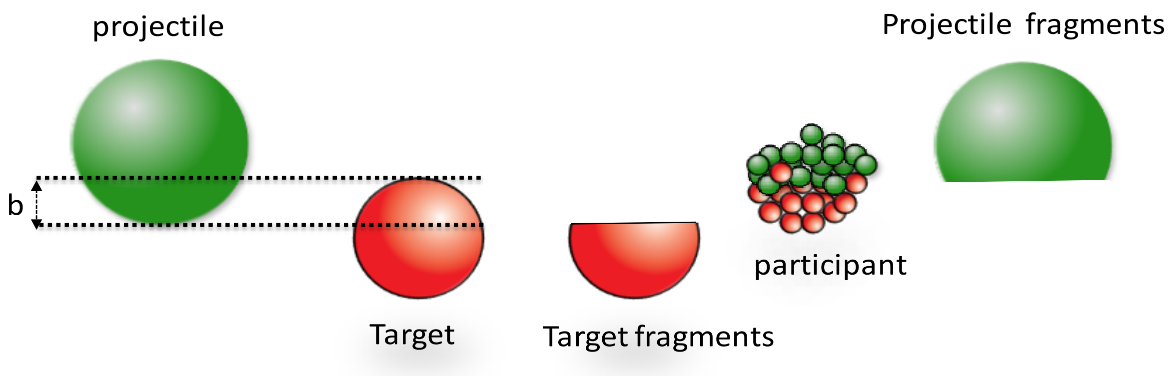

Figure 21: Nuclear reaction process of fragmentation.

Fragmentation reactions are widely used in rare-ion-beam facilities based on the in-flight and ISOL technique for many years, particularly in GANIL (France), GSI (Germany), MSU (USA), RIKEN (Japan) and Lanzhou (China), allowing the study of light and medium mass nuclei. Such experiences have created a large number of nuclei far from the valley of stability, both of neutron-rich side as well as the proton-rich side.

1.1.5 Spallation reactions: collision energy of several hundreds of MeV/A

Spallation is the process used to produce a large number of radioactive isotopes. This kind of reaction is obtained using a light nucleus (protons, neutrons, deuterons for instance) as a projectile at high energy, from several hundreds of MeV/A to several GeV/A [32]. They interact with a thick heavy target, usually high Z. The amount of isotopes produced by spallation process strongly depends on the projectile-target combinations [33]. This process allows achieving elements close to that of the target.

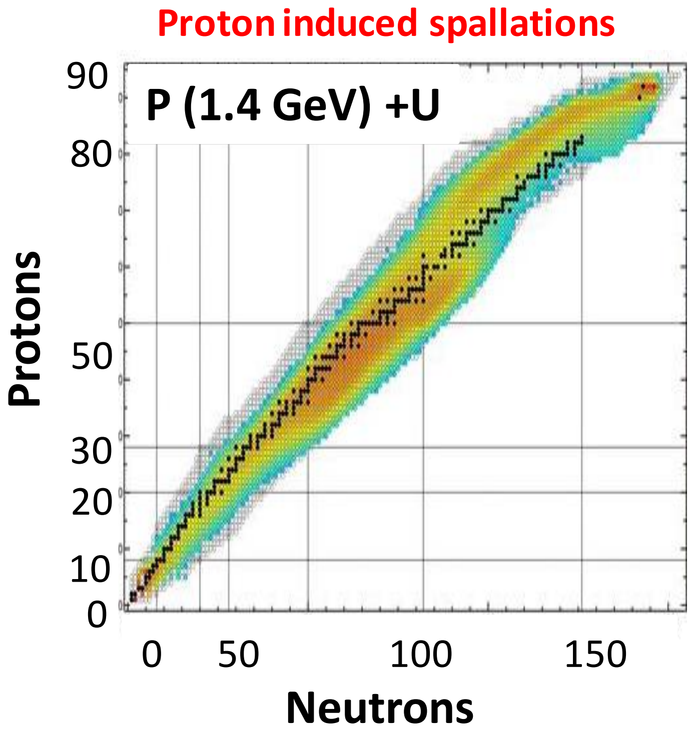

Figure 22: Nuclear chart representation of radioactive ion beams can be possible to produce by using the proton induced spallation reaction on Uranium target [34].

This reaction process is used at ISOLDE/CERN and ISAC/TRIUMF. At ISOLDE/CERN, the radioactive nuclides are produced using different thick targets. The targets are irradiated with a proton beam from the Proton Synchrotron Booster (PSB) at an energy of 1.4 GeV and intensity up to 2 µA. more than 600 isotopes were produced using this reaction. At ISAC/TRIUMF, the radioactive nuclides are produced using different thick targets, irradiated with a proton beam having the energy of 500 MeV.

According to the reaction process chosen to optimize the production of a particular isotope, the consequence on an ISOL target can be strongly different, as the profile and density of the energy deposited in the target can be very different. Each method has its advantages and drawbacks. Higher energy beams have longer ranges in the target material and thus a higher interaction probability if the target is long enough, but they also generally have a lower reaction cross-section regarding the particular isotope. Therefore, the design of the target must take these considerations into account.

As the reaction cross-section strongly differs for a particular radioactive isotope according to the processes (see Table 1).

Reaction	Primary beam, target couple	Primary beam Energy (MeV/A)	Cross-section (mb)
Fusion-evaporation	$^{20}Ne + ^{58}Ni$	5.5	6.10^{-2}
Fragmentation	$^{12}C + ^{93}Nb$	95	4.10^{-5}
Spallation	$P + ^{93}Nb$	200	2.10^{-03}

Table 1 : Reaction cross-section for the production of ^{74}Rb using the different previous reactions. The cross-section calculations are done with PACE code, FLUKA for fusion-evaporation and fragmentation reactions. The spallation cross-section is taken from the nuclear data library [35]

1.2 Radioactive ion beam production techniques

Mainly two techniques are used for the production of radioactive ion beams: In-Flight (IF) and Isotope Separation On-Line (ISOL) methods [36], [37]. Whatever is the method, it is necessary to get radioactive isotopes under the form of ion beams to transport them up to the experimental areas, and also to separate them from the other isotopes produced to avoid background noise in the detectors.

1.2.1 In-Flight method

The in-flight technique uses thin production targets (up to a few mg/cm^2). The fragments produced have energies close to the projectile ones, allowing them to cross the thin target and continue beyond it. They are in-flight separated with a magnetic separator and sent to various experimental areas. This very fast method allows the production of very short-lived isotopes. This production technique has been used in new installations in FRIB at MSU, FAIR at GSI, RIBF at RIKEN, and GANIL. Specifications of those facilities are reported in Table 2.

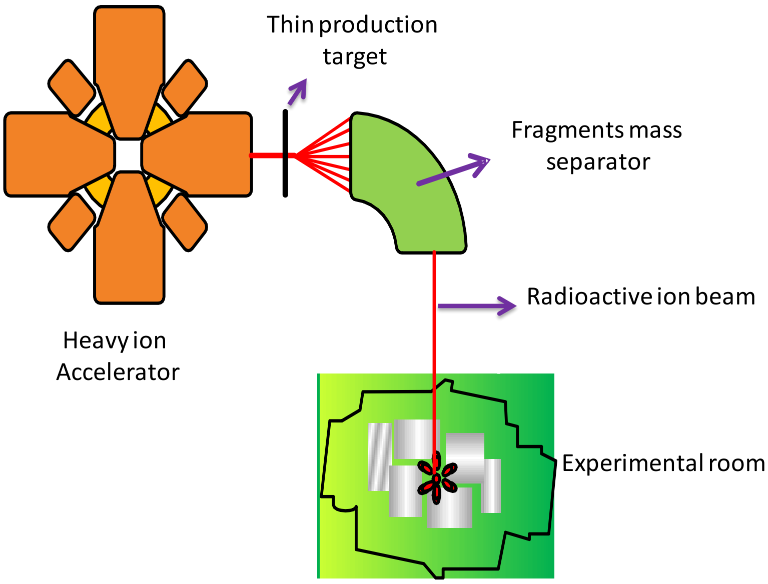

Figure 23: The in-flight technique for the production of radioactive ion beams.

Facility	Country	Accelerator	Primary beam and energy (MeV/A)	Intensity (pps)	Fragment mass separator
MSU/NSCL [38]	USA	Two coupled superconducting cyclotrons	O to U Up to 200	5.10^{11}	A1900
GANIL [39]	France	Two separated Cyclotrons	All stable beams Up to 100	10^{13}	SISSI+ALPHA
RIBF/RIKEN [40]	Japan	3 Ring cyclotron	Light particles to U Up to 350	5.10^{12}	BIG RIPS
FRIB [41]	USA	SIS 100 synchrotron	proton to U Up to 200	5.10^{11}	A2400
FAIR [42]	Germany	LINAC	proton to U Up to 2.10^{5}	$^{2}5.10^{9}$	Super FRS

Table 2 : Short summery of different facilities producing the radioactive isotopes using an In-Flight method.

1.2.2 ISOL method

In the ISOL (Isotope Separation On-Line) technique, Radioactive Ion Beams (RIB) are produced during the interaction of primary beams of ions with the nuclei of a solid or gaseous material (called target material) thick enough to stop the reaction products and primary beam. The produced secondary particles diffuse out of the target, effuse up to an ion source where they are converted into ions. When they leave the ionizing cavity, they are accelerated by an external voltage to form an ion beam. The extracted beams are separated by a magnetic mass separator before being sent to the experimental areas.

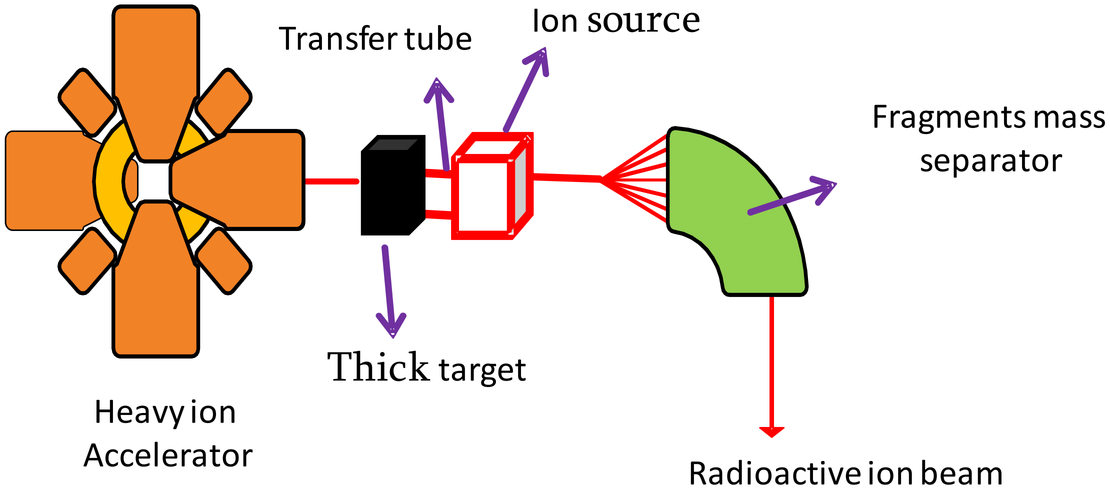

Figure 24: Schematic illustration of the ISOL technique for the production of RIBs

1.3 Yields at different facilities

1.3.1.1 Main features of world-class ISOL installations are given Table 3

Facility	Location	Projectile & energy (MeV/A)	Projectile current (µA)	Accelerator	The main nuclear reaction process
HIE-ISOLDE/CERN [43]	Switzerland	P (1400)	2	Synchrotron	Fission, fragmentation, spallation
SPIRAL-1/GANIL [39]	France	From C to U (up to 95)	10 to 0.1	Cyclotrons	Fusion-evaporation, fragmentation
SPIRAL-2/GANIL [44]	France	P to Ni (0.75-15 M)	5000	LINAC	Fusion-evaporation, Fragmentation, spallation
ISCA/TRIUMF [45]	Canada	P (500)	100	Cyclotrons	spallation
EXCYT/INFN [46]	Italy	C (45)	1	Cyclotrons	Fusion-evaporation
ALTO/IPNO [47]	France	e (50), stable elements	10	LINAC, Tandem	Photo fission, Fusion-evaporation

Table 3 : Characteristics and current post-accelerated main ISOL facilities.

In the above facilities given in Table 3, three major ISOL facilities delivering a large variety of beams can be counted in the world today, ISAC at TRIUMF in North America, ISOLDE at CERN and SPIRAL-1 at GANIL in Europe. At ISOLDE, a proton beam has an energy of 1.4 GeV/A use on different targets using spallation reaction. TRIUMF use a similar process as ISOLDE with energy an energy of 500 MeV/A, thus produces similar isotopes as ISOLDE. On the other hand, SPIRAL-1 makes use variety of primary beams from C to U with a variable medium energy of few MeV/A to 95 MeV/A from the cyclotrons on several targets (from C to Nb) allows to choose right combination of reaction, target and primary beam couple to deliver the particular ion beam on either sides of the stability valley.

Leading to our next development, In order to identify the regions of the nuclide chart where GANIL/SPIRAL-1 could be competitive and produce original beams, I have compared the intensities of those facilities with the one expected with the upgraded installation of SPIRAL-1.

1.3.2 Gaseous Ions

For more than ten years, radioactive ions have been produced at GANIL. The efficiency of the TISS has been progressively improved, leading to higher accelerated yields compared to TRIUMF and ISOLDE: while the yields represented in Figure 25 seem similar, one has to consider that GANIL rates correspond to ions readily multi-charged for post-acceleration, in contrast to those at TRIUMF and ISOLDE, which correspond to 1+ ions, and which will be further reduced by the 1+ to N+ charge beading before post-acceleration. For short-lived isotopes, the advantage of the GANIL Nanogan III source is reduced owing to its relatively large volume, which increases the losses during the diffusion and effusion process.

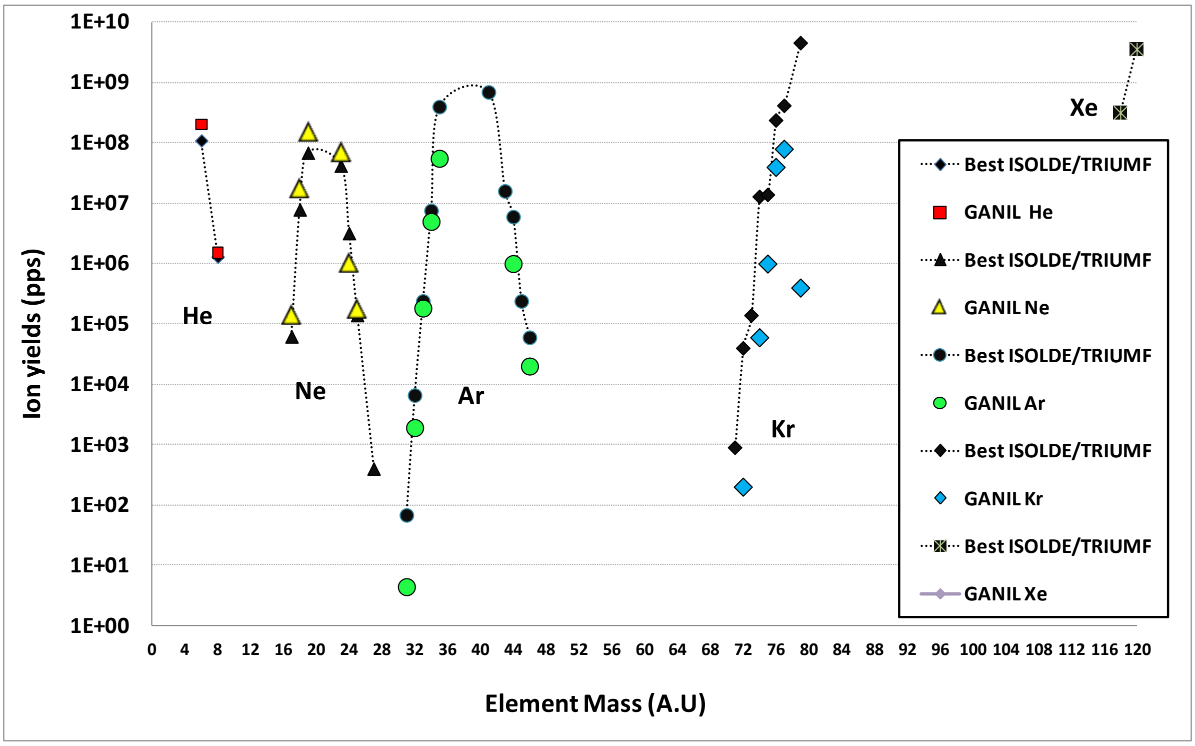

Figure 25: Singly charged ion yields produced from He, Ne, Ar, Kr and Xe at TRIUMF and ISOLDE (black dots) and multi-charged ion yields produced at GANIL (respectively red, yellow, green, and blue dots) versus the mass of isotopes. The GANIL rates correspond to multi-charged ions prior to post-acceleration.

1.3.3 Alkali Ions

The surface ionization sources proved to be an efficient and selective source to ionize the alkalis and alkali-earth elements. It has been developed at GANIL, never installed in the production cavern of SPIRAL-1 before the upgrade, but it could be possible now as the SPIRAL-1 Upgrade project is completed. The yields obtained On-line on a test bench are lower than the one obtained at TRIUMF and ISOLDE [2] but the GANIL ones have been obtained with non-optimized beams, delivered for other physics experiments and not for qualification tests of the surface ion source.

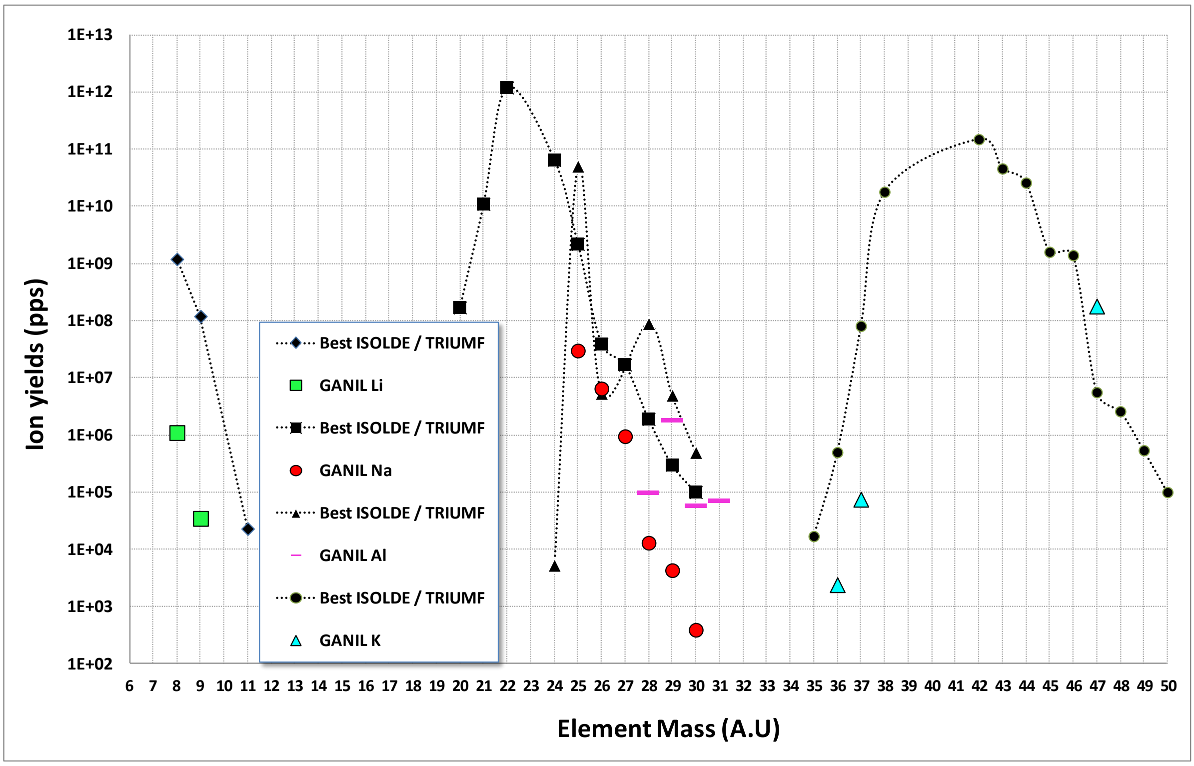

Figure 26: Singly charged ion yields produced from Li, Na, Al and K at TRIUMF and ISOLDE (black dots) and Li, Na, Al and K ion yields produced at GANIL (respectively green, red, purple and blue dots) versus the mass of isotopes. Experiments with accelerated beams would typically require 2.10^{6} pps of the 1+ beam, assuming a total acceleration efficiency including charge breeding, transport, and acceleration of the order of 0.5%.

The intensities at GANIL/SPIRAL-1 could be improved by choosing the right combinations of primary beam with the target. For example, a primary beam of ^{48}Ca (1.3.10^{12} pps) on graphite has been used to produce Lithium isotopes. Ca being far from Li, an important gain of Li production in the target can certainly be obtained by choosing a more appropriate primary beam like ^{18}O at 8.6.10^{12} and by using a higher primary beam intensity, up to 1.5 kW. The additional gain could also be obtained on the ionization using more efficient metals as *Re* in place of C, and by designing the TISS to generate an inner electric field in order to speed up the release of the ions and consequently to increase the ionization efficiency.

1.3.4 Metallic Ions

The association of the FEBIAD developed at ISOLDE with a SPIRAL-1 graphite target can lead to a competitive production, mainly for light elements (mass < 50) as shown in Figure 27. The GANIL intensities have been estimated for projectile fragmentation on graphite. Release efficiencies have been estimated from on-line data for elements up to Fe, and from diffusion effusion coefficients found in the literature for heavier elements.

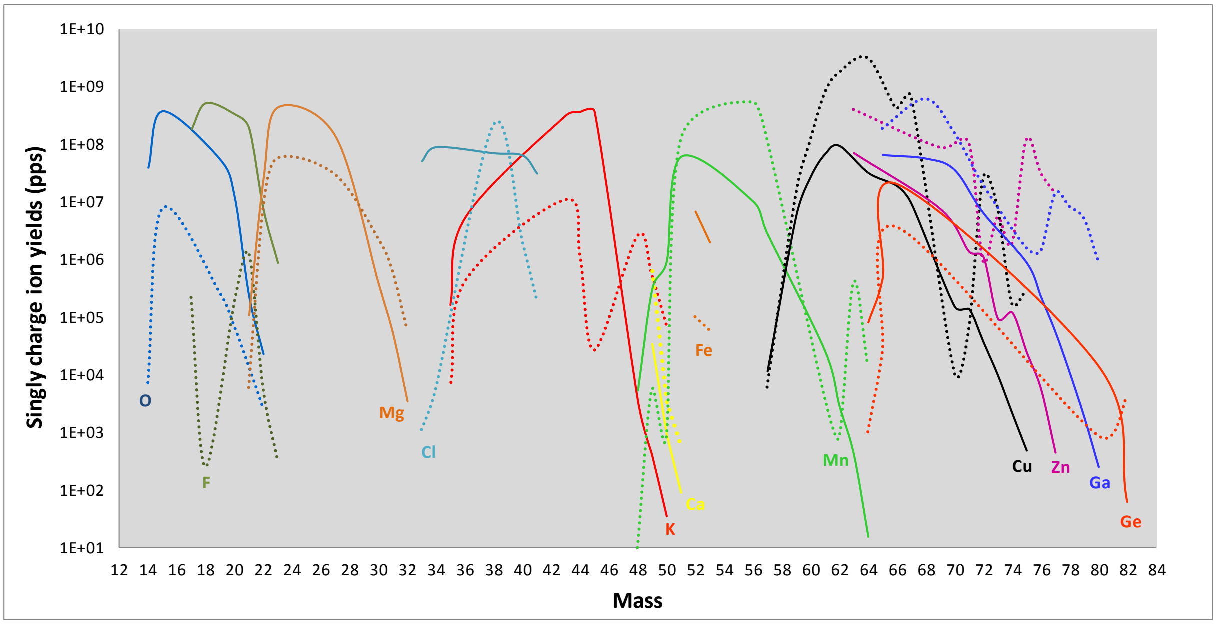

Figure 27 : Comparison between radioactive singly charge ion yields expected with the new graphite target+ FEBIAD TISS at GANIL (continuous lines) and current yields produced at TRIUMF and at ISOLDE (dotted lines) versus mass for O, F, Mg, Cl, K, Ca, Fe, Mn, Cu, Zn, Ga and Ge isotopes.

For heavier mass (>50), the graphite + FEBIAD is less competitive. Up to now, these isotopes could only be produced by fragmentation of the primary beam nucleus on graphite. In the framework of the SPIRAL-1 project, an extension of the operation rules license has been obtained from the French Nuclear Safety Authority. The use of heavier target materials is allowed, up to Nb ones. This opens a new production process which can lead to higher intensities of >50 mass isotopes [48].

1.3.5 Isotopic regions of interest

The previous study allowed me to clearly identify two regions where SPIRAL-1 could be competitive: the region of light masses up to mass ~50, and the region which is little explored by the other facilities as hardly accessible due to reaction processes used (spallation and fission). This region is the neutron-deficient intermediate mass isotopes one (from Kr to Xe masses). Their production is made easier at GANIL than at TRIUMF or ISOLDE as the fusion-evaporation process can be used thanks to the SPIRAL-1 primary beam–target possibilities.

This region of radioactive ion beams is also covered by ISAC and ISOLDE, but mainly close to the valley of stability. For farther isotopes, ion production rates decrease, see in Figure 28 and Figure 29 or two reasons: the in-target production rates decrease due to the decrease of the reaction cross-section, and their half-life decrease.

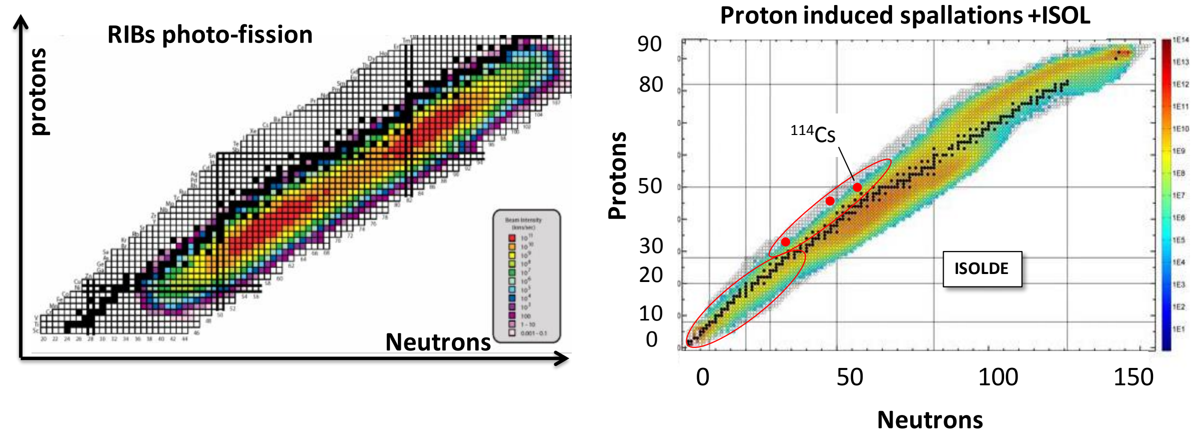

Figure 28: RIB production regions induced by the proton beam on Uranium Carbide target at ISOLDE and photo-fission at TRIUMF facilities.

Figure 28 also clearly show that the region of isotopes produced by spallation process is very large compared to the region covered by the fusion-evaporation process, leading to a relative production efficiency of the element of interest lower than with fusion-evaporation, which is Z equal to ~30 to 70 in Figure 28. Figure 29 show that the ^{74}Rb possible to produced using fusion-evaporation reaction. The risk of contaminants after the TISS must thus be reduced using the fusion-evaporation process.

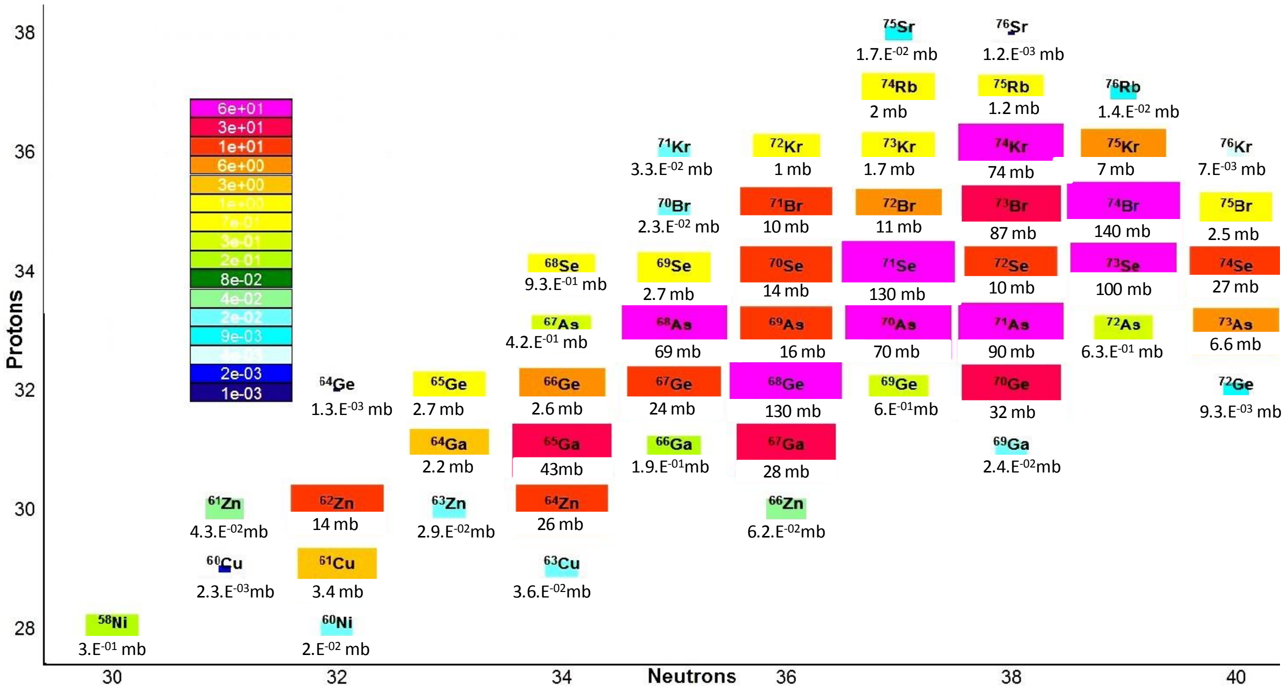

Figure 29: Example of fusion-evaporation products for the ^{20}Ne +^{58}Ni reaction at an energy of 110 MeV, the formation compound nucleus is ^{78}Sr. the size of the box corresponds to each nucleus cross-section, the higher is the cross-section, and the size is bigger. The highest cross-section obtained for ^{74}Br is 130 mb and lowest is 1.10^{-3} mba for ^{64}Ge. The calculations are done with PACE code [49].

1.4 SPIRAL-1 Upgrade

SPIRAL-1 is a "System of Production of Radioactive Ions Accelerated on-Line" based on the ISOL technique, which has been delivering radioactive beams of gaseous elements of high intensity and purity for physics experiments since 2001. So far, radioactive isotopes were produced by fragmentation of the primary beam on a thick carbon target. Then the secondary radioactive isotopes were ionized by Nanogan-III ECR ion source [23]. The formed ions were extracted as an ion beam. The extracted ion beam was transferred through the low energy beam line up to the physics experimental rooms.

The SPIRAL-1 upgrade aims at extending the production of radioactive ions to condensable elements. It consists of the installation of new singly charged ion sources in the production cavern and of a charge breeder out of the production cavern to make the ion charge state cope with the characteristics of the post-accelerator (Cyclotron CIME [50]). A schematic view of the upgraded SPIRAL-1 facility is given in Figure 30.

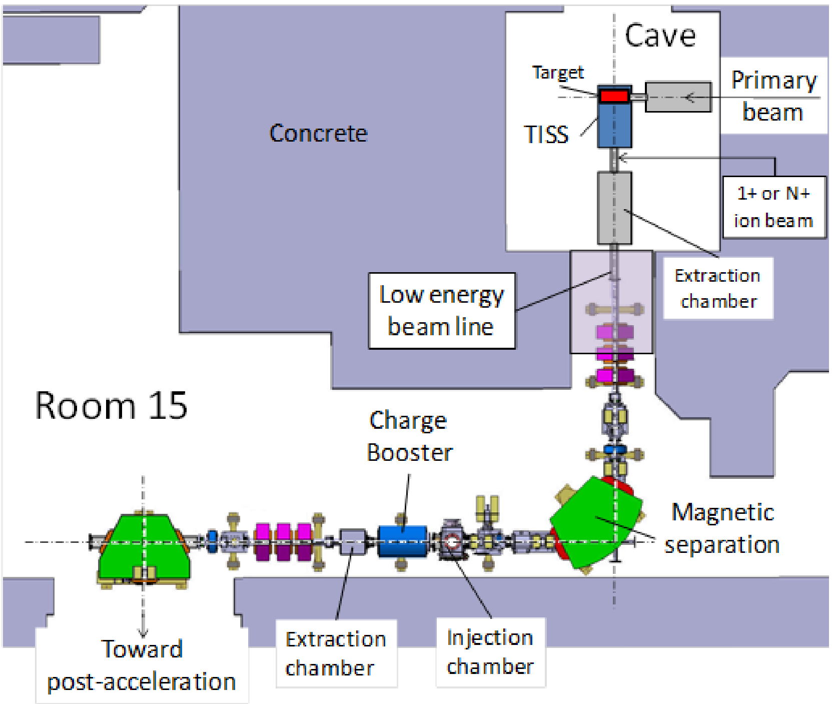

Figure 30: Top view of the Upgrade of the SPIRAL-1 facility. Purple parts represent concrete walls. Only ionizing radiation systems are installed in the cavern. As the technology of the breeder cannot be sufficiently hardened, it is installed out of the cavern, and after a magnetic separator.

With the upgraded SPIRAL-1 [2], it is now possible to use targets with a higher atomic number (up to Nb) and to combine them with different ion sources able to ionize metallic elements.

1.4.1 CIME Cyclotron

One of the figures of merit of the ISOL facilities is the purity of the RIBs. Laser ionization if often used to select the mass of the element. Combined to a magnetic separator which selects a given mass of isotopes at the exit of the TISS, the Laser additionally selects the atoms according to their electronic configuration. Unfortunately, this powerful technique can hardly be installed at SPIRAL-1, due to a lack of space. Nevertheless, ions can be separated based on mass to charge ratio when accelerated with the CIME “Cyclotron for Medium Energy Ions”. It makes possible to reach the low energies required for the study of the structure of nuclear matter close to the Coulomb barrier, from few MeV/A to 25 MeV/A [50]. The operating energy of CIME depends on the mass and charge of the element and the extraction energy of ion source thus varies from 10 kV to 34 kV. The ratio q/m of the ions injected into the cyclotron is between 0.1 and 0.5. The total transmission efficiency of the cyclotron can vary from 15% to 50% depending on the element, the emittance and the energy of the injected beam. It has been designed for two major concerns:

1. It is able to purify the beams before being guided to the experimental rooms.
2. The purified exotic beams are accelerated with a variable energy of 1.7 MeV/A to 26 MeV/A.

Once extracted from the TISS, the ions are transported in a low energy beam line, mass to charge separated in a magnet, injected in charge breeder if too weakly charged, mass to charge separated in a second magnet and then injected into the CIME cyclotron for post-acceleration. The extracted ion beam has a low energy and contains a mix of chemical species.

1.4.2 GANIL RIB production techniques on SPIRAL-1

The SPIRAL-1 facility was started with ECR ion source. Now, three kinds of ion sources are possible to use with the upgrade of the SPIRAL-1 facility, which is described in the following. The choice of the ion source mainly depends on two parameters: the physicochemical characteristics of the element to produce, which govern the atom-to-ion transformation time (AIT time) and the half-life of the isotope of interest.

1.4.2.1 ECR (Electron Cyclotron Resonance) Nanogan III ion source

Electron cyclotron Nanogan III type ion source uses a permanent magnetic field and an oscillating RF field to induce a cyclotron motion among charged particles. The RF frequency is set to accelerate the electrons around the magnetic field. When accelerated, they gather enough energy to snatch other electrons from the atoms. The chamber of the source thus simultaneously contained atoms, ions, and electrons, forming the ECR plasma, which expansion is partly governed by the magnetic field structure. As electrons can easily have a kinetic energy well over the first ionization potential of any element, this source can in principle ionize all the elements. More energetic are the electrons, higher can be the charge states. In the case of Nanogan III ECRIS, the most abundant charge state for Ar is 8+, which is sufficient to be post-accelerated. In case of heavier atoms, lower charge to mass ratios can be obtained. The use of a charge breeder is then required.

Due to its principle, ECRIS is not efficient for the ionization of condensable elements. In the case of gas, atoms pass through the plasma up to be ionized and then captured by the plasma before being extracted. In the case of condensable elements, atoms which are not ionized during their first flight across the plasma stick on the cooled wall of the ECRIS, reducing their chance to fly again and be ionized before decaying. For this reason, ECRISs are generally used mainly for gaseous RIBs.

1.4.2.2 FEBIAD (Forced Electron Beam Ionization by Arc Discharge) ion source

In FEBIAD ion source, the produced secondary radioactive atoms effuse through the transfer tube to the anode [51], [52]. The radioactive atoms are ionized in the anode cavity by electron impact. Owing to a voltage difference of ~150 V, electrons are accelerated between a hot cathode and an anode placed in front of the cathode.

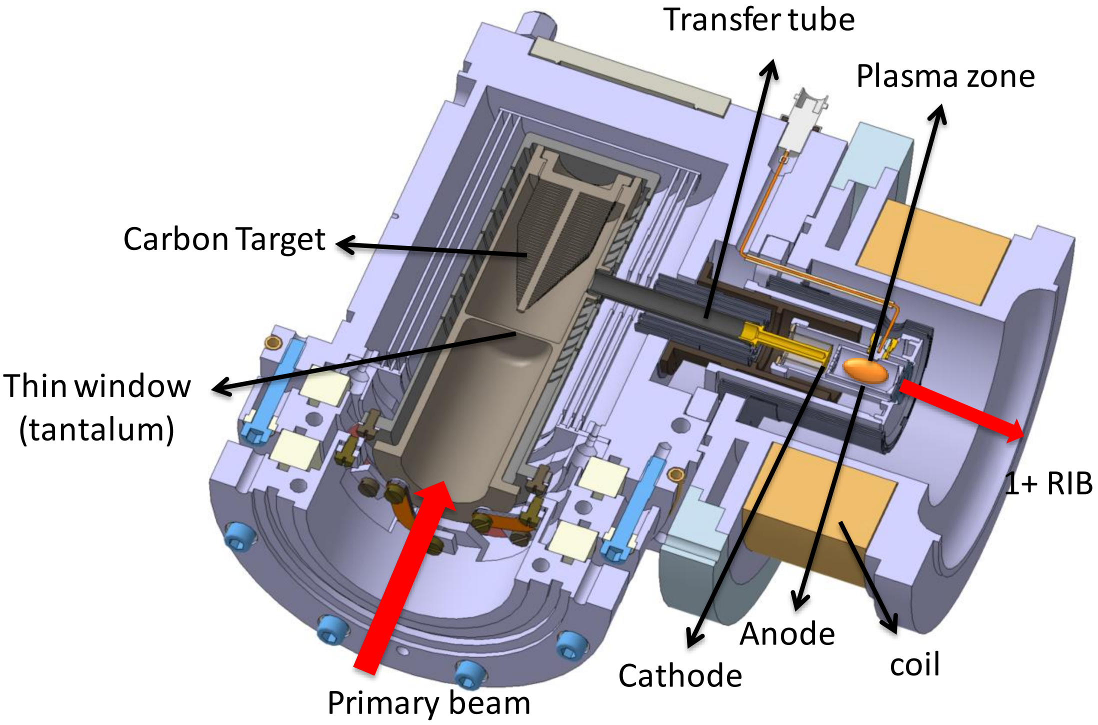

Figure 31: VADIS type FEBIAD ion source at GANIL.

The plasma is mainly confined by the wall of the anode cavity. A magnet surrounding the anode helps to reduce the effect of the space charge. The target cavity, transfer tube between target cavity and ion source, the cathode, and the anode are heated at 1800 K to 2300 K to accelerate the propagation of condensable elements and reduce the AIT time. The energy of the accelerated electrons is high enough to ionize any element. Nevertheless, as the ionizing cavity has a reduced volume and a relatively large aperture and as the sticking time can be important in front of the half-lives, the atoms often have an important probability to disappear from the source before being ionized, leading to typical ionization probability of the order of 10% or less [53].

The advantage of being able to ionize a large variety of elements can be a drawback in term of selectivity. Contaminants, which are also ionized, will have to be removed later in the delivery process. Nevertheless, the FEBIAD ion source is one of the most widely spread techniques which still works in several facilities.

1.4.2.3 Surface ion source

The surface ion source (SIS) [54], [55] is used to produce singly-charged ion beams from low first ionization potential elements (< 6 eV), mainly alkali elements. The principle is the following: a flux of atoms enters the volume of the ionizer, which merely and generally consists in a hot tube. Each atom makes one or more contacts with the surface of the walls. During each collision, the atom shares an electron with the surface. Once the atom left the surface, the electron can stay with it or on the surface, with a probability depending on the first ionization potential, the work function of the surface and the temperature. The principle description is given in chapter 2 (section 2.6).

1.5 The ISOL technique and challenges

In the ISOL (Isotope Separation On-Line) technique, the radioactive ion beams (RIB) are produced during the interaction of a primary beam with a solid target, thick enough to stop the reaction products. The secondary atoms spread through the matter up to the surface of the target, the process defined as diffusion. To favor their release, the target is heated at a temperature close to the maximum of the target material. Once in the target container, they move up to the ion source where they convert into ions.

The ions are extracted by a high voltage and then form an ion beam. As their lives are limited, AIT must take place in a delay as short as possible compared to their half-lives to avoid losses during the transformation process. Once the ion beam is formed, the isotopes are separated often using a magnetic mass to charge separator. Then the beam is delivered to an experimental area or is post-accelerated.

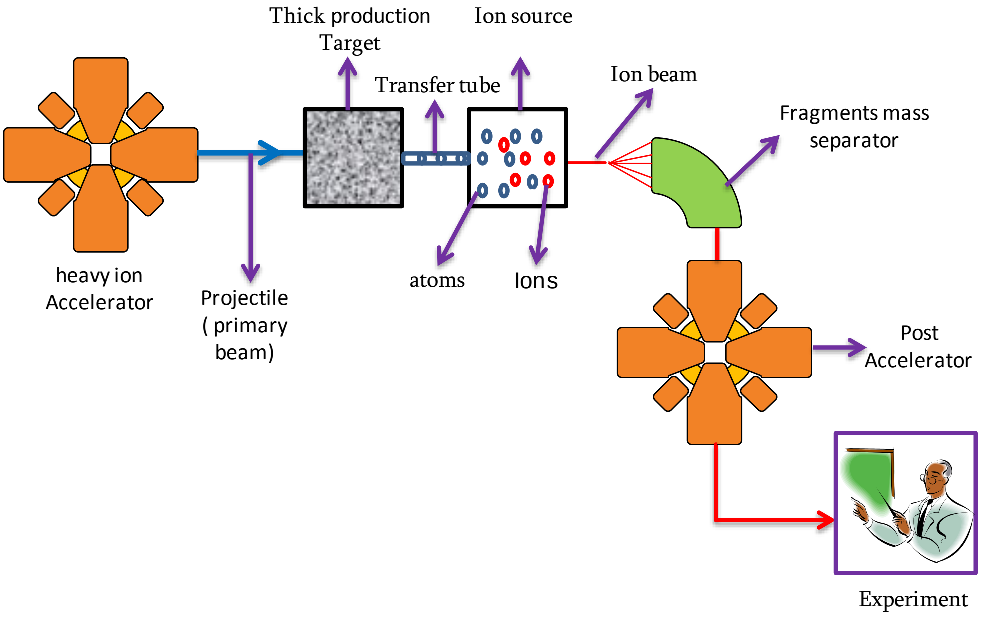

Figure 32: ISOL (Isotope Separation On-Line) method.

To cope with the need for statistical results, the experiments require intense RIBs. At the exit of a TISS, the rate of ions available is the direct product of the in-target production rate by the AIT efficiency. If these two parameters were independent, it would be easy to increase the RIB production rate, either by increasing the in-target production (larger target, more intense primary beams) or by increasing the AIT efficiency ("which is often easier to say than to make"). Unfortunately, in-target production rate and AIT efficiency are related. Increasing the size of the target, to cope with the primary beam power, or with its range, leads to increase the AIT time and thus decrease the AIT efficiency, especially for the short half-lived isotopes. There is thus necessarily an optimum design of the TISS for a given isotope [36]

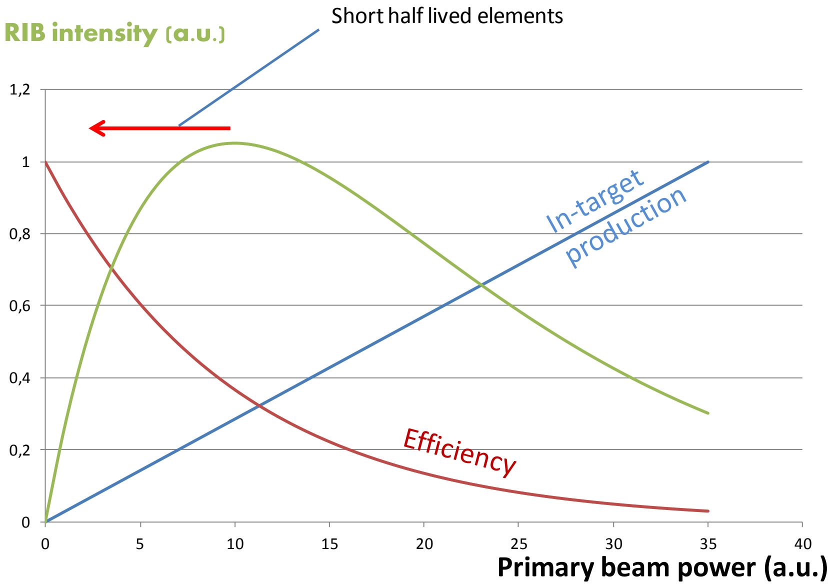

Figure 33: RIB intensity in function of primary beam power, in-target production and efficiency for short-lived elements.

To reduce the atom-to-ion transformation time, it is necessary to consider the different processes involved in the TISS.

The first one is the nuclear reaction process, which includes the primary beam (energy, nuclei, intensity) and the target thickness. Maximizing the cross-section minimizes the intensity of primary ions to produce a given amount of radioactive nuclei. Once the best cross-section identified, the target can be designed, if the target material chosen copes with the TISS constraints (irradiation damage, thermal requirements, feasibility, and availability)

Once produced, neutralized and thermalized in the target material, the reaction products have to leave the material. Once out, they have to propagate up to the ion source. During the propagation, the atoms undergo multiple collisions with the container walls and surface of the target. At each contact, there is a probability that the atoms will be re-absorbed or will stick to the surface for a certain time before being released. The final process involved in the TISS is ionization.

1.6 TISS optimization

The principle of the production system is given in Figure 17 (page 37). It involves 7 steps:

- Production of ^{74}Rb nuclei in a thin target of nickel using the ^{20}Ne@110 MeV on 3 µm thick ^{58}Ni foil
- The recoil nuclei pass through the Ni foil and through the TISS cavity
- The recoil nuclei are neutralized and thermalized in a catcher, made of graphite
- The release of the atoms out of the catcher material
- Ionization of the atoms by contact with the surface of the cavity
- Effusion of the ions, pushed toward an exit hole using an electric field
- Once out of the cavity, acceleration of the ions by a high voltage to form an ion beam

As mentioned earlier in (paragraph 1.3.5, pg.52), the region targeted in this Ph.D. is neutron-deficient region and elements having mass ~70. In this region, ^{74}Rb is requested by the physicists. Moreover, it has a short-half-live (64.8 ms) and is a chemically reactive element. It is challenging to produce such a short-lived element regarding the typical response time of TISSs.

^{74}Rb has been chosen as a case study, as its characteristics seemed interesting to demonstrate how the performances could be improved by optimizing the TISS design for a specific isotope.

This element was produced at ISOLDE [56] and ISAC [57] using the spallation reaction of a Nb target coupled to a surface ion source. The available intensities of singly charged Rb ions are respectively 2.10^3 pps and $1.7.10^4$ pps were measured after the TISS.

^{74}Rb can be produced by the fusion-evaporation reaction. The corresponding reaction cross-section is higher than other nuclear reaction process (see in Table 1, pg.47). And the region of products covered by this type of reaction is narrower, limiting the possible contaminants. As the energy of the primary beam is close to the Coulomb barrier and the reaction cross-section is relatively large, an important rate of reaction products can be obtained (see in Table 5, pg.96) for a limited primary beam power, which helps to reduce the size of the target.

Rb has a low first ionization potential and therefore can be easily ionized by contact with materials having a sufficient work function [17–22]. They so can be ionized right after their release from the catcher and can be pushed toward the aperture of the TISS by applying an electric field in the target cavity, avoiding separated volumes for target and for ion source.

As only a few elements are surface ionized, and as the production region covered by the reaction products is narrow, Rb will probably be the only element in the extracted ion beam.

The effectiveness of the TISS depends on all the parameters involved in the production processes: target characteristics, macroscopic dimensions of the TISS, TISS components and structure, temperature, type of ion source, characteristics of materials and of atoms, and also half-life of the radioactive isotope of interest. The optimization of several processes in terms of time is discussed in chapter 2.

Chapter 2: Optimization of processes in the ISOL technique

Abbreviations and symbols

J_P:	The flux of particles.	$m^{-2}.s^{-1}$
D:	Diffusion coefficient of the atoms in matter	$m^{2}.s^{-1}$
D_0:	Maximum diffusion coefficient for $T = \infty$	$m^{2}.s^{-1}$
k_B:	The Boltzmann constant	$J.K^{-1}.mol^{-1}$
T:	The absolute temperature	K
E_a:	The activation energy for the atoms to move	$J.mol^{-1}$
R:	Radius of the grain	m
$p(t)$:	The fraction of particles remaining in the target at time t	
N_0:	Initial number of atoms present in the target at t=0	
m:	m^th^ number of shell in grain	
$f_k(t)$:	The flux of particles leaving the grain	
λ_{Dm}:	Diffusion rate in m^th^ shell	s^{-1}
λ_D:	Diffusion rate	s^{-1}
X:	The mean number of collision	
τ_a:	The mean sticking time	s
τ_f:	The mean time of flight	s
β:	The mean speed of atoms (according to Maxwell-Boltzmann distribution)	$m^{2}.s^{-2}$
M:	The molar mass of the particle	kg
λ_e:	Effusion rate in the elementary volume	s^{-1}
γ :	Geometrical parameter (see appendix 2.3)	
A_{ap}:	Conductance between elementary volumes	
a:	Geomentrical parameter defining the overlap between the grains ($a = 1 \rightarrow no\ overlap$, ($a = \sqrt{2} \rightarrow overlap$) (see appendix 2.3)	
λ_E:	Effusion rate in the matter	s^{-1}
D_E:	Effusion coefficient in the matter	$m^{2}.s^{-1}$
d:	Thickness of the foil	m
n:	Integer	
λ_{En}:	The effusion rate in the n^th^ shell	s^{-1}

$F(t)$:	Total flux from the target	
λ :	Radioactive decay	s^{-1}
ρ :	Matter density	$g.cm^{-3}$
ρ_0 :	The maximum density of target material	$g.cm^{-3}$
F:	Factor related to the variation of the grain with density	
ε :	Total release efficiency out of material	
ε_{diff} :	Diffusion efficiency	
ε_{eff}:	Effusion efficiency	
E_0:	Binding energy of an atom with a surface	$J.mol^{-1}$
ω_0:	Typical frequency of molecular vibrations of atom	Hz
τ_0:	The oscillation period about the equilibrium position	s
ΔH:	Standard enthalpy	$J.mol^{-1}$
E_{des}:	desorption energy of atoms from surface	$Joules.mol^{-1}$
$< t >$:	Release mean time	s
t:	Time	s

2.1 Optimization of isotopic production rates

For each type of reaction, parameters like the target, primary beam and the incident energy have to be optimized in order to achieve the highest production rates of the isotope of interest. For spallation, fragmentation, and deep-inelastic reactions, it is most often advantageous to use a stable nucleus close to the desired final nucleus to enhance the production rate. This choice basically does not exist for fission because only a few quasi-stable fissioning nuclei exist. For these reactions, analytical codes have been developed which have a rather good predictive power for the reaction cross-sections.

For fusion-evaporation, the in-target rates are curtailing compared with the other nuclear reactions. The situation is different in the sense that a nucleus can be produced with different combinations of projectile, target and incident energy. Therefore, an optimization of these three parameters is needed for any nucleus to be produced. To do so, different codes are available [10], [62]–[65], some of them being analytical, others being of the Monte-Carlo type.

In the present work, In-target production rates for ^{74}Rb and ^{114}Cs are estimated using cross-sections issued from the PACE (Projected Angular-momentum Coupled Evaporation) fusion-evaporation code [10]. It uses a two-step scenario for the reaction: projectile and target nuclei completely fuse to create Compound nuclei through an angular-momentum dependent fusion model. In a second step, compound nucleus decay according to a statistical model approach of compound nucleus reaction. They take into account competition between different decay channels like proton, neutron, and α emission as well as γ decay and fission.

2.1.1 Choice of the primary beam-target material couple for the Rb and Cs isotopes

The production of very neutron-deficient ^{74}Rb and ^{114}Cs alkali isotope can be obtained through different reaction channels. Several primary beam and target combinations were investigated at different energies using the calculated fusion-evaporation cross-sections of the PACE code. The cross-sections are very sensitive to the collision energy. The calculations were done for each step of 5 MeV and the mean cross-section was divided by a factor of 11.2 [66], in order to obtain a more realistic estimation of the production rates. The calculations done for various couples were compared to choose the better combination of primary beam and target. The corresponding calculated cross-sections are reported in APPENDIX 2.1.

Finally, the ^{58}Ni target was chosen, combined with a ^{20}Ne primary beam at an energy of 5.1 MeV/A to produce ^{74}Rb isotopes. To produce the ^{114}Cs isotope, the ^{58}Ni target was fixed with a ^{58}Ni primary beam at an energy of 4 MeV/A.

2.1.2 Thickness optimization of the target

The possibility for the isotopes formed in a complete-fusion reaction to go through the target thickness and reach the catcher is mainly determined by the target thickness and the entrance geometry of a catcher. The produced fragments decelerate during their passage through matter. The recoil energy of the ^{74}Rb and ^{114}Cs and the energy losses inside the target material have been estimated using TRIM simulations. The results of energy losses in the target are presented in APPENDIX 2.2. The study is important to optimize the thickness of the target and catcher.

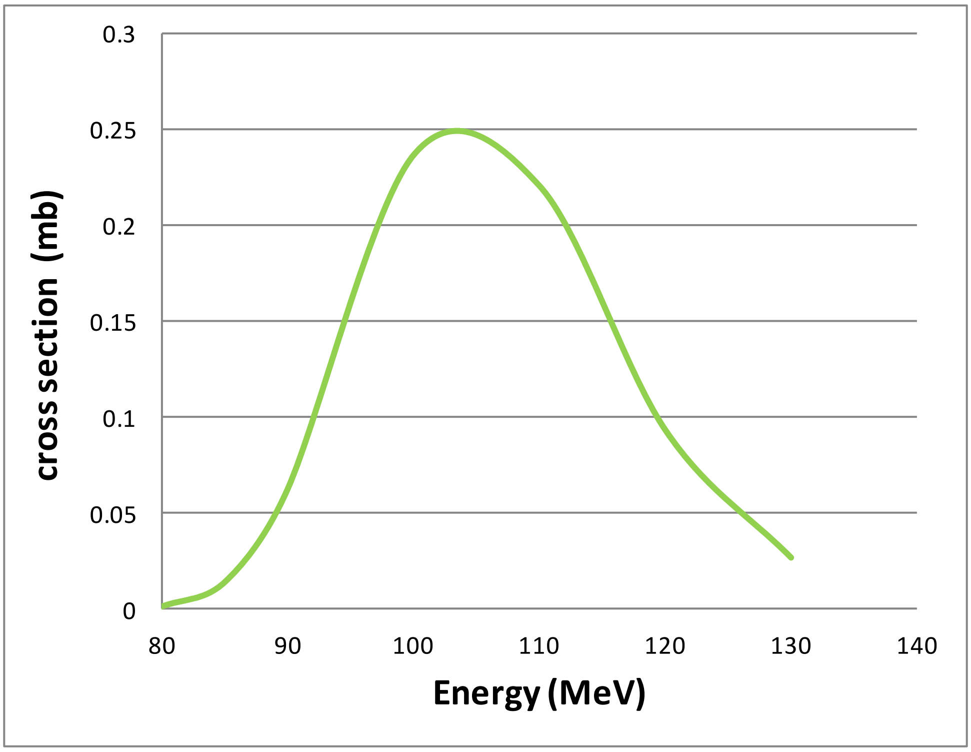

Figure 34: ^{74}Rb production cross-section in function of energy for the ^{20}Ne + ^{58}Ni reaction. The optimized energy to obtain the high in-target production rates within 3 µm of a thin nickel target.

Figure 34 represents in-target production cross-section of ^{74}Rb function of ^{20}Ne primary beam energy. The maximum appears at an energy of 105 MeV. To maximize the in-target production rate of ^{74}Rb, two important aspects are taken into consideration:

- The produced ^{74}Rb must have a sufficient energy to go out of the target, even when they are produced at the entrance of the target and thus they have to go through the whole thickness of the target. The maximum recoil energy of ^{74}Rb is estimated to be 28 MeV, which led to an optimal thickness of the Ni target of 3 µm. the detailed calculations are given in Appendix 2.2.
- ^{74}Rb can be produced from an impinging energy of 80 MeV up to the energy of 130 MeV as shown in Figure 34. Such energy range corresponds to a path of 12 µm for a ^{74}Rb beam impinging a nickel target at 130 MeV.

In the case of ^{114}Cs production, using the same process, a 6.5 µm thick ^{58}Nickel target was combined with a ^{58}Ni primary beam at an energy of 4 MeV/A.

The target diameter was chosen equal to 50 mm as the maximum diameter of the primary beam sent in the SPIRAL-1 facility is equal to 40 mm. The technical reason justifying to maximize the cross-section of the beam on the target is to reduce as much as possible the primary beam power density and thus the risk of local overheating of the target. The calculation of the target temperature was done using the Stephen-Boltzmann law [67], as only radiation effects are involved in the power dissipation from the target.

2.2 Choice of the catcher material

The catcher is used to stop the primary beam and the recoil nuclei coming from the target. The catcher should operate at a sufficiently high temperature to maximize the release of secondary radioactive isotopes. It must stand the temperature for a minimum of two weeks (operation requirement) and its temperature must be limited to limit the heat transfer to the target, which has a working temperature limit fixed at 1700 K. Reducing the working temperature of the catcher ensures a longer lifespan, but can also increase the impact on the AIT time.

For a given temperature, rapid release out of the catcher material requires small distance the atoms have to go through before leaving the material. Thin foils or fibers, or small grains separated by a large open porosity are preferred.

According to the principle of the TISS, the catcher material is heated by an electrical power and the power deposited by the primary beam. To enhance the possible primary beam power on the catcher, a catcher material having a high thermal conductivity and emissivity must be favored to help it cool. Moreover, the heating current flows through the TISS materials can generate the electric field. To do that, the materials using in the development of the TISS must have a sufficient electrical resistivity.

Graphite is a good candidate: the operating temperature is higher than 1700 K, commercially made of grains with various porosities, and more resistive than metals. The graphite having a thickness of 12 µm and density of 1.1 g/cm^3 is sufficient to stop ^{74}Rb isotopes (calculations are presented in APPENDIX 2.2). Doubling the thickness to favor the release toward the cavity rather than posterior of the catcher led to 26 µm, which is too thin for two reasons: it is very fragile and leads to a too high resistance compared to one of Ni target. After several studies a special type of graphite (PAPYEX [13]) material was selected, satisfying the requirements of electrical resistance, size of fibers, low density (1.1 g/cm^3) favoring an important porosity, high emissivity (0.45, see measurements §3.2), several possible commercial thicknesses, mechanical resistance (similar to flexible carton). A final thickness of 200 µm was chosen.

2.3 Release processes from the catcher material

To optimize the production and the release out of ISOL targets, many materials analytical models have been developed across the world [68] [18], [69]–[78]. Target materials are available in the form of molten materials, powder, fibers, and foils. The chemical composition can be pure or oxidized, carburized or made of other molecules, or made of alloys. Advanced targets are developed in the different facilities to cope with their local production conditions. Most of the materials studies (Ta, UC_x, CaO, Nb, ZrO_2, ThO_2, Ti, Zr, Nb, Ni, etc…) [33], [79] and different developments mainly done at ISOLDE/CERN [43] and ISAC/TRUMF [45]. The intensity and the energy of the primary ion beam are crucial to choose the target material and to design its shape.

In the present case, the production and release are separated into two different parts: the target material and the catcher. They can then be independently optimized. In the following, only the release process from the material is considered.

To optimize the release of atoms out of a material, the path of the atoms up to the surface of the material must be crossed in a time as short as possible with respect to their radioactive decay time. Thin foils, fibers, and small grains preferred.

At GANIL, graphite material has been using as a target. It is made of grains having micrometer in size.

2.3.1 Release of atoms from graphite.

Graphite is made of carbon grains compressed and sintered at high temperature. The resulting material is a solid block of grain with porosity depending on the synthesis process. We consider here that the catcher material is graphite made of powder.

When atoms are implanted in the matter, they stop in the grains. The range depends on their impinging energy. For energies of several MeV, the ranges of the atoms within the matter are higher than the typical size of the grains considered, *i.e.* some micrometers. The atoms are considered to be uniformly implanted within the grains. Once stopped, the atoms propagate through the matter up to the free volume between the grains, the propagation process is defined as "diffusion". Then they propagate in the free volume up to the surface of the catcher, the propagation in free volume is defined as "effusion". Diffusion and effusion processes times depend on the physicochemical features of the couple made of the catcher material and the diffusing atom, and on the operating conditions of the matter.

In case of radioactive atoms, the time of diffusion and effusion processes is in competition with the decay time of atoms. Regarding the release of atoms out of the matter, this competition leads to losses, especially for short-lived isotopes. **The goal of the present approach is to maximize the release efficiency of radioactive atoms out of the material by minimizing the release time.**

The approach is based on the following schematic (Figure 35). We assume that the grains are spherical. Each grain has a radius R. The atoms diffuse out of the grains, effuse up to the surface of the catcher material and once they reach the left or the right side, they are considered released out of the catcher. We did the following assumption, based on the probability the atoms have to take the different ways:

- Once out of a grain, the atoms will never come back in the grains, as the propagation in the grain is more difficult than in the free volume between the grains.
- Once out of the catcher, the atoms will never return, as the propagation in the catcher is more difficult than out of it.

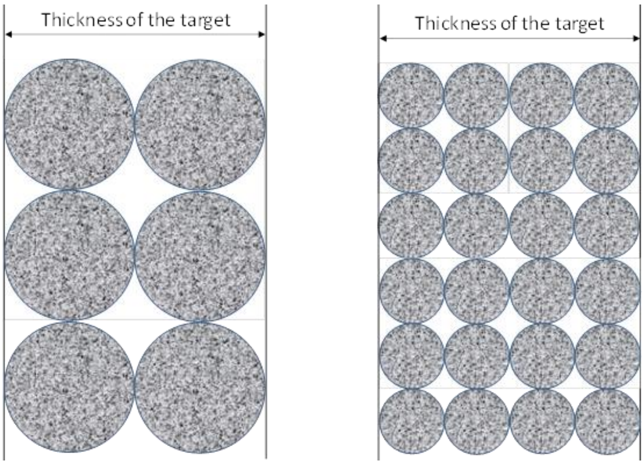

Figure 35: Basic representation of the graphite structure.

In the left part of Figure 35, grains are larger. The diffusion time out of the grains is longer than in smaller grains. Effusion out of an elementary volume formed by a group of 8 grains will also be longer. One could think that optimizing the release of the atoms out of the material could consist in reducing the size of the grains. But to reach the outer surface of the material, if its macroscopic dimensions are unchanged, the atoms also have to go through a series of elementary volumes, whose number increases as the grain size decreases. Diffusion and global effusion processes have opposite dependences on the grain size. There must be an optimum size for an optimal release time. The question addressed here is to obtain the optimum grain size.

To do this an analytical description, taking the two major processes into account was constructed. The following assumptions were made.

- The temperature is uniform over the material volume.
- The density of radioactive atoms in the grains is uniform at t=0 when release processes begin.
- The diffusion of the atoms within the grain material is isotropic.
- The effusion regime of the atoms is molecular (*i.e.* no collision between the atoms are considered).

2.3.2 Diffusion process

The migration of atoms in the matter is a kinetic process, and results in the propagation from high concentration to low concentration regions. Diffusion occurs as a result of the continuous random thermal motion of atoms. While in the matter, the atoms can also share electrons with the material and propagate as ions [80]. The rate of diffusion is greatly governed by the temperature and physicochemical characteristics of the atom and the medium in which it moves.

2.3.2.1 Phenomenological description of the diffusion process

A well-known diffusion phenomenon corresponds to the heat transfer from hot to cold regions of a material. The analytical description for the flow of heat induced by a temperature gradient is given by Fourier's law [81].

$$\boldsymbol{J_P = -k.\frac{dT}{dx}}$$

Equation 1

J_P is the heat flux, *i.e.* the flow of heat per unit area per unit time, $\frac{dT}{dx}$ is the position dependent temperature gradient, and k is the thermal conductivity. The minus sign indicates that the heat flows from high to low temperature regions.

The diffusion of atoms through a solid can be described by Fick's equations. Fick's first law [82] relates the flux J_P of particles, *i.e.* the amount of particles per unit area per unit time to the position dependent concentration gradient dC/dx

$$\boldsymbol{J_P = -D.\frac{dC}{dx}}$$

Equation 2

Minus sign indicates that the flux of particles goes toward low concentration regions. The coefficient D is the diffusion coefficient of the material has unit of area per time ($m^2.s^{-1}$). It fixes the ratio between the flux and the concentration gradient. It depends on the temperature and on the activation energy according to the Arrhenius expression:

$$\boldsymbol{D = D_0.e^{\left(-\frac{E_a}{k_B T}\right)}}$$

Equation 3

D_0 is the temperature independent pre-exponential factor in m^2.s^{-1}, k_B is the Boltzmann constant in J.K^{-1}.mol^{-1} and T is the temperature. E_a is the minimum energy required to initiate a diffusion process in Joules.mol^{-1}.

In the present case, the chemical process consists of an atom moving from one point to another. The energy state of the system formed by the atom and the material can be identical at two different points in the atom. This energy is results from the chemical bonds or/and potential energy at the atomic site. The atom moves under the influence of its thermal kinetic energy. At high temperature, in the limit fixed by the fusion temperature of the material, D tends to D_0. As E_a decreases, the dependence of D on the temperature decreases and for very low value of E_a, D tends to D_0. $E_a = 0$ means that the propagation process no longer depends on chemical reaction or potential barrier. The propagation is then only related to the kinetic energy and is called effusion.

2.3.2.2 Diffusion out of grains

Starting from Fick's laws, M. FUJIOKA [24] established an analytical expression of the fraction of stable atoms remaining at time t in materials having different shapes (sphere, fiber, and foil). In the case of spherical grains having a radius equal to R_s, the fraction $p(t)$ can be expressed as:

$$\boldsymbol{p(t) = \frac{6}{\pi^2}\sum_{m=1}^{\infty}\frac{1}{m^2}\,.\,e^{-(m^2\pi^2 D/{R_s}^2)t}} \qquad \textbf{Equation 4}$$

m is a parameter with no physical meaning. Nevertheless, it can be associated with a number corresponding to a shell containing a part of the atoms. N_0 is the number of atoms present at $t = 0$ in the catcher. We assumed that the catcher contains k grains. Hence, N_0/k atoms are initially contained in each grain. N_{0m}/k atoms are initially contained in the shell m of each grain. From $p(t)$, one can deduce that the flux $f_k(t)$ coming out of a grain at time t is equal to the sum of the flux delivered by each shell:

$$\boldsymbol{f_k(t) = \frac{1}{k}\sum_{m=1}^{\infty}\lambda_{Dm}N_{0m}.\,e^{-\lambda_{Dm}.t}} \qquad \textbf{Equation 5}$$

With $\lambda_{Dm} = \frac{m^2\pi^2 D}{R_S^2} = m^2\pi^2\lambda_D$ where λ_D is the diffusion rate in s^{-1}, equal to $\frac{D}{4R^2}$ and N_{0m} is equal to $\frac{1}{k}\frac{6}{\pi^2}\frac{N_0}{m^2}$. $\left(\text{Remark:} \sum_{m=1}^{\infty}\frac{6}{\pi^2 m^2} = 1\right)$. Replacing them by these expressions, one finds the total flux of atoms delivered by the grains within the volume of the material at time t:

$$\boldsymbol{f(t) = 6.\lambda_D.N_0\sum_{m=1}^{\infty}e^{-\lambda_{Dm}.t}} \qquad \textbf{Equation 6}$$

2.3.3 Effusion rate in the catcher

The effusion rate between the grains is defined as free voids. It can be estimated considering the geometrical volume (see Figure 36) included between 8 spheres and the aperture between them. This gives the mean flight time τ_f.

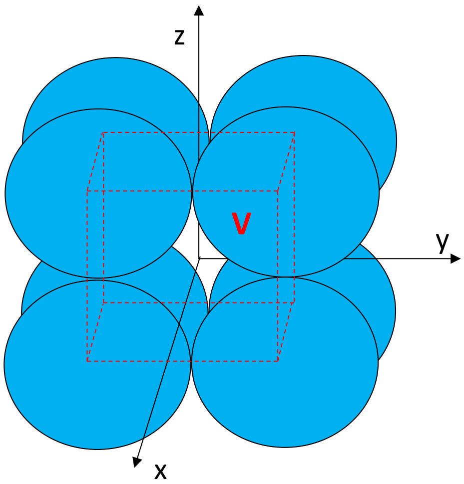

Figure 36: Representation of the position of the elementary cube.

In this configuration, the flux of atoms released in the “central” volume comes from eight-eighths of different spheres. The total flux is equivalent to that released by a single sphere. There are six apertures through which the atoms can escape, two per direction. As mentioned before, catchers are often made of foils. The atoms will mainly leave the foil along the direction perpendicular to the foil (x-direction on Figure 36). Along y and z-direction, the flux of atoms leaving one particular elementary volume will be balanced by the flux coming from the adjacent cubes (see Figure 37). As the atoms are not perceptible, we can neglect the probability for the atoms to leave the free volume of the cube through the y and z apertures, and then consider that the volume presents only two apertures along the x-axis. The calculations are detailed in Appendix 2.3

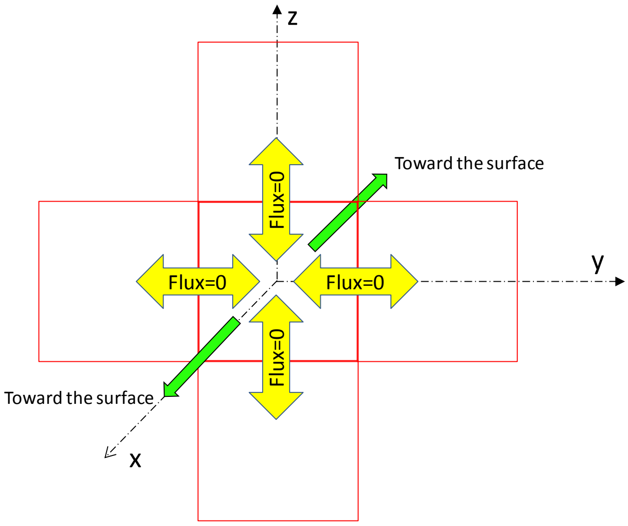

Figure 37: Flux along the different directions. The foil is assumed to be in the yz-plane.

2.3.3.1 *Analytical description of the atoms in voids*

Once in the inter-grain free voids, the atoms propagate through a medium. It can be considered on a microscopic scale. Macroscopically a homogeneous material has a grains size is sufficiently small compared to the dimensions of the catcher. This last condition is generally fulfilled in the case of graphite used in ISOL systems, where the typical size of the grains is of the order of 1 µm and the thickness of the foil is of the order of one mm. Derived from the calculations in [24], the analytical expression of the atom flux leaving the catcher material having a foil geometry is given by:

$$\boldsymbol{f(t) = 8.\lambda_E.N_0 \sum_{n=0}^{\infty} e^{-\lambda_{En}.t}} \qquad \textbf{Equation 7}$$

Where λ_E is the effusion rate, and is equal to D_E/d^2. D_E is the effusion coefficient of the atoms in the catcher and d is the thickness of the catcher. N_0 is the number of atoms effusing in the volumes between the grains. n is an integer which is related to the planar shell n containing N_n atoms as:

$$N_n = \frac{8.N_0}{(2n+1)^2\pi^2} \left(\text{Remark: } \sum_{n=0}^{\infty} \frac{8}{(2n+1)^2\pi^2} = 1\right).$$

And λ_{En} is the effusion coefficient of the atoms out of the shell n and defined as:

$$\boldsymbol{\lambda_{En} = (2n+1)^2\pi^2\lambda_E} \qquad \textbf{Equation 8}$$

An important remark must be made about λ_e and λ_E, which leads to establish the relation between them. λ_e corresponds to a microscopic effusion process within a volume defined by a small number of grains (8 in our case). It is therefore related to the size of the grains. λ_E corresponds to a macroscopic process and is related to the size (or thickness, in the present case) of the catcher foil. Both are related through the effusion coefficient D_E which is an internal parameter and therefore independent of the scale on which the effusion process is observed. The difference in λ_e and λ_E comes from the size of the object where the effusion occurs. In the case of our elementary volume given in Figure 36, the relevant dimension is the radius R, and λ_e must then be equal to D_E/R^2. As we also have established a relation between λ_e and the local effusion parameters ($\lambda_e = \gamma.\beta/R$), we obtain:

$$\frac{\gamma.\beta}{R} = \frac{D_E}{4R^2}$$

Thus

$$\boldsymbol{D_E = \gamma\beta R} \qquad \textbf{Equation 9}$$

In the case of a catcher having a thickness equal to d, the effusion rate λ_E will be equal to

$$\boldsymbol{\lambda_E = \frac{\gamma\beta R}{d^2}} \qquad \textbf{Equation 10}$$

This expression represents an important step in our approach since it connects the microscopic structure of the grain to the macroscopic effusion features of the catcher. Since the diffusion out of the grains also takes into account the size of the grain, it will be possible in the following equations to describe diffusion and effusion processes out of a macroscopic catcher while taking into account its microscopic structure. The detailed analytical calculations are reported in APPENDIX 2.3.

2.3.4 Diffusion-Effusion processes

We consider in the following paragraph that the release process of the atoms from the catcher occurs in two consecutive steps, the diffusion of the atoms out of the grain and then their effusion out of the catcher. The probability that the atom returns back to a grain or to the catcher is neglected once they have left. This assumption is indeed not fully realistic: neither the diffusion nor effusion is a one-way process. However, this assumption is justified by the diffusion and effusion rates which lead the atoms to leave the catcher material.

The process treated in two consecutive steps simplifies the analytical description. The previous flux of atoms released by the grains is boosted by the effusion process. The variation with the time of the number x_n of atoms present in the free volumes between the grains and included in the shell n is equal to the difference between the flux effusing out of the shell n and the flux of atoms contained in the shell n and coming from the grains, and can be expressed as:

$$\left.\frac{dx_n(\mathrm{t})}{dt}\right|_{In\ the\ free\ volume} = -\lambda_{En}\, x_n(\mathrm{t}) + \ 6.\lambda_D.N_n \sum_{m=1}^{\infty} e^{-\lambda_{Dm} t}$$

This gives us the total flux $F(t)$ coming out the catcher

$$\boldsymbol{F(t) = \ 48.\lambda_D.\lambda_E.N_0 \sum_{n=0}^{\infty} \sum_{m=1}^{\infty} \frac{1}{\lambda_{En}-\lambda_{Dm}} \left[e^{-\lambda_{Dm}\, t} - e^{-\lambda_{En}\, t}\right]} \qquad \text{Equation 11}$$

As the evolution of the flux of atoms in the catcher and out of the catcher is now related to the diffusion and effusion rates, we have to express these rates as a function of the radius of the grains. If the radioactive decay constant λ is taken into account during the diffusion and effusion process in the catcher, the total release rate of a given radioactive element coming out of the catcher can be expressed as:

$$\boldsymbol{F(t) = \ 48.\lambda_D.\lambda_E.N_0.e^{-\lambda t} \sum_{n=0}^{\infty} \sum_{m=1}^{\infty} \frac{1}{\lambda_{En}-\lambda_{Dm}} \left[e^{-\lambda_{Dm}\, t} - e^{-\lambda_{En}\, t}\right]} \qquad \text{Equation 12}$$

The optimum grain size can be obtained by calculating the mean release time out of the catcher:

$$\boldsymbol{< t >= \frac{\sum_{m=1}^{\infty} \sum_{n=0}^{\infty} \frac{\lambda_{En}+\lambda_{Dm}+2\lambda}{(\lambda_{Dm}+\lambda)^2 (\lambda_{En}+\lambda)^2}}{\sum_{m=1}^{\infty} \sum_{n=0}^{\infty} \frac{1}{(\lambda_{Dm}+\lambda)(\lambda_{En}+\lambda)}}} \qquad \text{Equation 13}$$

It depends on only a few parameters: the microscopic radius R of the grains, the diffusion coefficient D of the grain material, the effusion coefficient D_E , the macroscopic thickness d of the catcher. Among these parameters, the determination of the diffusion coefficient of the atoms in the matter remains an issue.

R is usually known from the mesh size of the sieve used to select the grains. The largest grains have a size equal to the size of the mesh, and the grains having a smaller size than the mesh are also collected. Thus we have to consider the presence of the small grains between the larger grains, and this increases the density of the material. Before comparing our calculations to experimental results, we have estimated the effect of these smaller grains, or the effect of the density on the release mean time. Those calculations are detailed in APPENDIX 2.3. The effect of the density has been taken into account in the following paragraphs.

2.3.5 Calculation of the optimum grain size

The optimum grain size is defined as the size corresponding to the minimum value of the release mean time from the catcher. The maximum of the mean release time is necessarily limited by the half-life of the isotope considered. The minimum mean release time only depends on the times of diffusion and effusion processes.

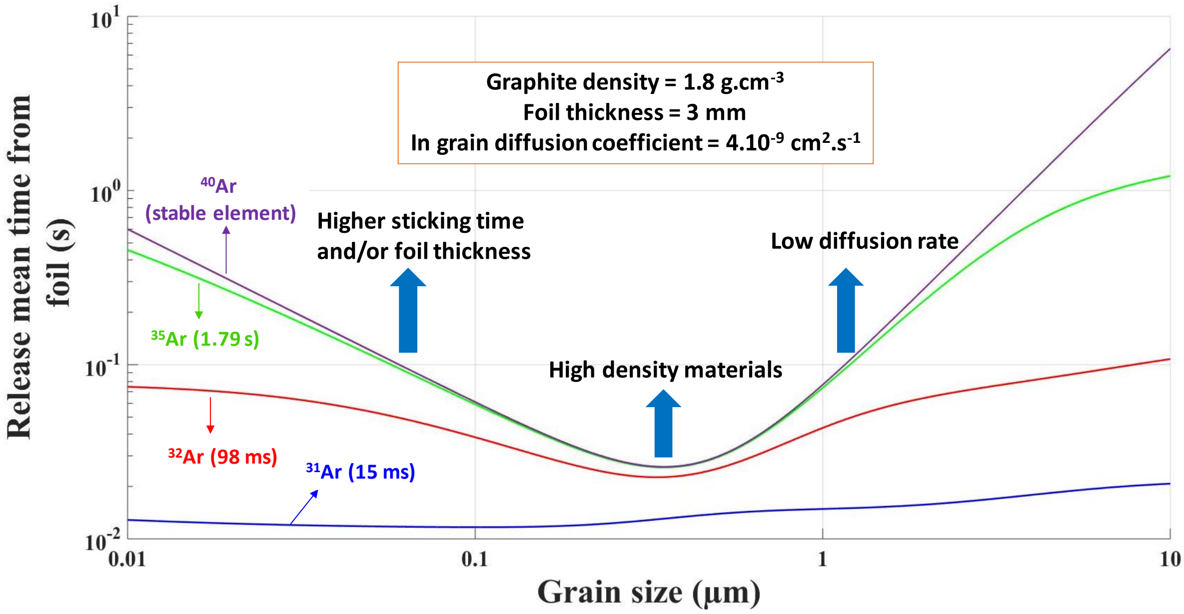

Figure 38: Influence of grain size on release mean time of catcher.

Figure 38 shows the optimum grain size of a material in which Ar isotopes of different half-lives diffuse and effuse. The release meantime has been calculated for C. Eléon's operating conditions [23]: the size of the grain was equal to 1 µm, the density was equal to 1.8 g/cm^3 and the temperature was equal to 2100 K. The diffusion coefficient was deduced from the experimental results and was 4.10^{-09} cm^2.s^{-1}.

For larger grains, the diffusion time dominates and increases the release time. For smaller grains, the diffusion time becomes negligible compared to the effusion time, which thus dominates. If the density increases, the release time increases.

We observe that the mean release time decreases when the half-life of the isotopes decreases. Indeed this does not mean that the speed of the atoms depends on the isotope considered, but means that the mean release time is determined by the atoms having a probability to be released from the material. The isotopes starting from a point too deep inside the material have little chance to reach the surface before decaying. The short mean release time calculated for ^{31}Ar means that very small quantities of ^{31}Ar atoms are released.

The description shows that an optimum grain size exists for each radioactive element, which is not the smallest grain size. So looking for a catcher material made of grains with a smaller size seems to be not justified yet.

2.3.6 Catcher Release efficiency

As the processes of diffusion and effusion are considered sequentially, the release efficiency can be calculated by the product of the diffusion efficiency ε_{diff} and the effusion efficiency ε_{eff}.

$$\boldsymbol{\varepsilon = \varepsilon_{diff} \times \varepsilon_{eff}}$$ **Equation 14**

According to the expression provided in [24] for the diffusion of atoms out of a grain, the diffusion efficiency is given by the expression.

$$\boldsymbol{\varepsilon_{diff} = 3\frac{\sqrt{\frac{\lambda}{\lambda_D}}.coth\sqrt{\frac{\lambda}{\lambda_D}}-1}{\frac{\lambda}{\lambda_D}}}$$ Equation 14

And the release efficiency of atoms out of a foil having a thickness “d” is given by the expression.

$$\boldsymbol{\varepsilon_{eff} = 2\sqrt{\frac{\lambda_E}{\lambda}}.tanh\left[\frac{1}{2}\sqrt{\frac{\lambda}{\lambda_E}}\right]}$$ Equation 15

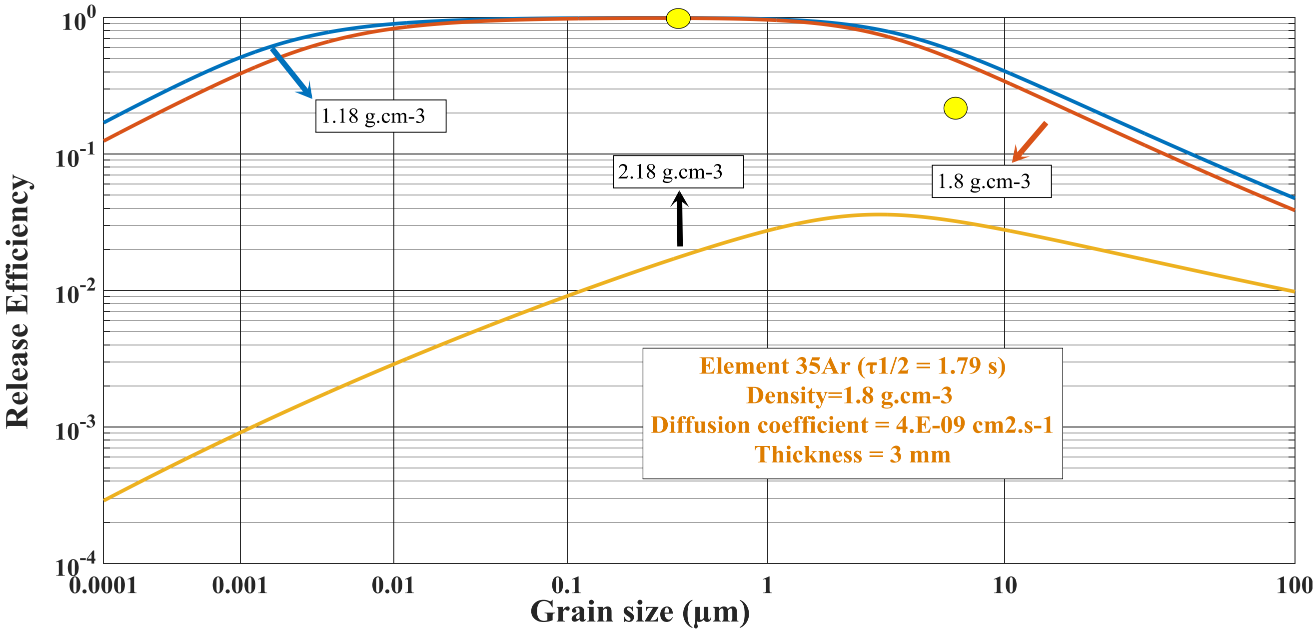

Figure 39: Release efficiency versus grain size for three different densities. Yellow dots are experimental measurements.

Figure 39 represents the release efficiency of the catcher versus the radius R of the grain size . The 1.18 g/cm^3 density assumes no overlap between the grains, just a point like contact in each dimension. A density of 1.8 g/cm^3 corresponds to a material previously tested and assumes an overlap between the grains. A density of 2.18 g/cm^3 corresponds to a density close to the maximum, before closure of the apertures between the elementary volumes.

For grain sizes ranging from 50 nm to 1 µm and a density of 1.18 g/cm^3, the release efficiency is close to 100%. In this range, the efficiency difference between 1.8 g/cm^3 and 1.18 g/cm^3 densities is therefore not significant. These results can be interpreted to say that there would be no point in looking for lower density materials, which are often more difficult to synthesis, which lead to larger catcher volumes and from which the energy deposited by the primary beam is more difficult to remove. Nevertheless, the assumption of the present description does not take into account, not spherical grain shapes, which can lead to open porosity lower than the one induced by spherical grains.

As shown in Figure 39, decrease of the density from 2.18 g/cm^3 to 1.18 g/cm^3 leads to an increase in release efficiency by a factor of 30 for 1 µm grains. The effect of the density is more important on the effusion than on the diffusion, as the increase of the density mainly acts on the size of the voids.

2.3.7 Catcher specifications and conclusions

The model is thought to be suitable for grainy ISOL material constructed from powdered components.

In the case of ^{35}Ar in graphite, the optimum grain size would be equal to 0.3 µm at 2100 K. This value reproduces previous observations but the agreement with materials used in the present study requires experimental conformation.

For each radioactive element, there is an optimum grain size, which is not the smallest size.

Reducing the grain size helps the release out of the grain, but must be combined with a sufficient porosity to help the release out of the catcher. Nevertheless, in the frame of our assumptions and for ^{35}Ar, a graphite density 20% lower than its maximum (2.26 $g.cm^{-3}$) is sufficient to reach release efficiency equal to 98%.

Having large porosity has also a consequence on its thermal characteristics, which has not been considered here.

These conclusions cannot be easily transposed to the production target, which must also be optimized to maximize the in-target production of radioactive isotopes. Minimizing the density to maximize the release out of the target material has been a consideration for years in the ISOL target material design. But its consequence on the macroscopic geometry of the target must also be taken into account if one wants to optimize the whole atom-to-ion transformation efficiency. To conserve the same production rate of nuclei in the target, the number of target atoms in interaction along the path of the impinging ions must be conserved. So the target must be lengthened if the target density is smaller. The total volume of the target will then be larger, increasing the release time of the atoms out of the target container.

For the target materials made of grains, the diffusion and effusion processes are in competition and low density materials release particles faster from catcher. Therefore, it is better to develop a target made of low density materials for faster release.

These calculations were applied for ^{74}Rb and ^{114}Cs. The diffusion coefficient is 2.10^{-8} and $2.5.10^{-8}$ $m^2.s^{-1}$ [83], the thickness of the catcher is 26 µm and 32 µm for ^{74}Rb and ^{114}Cs respectively. The temperature considered in the calculations was 1700 K, density was 1.1 $g.cm^{-3}$. The corresponding mean release time from the catcher is 0.6 ms, 0.7 ms for ^{74}Rb and ^{114}Cs, and respectively and the optimum grain size is equal to 0.6 µm.

2.4 Sticking time of atoms on the surface

2.4.1 Introduction

Once released from the catcher material, atoms effuse in a vacuum. The typical vacuum level of ISOL target ion source systems (TISS) satisfies molecular-flow conditions (or is close to) limiting undesired chemical reactions. In this regime, a particle undergoes many more particle-target container wall collisions than particle-particle collisions. This means that a particle coming from the target surface freely flies in a straight line until reaching another surface where it can be adsorbed and then desorbed. The propagation of particles under these conditions is defined as effusion.

For chemically reactive atoms, the binding of an atom on the surface defined adsorption and release of an atom from surface defined as desorption. The delay caused by one adsorption-desorption cycle (or sticking per contact) has to be multiplied by the total number of hits. It is important compared to the time of flight.

The sticking time on the different materials constituting the inner parts of the chamber is part of the AIT time and is therefore to be considered in the competition with radioactive decay. It can be reduced by heating the materials, up to a temperature close to the fusion limit. The drawback of this method is a reduction of the lifespan of the materials. An alternative method is the reduction of the sticking time by an optimization of the atom-material pair. To optimize AIT time, it is necessary to know the sticking time for each atom-material pair, which is unavailable in the literature. When it available, the experimental conditions were different. Sticking time results from experiments or calculations performed in close conditions were presented in [26], have been used.

2.4.2 Surface adsorption

The interaction of atoms with the surface has been studied [26], [84]–[86] to a great extent. The stochastic process is generally described as an atom trapped in a potential well with characteristics defined by both the atom and the material. Their binding energy is represented by a time dependent distribution. When the atom reaches the region of the distribution corresponding to energies higher than the depth of the potential well, the atom can leave the surface. An increase of temperature induces a shift of the distribution towards higher energy, fostering the release rate of the atoms from the surface of the material. The energy distribution is also related to the vibrations of the atoms at the surface of the material. Above a given magnitude of oscillation, the bound is broken and the atom is released from the surface. The relation between binding energy (generally called activation energy of desorption, E_{des} is a negative energy in (eV) and time has been first proposed by Langmuir [87]. Then it was first developed by Frenkel [27] using the method of classical statistical mechanics. In his developed.

$$t = t_o . e^{-\left(\frac{E_{des}}{k_B . T}\right)}$$

Where $t_0 \approx 10^{-13} s$ is the minimum oscillation period around the equilibrium position (perpendicular to the surface) for an infinite temperature. Above this period, the energy is higher than the binding energy. k_B is the Boltzmann constant (unit) and T is the absolute temperature (in K).

The goal here was to determine if a clear correlation exists between atomic stickiness, the surface material and the sticking time. The idea was to extract useable rules or tendencies that could be used to optimize the atom-material pair and minimize the sticking time. Obvious parameters explored were the first ionization potential of the atoms and the work-function of the material. However, their relation to the binding energy cannot be directly established. Moreover, absolute values of first ionization potential and the surface work function can be significantly different [88]–[90], which restraining the present discussion to trends of the sticking time. To avoid the use of an analytical description of the sticking process and the extraction of adsorption model-dependent results, desorption energies of atoms from different metallic surfaces were used. They were determined by

Eichler using an empirical model for Cs, Rb, K, Na, Ba, Sr, Ca, Mg atoms sticking on Nb, Zr, Al, Ta, W, Cu, Re and Ir surfaces for one part, and for La, In, Ti, Bi, Pb, Ag, Cu, Po, Cd and Hg atoms sticking on Mo, Fe, W surfaces for a second part. Using these desorption energies and the Frenkel equation, the sticking time t versus the first ionization potential of the atoms and the work-function of the materials was calculated.

2.4.3 Sticking time in correlation with first ionization potential and work function

Except for noble gases, all other elements are able to sticks to the surfaces. The sticking-time is presented separately for alkalis (Figure 40) and alkaline earth elements (Figure 41). Others elements, from IIIA to VIIB columns of the Mendeleïev table, have been gathered on the same graph (Figure 42).

The sticking-time only depends on the atom, on the surface material and on the temperature. It was calculated for a temperature of 1600 K in order to make it comparable with the experimental results obtained a few years ago [14] within the 1400-1700 K temperature range.

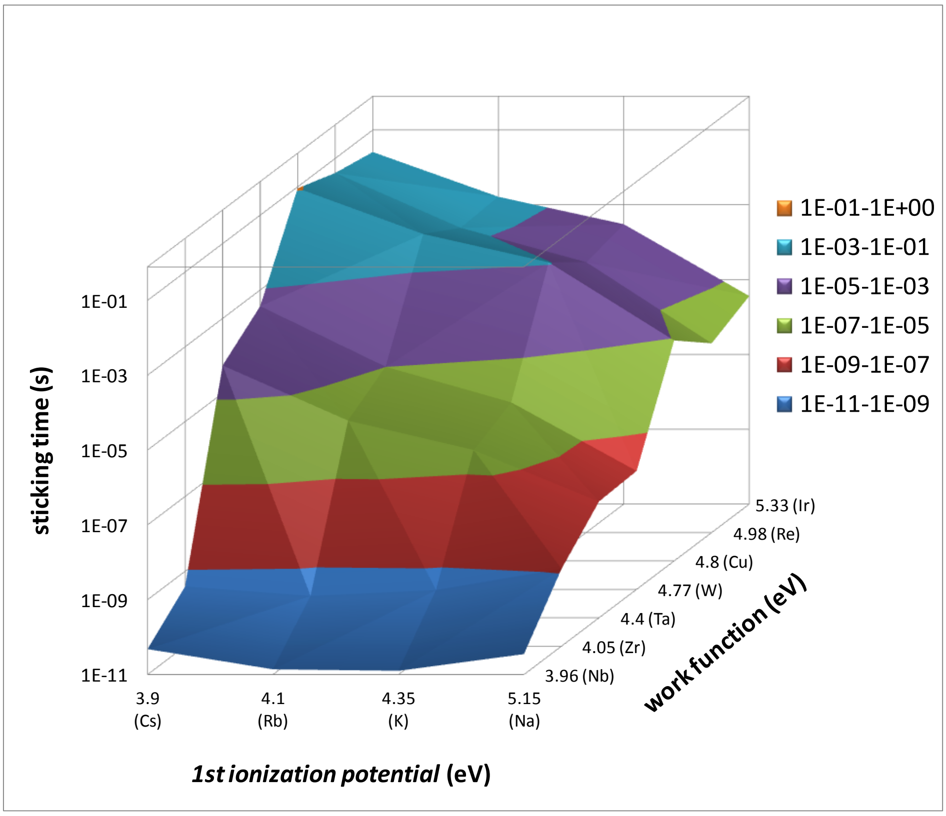

Figure 40: The sticking time of alkali elements (Cs, Rb, K and Na) on refractory metals (Nb, Zr, Ta, W, Cu, Re and Ir).

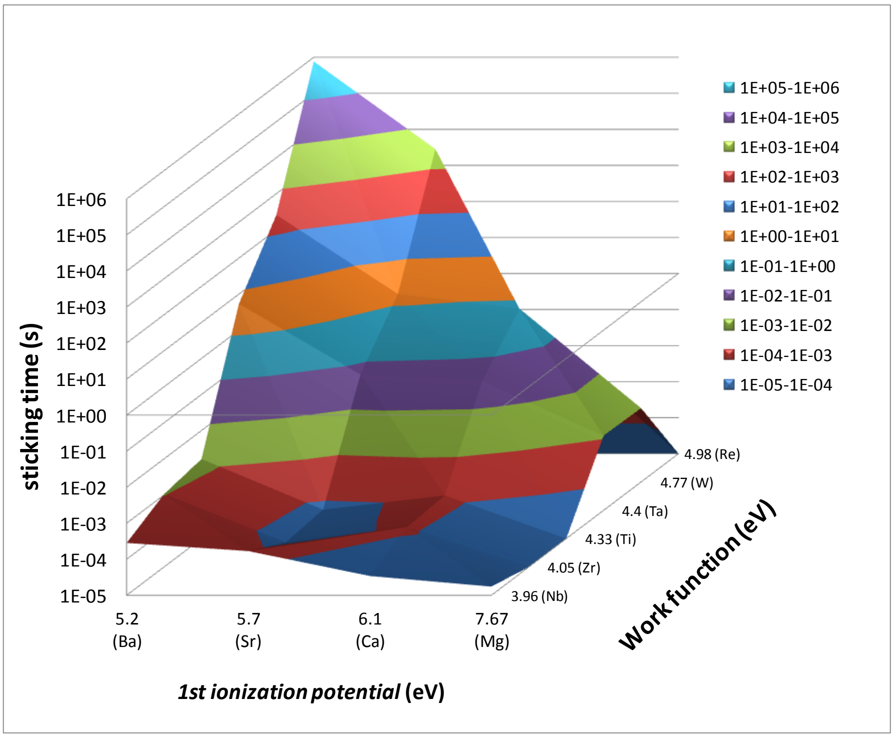

Figure 41: The sticking time of alkali earth elements (Ba, Sr, Ca and Mg) on refractory metals (Nb, Zr, Ti, Ta, W and Re).

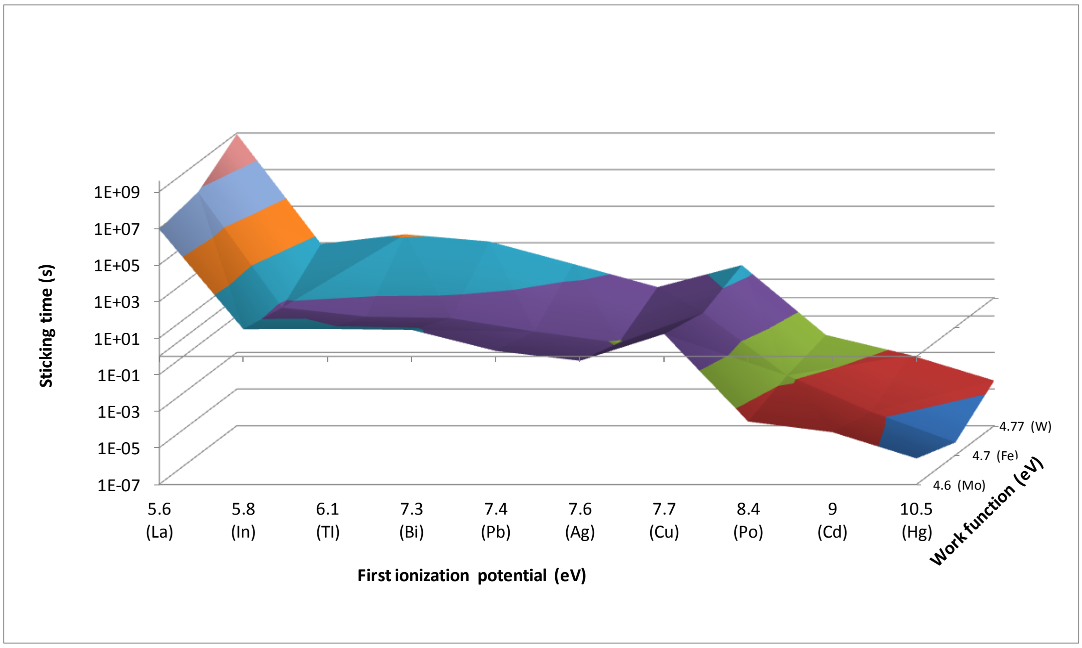

Figure 42: The sticking time of elements of the groups (IIIB to IIA) on different metals (Mo, Fe and W).

The above figures present the evolution of the sticking time of atoms on different refractory metals versus first ionization potentials of atoms and work functions of materials. Among the metallic material considered, niobium has the lowest work function (W_{Nb}~3.96 eV) and iridium has the highest (W_{Ir}~5.33 eV). In case of alkali atoms, having the lowest first ionization potentials, ranging from 3.95 eV for Cs to 5.15 eV for Na, the sticking time per contact on Nb varies from 4.8×10^{-10} s to 1.3×10^{-11} s, and from 2.6×10^{-2} s to 3.6×10^{-6} s on Ir.

In the case of alkaline-earth atoms, the first ionization potentials range from 5.2 eV for Ba to 7.67 eV for Mg. The corresponding sticking time respectively varies from 2.8×10^{-4} s to 1.7×10^{-5} s on Nb (W_{Nb}~3.96 eV), and varies over a wide range of values from 7.6×10^{5} s to 2.8×10^{-4} s on Re (W_{Re}~4.78 eV).

In the case of metallic atoms on metallic materials, the trend of the sticking time evolution versus the work function of the materials is more difficult to comment as the range of work function values covered from Mo (W_{Mo}~4.6 eV) to W (W_{W}~4.77 eV) is too narrow. Nevertheless, the sticking time again tends to decrease as the work function decreases, whatever are the sticking atoms considered. Over the large first ionization potential range considered, going from 5.6 eV for La to 10.5 eV for Hg, the sticking time decreases by 14 orders of magnitude, from 8.8×10^{8} s for La on W to 2.6×10^{-6} s for Hg on Mo. Apart for In and Cu sticking times, which seems to have a different behavior considering the mean trend observed in Figure 42, the sticking time decreases regularly as the first ionization potential increases.

All the curves show that the sticking time decreases as the first ionization potential increases and as the work-function decreases. This calculations gives a useful rule to choose the materials constituting apparatus in which sticking time must be minimized.

2.4.4 Comparison with experimental results

It is quite difficult to find experimental results of sticking time for different atoms-surface material couple in the literature. When available they are often difficult to compare as obtained in different conditions (roughness of the surface, temperature, experimental setup). A comparison of the calculated sticking time with literature [14]. For alkali elements sticking time on a C surface was extracted from Figure 40.

Low energy (1keV) pulses of alkali ions were sent into a graphite cavity of some tens of cm^3 through an entrance aperture. They were caught in a graphite foil and effused in the cavity until they escaped via through the exit aperture. The response time between the injection and extraction of the ions was measured, which depends on the time of flight of the atoms within the cavity and dwell time on the surface. The number of flights between the walls of the cavity was estimated using a Monte-Carlo code [91] and could be approximated using the ratio of the inner surface of the cavity divided by the aperture areas. Once this time of flight deduced from the total response time, the remaining response time was divided by the number of hits that gives the sticking time per contact. Figure 43 they are compared to the values calculated using the Frenkel equation for Cs, Rb, K, and Na.

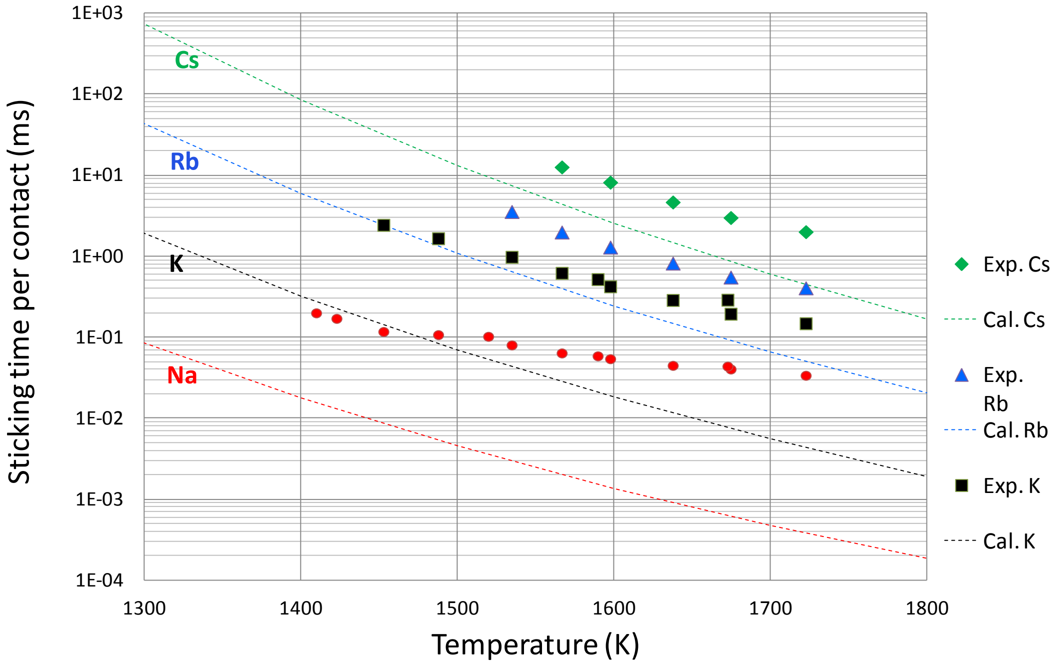

Figure 43: The sticking time of alkalis as a function of temperature.

The results shows that sticking times are longer for alkalis with a lower first ionization potential, in agreement with the trend observed in Figure 40. As expected, sticking time decreases as the temperature increases. Nevertheless, two obvious comments can be made: experimental values are all above the calculated ones, and the difference increases with the first ionization potential (from Cs to Na) up to two orders of magnitude in case of Na at 1723 K.

The second remark is that the experimental sticking times lie closer to calculated ones as the temperature decreases, or that the sticking time decreases more slowly as the temperature increases. Both remarks can find a qualitative explanation on the graphite surface used for measurements. Its roughness was of the order of 1.6 µm, offering traps in which atoms can reflect and spend more time than on a perfect surface, *i.e.* which would have a roughness lower than 10^{-10} m. The sticking time decreases exponentially with the temperature whereas the time of flight depends on the square root of the temperature, this last parameter conserves a relative influence on the sticking time and is more important at higher temperature. In the case of the more sticky elements, the influence of the time of flight must be less important and the relative difference between calculated and experimental sticking time values must be lower. This behavior is clearly observed in Figure 43 for Cs, which sticks on carbon longer than for other alkalis.

2.4.5 Conclusions

As far as we know, this is the first time the sticking time of particles is represented as a function of the first ionization potential and the work function of the surface material. In summary, the key finding of this work is that the sticking time is inversely proportional to the first ionization potential of the particle and directly proportional to the work function of the surface material. The particles sticking time can be reduced two to four orders of magnitude by using lower work function materials. The sticking time can be reduced by heating the surface at higher temperatures. The process of heating the surface can lead to material structural breakdown. The reduction in sticking will improve the atom to ion transformation efficiency, and it is important when dealing with short-lived radioactive elements.

The work presented in this thesis will provide the opportunity to optimize combinations of atom/surface pairs to improve the performance of the target ion source systems. The sticking of isotopes on surfaces results in slowing down the release process. It can be considered as a reduction of the mean velocity of the atom. The effusion step is the limiting factor in time for the production of the short-lived elements.

The results show that the effusion step sets the limit of the TISS. In the case of long surface sticking times, severe delay losses may additionally arise from back-diffusion of particles already released from the target. It is necessary to find a way to reduce the number of collisions for short-lived radioactive isotopes.

2.5 Effusion process in the TISS cavity

Effusion corresponds to a continuous random motion of particles. Over time, some particles will pass through the exit aperture of the TISS. The produced particles diffuse from the structure of the grains to the container. In the molecular vacuum regime of the TISS, the *TOF* is expressed according to the average distance traveled between two collisions "D_v", the mass "m" of the particle, temperature "T" and the Boltzmann constant k_B:

$$TOF = D_v \sqrt{\frac{m}{3k_B T}}$$

At each collision, the atom spends time on the walls before being released from the surface. The total effusion time of an atom in the cavity can be calculated by multiplying the sum of the mean time of flight τ_f and sticking time τ_s per contact by the number X of flights:

$$T_e = (\tau_f + X * \tau_s)$$

The mean free path and number of collisions independent of the atomic mass and the surrounding temperature. It depends only on the cavity geometry. The effusion time is therefore directly related to the size of the cavity, via the speed of the atoms. A compact TISS would be expected to have shorter effusion times.

Another way is to ionize the atoms in the target cavity and then guide them towards the cavity exit by an electric field. In this way, it is possible to reduce the number of collision, the associated sticking time and the time of flight. This possibility can be implemented only after the formation of ions. The simplest case is to start with alkali atoms, since they are easily ionized on contact with a hot surface.

2.6 Principle of the surface ion source

The surface ion source (SIS) is used to produce singly-charged ion beams from low first ionization potential elements (<6 eV), mainly alkali elements. The principle is the following: atoms hit a hot material and shares an electron with the surface. Once the atom leaves the surface, the electron stays with it, or on the surface, with a probability dependent on the first ionization potential, the work function of the surface and the temperature.

Since it is inefficient for atoms with higher first ionization potentials, the surface ionization process is selective and is therefore recommended for the production of alkali ions using the ISOL method.

Remark:

Physico-chemical characteristics of the surface material and of the atom couple govern surface ionization and sticking processes. Our goal is to optimize the whole AIT efficiency, by limiting the sticking time and by maximizing the surface ionization efficiency. We have seen in paragraph 2.4 that a low work function material is needed to limit the sticking time. If one now considers the ionization process, the work function of the material must be higher to maximize the efficiency. A compromise is therefore necessary, but this aspect has not been studied in the present work.

The fundamental principles and analytical descriptions of surface ion source are clearly described in the literature [55], [58], [59], [92]–[94].

According to founding work led by Langmuir, the probability ε_+ for an atom to be ionized at each contact with the surface is given by the following equation:

$$\boldsymbol{\varepsilon_+ = \frac{1}{1+\frac{g_0}{g_i}.e^{\frac{W_i-\emptyset}{k_B T}}}}$$

Where k_B is Boltzmann constant, T is the surface temperature of the material, W_i is the first ionization potential of the element, Ø is the work function of the material and g_0 and g_i represent the statistical weights of the ionic and atomic ground states (for the alkali elements, $g_0/g_i = 1/2$).

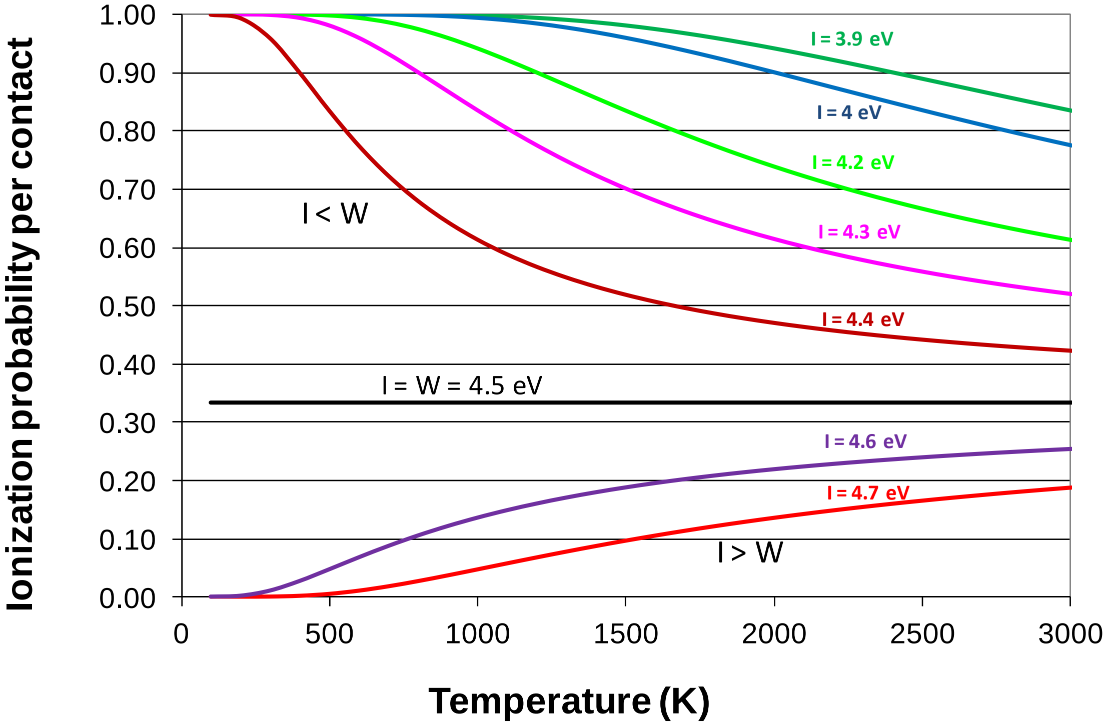

Figure 44: Ionization probability per contact versus elements on a graphite surface. The black line corresponds to a work function (Ø) equal to the first ionization potential (W_i). The lines above the black line represent the case of (W_i<Ø). The lines below correspond to (W_i>Ø).

Figure 44 illustrates the ionization probability per contact with respect to the temperature of the surface. The ionization efficiency depends on the first ionization potential (W_i) of the element, work function (Ø) of the material and temperature.

For Ø higher than W_i, the ionization probability is close to 1 at low temperature, and decreases when the temperature increases. For a given material and thus for a given work function, the decrease of the ionization probability with the temperature increase is faster when the first ionization energy of the atom comes closer to the work function value.

For Ø lower than W_i, the ionization probability is close to 0 at low temperature, and increases when the temperature increases. For a given material and thus for a given work function, the increase of the ionization probability with the temperature increase is faster when the first ionization energy of the atom comes closer to the work function value.

In both cases, the efficiency limit at high temperature is equal to 0.33.

In the case of ^{74}Rb (W_i=4.18 eV), the ionization efficiency on graphite (Ø=4.5 to 5 eV) and on Ni (Ø=5.04 to 5.35 eV) both range from 98% to 100% at a temperature of 1700 K.

In the case of ^{114}Cs (W_i=3.9 eV), the ionization efficiency on graphite and on Ni is equal to 100% at a temperature of 1700 K.

Chapter 3: Design of the TISS for the production of alkali and alkali-earth isotopes

The goal of this development is to demonstrate how efficient can be an Isotope Separation On-Line (ISOL) Target Ion Source System (TISS) if it is optimized for the production of a specific radioactive ion beam.

This new TISS aims for the production of very short-lived elements. Here, very short-lived means elements whose half-life is less than 10 ms for gases, and less than 100 ms for alkaline, alkali-earth, and metallic elements.

To produce such very short-lived elements, it is required to optimize the whole TISS in order to reduce decay and delay losses during the atom-to-ion transformation (ATI) process and to reduce the ATI time. Therefore, the typical time of whole ATI time should be as short as possible regarding the half-life of the radioactive atoms.

As explained in chapter 2, ^{74}Rb (64.8 ms) ion has been chosen as a case study, and ^{114}Cs (570 ms) as possibly produced using the same TISS. It answers the request made by physicists. It has suitable physicochemical characteristics making it well adapted for a competitive production with the innovative system proposed in this Ph.D. work. It can be produced by fusion-evaporation, it has a mass which can be handeld by the upgraded SPIRAL-1 [2] facility (charge breeding and post-acceleration). ^{74}Rb has a low first ionization potential and can thus be selectively ionized by surface ionization. Possible optimizations discussed in chapter 2 should lead to a performant TISS.

In the following paragraph the technical design of the TISS which takes into account the conclusions of chapter 2 is described.

3.1 Description of the TISS design principle

Figure 45 presents a cross-section view of the TISS for the production of ^{74}Rb and ^{114}Cs. This design is a result of an optimization in response time, efficiency and flexibility in both mounting and operation. It mainly consists of radial foils of 50 mm in diameter intersected by 12 mm graphite grid (0.8 mm thick). Reliant on primary beam, the first foil act as a target (^{58}Ni) and second act as catcher. A 3 µm and 6.5 µm thin target foils are used for the production of ^{74}Rb and ^{114}Cs. Foils are fixed with two radial flanges directly connected to the grid. This system is called the cavity or the TISS. A current is injected in the walls of the cavity, *i.e.* walls of the ring and of the foils, through a flexible tantalum band situated away from the exit aperture of the TISS. The current leaves the cavity through a graphite wheel connected to the cavity at the exit aperture. Both extremities of tantalum band and graphite wheel are fastened to cooled parts, current feed through and vacuum chamber respectively.

Owing to the current flowing through the resistive materials of the cavity, the cavity is heated and an electric field oriented towards the exit aperture is created within the cavity.

^{74}Rb ions are produced by fusion-evaporation using a primary beam of neon ^{20}Ne (intensity of 1.8.10^{13} pps at an energy of 5.5 MeV/A) striking a nickel target (^{58}Ni) having a thickness of 3 µm. In case of ^{114}Cs, the primary beam is ^{58}Ni (intensity of 3.10^{12} pps at an energy 4 MeV/A).

The produced isotopes and the primary beam are stopped in the thin graphite catcher 12 mm beyond the target.

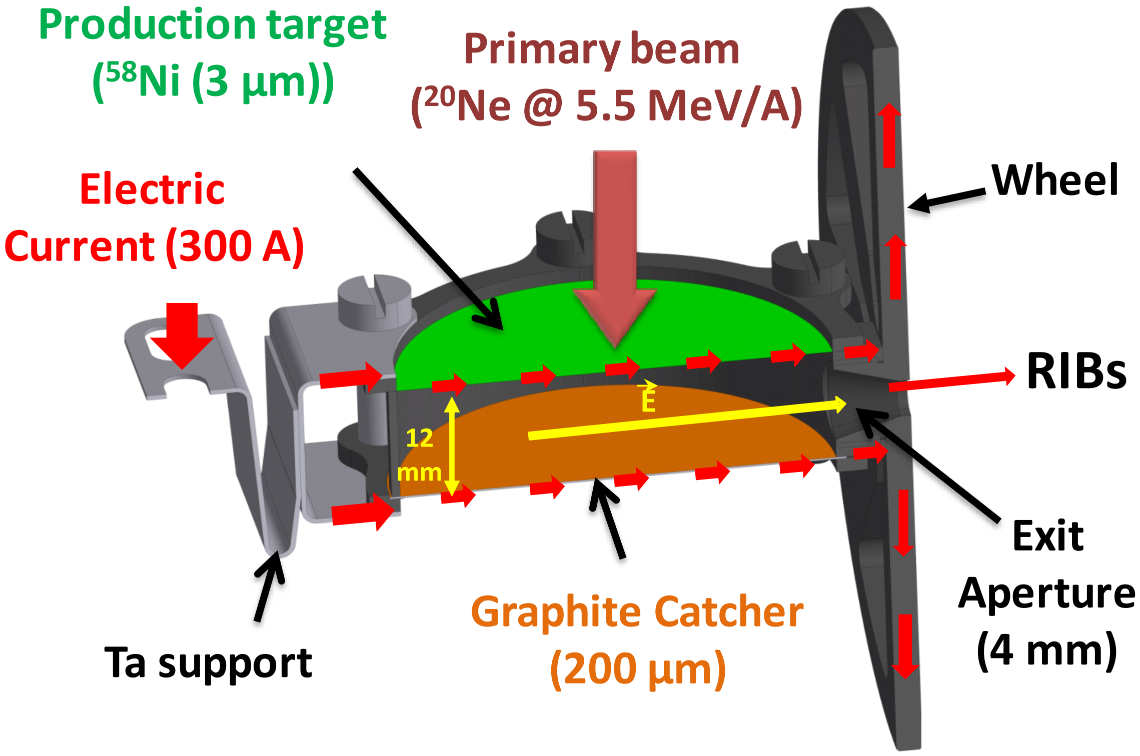

Figure 45: Cross-section view of the TISS for the production of ^{74}Rb isotopes.

The secondary radioactive isotopes diffuse and effuse out of the catcher, are ionized by contact with the hot surfaces of the cavity and are pushed towards the exit hole by an electric field.

According to the supplies in the production cavern of SPIRAL-1, where this TISS will be installed *in fine*, 300 A of current are potentially available to heat the cavity walls.

The cavity is made of TOYO TANSO graphite (IG-19 type) [95]. It helps to cool the catcher and target by radiative heat transfer. The properties of graphite are mentioned in APPENDIX 3.1.

3.2 High-temperature material study

ISOL TISS requires a comprehensive knowledge of thermal and physicochemical properties of materials involved in the technical design, which are important for heat transfer, thermal and electric calculations. Complete data sets are rarely available in the literature and when available have often been obtained in different experimental conditions. As a recurrent need of data about resistivity and emissivity of materials is expressed by the designers of TISS at GANIL and probably in other facilities, a systematic study has been carried out to overcome the frequent shortcomings observed in the literature.

3.2.1 Motivation

When the intense ion beam bombards the target, it dissipates heat. It is necessary to balance target temperature by thermal radiation, or heat transfer in the container. Thermal radiation is the dominant heat transfer mechanism from the target to the container at higher temperatures. Temperature and emissivity are the parameters that determine the amount of radiation power emitted by the material. The emissivity not only depends on the material (element, purity, surface structure, porosity) but also on the temperature, wavelength, and its determination depends on the measurement conditions. Therefore, experimental conditions and processes must be identical results to be comparable.

Thermocouples are widely used for the measurement of temperature. Since they are in contact with the point of measurement, their intrusive nature can modify the real temperature. They provide a single point measurement and thus cannot give a temperature distribution.

Several direct and indirect techniques are used for measuring the emission radiations from hot points such as an infrared pyrometer, radiometer, and single color pyrometer and multi-wavelength pyrometer [96]–[102]. Among all the techniques multi-wavelength pyrometer techniques is an improved tool to measure accurately and it is a non-interactive and direct technique.

In this work a multi-wavelength pyrometer has been used to measure the emissivity of several refractory materials, often used in TISS design processes (Ni, PAPYEX, W, Ta, Mo, Nb, V, Ti, Co, Fe and stainless steel) in the range of temperature from 973 K to more than 2300 K. As the resistivity is also a useful parameter, the experimental system has been designed to measure both emissivity and resistivity.

3.2.2 Description of the experimental setup and measurement process

The experimental set-up developed and built at GANIL and used in this work is represented in Figure 46. The band sample to characterize is installed in a vacuum chamber maintained at a pressure of 10^{-7} mbar to avoid damaging the sample heated at high temperature by chemical reaction with a too high level of gas. Two cooling circuits allow a high current to go through the band of material. The band, 10 cm long, 1 cm large and with different thicknesses according to its resistivity expected at high temperature, is maintained in position by two cooled clamps covered by Ta and connected to the current connections. Owing to the thermal conductivity of the materials, a thermal gradient appears along the band when heated. To measure the emissivity and the resistivity in a thermally homogeneous region of the band, only the central part of 3 cm long has been considered. At its extremity, two wires of Ta have been fixed to measure the voltage. Their diameter has been chosen very thin (1 µm in diameter) to limit thermal perturbation at the contact point. They are connected to a voltmeter situated out of the vacuum chamber.

A power supply (I_{max} = 500 A and V_{max}= 30 V, controlled in power) has been used to heat the sample. The current was measured via the supply control panel and using an ammeter.

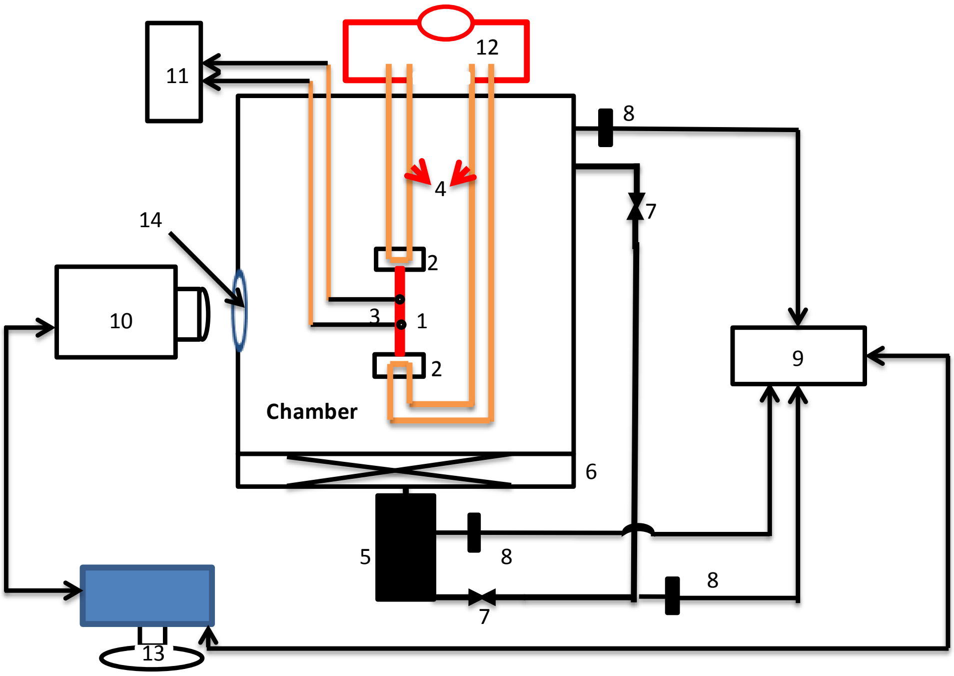

1. Sample
2. Tantalum crucible
3. Tantalum Wires
4. Copper tubes
5. Turbo pump
6. Turbo pump valve
7. Gate valve
8. Pressure gauge
9. Pressure indicator
10. Pyrometer
11. Voltmeter
12. Power supply
13. PC
14. Glass window

Figure 46: Setup to measure the emissivity and resistivity properties of materials within the 973 K to 2300 K temperature range.

The sample is suspended in front of a sapphire (Al_2O_3) window having a transmission efficiency of 87% [103]. As the pyrometer is placed out of vacuum chamber, a window was needed. The transmission efficiency measurements of different windows considered are discussed in APPENDIX 3.2. The emissivity and temperatures were measured under steady-state thermal equilibrium. The resistivity is calculated by the voltage and current. The resistivity values obtained in this way are compared to material data sheets and values found in the literature. The emissivity vary from one point to point, it is quite difficult to measure and data did not exist in the literature. In this experiment, the emissivity was measured with a bi-chromatic pyrometer, it is able to measure the emissivity at the exact point on the surface.

3.2.3 Experimental results

Temperature measurements were carried out by increasing the heating power with steps of 10 W, starting from 0 W up to 1500 W for different samples, which quite enough to reach the temperature of 2300 K. The electrical current level was kept constant for about 15 min at each step, in order to let the temperature stabilize, and then to perform steady state temperature measurements. Figure 47 shows electrical resistivity of different materials in function of temperature, Figure 48 shows emissivity in function of temperature for various materials. The experimental data were compared with other experimental data and are presented in APPENDIX 3.2

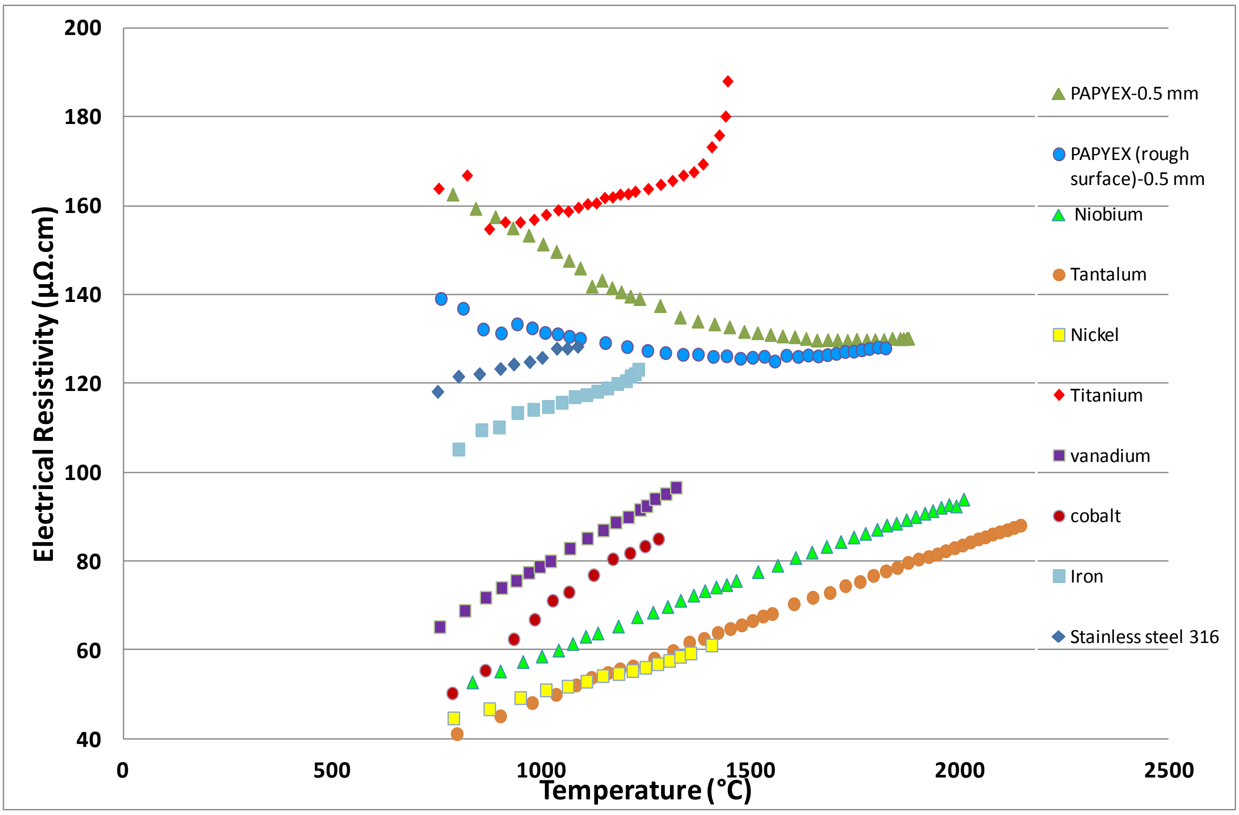

Figure 47: Electrical resistivity function of temperature for several materials. The estimated error bar is ± 5.1 % of the values.

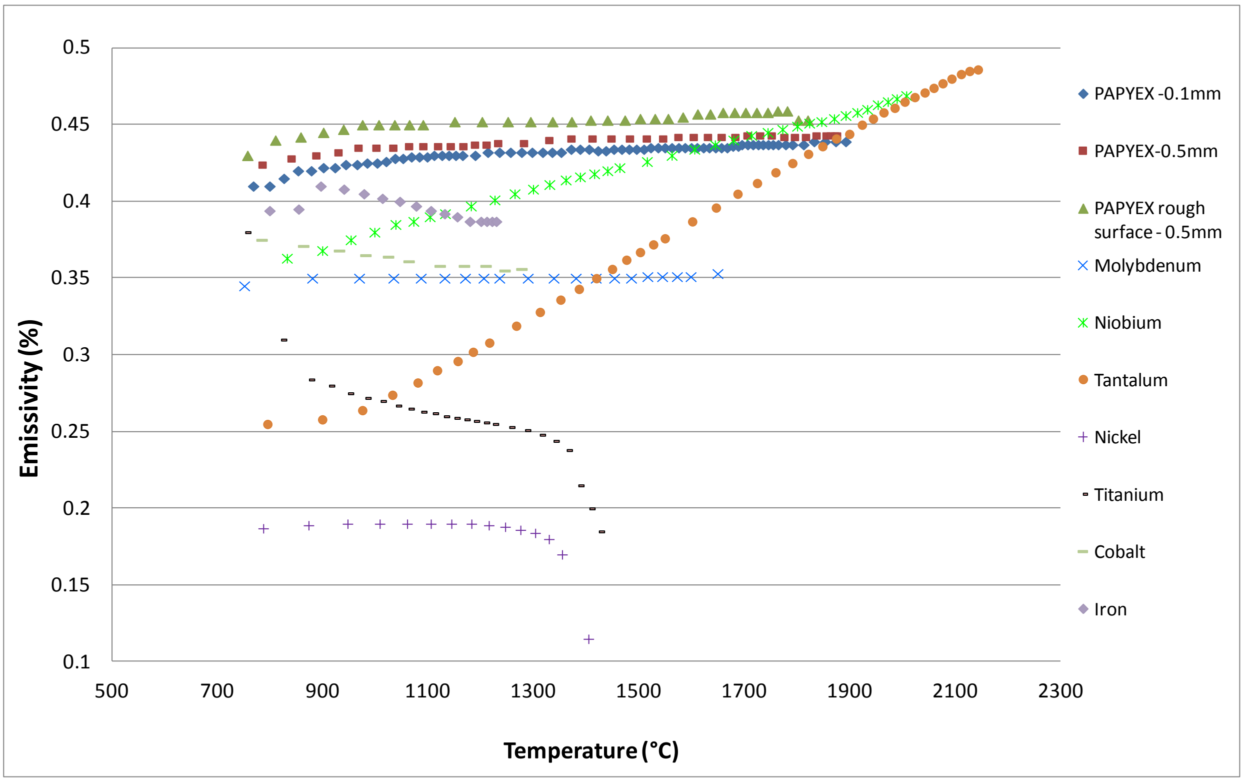

Figure 48: Emissivity variation with respect to temperature. The emissivity was measured for different materials with a Bi-chromatic pyrometer. The estimated error bar is ± 5.3 % of the values.

Figure 48 shows the measured emissivity of pure nickel and PAPYEX as well as for other materials. The emissivity is found to be constant for nickel and decreases rapidly from 1600 K to 1700 K. This is due to the maximum operating temperature and the sample evaporates rapidly thus deposited on the transmission window of the chamber. It reduces the transmission efficiency. Therefore, the measured emissivity is lower than the actual emissivity. In the case of PAPYEX, the emissivity is increased slightly with the increase in temperature. This data is used to evaluate the electric field and thermal calculation of TISS (section 1.4).

3.3 Catcher design

The primary beam must be stopped before reaching the inner wall of the vacuum chamber. The catcher must be thick enough to stop it, thin enough to cope with the thermo-electrical constraints and present a high release capacity of recoils.

The catcher is heated simultaneously by the passage of the current through it and by the primary beam power deposition. Its cooling is ensured by heat transmission to the container by thermal radiation. Materials having high thermal emissivity are thus required.

Papyex has been chosen as a catcher material, which is a tissue of graphite fibers having a lifespan under a vacuum of several weeks at 2300 K. The thickness of the foil is 200 µm, chapter 2 specifications. It has enough thermal and electric properties to transfer the heat and generate the electric field. A picture of the microscopic structure of PAPYEX is presented in Figure 49.

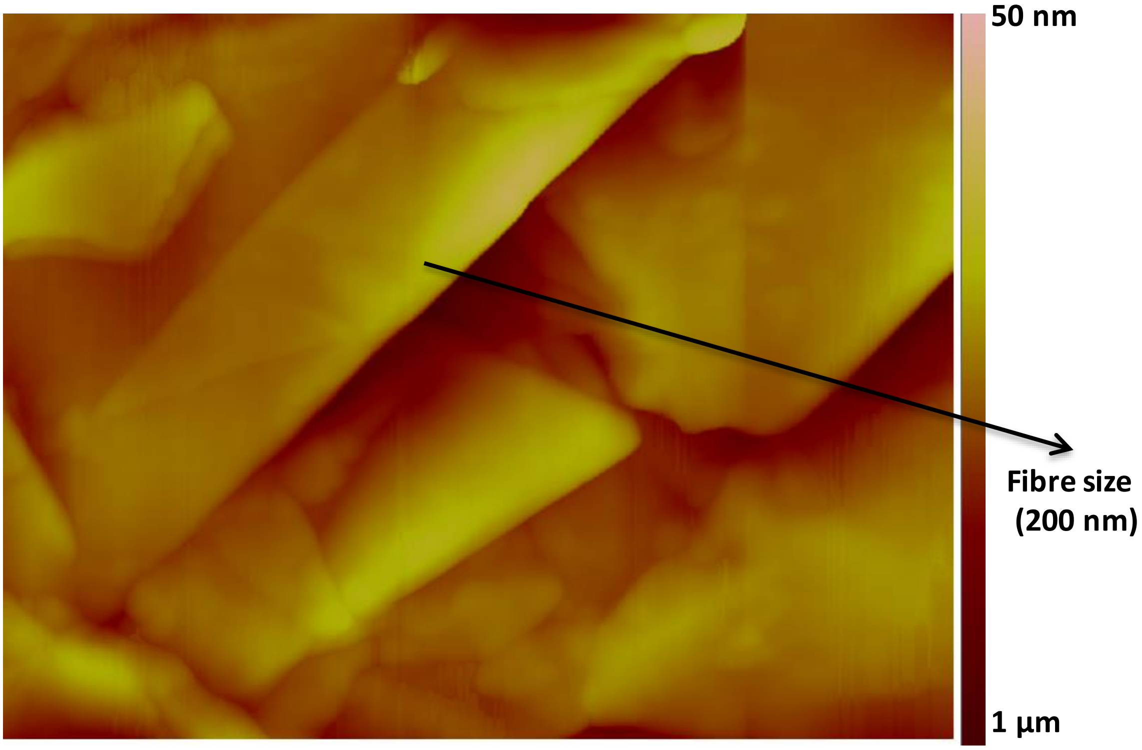

Figure 49: Microstructure of PAPYEX graphite measured with Atomic Force Microscopy (AFM). The color scale on the right indicates the size of the different parameters in the image according to its color.

The structure of the catcher was measured with atomic force microscopy (AFM) [104] in the GREYC laboratory (Caen) by Sandeep Kumar Chaluvadi. According to the software treatment of the measurements made on the surface, the typical size of the structure is roughly equal to 200 nm and the roughness is equal to 20 nm (RMS). The porosity and density were measured by Julien Guillot IPNO (L'Institut de physique nucléaire d'Orsay) using He Pycnometry. The density was 1.15 g.cm^{-3} and the porosity was equal to 49.2 % of the total volume. Moreover, once in the empty volume of such material, almost all the atoms can propagate by effusion up to the surface of the Papyex as the open porosity is equal to 44.3 % of the total volume.

3.4 Temperature and electric field in the TISS cavity

Despite the desire for of simplicity and the relatively a compact design compared to TISSs currently used at GANIL (and in other facilities). The TISS remains too complex to evaluate precisely the electric field and the temperature distribution generated by the electrical current flowing through the cavity walls. Additionally, the target and catcher are heated by the primary beam power. Therefore, it is necessary to use a finite element method (ANSYS) to evaluate the temperature and the potential difference in the cavity. ANSYS [15] is used for structural analysis, including linear, nonlinear and dynamic studies. This simulation product provides finite elements to model the materials behavior and equation solvers for a wide range of mechanical design problems. It also includes thermal-structural and thermo-electric options.

The goal was to obtain a temperature as uniform as possible, close to 1600 K in the cavity and an electric field of the order of 1 V/cm for a current lower or equal to 300 A. After several iterations, by changing the thickness of the catcher, of the counter-flanges, of the cavity, and by changing the graphite of the cavity to change the resistivity while conserving its low porosity, the following parameters have been fixed:

- All the relevant material parameters of graphite used for the cavity, Ni and Papyex, dimensions, material, resistivity, emissivity, and isotropic characteristics, injected current in the cavity, boundary conditions, power induced by primary beam were taken in the simulations.

The results of the electric field and temperature range for different materials are given in Table 4.

Potential difference	Material of the cavity container	Screw	Production target	Stopper	Temperature in TISS cavity
0 – 4.56V	POCO ZXF-5Q [105]	CX-31	Nickel	Papyex	1300 – 1830 K
0 – 4.14V	IG-19 [95]	CX-31	Nickel	Papyex	1260 – 1800 K

Table 4: Electric field and temperature results of the cavity for different types of graphite grid materials. The simulations done with ANSYS.

From the results, the IG-19 type graphite gives a lower electric field than POCO graphite. The IG-19 graphite was chosen due to the high emissivity. It helps to dissipate the heat to the walls in the form of radiations. The temperature in the cavity varies from 1260 K to 1800 K. The maximum temperature observed is on the PAPYEX. The maximum temperature observed on the nickel is 1630 K, which is 340 K lower than the fusion temperature. The thermo-electric simulations are represented in Figure 50 and Figure 51.

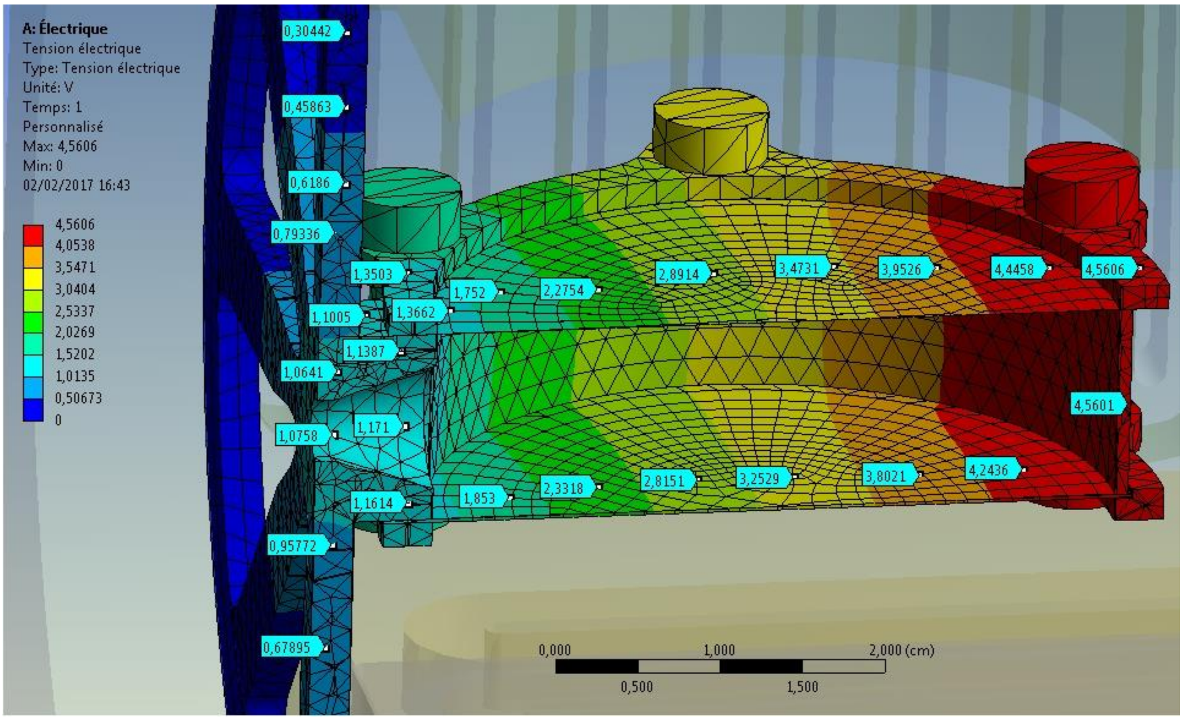

Figure 50: Electric field simulations of the cavity. Maximum potential ~4.5 V, minimum ~1.1 V over a diameter of 50 mm, leading to a mean electric field of 0.68 V/cm.

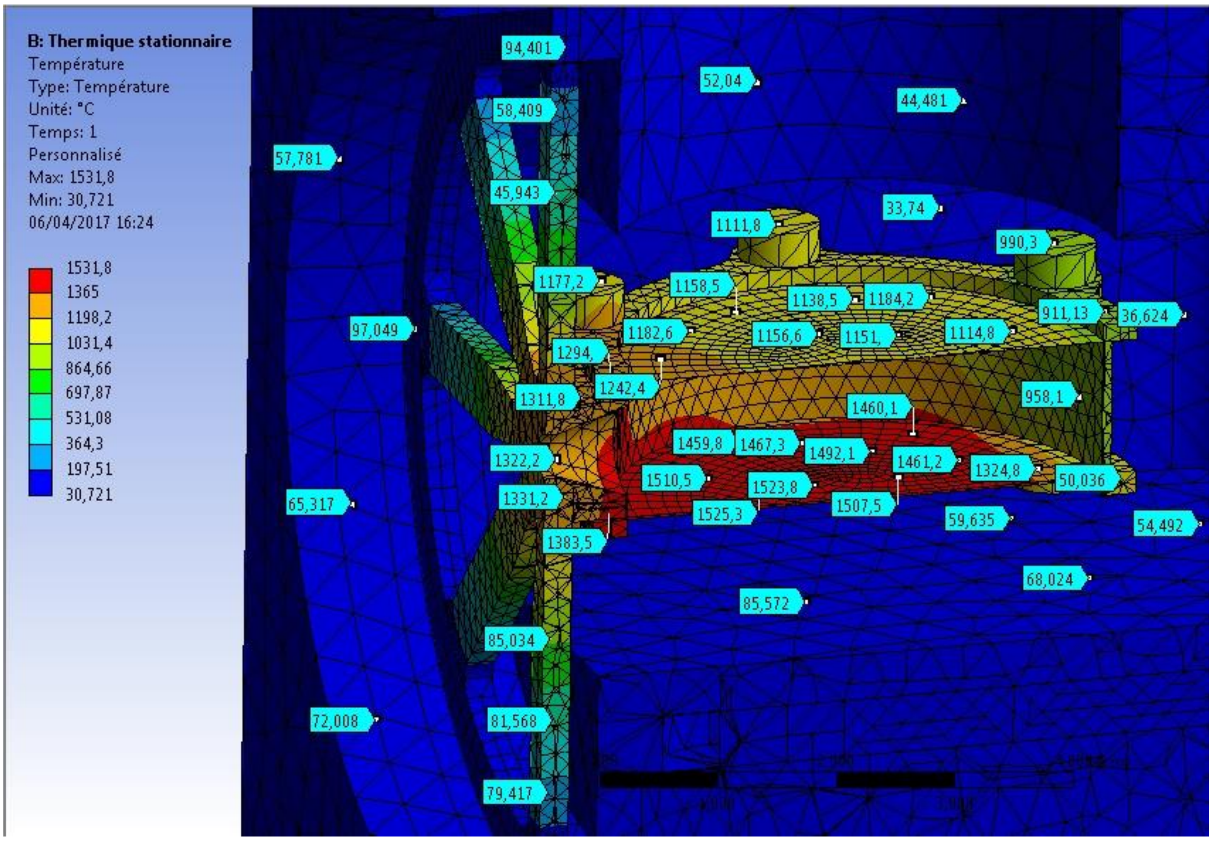

Figure 51: Thermal simulations of the temperature in the cavity, taking into account the power deposited by the primary beam in the Ni target foil (38 W), in the catcher (270 W) and the electrical power (~1350 W).

In the simulations, to calculate the potential difference in the cavity, a current of 300 A was taken and used to heat the cavity in relay conditions. The true primary beam power of 308 W of which 38 W is lost in 3 µm of nickel target and remaining power of 270 W is deposited in the catcher (PAPYEX). The power losses in the target and catcher are calculated with TRIM simulations. From Figure 50, we can see the variation of potential between the ends of the cavity is 3.4 V.

To increase the accuracy of the calculation, the mesh density has been increased in the regions of contact between the production target and the walls of the cavity. Expected for the high-density mesh, the results were seem to be independent of the mesh density.

3.5 Minimization of the effusion time

3.5.1 Free effusion and effect of an electric field

Without an electric field and in a simple volume having an aperture, the probability that the atoms find the aperture is proportional to the ratio between the aperture area and the inner surface area of the cavity.

To increase the probability, and decrease the effusion time of the ions in the cavity, an electric field is used to push the ions towards the exit aperture. The distance between the walls of the cavity (12 mm at minimum) and the magnitude of the electric field (0.68 V/cm) leads ^{74}Rb ions emitted perpendicularly from the surface with thermal energy (at 1600 K).

To evaluate the advantages of an electric field and to know more precisely its effect on the effusion time, we performed simulations using SIMION by considering the potential difference obtained from the ANSYS electrical simulations (section 3.4).

3.5.2 Monte-Carlo simulations

We assume that the effusion process satisfies the molecular regime conditions in the target cavity. The momentum of atoms under those conditions is simulated with the ion and electron tracking simulation program SIMION [106]. It is used to calculate electric fields. SIMION data recording options used to record particles termination position, velocities, time of flight, energy. It also calculates the trajectories of charged particles in electric and magnetic fields, including time-dependent fields. We used SIMION Version 8.1 to calculate the effect of electric field on the trajectories of ions.

The code tracks the particles starting from the target surface up to the exit of the cavity. From these simulations, it is possible to determine the time of flight (TOF) of the particles before their exit out of the cavity and also the number of collisions inside the cavity. The sticking time of the particle on the surface is not present in this code. This means that the particles are either re-emitted or trapped in the material. Nevertheless, knowing the number of contacts and having an estimation of the sticking time (paragraph 2.4), the overall sticking time can be estimated.

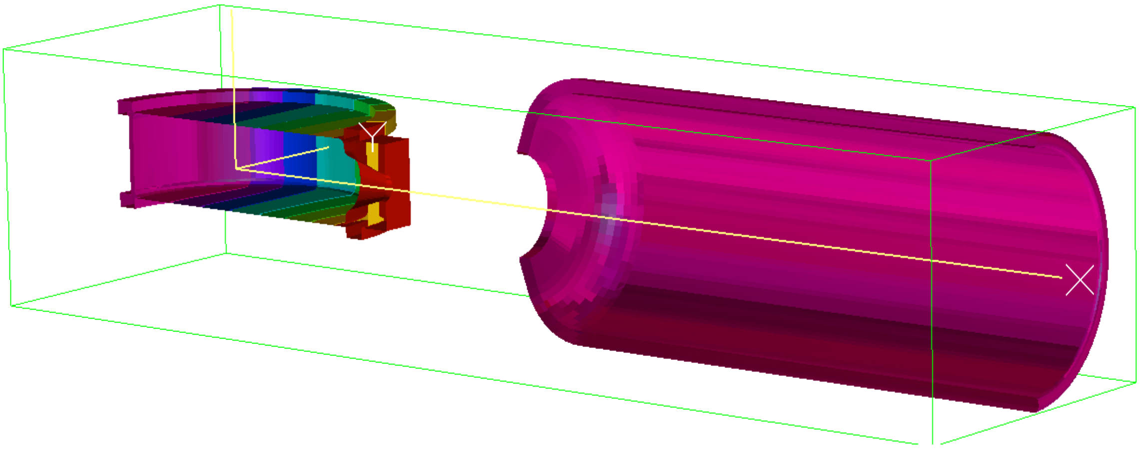

Figure 52: Model of the TISS designed for SIMION simulation. The atoms are generated in the cavity and leave it towards the extraction electrode (pink color). The diameter of the exit hole is 4 mm and the extraction electrode is 12 mm. The potential difference is 10 kV.

The 3D design is done with CATIA [107] imported to SIMION simulations. The singly charged $^{74}Rb^{+}$ ions were considered in the simulations. The generation of ions was assumed uniformly distributed on the nickel target, over a central diameter of 40 mm. The produced fragments respect the Maxwell-Boltzmann speed distribution with an average mean speed of 698 m/s. To create an electric field in the cavity, the cavity was divided into nine electrodes including one extraction electrode. We applied voltage on each electrode, which we obtained from the Electric field simulations of ANSYS. The extraction voltage between the cavity and the extraction electrode was equal to 10 kV. All the simulations were performed with 10,000 ^{74}Rb ions.

Lua code [108] was used to describe the reflections of the atoms on the walls, following an angular probability distribution according to Knudsen's law [109].

In the code at each collision with the walls of the cavity, an atom or an ion loses the memory of the velocity they had before the collision. They continue to effuse in the cavity until they leave it. Once out, the probability they have to come back is zero. With this code, it is possible to calculate the time of flight, number of collisions in the cavity, the proportion of ions exiting the cavity and it is also possible to extract the results of simulations into a file. More details about this code can be found in APPENDIX 3.3. The results of the simulation for ^{74}Rb are presented in Figure 53 and the results for ^{114}Cs are presented in APPENDIX 3.3.

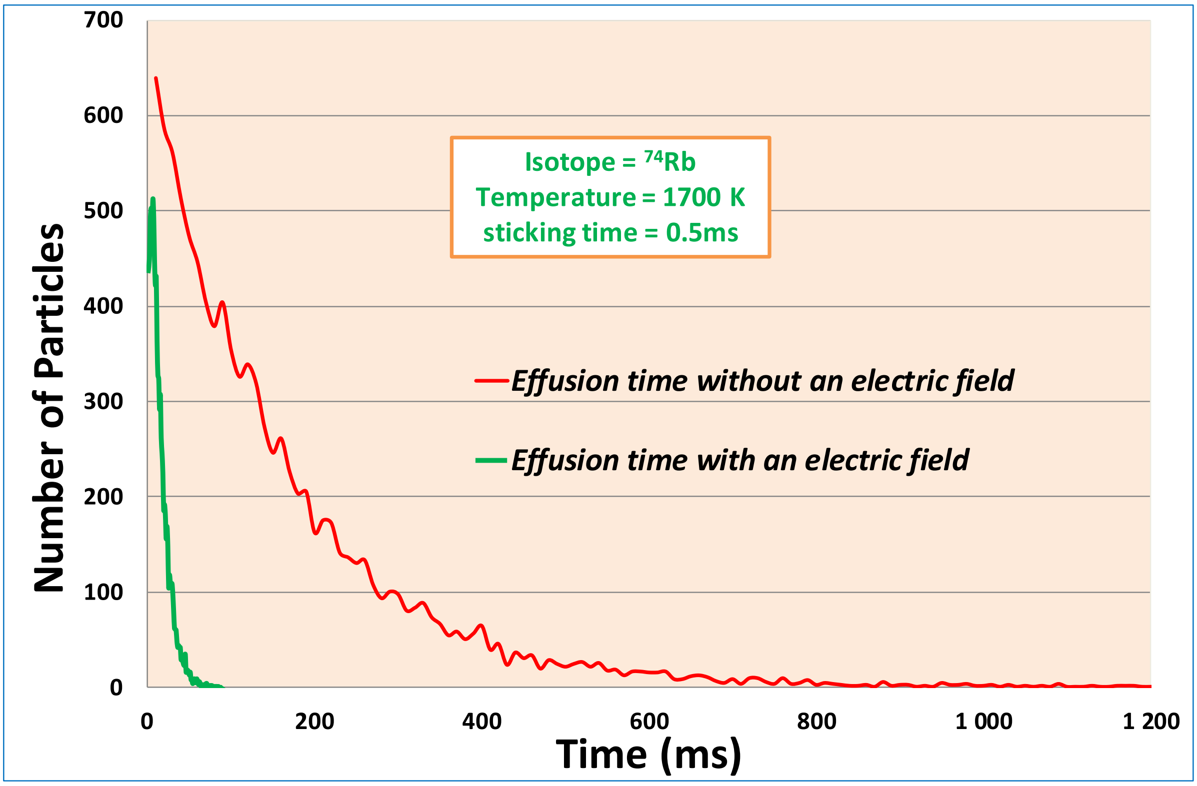

Figure 53: Effect of electric field on effusion time. The red line represents effusion time without an electric field and the green line indicates the effusion time with an electric field. The sticking time was taken into account in the calculations, and is equal to 0.5 ms.

To perceive the effect of electric field on the effusion time, the simulations are accomplished with the electric field and without electric field (Figure 53). With an electric field, the number of particle collisions with the cavity walls was strongly reduced, as was the effusion time, from ~100 ms (without E field for 50%) to 12 ms (with E field). The corresponding effusion efficiencies for ^{74}Rb are respectively equal to 39% and 84%

Similar simulations were carried out for ^{114}Cs singly charged ions. The ions were uniformly distributed on the catcher, over a disk of 40 mm in diameter. Their speed follows the Maxwell-Boltzmann distribution with an average mean speed of 561 m/s at 1700 K. The sticking time per contact considered in the calculations was equal to 1 ms [14]. Without an electric field, the total effusion time is equal to ~190 ms, and with an electric field, the total effusion time drops to 27 ms, leading to extraction efficiencies of 75% and 97% respectively for ^{114}Cs (570 ms). In these calculations, the decay time is taken into consideration. As the half-life of ^{114}Cs is longer than of ^{74}Rb, the effect of the electric field on the efficiency is lower but the important point is high effusion efficiency.

3.6 Estimation of the TISS total efficiency

Once produced, radioactive isotopes have to get through three processes for the formation of an ion: diffusion out the target material, effusion up to the ion source and ionization. If one assumes that these three processes are sequential, the total efficiency ε_{ai} of atom-to-ion transformation is given by:

$$\varepsilon_{AIT} = \varepsilon_{Catcher\ release} \times \varepsilon_{Effusion} \times \varepsilon_{Ionisation}$$

The processes can be reduced to two considering the ionization efficiency is very close to 100% for both ^{74}Rb and ^{114}Cs, according to calculations in paragraph 2.6, pg.72.

In the case of this TISS, the assumption that catcher release and effusion are sequential processes seems reasonable as the atoms are unlikely to go back into the catcher once released, as the probability the atoms have to leave the cavity is far greater than the probability they re-penetrate the catcher material.

As previously written in paragraph 2.3.6, pg.72, the release efficiencies of ^{74}Rb and of ^{114}Cs out of the catcher are respectively equal to 90% and 97%. From the paragraph 3.5.2, the effusion efficiency is equal to 85% and 96%. Thus the atom-to-ion transformation efficiencies of ^{74}Rb and of ^{114}Cs are calculated to be respectively equal to 77% and to 93%.

3.7 Estimation of radioactive ion beam intensities

The radioactive ion beam (RIB) intensity produced by the TISS can be expressed as the product of the in-target yields $Y_{in-target}$ by the atom-to-ion transformation efficiency ε_{AIT} of the target ion source system (TISS).

$$I_{RIB} = Y_{in-target} * \varepsilon_{AIT}$$

3.7.1 Production of ^{74}Rb and comparison with other facilities

The in-target rate of ^{74}Rb produced by the interaction of ^{20}Ne on ^{58}Ni nickel target was estimated using the following parameters. Ni target 3 µm thick, the density of 8.95 g.cm^{-3} and the primary beam energy of 110 MeV at an intensity of 1.89.10^{13} pps. The cross-section of reaction has been calculated prior to this Ph.D. work by B. Blanck using different codes: CASCADE [62], HIVAP [64], CANBLA [63], [65], PACE [10], GEMINI++[110]. The average cross-section was taken from all these codes and divided by a safety factor 11.2, which is results in a cross-section of 6.10^{-2} mb and to an in-target production rate of 2.6.10^{4} pps.

Different methods have previously been used to produce a ^{74}Rb beam. Some of them are presented in Table 5. Two facilities, ISAC at TRIUMF and ISOLDE at CERN produce ^{74}Rb by spallation reactions induced in a Nb target using a high energy proton beam, combined with a Re surface ionization source [56], [57]. ^{74}Rb can also be produced (not yet done) at GANIL using the upgraded installation of SPIRAL-1 using the fragmentation process of a Nb target bombarded by a ^{12}C primary beam (95 MeV/A). It will also be possible to produce ^{74}Rb at the SPIRAL-2/S^{3} facility using fusion-evaporation reactions with a primary beam of ^{36}Ar (2.9 MeV/A) on a ^{40}Ca target.

Despite a lower in-target production rate in the case of the fusion-evaporation technique proposed in the present work, the ion production rate at the exit of the TISS is expected to be one of the most intense if the AIT efficiency is confirmed.

Looking at the primary beam powers and at the AIT efficiencies, one can globally observe that the use of high power primary beams is correlated with low atom-to-ion transformation efficiencies. This remark has been one of the starting points of the present study for two reasons: the first one was to evaluate how intense could be the ion beams at the exit of the TISSs by optimizing the AIT efficiency rather than the in-target production. This was motivated by a wish of engineers responsible for the accelerator operation who have observed that the use of very intense and energetic primary ion beams has significant consequences in terms of radioprotection, shielding, radiation damage, maintenance, delays, activation and radioactive releases. Resources needed to manage these constraints increases with the magnitude of the radioactivity produced. The possibility for GANIL to produce competitive beams by fusion-evaporation process thanks to the variety of its primary beams is a great advantage they would like to make the best of.

	Produced at TRIUMF	Produced at ISOLDE	Estimated on the S^3 facility at GANIL [111]	current system on SPIRAL-1 at GANIL	the new system on SPIRAL-1 at GANIL
Primary beam power	Proton (500 MeV) 50 kW	Proton (600 MeV) 1.2 kW	^{36}Ar (2.9 MeV/A) 210 W	^{12}C (95 MeV/A) 3.65 kW	^{20}Ne (5.1 MeV/A) 308 W
Target	^{93}Nb	^{93}Nb	^{40}Ca	^{93}Nb	^{58}Ni
Reaction	Spallation	Spallation	Fusion-evaporation	Fragmentation	Fusion-evaporation
In target productions	$1.2.10^8$	3.10^6	$6.5.10^4$	$4.1.10^5$	$3.4.10^4$
Efficiency	0.01%	0.06%	4%	1%	~77%
SIS	Rhenium	Tungsten	Tungsten	Tungsten	Graphite
intensity (pps)	$1.7.10^4$	$1.8.10^3$	$2.6.10^3$	4.10^3	$2.6.10^4$

Table 5: Comparison of ^{74}Rb intensities, In the case of ISOLDE and TRIUMF, the beam intensity was delivered. In the case of SPIRAL-1 and S^3, the intensities are estimated.

3.7.2 Production of ^{114}Cs and comparison with other facilities

^{114}Cs can be produced using a primary beam of ^{58}Ni (intensity of 3.10^{12} pps at an energy 4 MeV/A) on a target of ^{58}Ni (6.5 µm thick). Using the same process and code as for ^{74}Rb, an average cross-section equal to $1.3.10^{-1}$ mb was found. The estimated intensity rate is equal to $2.6.10^4$ pps.

Three different methods used or envisaged to produce ^{114}Cs beam at other radioactive ion beam installations are compared (Table 6). For now, only ISOLDE (CERN) succeeds in producing it by spallation in a 20 cm thick (122 g/cm^2) target of molten lanthanum metal kept at an approximate temperature of 1600 K. The target is bombarded with a 1 µA proton beam at 600 MeV. Tantalum SIS is used for ionization. The source is kept at 1300 K. The production yields estimated to be around 5 pps/sec.

GANIL/SPIRAL-2/S^3 expects to produce ~4.10^3 ^{114}Cs ions per second using the in-flight method, by bombarding a ^{58}Ni target (500 µg.cm^{-2}) with a primary beam of ^{58}Ni (4 MeV/A, 1.10^{13} pps).

With the proposed TISS, the in-target production expected is lower than with S^3 but the higher the AIT efficiency is expected to compensate, leading to a higher ion production rate estimated at $2.4.10^4$ pps.

	Produced at ISOLDE	Estimated on the S^3 facility at GANIL	Expected with the new system on SPIRAL-1 at GANIL
Primary beam power	Proton (600 MeV) 1.2 kW	^{58}Ni (4 MeV/A) 500 W	^{58}Ni (4 MeV/A) 115 W
Target	La	^{58}Ni	^{58}Ni
Reaction	Spallation	Fusion-evaporation	Fusion-evaporation
In target productions	$3.4.10^5$	$1.15.10^5$	$2.4.10^4$
Efficiency	0.005%	4%	90%
SIS	Tantalum (Ta)	Tungsten (W)	Graphite and nickel
Ion beam intensity (pps)	17	$4.6.10^3$	$2.1.10^4$

Table 6: Comparison of ^{114}Cs intensities, SPIRAL-1, and S^3 intensities are estimated ones. At ISOLDE, intensities are delivered values.

3.8 Conclusions

The optimization of different aspects of the TISS, in target production, release of atoms out of the catcher, geometry of the TISS, the simplicity of the design and effusion process, have led to competitive estimated rates of ion production for ^{74}Rb and ^{114}Cs compared to other facilities. These encouraging estimations rely on an optimized AIT efficiency, yet to be experimentally demonstrated in off-line (without primary beam on the target) and later online (with primary beam).

The next chapter describes the main tests planned once the TISS is assembled and up to its use in SPIRAL-1.

Chapter 4: characterization of the TISS

4.1 Introduction

The present TISS R&D has been realized with the aim of producing new radioactive ion beams at the SPIRAL-1 facility. Before installing the TISS in the production cavern and irradiating with the primary ion beam. Firstly, it must be characterized off-line.

The characterization can be divided into four steps:

- Once the system assembled, the first step consists in testing the cooling circuits, the tightness of the vacuum chamber, the conformity of the mechanical parts to match the installation of the production cavern, and the conformity of all the supplies, being only electrical with the present TISS.
- The second step consists in testing the thermo-mechanical behavior at a nominal temperature over 3 weeks, as the minimum lifespan required for the operation is 2 weeks. Temperatures of different points are measured through the primary beam injection porthole and through the beam extraction aperture, using pyrometers.
- The third steps consist of the injection of atoms or ions in the TISS to measure the atom-to-ion transformation efficiency.
- If previous tests are validated, the TISS can be installed in the production cavern to measure the radioactive ion beam production by irradiating the target with the primary ion beam.

In these four steps, the first and second step results are presented in this thesis report. Due to a lack of time, the third and fourth one will be carried out later.

The mechanical design of the device was made while trying to respect the conclusions of primarily studies. Once the parts of the device realized, it was assembled, in a process requires sustained attention the fragility of the individual elements (sheet of 3 µm Ni, cavity with 0.8 mm graphite wall and 200 µm of PAPYEX foil fixed between two thin graphite flanges assembled with 6 M4 size bolts made of fiber reinforced graphite. Figure 54 shows the different parts used to build the TISS.

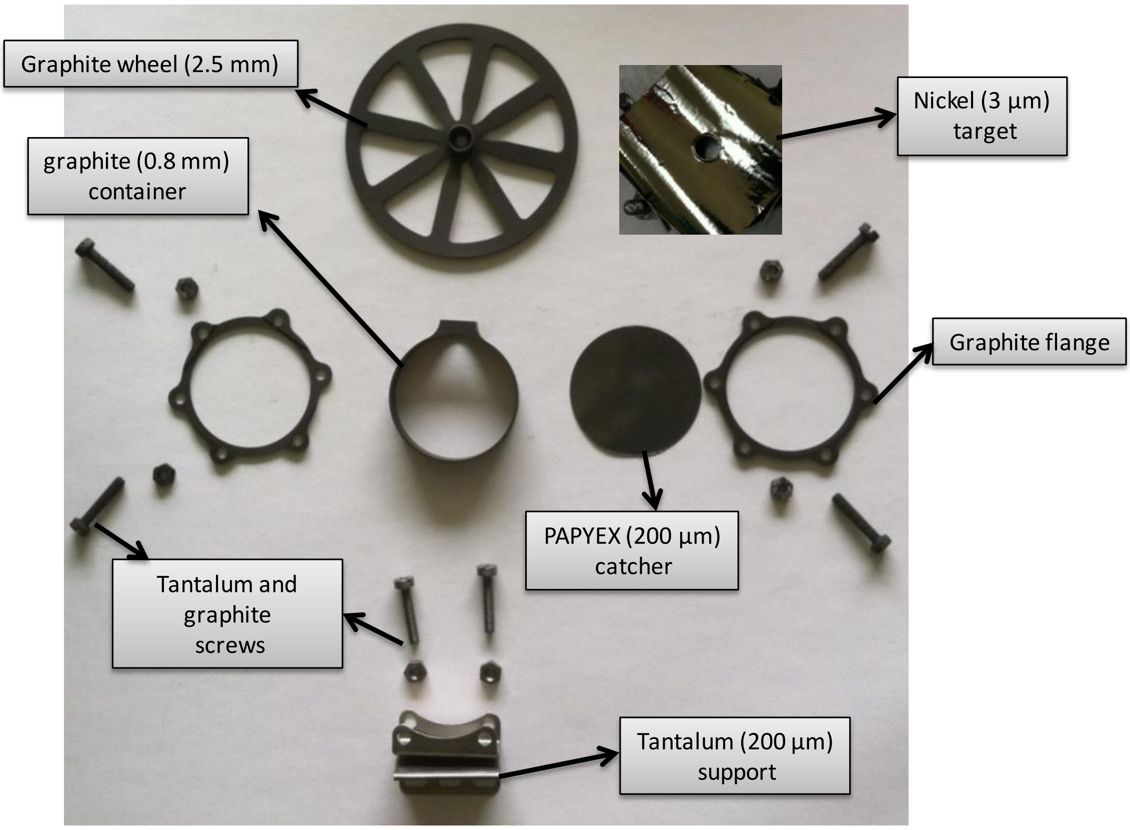

Figure 54: Different parts used to build the TISS.

The assembly of TISS is represented in Figure 55. A hole has been realized in the center of the nickel foil to have the possibility to have a look at the catcher and measure its temperature and to inject a beam of alkali ions in the cavity.

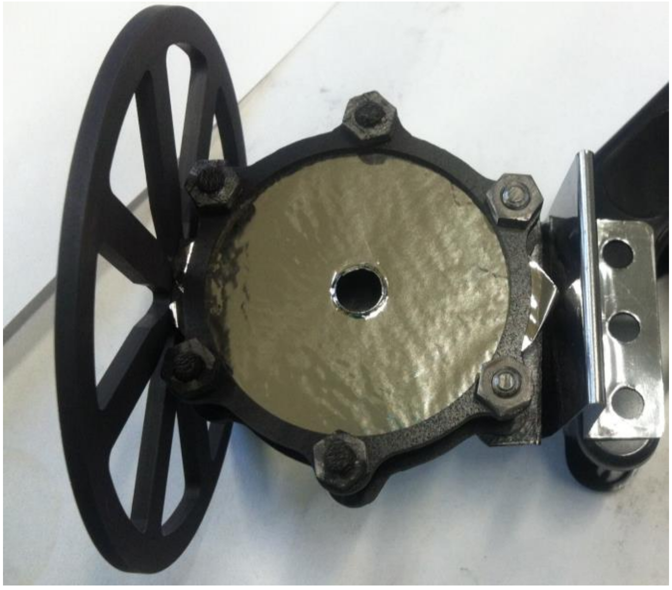

Figure 55: Mechanical assembly of the TISS.

The inner diameter of the cavity is 43.6 mm with a height of 12 mm. As the flanges are very thin, the bolts are softly tightened, without tools. The cavity is connected at the end with a tantalum band chosen sufficiently thin to avoid thermo-mechanical constraints, which can reduce the constraints on the graphite wheel. The tantalum is connected to a cooled copper part. To improve the contact between rigid Ta and Cu parts, and Ta and graphite, two foils of PAPYEX graphite 0.5 mm thick are placed in-between them. Once the device built, it was installed on the SPIRAL-1 test bench.

4.2 Thermal test on SPIRAL-1 TISS test bench

4.2.1 Test bench

The test bench is dedicated to the systematic characterization of the TISS which must be later installed in the production cavern, and to the test of new target and ion source systems developed as a part of research and development program of SPIRAL-1.

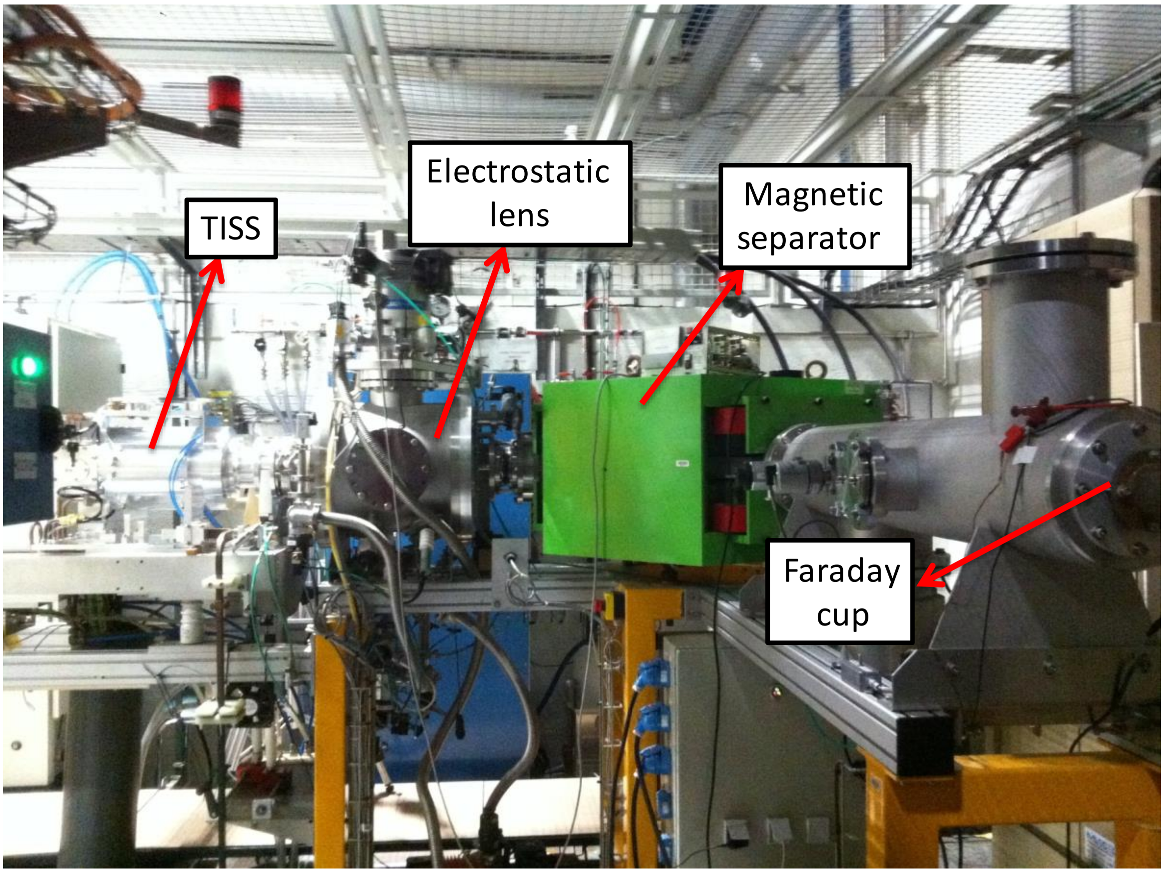

Figure 56: Picture of the SPIRAL-1 test bench. It contains the following instruments: front end chamber containing an electrostatic lens and equipped with vacuum turbopumps, magnetic dipole separator, slits and Faraday cup. The TISS environment reproduces the one present in the production cavern.

The TISS is combined with a specific extraction nozzle. They are fixed on a common plat which can be installed either on the test bench or in the production cavern. The extraction of the ion beam at the source exit is assured by an electrode connected to the ground potential and it focus with an electrostatic lens. The beam of interest is selected using a fixed rigidity dipole of 0.153 Tm, which typically corresponds to an ^{84}Kr beam at 10 kV. At the dipole output, a system of vertical slits makes possible to select the beam of interest. The beam current measurement is performed by collecting ions in a Faraday cup. It is made from a copper cup of 40 mm internal diameter, equipped with a polarized guard ring to confine the emitted electrons. All the chambers are maintained at a pressure of 5.10^{-7} mbar using vacuum turbopumps.

4.2.2 Primary Heating test results

The temperature is measured through a porthole using an optical disappearing filament pyrometer [112]. These calibrations make it possible to precisely determine the temperature of the target and of the catcher. The emissivity coefficients used during the measurements are 0.45 for the catcher (PAPYEX) and 0.2 for the target (Nickel) (see paragraph 3.2, pg.86). The measurement uncertainty of the pyrometer is 0.6% (given by supplier).The uncertainty in the adjustment of the pyrometer was estimated to be 0.5% and the transmission efficiency of the window is 3%. Thus the overall uncertainty is equal to 3.1%. The experimental set-up used to heat the TISS in this work is presented in Figure 57.

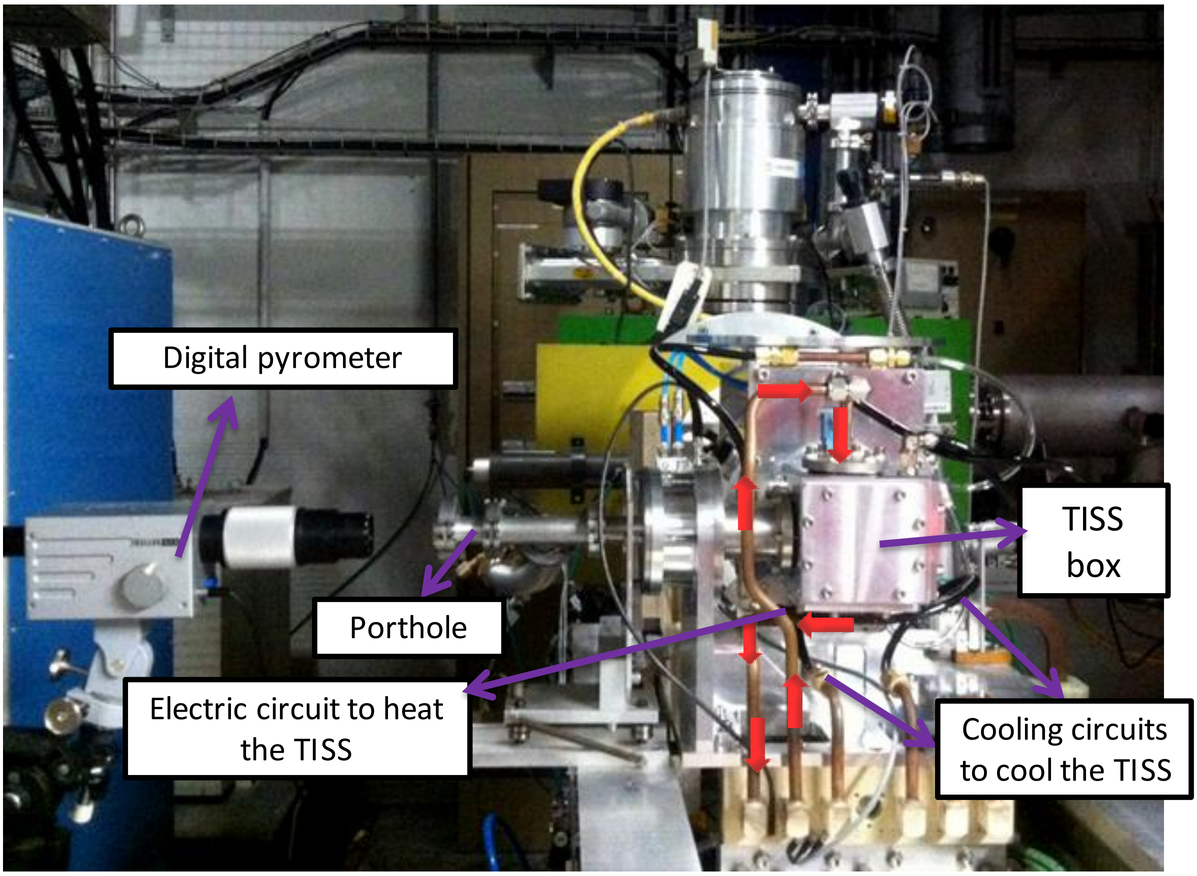

Figure 57: The heating setup on the SPIRAL-1 test bench at GANIL. The pyrometer is placed in front of the porthole to measure the temperature of the target and catcher. The red arrow shows the passage of current to heat the TISS. Cooling circuit is used to cool down the TISS.

One power supply (I_{max} = 500 A and V_{max}= 30 V) is used to heat the TISS. The TISS is heated by the electrical current passing through the copper tubes. Both the chamber and copper tubes are cooled by the water circulation.

The temperatures of the target and catcher are indicated in Figure 58. The catcher has a greater temperature gradient than the target because it has higher resistance in compared to the target.

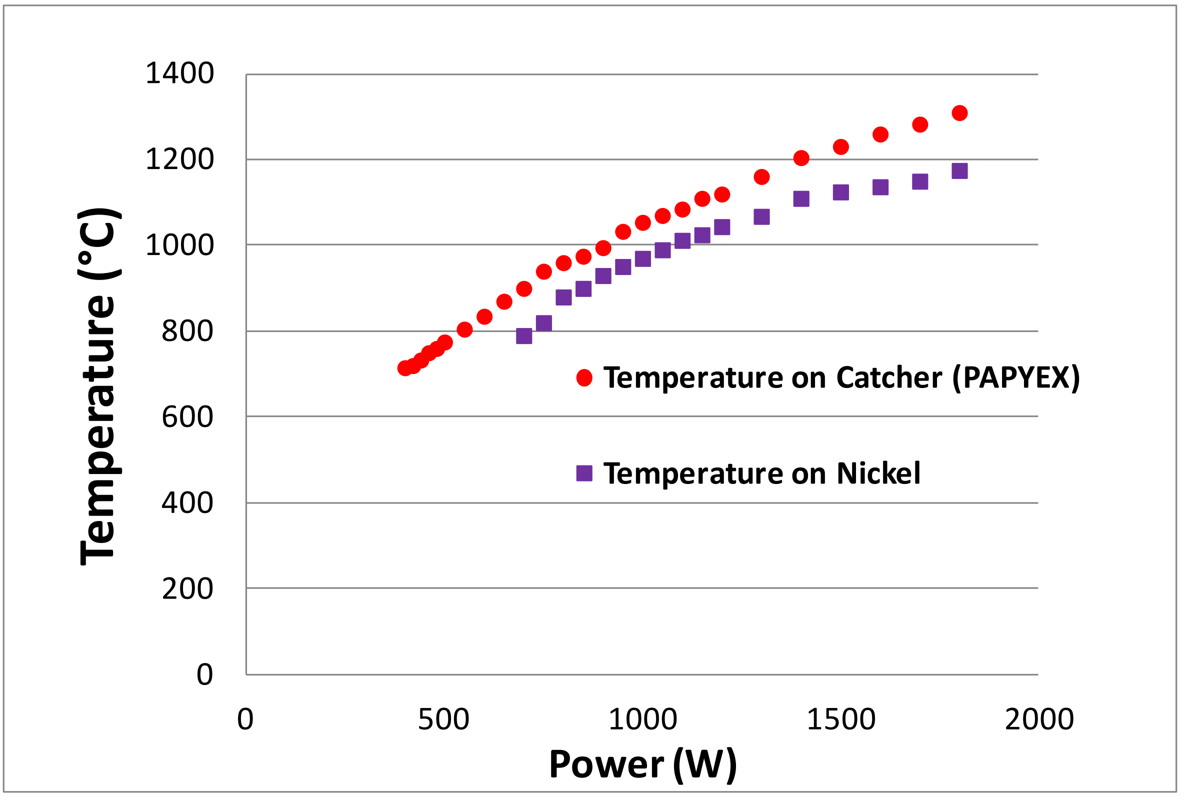

Figure 58: Evolution of the temperature of the target (Nickel, solid triangles) and catcher (PAPYEX, solid circle) as a function power. The maximum power was set at 1560 W.

Figure 58 shows the evolution of the temperature of the target and catcher as a function of the power applied to the TISS. As the PAPYEX resistance is lower than that of nickel. It was expected to observe a higher temperature on the catcher than on the target, and it is so. Nevertheless, the temperature on the target was not uniform: it was higher on the outer diameter (more than 1583 K) than in the central region (1430 K, see Figure 59).

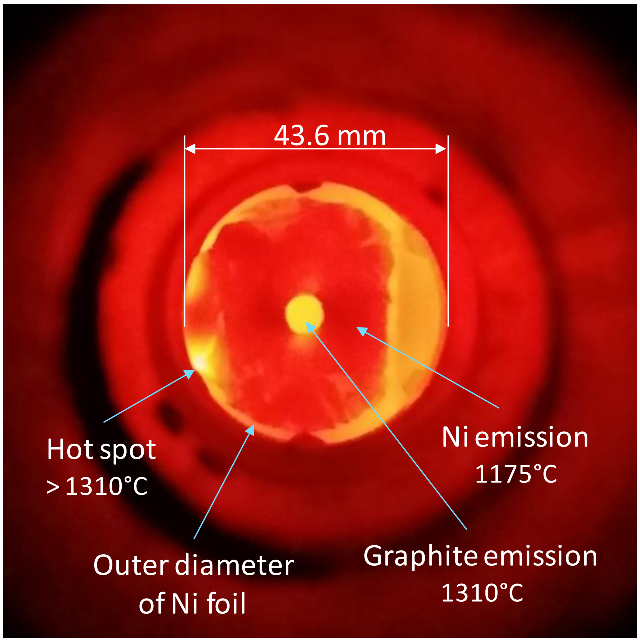

Figure 59: Picture of the Ni target widow for an electrical power of 1560 W. Catcher temperature: 1583 K. Temperature of the Ni target in its central region: 1430 K.

After two days of continuous operation, the nickel target was ruptured:

1. The first explanation is probably overheating of external region, where the nickel foil is in contact with the graphite ring of the cavity, particularly in the region close to the exit hole, where the heat dissipation by radiation is lower than elsewhere in the TISS, due to a reduced radiation area.
2. A second reason could be a poor and thus resistive contact of the nickel with the container, leading to a local overheating.

These issues will have to be addressed by refining the thermal models and by performing the suitable modifications on the TISS. Even if the target was broken, the TISS was left under heating for two weeks to test the lifespan of the remaining parts.

4.2.3 Comparison of experimental results with simulations

Electric field

The results obtained were compared to the temperature and electric field simulations in the cavity. The latter is critical in the present development, and it was of outmost importance to know it. Unfortunately, only the TISS potential difference was measured, which gives an indication of the potential difference between the extremities of the cavity.

The measured electric potential and temperatures were then used in the simulation. The resistivity of PAPYEX and nickel are equal to 310 µΩ.cm and 60 µΩ.cm respectively, and the emissivities are equal to 0.45 for PAPYEX and 0.2 for nickel, according to the measurements presented paragraph 3.2.

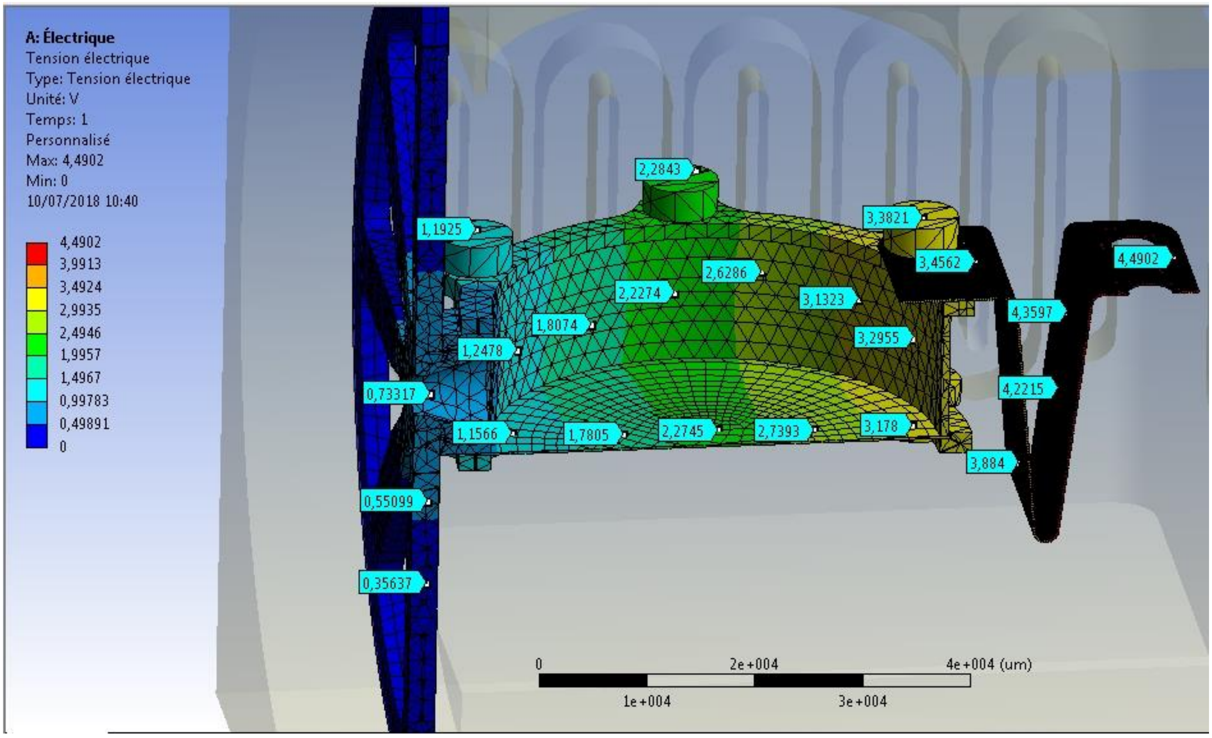

Figure 60: Results obtained using the ANSYS code which gives the evolution of the electric potential along the TISS at a current of 230 A.

According to the Figure 60, the potential difference between the extremities of the Ta band is close to 1 V for a current of 230 A, and the potential difference between the center of the graphite wheel the outer diameter is close to 0.7 V, leading to a total potential difference applied on the connectors of 1.7 V. As the full voltage applied to the whole circuit was equal to 6.5 V, potential difference of 4.8 V on the cavity is deduced and thus an electric field close to 1 V/cm, which is close to the expected value.

The total resistance of the cavity, as deduced from the experiment (21 mΩ, 4.8 V/230 A), is significantly higher than expected (11.6 mΩ, 3.5 V/300 A). This difference will have to be considered during the improvement of the cavity. (This difference cannot be explained by the disappearing of the target foil, which can lead to only ~1% of the variation of the total resistance).

Temperature

According to the thermal simulation (Figure 61), the maximum temperature is obtained on the container near the exit hole of the cavity. This region was not visible during the measurements. Moreover, the thermal simulations show a global temperature of ~350 K lower than the experimental temperature for the same injected current (230 A). It is therefore possible that the real temperature close to the exit hole was significantly higher than that predicted. This could explain the rupture in the nickel target, since its periphery is in direct contact with the container.

This thermal issue will have to be considered during the improvement of the cavity. A variation of the thickness of the cavity, close to the exit hole, could reduce the resistance of the wall in this region and thus decrease the temperature by decreasing the Joule effect.

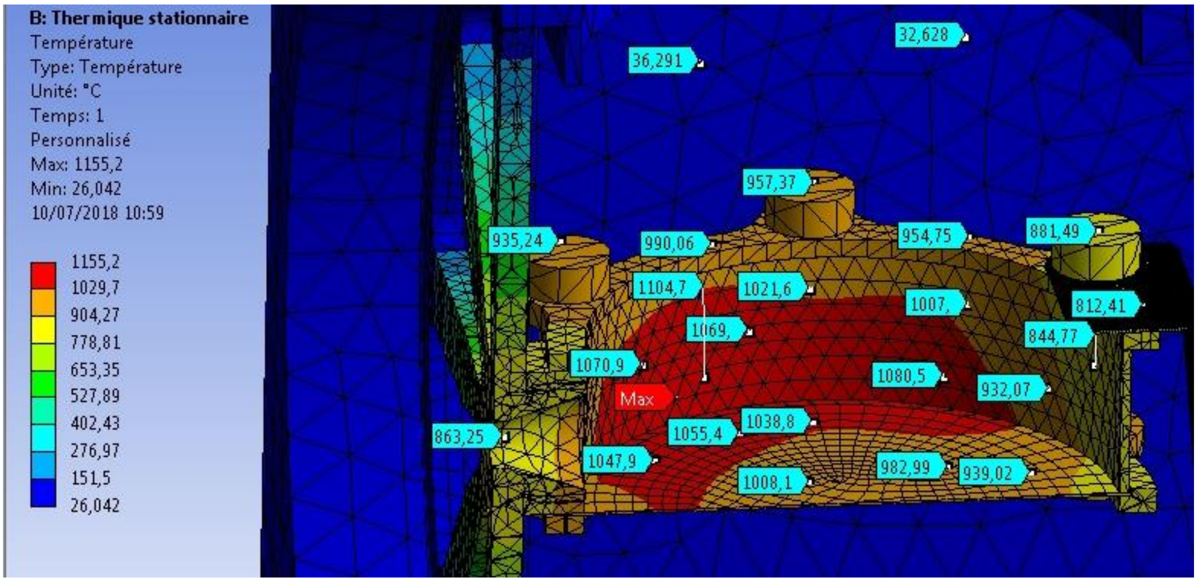

Figure 61: Result of temperature calculation in the TISS performed using the ANSYS code, confirming that the cavity has a higher temperature in the region close to the exit aperture.

4.3 Measurement of AIT efficiency and response time

To measure the response time of the TISS, a compact ion gun delivering stable alkali ions has been developed to test target ion source systems at GANIL. This ion gun was dedicated to the characterization of TISS aiming to produce radioactive ions of alkali. Not only does this saves valuable running time of the GANIL cyclotrons but also reduces the radioactive contamination of the TISS. This device quantifies the effect of parameters (temperature, the electric field inside cavities, ionizing material) on the performance of the TISS, response time and AIT efficiency. The details of the measurements and the results obtained are presented in the following sections.

4.3.1 General principle

To measure the AIT efficiency of a TISS, a flux F_{inj} of atoms or ions is injected. At the output, a flux F_{ext} of ions is extracted. The total efficiency of the source is expressed by the ratio of these two flux:

$$\varepsilon = \frac{F_{ext}}{F_{inj}}$$

The measurement of AIT efficiency of a TISS using stable atoms is possible if an additional measurement of the AIT response time is performed.

If the atoms or ions are radioactive, the AIT efficiency depends on the AIT efficiency of the TISS for stable atoms and on the radioactive decay, leading to losses and thus to a lower efficiency.

4.3.2 Method to measure the efficiency of the source

Whatever the injection method (for example, evaporation of atoms from an oven or flux of gas through a calibrated leak), measuring a flux of atoms is more difficult than measuring a current of ions. Injecting a current of alkali in our TISS has thus been favored.

Injecting a beam of ions also offers the possibility to easily control the current and to pulse it using electrostatic elements. For typical AIT response times of the order of 10 ms, the pulse duration must be of the order of 1 ms to limit the effect on the measurement of the response time. Short pulse durations can be easily obtained with standard electronic components.

Using higher energy ion beams delivered by accelerators allows the ions to penetrate deeply in the matter and thereby allow to obtain AIT response times close to the experimental conditions expected for RIB production. In this way, the results contain the contribution of each process, it can be calculate using the theoretical models.

A second method consists of implanting an ion beam in the production target at low energy (1 keV). The general principle is show in Figure 62. Ions are injected in the TISS under study. At the exit of the cavity, the ions are accelerated and separated based on the mass over charge ratio. Their currents versus time are measured on an oscilloscope triggered by a pulser controlling the ion emission from the gun.

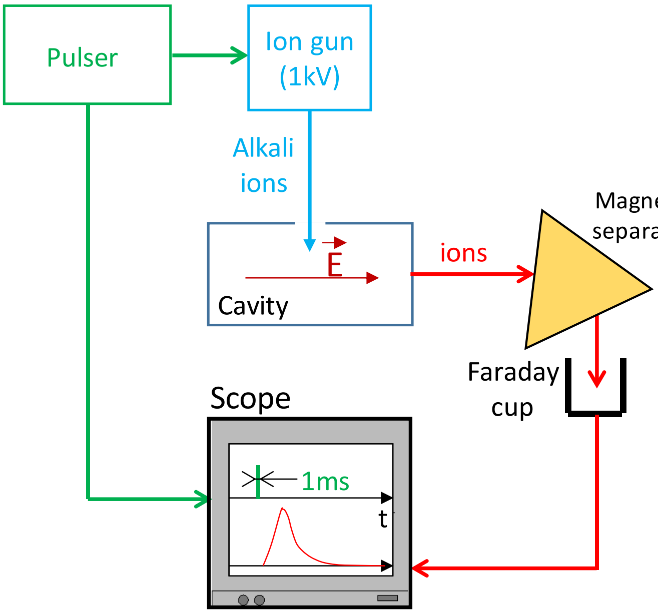

Figure 62: General principle of the response time measurement of the TISS cavity performed using an ion gun.

By measuring the flux of ions at the output of the TISS, it is possible to deduce the effusion and ionization processes. The diffusion process can be neglected since the impinging ions are implanted on the surface of the releasing material. This method can be used with stable ions [113] but also with radioactive ions [21]. The detection of radioactive ions, as much more sensitive than that of stable ions, makes it possible to limit the injected intensity and to overcome the heating of the target by the incident beam.

4.3.3 Method using an ion gun

The second method has been chosen to measure the AIT efficiency and response time of the TISS. More details are given in appendix 4.1.

An ion gun is a device used to generate, accelerate and focus a beam of ions. In the present work, ions are a stable alkaline ion, produced using the system schematically described in Figure 63. The impinging energy of the ions can be adjusted around 1 keV to ease their transport while limiting their range in the catcher to a few nanometers.

Commercially available alkaline emitters (called pellets) have been used [114]. The pellet is heated by an inner filament. The alkali ions are extracted by an electric potential applied between the pellet and an electrostatic electrode (called a Wehnlet lens). The Wehnelt lens can act as a fast pulser, by activating it with brief pulses of negative voltage.

Alkali ions are accelerated and focused by an electrostatic lens. The beam is then transported up to a cavity, via a diaphragm.

The HV platform has been designed to obtain the beam intensity delivered by the ion gun. The measured intensity values are sent to oscilloscope via an optical fiber and using an analog to optical converter. The converter able to convert continuous and alternative signals up to 1 MHz frequency and can thus measure pulses of current.

The cavity is used as a Faraday cup to characterize the ion gun performances. Once characterized, it will be used to test the TISS performance, by replacing the Faraday cup cavity by the TISS cavity.

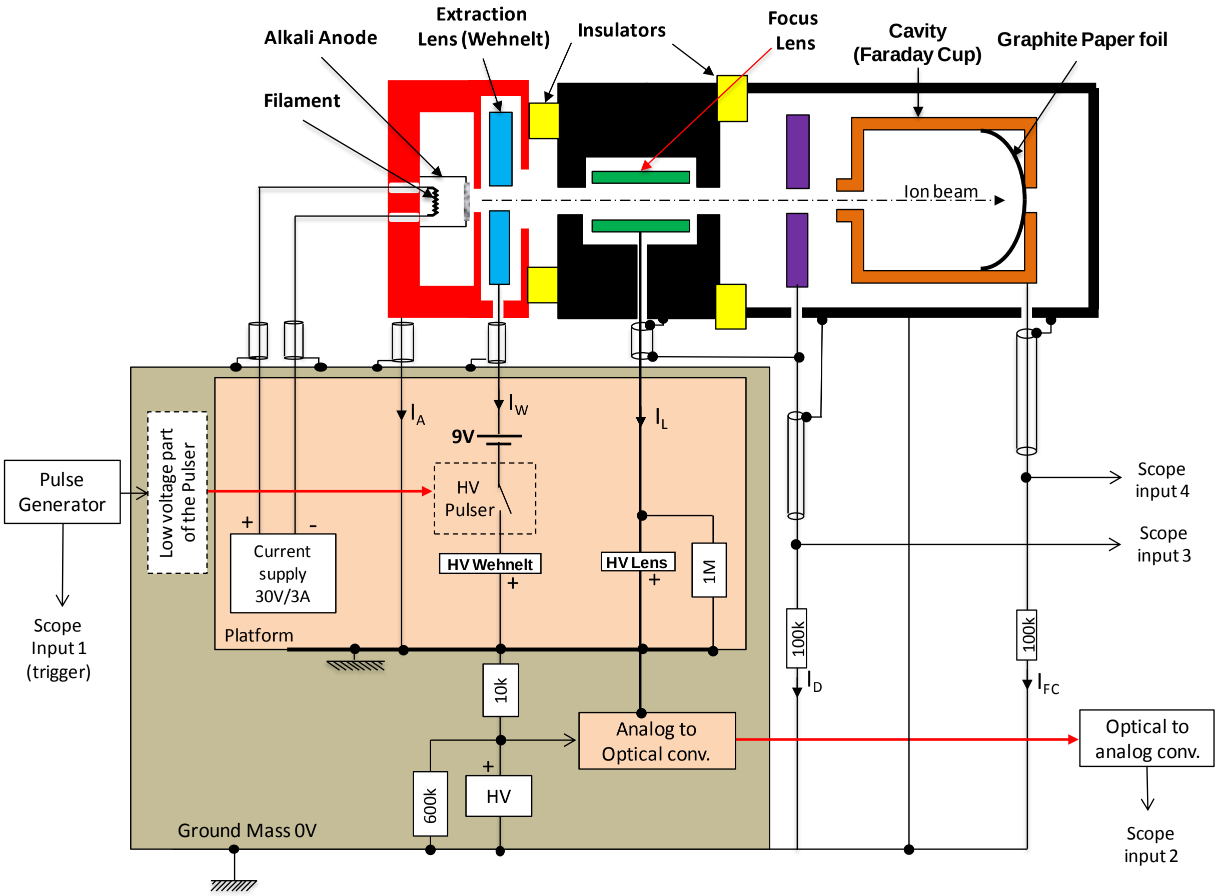

Figure 63: Principle of the ion gun test bench and of its HV platform.

Ions are injected into the TISS cavity through a 5 mm diameter hole in the center of the Ni foil (see Figure 55). The ions are stopped at the surface of the catcher (the path of lithium, sodium, potassium, rubidium and cesium atoms at 1 keV is respectively 141 A°, 60 A°, 56 A°, 61 A° and 70 A° in PAPYEX graphite having density 1.1 $g.cm^{-3}$). Under the effect of the high temperature (17000 K) in the cavity, they diffuse out of the stopper and effuse into the cavity. Owing to their very short range in Papyex, the diffusion time is neglected. Once in the cavity, Rb atoms are ionized and pushed towards the exit aperture and accelerated by the electric potential applied on the extraction electrode. They are mass separated in a magnetic dipole and their current is measured using a Faraday cup. Ion gun and Faraday cup current is injected in an oscilloscope. The delay, the magnitude and the duration of the signal allow to extract the response time and AIT efficiency.

During this Ph.D., the HV platform was refurbished to adapt the TISS for these measurements, and performed the characterization tests. Figure 64 shows an example of signals delivered by the ion gun, collected on the diaphragm and on the Faraday cup.

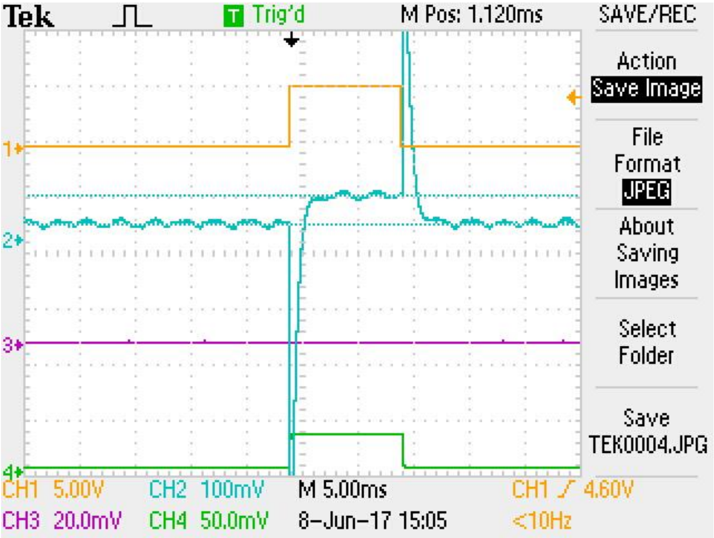

CH1 5.00V CH2 100mV M 5.00ms CH1 ⁄ 4.60V
CH3 20.0mV CH4 50.0mV 8−Jun−17 15:05 <10Hz

Figure 64: Example of signals obtained with the ion gun. The orange line indicates the ion gun current which is equal to 520 nA. The cyan color indicates current on the focus lens, on the wehnelt lens and losses in the chamber. The green line indicates the current on the Faraday cup which is equal to 320 nA.

4.3.4 Description of the ion gun coupled to new TISS

The installation of the ion gun with TISS is given in Figure 65. The vacuum chamber of the experimental device is composed of five flanges, two of them being electrically insulated from each other by alumina rings, in order to polarize them independently.

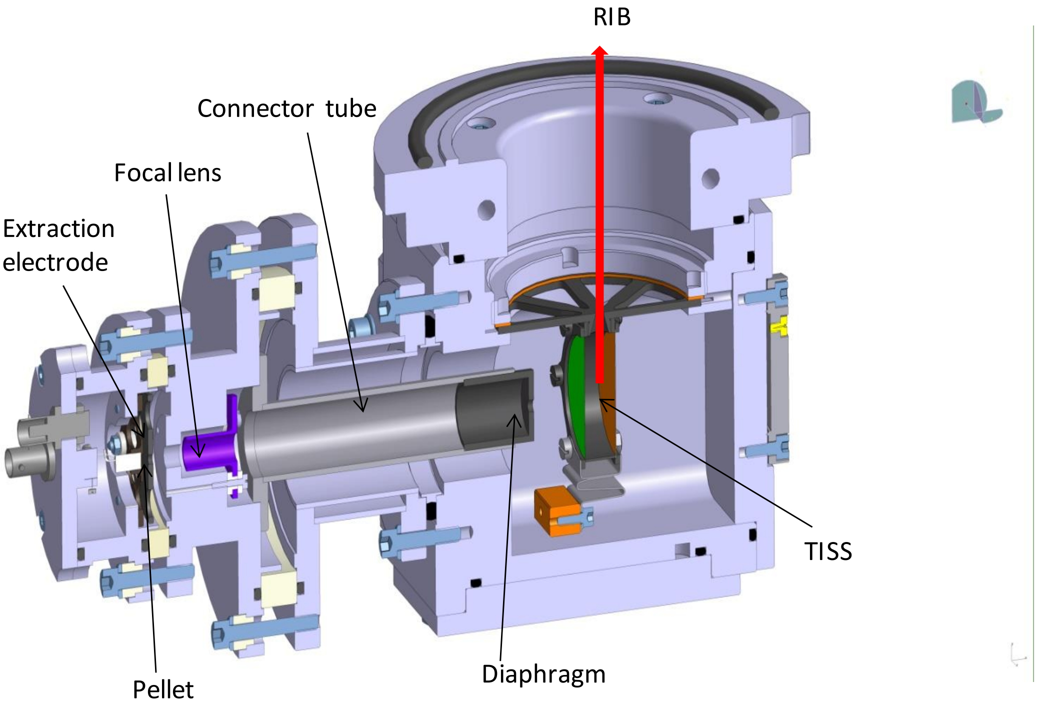

Figure 65: Mechanical drawing of the ion gun connected to the TISS chamber.

The power dissipated in the cavity is of the order of 2 kW and these flanges are cooled by a water circuit. The pellet of the ion gun is heated by a filament, which needs ~10 Watts to evaporate a current of ions sufficient for our measurements (~1 µA).

All the mechanical parts are now available for the AIT efficiency and response time. Once the issue related to the over-heating of the Ni target fixed, the next step will consist in mounting the ion gun on the TISS and in characterizing its performances.

5. Conclusion

A TISS has been conceived in order to respond to produce new competitive radioactive ion beams at GANIL/SPIRAL-1 and to determine to which extent it is possible to improve production performances by optimizing a target ion source system dedicated to the production of a specific radioactive ion beam.

The short-lived alkali isotope of ^{74}Rb has been chosen as a case study for the following reasons:

- it is interesting for physicists, as shown through the letters of intent sent GANIL for the SPIRAL-1 facility
- It is far from the valley of stability and in a region poorly explored by other ISOL facilities,
- It has a short half-life and is chemically reactive, making the competition between radioactive decay and AIT efficiency challenging and needed to demonstrate experimentally.
- It has a low first ionization potential making it convenient for the TISS technique envisaged.

By studying and improving the processes involved in the TISS designed, *i.e.* in-target production by fusion-evaporation, implantation in and release out of graphite, effusion, and ionization, an AIT efficiency of 75% is predicted, leading to an ion beam intensity of the order of 10^4 pps at the exit of the TISS.

The estimated performances would allow the GANIL / SPIRAL-1 installation to deliver beams of ^{74}Rb and ^{114}Cs with competitive intensities compared to other installations.

The production device was developed using results obtained during this Ph.D. work, to cope with physics objectives and with the conditions of the SPIRAL-1 operation. Reliability and thus simplicity was essential. The system meets this requirement.

The instrumentation needed for tests existed (test bench of SPIRAL-1) or have been specifically designed (Ion gun platform and adaptation of the ion gun on the TISS). The TISS has been assembled and placed on the test bench. The compatibility of the services, of the mechanics and the vacuum seal, has been checked. The second step, which is a thermo-mechanical behavior test, has been partly fulfilled: the nickel target was ruptured after some hours at maximum temperature but the graphite cavity and catcher have worked for 18 days without failure. A complete diagnostic will be carried out once 3 weeks of operation completed, which seems to be accessible, as no sign of degradation of the system has been observed so far.

The electric field of ~1 V/cm required in the cavity and which strongly guided the design of the TISS is obtained. Nevertheless, more precise knowledge of resistivity and emissivity is necessary to make the thermal and electrical simulations fit with the experimental results (almost a factor of 2 on the resistance of the whole TISS circuit).

Due to a lack of available or consistent values in the literature, additional studies have been performed to answer questions about sticking times, resistivity, and emissivity, in experimental conditions close to those of the present TISS. A specific setup has been realized and used to measure resistivity and emissivity of several metallic elements. Among the set of results, which have been obtained in identical measurement conditions, some have been used for the design of the TISS.

6. Prospectives

In the case of the production of ^{74}Rb and ^{114}Cs ion beams, the combined techniques of fusion-evaporation, low implantation of recoils in a catcher, ionization of the atoms right from the target cavity equipped with an electric field leading to promising production rates. The success of the technique depends to a large extent on the ability the TISS has to ionize the atoms right from their release out of the catcher. In case of heavy alkali, the first ionization potential is sufficiently low to ensure their ionization by contact with the hot surface of the TISS cavity. In the case of higher first ionization potential atoms are more difficult to ionize and can hardly be ionized by a hot surface, making the TISS proposed for Rb and Cs less attractive. Nevertheless, would it be possible to take partly advantage of this design to produce ion beams of other chemical elements, still in the region of neutron-deficient intermediary masses and short half-lived isotopes?

Once produced in the target and implanted in the catcher, the chemical characteristics of the atoms and their mass greatly influence the AIT efficiency (for a fixed TISS and working conditions), by acting on their release out of the catcher, on their sticking time, on the propagation of the atoms in the cavity, and on the efficiency of a given ionizing method. As shown in the manuscript, the first ionization potential of the atoms is of first importance. Regarding the techniques used to ionize the elements, which are strongly related to the first ionization potential, chemical elements can be shared in three groups: alkali, noble gases, and metallic elements. Could the alkali technique be transposed to noble gases and metallic elements?

In the following, one assumes a cavity having the same geometry and structure as for alkali: a target foil, a catcher and a ring in-between, maintained at high temperature. Isotopes are produced in the target and stop in the catcher. As superficially implanted, they are rapidly released out of the catcher material. In the case of Kr and Xe noble gases, due to their high first ionization potential, the delay induced by chemical effects during their effusion in the cavity can be neglected. Their effusion out of a so small cavity is rapid (3 ms for Kr and 3.5 ms for Xe) regarding the half-lives of isotopes far from the valley of stability (^{71}Kr, $\tau_{1/2}$=100 ms or ^{110}Xe, $\tau_{1/2}$=93 ms for instance). Thus ionizing the atoms in the cavity to reduce the effusion time is of little interest. The cavity could be used as designed for alkali, with a suited target foil and primary beam, and connected to an ECR ion source which has proven its efficiency to ionize gases and has a relatively short response time (~100 ms, [115]).

In the case of metallic atoms, the same principle could be envisaged but the chemical delays in the cavity will increase the effusion time. For the most volatile metals, for which the delay of release out of the cavity under the form of the atom could be acceptable regarding their half-lives, a FEBIAD type ion source [7] could be connected at the exit of the cavity. Combination of such source with a graphite target has already been realized for SPIRAL-1 [116]. The experimental efficiency obtained is typically between 5 to 10%.

In the case of less volatile elements, the in-cavity delay could be too important for short-lived isotopes. As done for alkali, the principle of an electric field applied in a compact cavity including the target, the catcher and containing an ionization principle, could certainly improve the AIT efficiency of the TISS. This technical combination will be one of the next challenges of the SPIRAL-1 group.

Appendices

Appendix 2.1

Choice of the primary beam-target material couple

To optimize the reaction rate for the production of a specific nucleus, there are three parameters which can be varied: the beam ions, the beam energy, and the target nuclei. Different codes are available to calculate reaction cross sections, some of them being analytical, others being of Monte-Carlo type.

In the present work, in-target production rates are estimated using cross-sections issued from the PACE (Projected Angular-momentum Coupled Evaporation) fusion-evaporation code. It uses a two-step scenario for the reactions: projectile and target nuclei completely fuse to create compound nuclei through an angular-momentum dependent fusion model. In a second step, the compound nucleus decays according to a statistical model. Decay paths take into account competition between different channels such as proton, neutron, and α emission as well as γ decay and fission.

The production of very neutron-deficient ^{74}Rb and ^{114}Cs alkali isotopes is possible through different reaction channels. To optimize the production rates, several primary beams and target combinations were investigated at different energies using PACE. The results are listed in Table 7 and Table 8.

Primary beam	Intensity (pps)	Target	Energy (MeV)	Cross-section (mb)	Estimated yields (pps)
^{40}Ca	6.25x10^{+12}	^{42}Ca	165	6.47x10^{-2}	1.22x10^{+4}
		^{46}Ti	370	1.97x10^{-3}	3.22x10^{+2}
^{36}Ar	9.37x10^{+12}	^{46}Ti	260	7.94x10^{-3}	1.95x10^{+3}
			310	2.34x10^{-3}	5.5x10^{+2}
^{32}S	9.37x10^{+12}	^{46}Ti	180	3.96x10^{-3}	9.31x10^{+2}
		^{51}V	245	1.33x10^{-3}	2.95x10^{+2}
^{20}Ne	**1.87.10^{+13}**	**^{58}Ni**	**110**	**6.55x10^{-2}**	**2.55x10^{+4}**

Table 7: The cross-sections are calculated for ^{74}Rb production using the PACE code at different collision energies. The yields are estimated for different reactions and the energies shown here correspond to the highest production cross sections. The green typeface highlights the primary beam-target combination for which the production yields are the highest.

Table 7 shows the cross-section of ^{20}Ne on ^{58}Ni is close to the cross-section of the more symmetric ^{40}Ca on ^{42}Ca system. The primary beam intensity available at GANIL is higher for Ne than for Ca, and so Ne beams should provide higher ^{74}Rb production rates. Moreover, technically, a thin target of Ni (some µm) is easier to design than a thin target of Ca. ^{20}Ne on ^{58}Ni combination has thus been chosen as the best beam-target pair.

Primary beam	Intensity (pps)	Target	Energy (MeV)	Cross-section (mb)	Estimated yields (pps)
^{58}Ni	$3.12\text{x}10^{+12}$	^{58}Ni	230 290	$1.3\text{x}10^{-1}$ $3.94\text{x}10^{-2}$	$8.4\text{x}10^{+3}$ $2.6\text{x}10^{+3}$
^{40}Ca ^{36}Ar ^{32}S	$9.37\text{x}10^{+12}$	^{93}Nb	410 320 290	$6.14\text{x}10^{-6}$ $4.2\text{x}10^{-6}$ $1.13\text{x}10^{-5}$	$4.9\text{x}10^{-1}$ $5.1\text{x}10^{-1}$ 1.37
^{28}Si	$1.25\text{x}10^{+12}$	^{92}Mo	180	$1.13\text{x}10^{-3}$	$1.82\text{x}10^{+2}$

Table 8: The cross-sections are calculated for ^{114}Cs using the PACE code at different collision energies. The yields are estimated for several reactions and the energies correspond to the highest production cross sections. The green typeface highlights the primary beam-target combination for which the production yields are the highest

In the case of ^{114}Cs, nickel on nickel seems to be the best reaction to maximize yields.

Appendix 2.2

SRIM SIMULATIONS

The Stopping and Range of Ions in Matter (SRIM) code is a Monte-Carlo simulation code which is widely used to compute a number of parameters relevant to ion beam implantation and ion beam processing in materials. It is a collection of software packages initially developed in 1985 by Ziegler and Biersack. Stopping power and projected range as a function of particle energies are very useful for computation in a wide range of applications. It calculates the range of ions in matter and the straggling distribution for elements with energies ranging from 10 eV to 2 GeV.

The core of SRIM is the Transport of Ions in Matter (TRIM) program. It is able to handle calculations involving multi-layer targets. It describes the range of ions in matter and also gives the details of other aspects such as Ion distributions, Recoil distributions, Ionization, Energy losses and target damage.

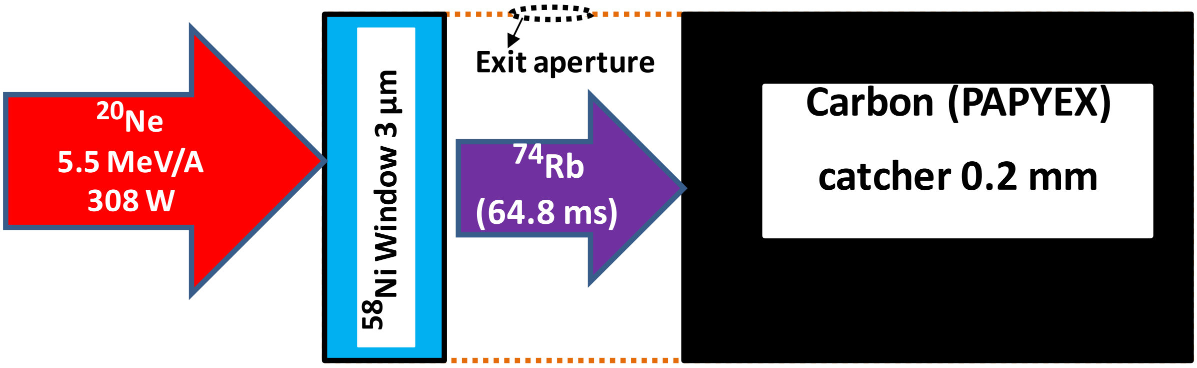

Figure 66: Schema of ^{20}Ne ions bombarding a ^{58}Ni target to produce ^{74}Rb through fusion-evaporation.

In the present work, a primary beam of ^{20}Ne with an energy equal to 5.5 MeV/A hits a Ni target of ~3µm. Due to the thickness of the Ni target and the low energy transfer of ^{20}Ne ions in the foil, most of the ions continue beyond the target, up to the carbon catcher. The ^{20}Ne ions interacting with the Ni nuclei can lead to the production of heavier nuclei by fusion. To conserve total momentum, compound nuclei recoil through the Ni foil. In the case of ^{74}Rb, the foil must be thin enough to let the ^{74}Rb go through the whole thickness, wherever they are produced, at the entrance of ^{20}Ne in the Ni foil or close to their exit. ^{74}Rb then recoil out of the foil and continue on to the carbon catcher where they are stopped.

The SRIM code has been used to optimize the thickness of the nickel target and to determine the minimum thickness the catcher must have to stop the ^{74}Rb recoils.

To get the maximum number of ^{74}Rb out of the nickel window, it is necessary to know the range of rubidium in the nickel at its calculated average recoil energy of 28 MeV (see Figure 67).

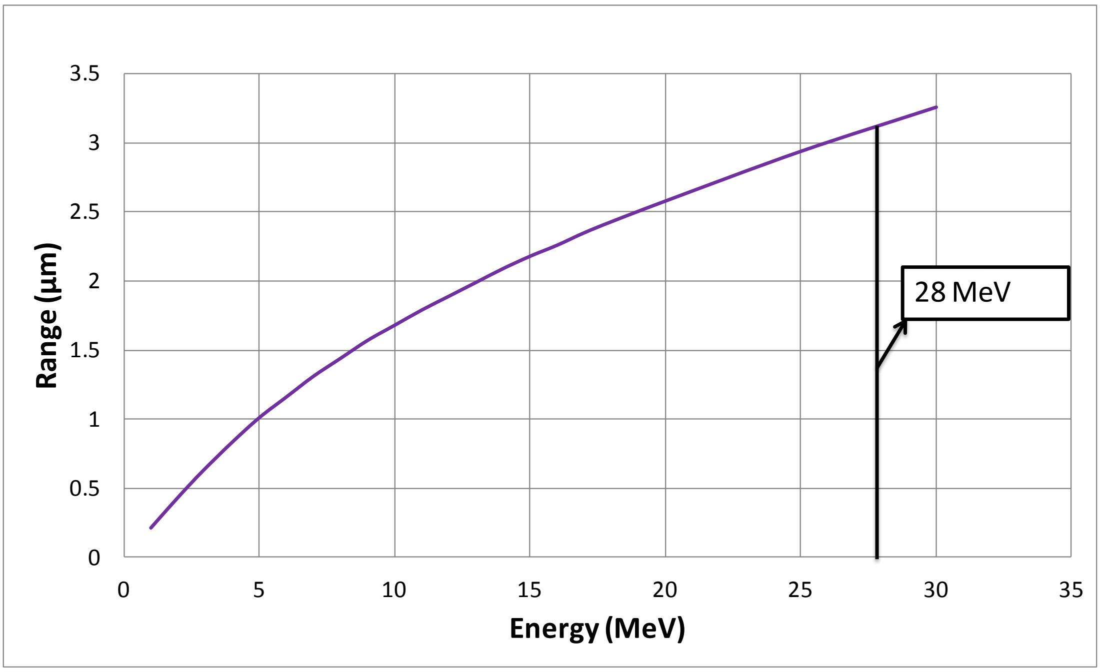

Figure 67: The range of ^{74}Rb isotopes in a nickel target versus the ^{74}Rb kinetic energy.

The calculation shows that the range of rubidium in nickel is 3.2 µm at an incident energy of 28 MeV. The rubidium depth in the graphite depends on the residual kinetic energy. Those produced at the entrance of the Ni target will lose all their energy within the nickel foil and reach the carbon catcher with a kinetic energy lower than that of the recoils produced near the exit face. ^{74}Rb ions produced at the exit of the Nickel window will then penetrate deeper into the graphite catcher (~13µm) as compared to those produced at the entrance (0.5 µm). The range of ^{74}Rb in graphite paper (PAPYEX), used as a catcher, is presented Figure 68.

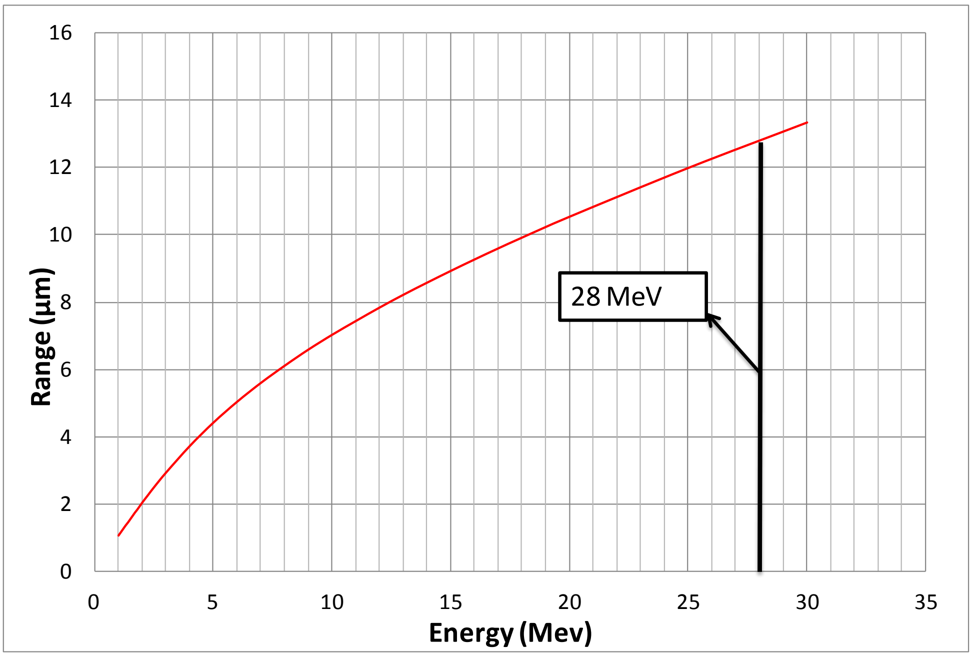

Figure 68: The range of ^{74}Rb isotopes in a graphite paper (PAPYEX) catcher versus the ^{74}Rb kinetic energy.

As most of the ^{74}Rb are stopped within the first 13 µm, a minimum thickness of 25 µm of PAPYEX is chosen to favor their release towards the entrance side of the Papyex and so to increase the probability thay they could be released in the cavity situated between the Ni foil and the Papyex foil.

13 µm is a minimum thickness. The final thickness of the Papyex will depend on other considerations, which are the energy deposited by the primary beam and the consequent temperature of the Papyex, the resistivity of the foil which is an important parameter influenced by both the temperature of the system and the electric field in the cavity, and the commercial availability of different Papyex thicknesses.

To avoid damaging the catcher and target materials by overheating, it is important to know the power deposited by the primary beam. The power is the product of the energy lost in the Papyex by the ions (represented in Figure 69) multiplied by the intensity of the primary beam.

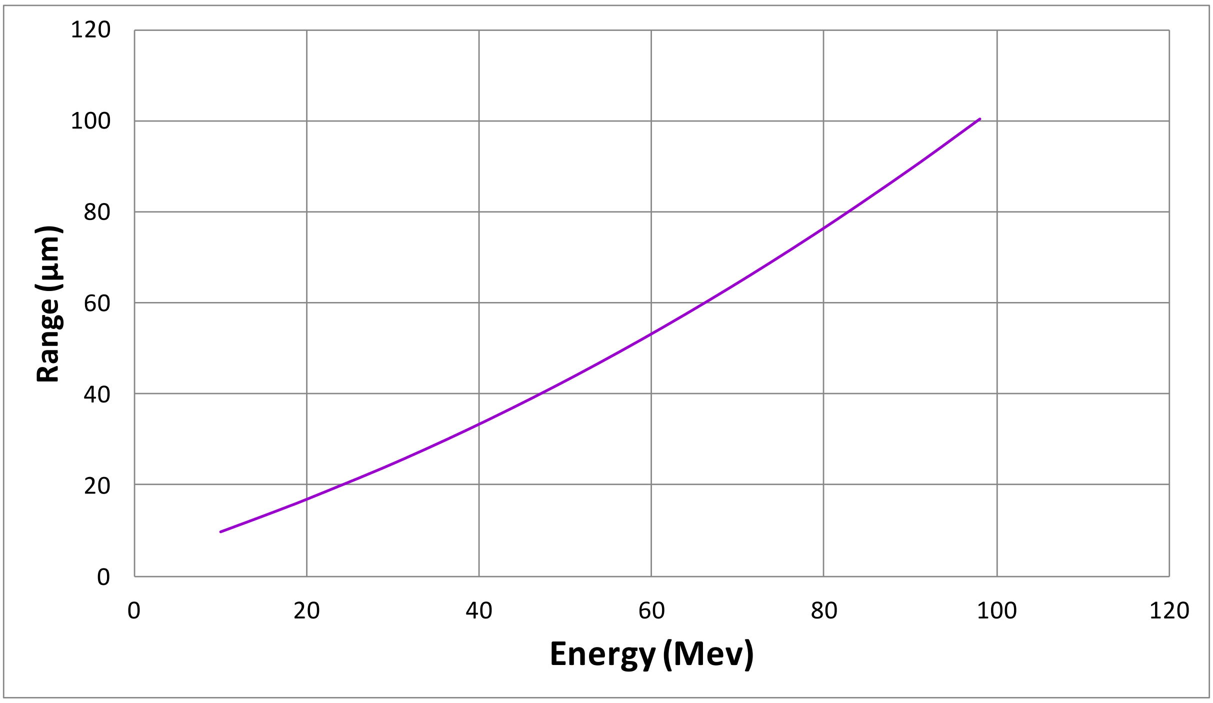

Figure 69: The range of ^{20}Ne in PAPYEX at an energy of 98 MeV.

The energy of the ^{20}Ne primary beam is 110 MeV. The energy loss of ^{20}Ne in a 3.2 µm thick ^{58}Ni target is 12 MeV. The remaining energy of the primary beam, downstream from the target, is then 98 MeV. To stop this beam 100 µm of graphite Papyex with a density of 1 g/cm^3 is sufficient. As the minimum thickness of Papyex commercially available is 200 µm, this thickness is used. The fact that the primary beam is totally stopped within the Papyex catcher has been taken into account during the thermal simulation. And the electrical resistivity of 200 µm of Papyex has been taken into account during the electrical stimulation.

In these thickness and energy loss conditions, the power deposited by the primary beam in the Papyex catcher will be 274 W at most, using the maximum beam intensity delivered by the GANIL cyclotrons.

APPENDIX 2.3

Release processes out of the target

The following appendix presents the whole approach followed to describe analytically the release processes out of a target made of grains. The main points and conclusions are presented in chapter 2. Presenting the calculations in detail gives the opportunity for the reader to verify them and eventually to apply the approach to other target microstructures. Rather than dividing specific parts of the approach in different appendices, and so taking the risk of fragmenting the explanations, the whole approach is presented here.

Release of atoms out of a graphite target.

When the primary beam hits the target, radioactive atoms can be produced within the grain structure of the target. To exceed the Coulomb barrier and induce nuclear reactions, the energy of the primary beam must be higher than ~5 MeV/A, leading to beam ranges in matter beyond some tens of µm at least, and reaching several cm in the case of very energetic primary ion beams of low atomic number. Reaction products are considered to be uniformly produced within the grains having typical dimensions of a few µm or less. Once stopped in the grains, the atoms propagate by “diffusion” within the material, up to “free” inter-grain volumes, where they propagate by “effusion” to the surface of the target. Diffusion and effusion processes takes time and depends on the physical-chemistry features not only of the target material and the atom produced, but also on the working conditions of the target. These processes are in competition with the radioactive half-life of the atoms produced. This competition leads to losses, and is more important for short-lived isotopes.

The goal of the present study is to maximize the release efficiency of radioactive atoms from grainy target material by minimizing the release time.

Our approach is based on the following logic (using Figure 70). We assume that the grains are spherical. Real grains are not spherical but we consider their average shape is spherical. Each grain has a radius R. The atoms diffuse out of the grains, effuse up to the surface of the target and once they reach the left or right hand side, they are considered as being released from the target. Several assumptions, based on the probability the atoms have to take the different ways were considered:

Once released from a grain, the atoms do not re-enter, since the propagation inside the grain is more difficult than in the free volume between the grains

Once released from the target, atoms do not re-enter, since the propagation inside the target is more difficult than outside.

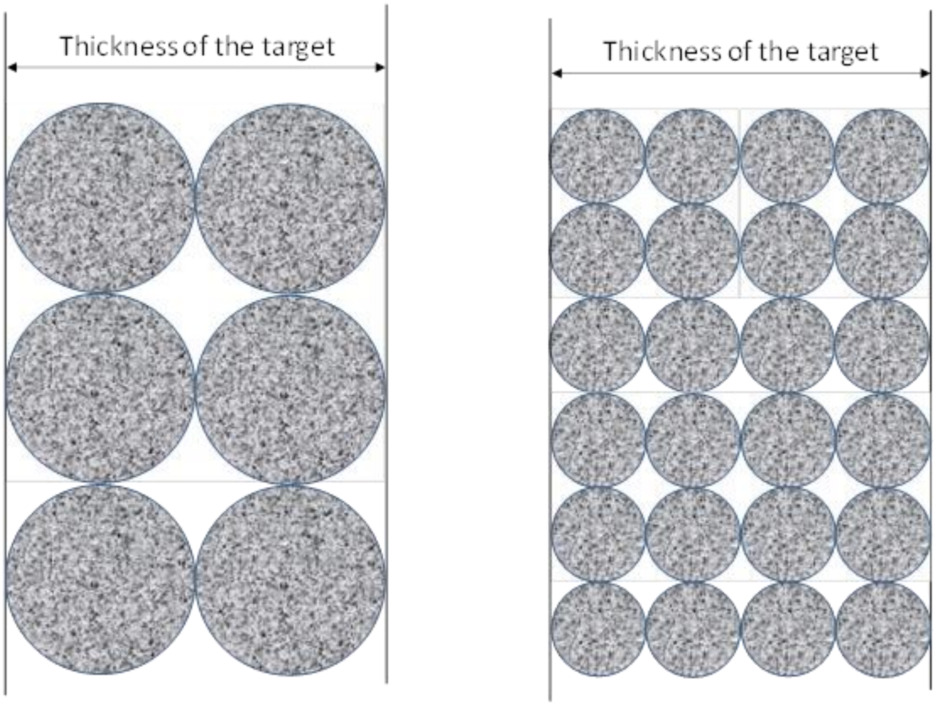

Figure 70 : Basic representation of the graphite structure. A diamond structure could also have been chosen.

In the left part of Figure 70, the grains are large. The diffusion time out of the grains will be longer than in smaller grains shown on the right hand side. Effusion out of an elementary volume formed by a group of 8 grains will also be longer. One could think that optimizing the release of the atoms out of the target could simply consist of reducing the size of the grains. However, to reach the outer walls of the target, if the total thickness remains unchanged, the atoms also have to go through a series of elementary volumes, of increasing number as grain sizes decrease. Since diffusion and global effusion processes have opposing dependencies as a function of the grain size, there must be an optimum grain size corresponding to an optimal release time.

The question we address is: What is the optimum size of the grains?

To find the optimum size of the grain, we built an analytical description taking both effusion and diffusion processes into account, keeping the grain size as a parameter in the equations. Our goal was to build a description from which the tendencies of the effect of the grain size on the release behavior, and a rough estimation of the optimum grain size could be directly extracted.

In the framework of this description, we made the following assumptions

- The temperature is uniform over the target volume
- The production of radioactive atoms in the matter of the grains is uniform.
- The production of radioactive atoms in the matter of the target is uniform.
- The diffusion of the atoms within the matter of the grains is isotropic.
- The effusion regime of the atoms is molecular (i.e. no collisions between the atoms).

Diffusion process

Phenomenological description of the diffusion process

A well-known diffusion phenomenon corresponds to the heat transfer from hot to cold regions of a material. The analytical description for the flow of heat with a temperature gradient is given by Fourier's law [4].

$$\boldsymbol{J_P = -k.\frac{dT}{dx}} \qquad \textbf{\textit{Equation 6}}$$

J_P is the heat flux, i.e. the flow of heat per unit area and time, $\frac{dT}{dx}$ is the temperature gradient, and k is the thermal conductivity. The minus sign indicates that the heat flows from high to low temperature.

Fick's first law

Fick actually developed his phenomenological description of diffusion on the basis of Fourier's work on heat conduction. The fundamental mathematical expression describing the flow of particles is given by Fick's first law [5]. It relates the flux J_P of particles (in particles.m^{-2}.s^{-1}) to the concentration gradient $\frac{dC}{dx}$

$$\boldsymbol{J_P = -D.\frac{dC}{dx}} \qquad \textbf{\textit{Equation 7}}$$

Minus sign indicates that the flux of particles goes towards low concentration regions. The coefficient D is the diffusion coefficient of the material (m^2.s^{-1}). It fixes the ratio between the flux and the concentration gradient. It depends on the temperature and on the activation energy according to the Arrhenius expression:

$$\boldsymbol{D = D_0.e^{\left(-\frac{E_a}{RT}\right)}} \qquad \textbf{\textit{Equation 8}}$$

D_0 is the temperature independent pre-exponential factor in m^2.s^{-1}, R is the universal gas constant in J.K^{-1}.mol^{-1} and T is the temperature in Kelvin. E_a is the minimum energy required to start a process in Joules.mol^{-1}. In the present case, the chemical process consists of an atom in motion, being displaced from one site to another. The energy state of the system formed by the atom and the material can be identical for two different sites of the atom. This energy is related to chemical bonds and/or the potential energy of the atomic site. To move, the atom can take this energy from the temperature of the material. For high temperatures, in the limit fixed by the fusion temperature of the material, D tends to D_0. As E_a decreases, the dependence of D on the temperature decreases and for very low values of E_a, tends to D_0. $E_a = 0$ means that the propagation process no longer depends on chemical reaction or potential barrier. The propagation is then only related to the kinetic energy and is called effusion.

Application to a material composed of grains

In the case of radioactive ion beams produced by the ISOL (Isotope Separation On Line) technique, radioactive atoms are created in the grainy material and diffuse out. Starting from Fick's laws, M. Fujioka [6] established the analytical expression of the fraction of stable atoms remaining at time t in target materials having different shapes. In the case of spherical grains of radius R, the fraction $p(t)$ can be expressed as:

$$\boldsymbol{p(t) = \frac{6}{\pi^2}\sum_{m=1}^{\infty}\frac{1}{m^2}\,.\,e^{-(m^2\pi^2 D/R^2)t}} \qquad \textit{Equation 9}$$

where m is a mathematical parameter which has no physical meaning but can be interpreted as a number corresponding to a shell containing a part of the atoms.

N_0 atoms are produced at time $t = 0$ in the target. We assumed that the target contains k grains. Hence, N_0/k atoms are initially contained in each grain. N_{0m}/k atoms are initially contained in the shell m of each grain. From $p(t)$, one can deduce that the flux $f_k(t)$ coming out of a grain at time t is equal to the sum of the flux delivered by each shell:

$$\boldsymbol{f_k(t) = \frac{1}{k}\sum_{m=1}^{\infty}\lambda_{Dm}N_{0m}.\,e^{-\lambda_{Dm}.t}} \qquad \textit{Equation 10}$$

With $\lambda_{Dm} = \frac{m^2\pi^2 D}{R^2} = m^2\pi^2\lambda_D$ where λ_D is the diffusion rate in s^{-1}, equal to $\frac{D}{R^2}$ and N_{0m} is equal to $\frac{1}{k}\frac{6}{\pi^2}\frac{N_0}{m^2}$. $\left(\text{Remark:} \sum_{m=1}^{\infty}\frac{6}{\pi^2 m^2} = 1\right)$.

Using these expressions, the total flux released by one grain is written:

$$\boldsymbol{f_k(t) = \frac{6.\lambda_D.N_0}{k}\sum_{m=1}^{\infty}e^{-\lambda_{Dm}.t}} \qquad \textit{Equation 11}$$

The total flux of atoms delivered within the volume of the target at time t is then:

$$\boldsymbol{f(t) = 6.\,\lambda_D.\,N_0\sum_{m=1}^{\infty}e^{-\lambda_{Dm}.t}} \qquad \textit{Equation 12}$$

Effusion process

Once released from the grains, the atoms mainly migrate within the solid material through the most open route, and this corresponds to the spaces between grains. The atoms finally end up on the target surface, where they are completely released.

The question is: How long does it take for atoms to leave an elementary volume V (shown in Figure 71) defined by 8 spheres?

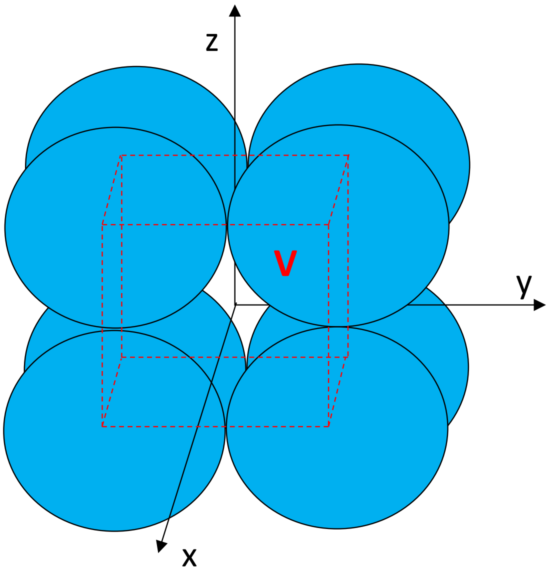

Figure 71: Representation of the position of the elementary cube

In this configuration, the flux of atoms released in the "central" volume comes from eight eighths of eight different spheres. The total flux is therefore equivalent to the one released by one sphere. There are six apertures through which the atoms can escape, two per direction. As mentioned before, targets are often made of foils. The atoms will exit mainly along the direction perpendicular to the foil (x direction), their propagation within the foil layer being less probable (y and z direction). Moreover, through each exit route from the central cube along y and z directions, the flux of atoms exiting a cube adjacent to the central one (see Figure 72) is equal to the flux leaving the central cube. Given the atoms are not discernible, we can neglect the probability that they exit the free cube volume through y and z apertures. The cube can therefore be considered to present only exit two apertures, along the x axis.

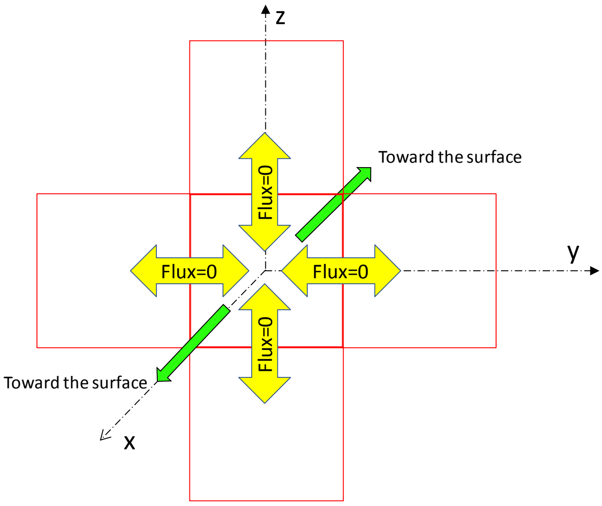

Figure 72 : The flux in different directions. The foil is assumed to be parallel to the yz-plane.

In molecular regime and for simple volume geometry, the relation at time *t* between the flux *dn/dt* of atoms leaving the volume and the number *n(t)* of atoms contained in the volume is:

$$\boldsymbol{\frac{dn}{dt} = \lambda_e . n(t)} \text{ with } \boldsymbol{\lambda_e = \frac{conductance\ of\ the\ aperture}{volume}}$$ *Equation 13*

Where

Conductance of the aperture = $\beta . A$ and the speed β is equal to $\sqrt{\frac{8kT}{\pi m}}$ where

- k is Boltzmann constant : 1.38064852 × 10^{-23} ($m^2.kg.s^{-2}.K^{-1}$)
- T is temperature (in K)
- m is molecular weight of an ion (in kg)

The area A of one aperture is equal to the area of one face of the cube minus the area of the disc divided, as shown in Figure 73, in four segments:

$$A = (4 - \pi)R^2$$

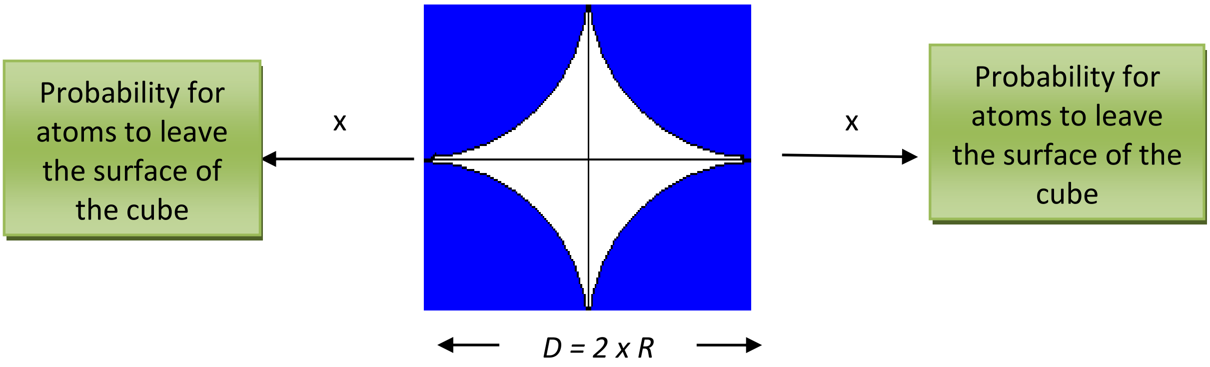

Figure 73 : An elementary cube (order 1).

The volume of the cube represented in red in *Figure 71* minus the volume of the eight eighths of a sphere is equal to

$$V = 4.\left(2 - \frac{\pi}{3}\right).R^3$$

Therefore, the effusion rate λ_e is given by

$$\boldsymbol{\lambda_e = \frac{\beta . A}{V} = \frac{\beta(4-\pi)}{4\left(2 - \frac{\pi}{3}\right)}\frac{1}{R} = \frac{\beta . \gamma}{R}}$$ *Equation 14*

And the typical effusion time T_e is given by

$$T_e = 1/\lambda_e$$

The expression λ_e gives us the relation between the effusion rate and the size of the grain. γ is a coefficient related to the geometry of the material structure and in the case of spheres without overlap, γ =0.225.

To fix numbers, here we consider the effect of large and small grains on effusion:

- For a grain diameter of 3 mm, which corresponds to a sphere having a diameter equal to the thickness of a graphite target, for ^{35}Ar atoms and a temperature of the target of 2000°C, the release rate by effusion λ_e would be equal to 4.2.10^4 Hz and the typical time is 16.2µs. A grain of 3 mm in diameter would not be really considered for target material synthesis.
- For a grain diameter of 1 µm, for ^{35}Ar atoms and a target temperature of 2000°C, the effusion rate λ_e is 1.3.10^8 Hz and T_e is 5.5 ns.

Once in the free voids between the grains, the atoms have to propagate through a medium which can be seen on a microscopic scale as a labyrinth, and macroscopically as a homogeneous material if the size of the grains is sufficiently small compared to the dimensions of the target. This last condition is generally fulfilled in the case of graphite used in ISOL systems, where typical grain sizes are the order of 1 µm and the foil thickness of the order of some tenths of mm. The analytical expression of the atom flux leaving a foil shaped target material (i.e. having a dimension along one axis significantly lower than its dimensions in the two other axis), as derived by M. Fujioka [6], is given by:

$$\boldsymbol{f(t) = 8.\lambda_E.N_0 \sum_{n=0}^{\infty} e^{-\lambda_{En}.t}} \qquad \textit{Equation 15}$$

Where λ_E is the effusion rate, and is equal to D_E/d^2. D_E is the effusion coefficient of the atoms in the target and d is the thickness of the target. N_0 is the number of atoms effusing in the volumes between the grains. n is an integer which is related to the planar shell n containing N_n atoms as:

$$N_n = \frac{8.N_0}{(2n+1)^2\pi^2} \qquad \left(\text{Remark: } \sum_{n=0}^{\infty} \frac{8}{(2n+1)^2\pi^2} = 1\right).$$

and λ_{En} is the effusion coefficient of the atoms out of the shell n and defined as:

$$\boldsymbol{\lambda_{En} = (2n+1)^2\pi^2\lambda_E} \qquad \textit{Equation 16}$$

An important remark must be made about λ_e and λ_E, and their relation. λ_e corresponds to a microscopic effusion process within a volume defined by a small number of grains (8 in our case). It is thus related to the size of the grains. λ_E corresponds to a macroscopic process and is related to the size (thickness in the present case) of the target. Both are related by the effusion coefficient D_E which is an intensity parameter and which therefore does not depend on the scale at which the effusion process is observed. The difference in λ_e and λ_E comes from the size of the object where the effusion occurs. In the case of our elementary volume, shown in Figure 71, the relevant dimension is the radius R, and λ_e must then be equal to D_E/R^2. Since we have also established a relation between λ_e and the local effusion parameters ($\lambda_e = \gamma.\beta/R$), we can write:

$$\frac{\gamma.\beta}{R} = \frac{D_E}{R^2}$$

Thus

$$\boldsymbol{D_E = \gamma\beta R} \qquad \textit{Equation 17}$$

In the case of a target having a thickness equal to d, the effusion rate λ_E will be equal to

$$\boldsymbol{\lambda_E = \frac{\gamma\beta R}{d^2}} \qquad \textit{Equation 18}$$

This expression is one important step in our approach since it connects the microscopic structure of the grain to the macroscopic effusion features of the target. As the diffusion out of the grains also takes into account the size of the grain, it will be possible, as we show in the following, to describe the diffusion and effusion processes out of a macroscopic target while taking into account its microscopic structure.

Diffusion-Effusion process

We consider in the following paragraph that the release process of the atoms out of the target occurs in two consecutive steps, the diffusion of the atoms out of the grain and then their effusion out of the target. The probability that the atom re-enters the grains or the target once they have exited, is neglected. This assumption is indeed not fully realistic: neither diffusion nor effusion are one-way processes. This assumption is simply justified by the diffusion and effusion rates, implying atoms use the easiest way to exit the target material.

Considering the process in two consecutive steps simplifies the analytical description. The previous flux of atoms released by the grains is the feeding term of the effusion process. The variation with the time of the number x_n of atoms present in the free volumes between the grains and included in the shell n is equal to the difference between the flux effusing out of the shell n and the flux of atoms contained in the shell n and coming from the grains, and can be expressed as:

$$\left.\frac{dx_n(\mathrm{t})}{dt}\right|_{In\ the\ free\ volume} = -\lambda_{En}\,x_n(\mathrm{t}) + 6.\lambda_D.N_n\sum_{m=1}^{\infty} e^{-\lambda_{Dm}t}$$

This gives us

$$\boldsymbol{x_n(t)|_{\substack{In\ the\ free\\ volume}} = 6.\lambda_D.N_n\sum_{m=1}^{\infty}\frac{1}{\lambda_{En}-\lambda_{Dm}}\left[e^{-\lambda_{Dm}t}-e^{-\lambda_{En}t}\right]} \qquad \textit{Equation 19}$$

To establish the total flux $F(t)$ coming out the target, we sum over n, that is, the flux coming from each shell ($= \lambda_{En}.x_n(t)$). This leads to

$$\boldsymbol{F(t) = 48.\lambda_D.\lambda_E.N_0\sum_{n=0}^{\infty}\sum_{m=1}^{\infty}\frac{1}{\lambda_{En}-\lambda_{Dm}}\left[e^{-\lambda_{Dm}t}-e^{-\lambda_{En}t}\right]} \qquad \textit{Equation 20}$$

As the evolution of the atoms in the target and out of the target is now related to the diffusion and effusion rates, we express these rates as a function of the grain radius.

If the radioactive decay rate λ is taken into account during the diffusion and effusion in the target, the total release rate of radioactive elements coming from the target can then be written:

$$\boldsymbol{F(t) = 48.\lambda_D.\lambda_E.N_0.e^{-\lambda t}\sum_{n=0}^{\infty}\sum_{m=1}^{\infty}\frac{1}{\lambda_{En}-\lambda_{Dm}}\left[e^{-\lambda_{Dm}t}-e^{-\lambda_{En}t}\right]} \quad \textit{Equation 21}$$

In order to optimize the grain size, we calculate the mean release time $\langle t\rangle$ from the target:

$$\langle t\rangle = \frac{\frac{1}{N_0}\int_0^{\infty} t\,F(t)dt}{\int_0^{\infty} F(t)\,dt}$$

As $\int_0^{\infty} t^n\, e^{-at}dt = \frac{\Gamma(n+1)}{a^{n+1}} = \frac{1}{a^2}\; for\; n = 1$

$$\boldsymbol{\langle t\rangle = \frac{\sum_{m=1}^{\infty}\sum_{n=0}^{\infty}\frac{\lambda_{En}+\lambda_{Dm}+2\lambda}{(\lambda_{Dm}+\lambda)^2(\lambda_{En}+\lambda)^2}}{\sum_{m=1}^{\infty}\sum_{n=0}^{\infty}\frac{1}{(\lambda_{Dm}+\lambda)(\lambda_{En}+\lambda)}}} \quad \textit{Equation 22}$$

We see here that the mean release time depends on few parameters: the radius R of the grains, the diffusion coefficient D of the grain material, the thickness d of the target and the thermal speed β of the atoms. d and β are easy to determine experimentally. In this approach, the diffusion coefficient of the atoms in the matter remains an issue, as does the true microscopic geometry.

R can be deduced from the mesh size of the manufacturing sieve. The largest grains have size equal to that of the mesh, and are collected along with the smaller grains. In the final graphite, depending on the compression and sintering processes, the global arrangement is denser than in the previous description where only the presence of the largest grains was assumed. We thus have to consider the presence of small grains between large grains, leading to an increase in the material density. Before comparing our calculations with experimental results, we first evaluate the effect of these smaller grains, or the effect of the density, on the average release time.

Density versus grain size

To take into account the presence of the small grains, we assume that they can be represented overlapping larger sphere volumes (see Figure 74).

Without overlap, the density of the target can be determined using the general definition:

$$\boldsymbol{Density} = \frac{\boldsymbol{volume\ of\ sphere} \times \boldsymbol{maximum\ density\ of\ carbon}}{\boldsymbol{volume\ of\ cube}}$$

Equation 23

In the case of overlap, we estimate the volume V_{SC} of a sphere included in a cube as being

$$V_{SC} = V_{sphere} - 6V_{cap}$$

where V_{cap} is the green shaded volume in Figure 74, which we then divide by the volume of a cube. Each cap has a volume $\frac{\pi h^2}{3}(3R_s - h)$ where h is the height of the spherical cap and $h = R_s - R$.

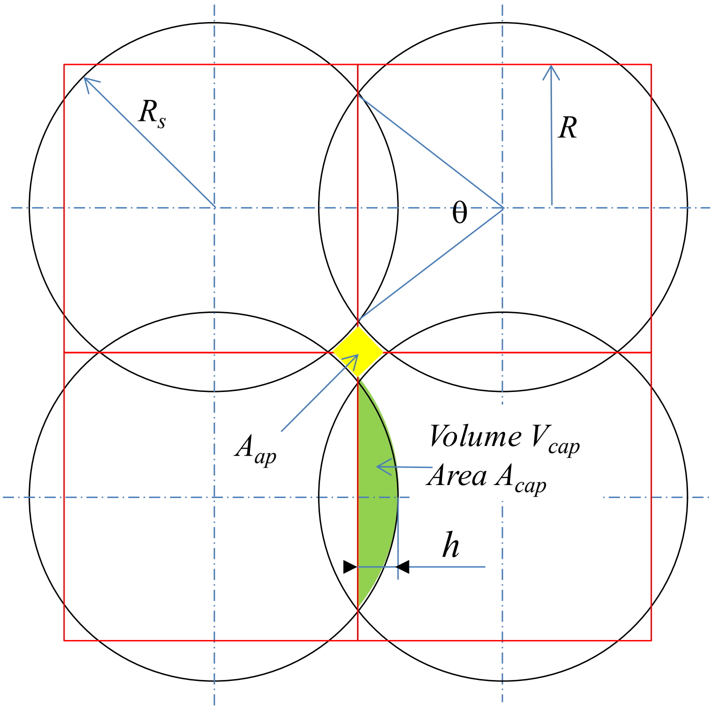

Figure 74 : schematic view of a set of four overlapping spheres

The volume of the sphere is equal to $\frac{4}{3}\pi R_S^3$. Therefore, V_{sc} is equal to:

$$\boldsymbol{V_{SC} = \frac{4}{3}\pi R_s^3 - 6\left[\frac{\pi h^2}{3}(3R_s - h)\right]}$$

Equation 24

If one calls α the ratio between R_s and R ($R_s = \alpha R$), the density is then

$$\boldsymbol{\rho = \frac{V_{SC}}{V_{cube}}\rho_0 = \frac{\pi}{12}(-4\alpha^3 + 9\alpha^2 - 3) * \rho_0}$$

Equation 25

This expression gives the density as a function of the overlap defined by α (shown in Figure *75*). ρ_0 is the maximum density of the material. In the case of carbon, ρ_0 is equal to 2.26 g/cm^3. Without overlap, the sphere is totally included in the cube, $\alpha = 1$ and ρ is equal to 1.185 g/cm^3. For an overlap corresponding to closed apertures between the grains, $\alpha = \sqrt{2}$ and the density is equal to 2.18 g/cm^3.

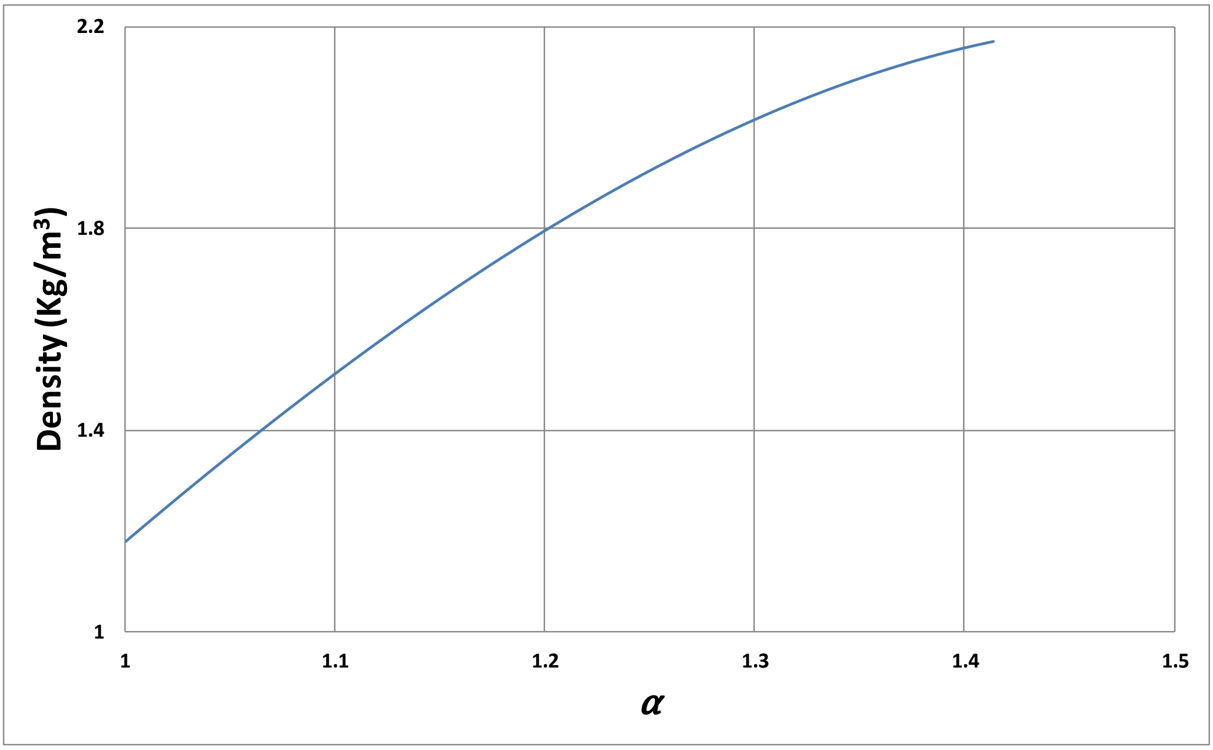

Figure 75: Variation of density with respect to the parameter α.

Effect of the density on the release rates

The two following paragraphs describe effect of the density on the diffusion and effusion rates.

Influence of the density on the diffusion rate

We still consider graphite made of spheres with free elementary volumes between eight spheres.

According to equation 7 the diffusion flux can be described to be the sum of flux $f_m(t) = 6.\lambda_D.N_0.e^{-\lambda_{Dm}.t}$ leaving shells marked by the index m. In terms of algebra, the diffusion out of a spherical shell m is identical to the description of atoms effusing out of a sphere of suitable exit aperture area A_m and volume V_m. Absolute values of A_m and V_m are unknown, but diffusion or effusion rates must be proportional to the ratio A_m/V_m. Both A_m and V_m must also be proportional to the area through which the atoms can leave the grain, and to the volume of the grain. Our present goal is to determine the effect of overlap on this ratio.

In the case of no-overlap between grains, the ratio A_m/V_m is written:

$$\left.\frac{A_m}{V_m}\right|_{no-overlap} = 4\pi R_s^2.\frac{3}{4\pi R_s^3} = \frac{3}{R_s} = \frac{3}{R}$$

In the case of overlapping spherical volumes, the diffusion volume is equal to the volume of one sphere minus the volume of six overlapping caps:

$$V_D = \frac{4\pi R_s^3}{3} - 6 * \left[\frac{\pi h^2}{3}(3R_s - h)\right] = \frac{2\pi R^3}{3}[-4\alpha^3 + 9\alpha^2 - 3]$$

The area A_D is equal to the area of the sphere minus the area of six caps:

$$A_D = 4\pi R_s^2 - 6 * [2\pi R_s(R_s - R)] = 4\pi\alpha R^2(3 - 2\alpha)$$

The ratio A_m/V_m is then:

$$\left.\frac{\boldsymbol{A_m}}{\boldsymbol{V_m}}\right|_{\boldsymbol{overlap}} = \frac{\boldsymbol{6\alpha(3-2\alpha)}}{\boldsymbol{R}[\boldsymbol{-4\alpha^3+9\alpha^2-3}]} \qquad \textit{Equation 26}$$

The density correction factor F to be applied to the diffusion rate is then:

$$\boldsymbol{F} = \frac{\boldsymbol{A_m/V_m|_{overlap}}}{\boldsymbol{A_m/V_m|_{no-overlap}}} = \frac{\boldsymbol{-4\alpha^2+6\alpha}}{\boldsymbol{-4\alpha^3+9\alpha^2-3}} \qquad \textit{Equation 27}$$

Combining Eq.27 and the α parameter density dependence, we can represent the density correction factor as a function of the density (as shown in Figure 79).

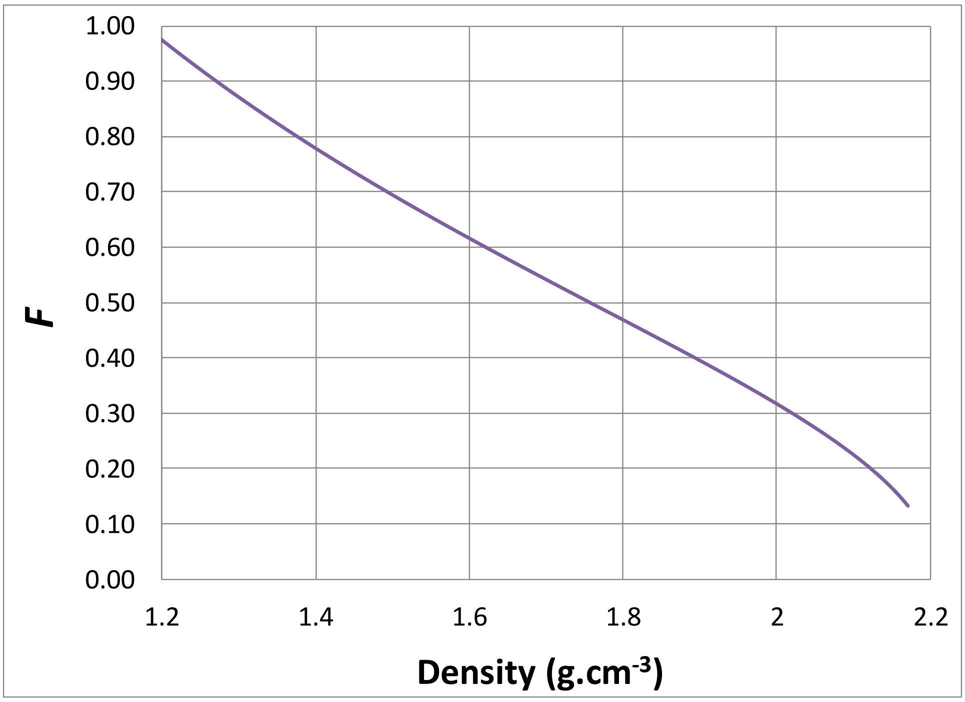

Figure 76 : The density correction factor F versus density.

Over the density range considered, the density correction factor F ranges from 1 to 0.13.

Influence of the density on the effusion rate

The density also affects the effusion process. The effusion rate λ_e can be extracted from the ratio of the conductance of the free volume (Eq.8).

The aperture area A_{ap} between four spheres is equal to the area of one face of the cube ($A_{face} = 4R^2$) minus the area of the disc included on one face of the cube:

$$A_{ap} = A_{face} - \left(A_{disc} - 4 \times A_{cap}\right)$$

The area of the disc is πR_s^2, and the area A_{cap} of the cap, shown as a green shaded segment in Figure 74 is equal to the area A_{sector} of the circular sector minus the area A_{tri} of the triangle:

$$A_{cap} = A_{sector} - A_{tri}$$

$$= \frac{1}{2} R_s^2 \theta - \frac{1}{2} R_s^2 sin\theta$$

$$A_{cap} = R_s^2 \left[\alpha^2 cos^{-1}\left(\frac{1}{\alpha}\right) - \sqrt{\alpha^2 - 1}\right]$$

The area of A_{cap} is then:

$$A_{cap} = (2R)^2 - \left\{\pi R^2 - 4R^2 \left[\alpha^2 cos^{-1}\left(\frac{1}{\alpha}\right) - \sqrt{\alpha^2 - 1}\right]\right\}$$

Considering an overlap between grains, which depends on the α parameter, the microscopic effusion rate λ_e defined in equation (8) can then be written as:

$$\boldsymbol{\lambda_e = \beta.\left[\frac{\left[4 - \pi\alpha^2 + 4\alpha^2 Arcos(1/\alpha) - 4\sqrt{\alpha^2 - 1}\right]}{R\left\{8 - \frac{2\pi}{3}\left(-4\alpha^3 + 9\alpha^2 - 3\right)\right\}}\right] = \beta.\gamma} \qquad \textit{Equation 28}$$

The effusion rate is shown in *Figure 77* as a function of density. After a small increase for a density close to the minimum over the range considered (1.28 g/cm^3 to 2.18 g/cm^3), it decreases continuously as the density increases, up to zero where the density corresponds to closing the paths between microscopic volumes (that is, $A_{ap} = 0$).

As for the diffusion rate, the conclusion is that the use of low density material favors the effusion rate.

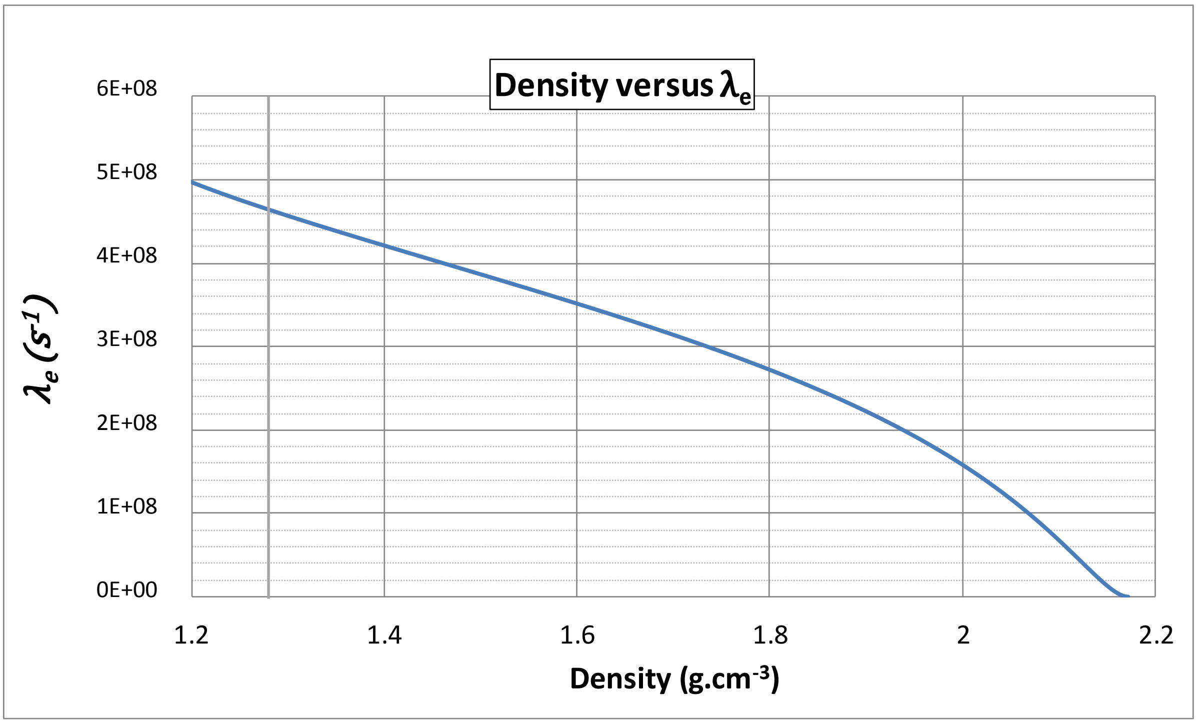

Figure 77 : Evolution of effusion rate λ_e versus density.

How to determine the diffusion coefficient?

We know that the diffusion coefficient varies for different materials and temperatures. We extract from literature (G.J. Beyer [7]) the diffusion coefficients of different metallic materials. Values range from 10^{-13} to 10^{-5} cm^2.s^{-1} and we assume that the atom diffusion coefficient in the graphite grains is within this range.

In the framework of C. Eléon's PhD work [8], the release of ^{35}Ar atoms from graphite material was considered. Effusion and diffusion processes matter were not separated, and a global release coefficient was obtained experimentally. Whatever the atom release description, using non-separated processes or separated as in the present approach, the total release efficiencies must be the same:

$$\varepsilon_{global}\Big|_{C.Eléon} = \varepsilon_{Diffusion}.\,\varepsilon_{Effusion}\Big|_{present\ work}$$

The effusion coefficient can be estimated from the geometry of the graphite structure, as shown before. To determine the diffusion coefficient, its value has been adjusted up to make the right term fulfil the experimental efficiency of reference [8] (0.98 for ^{35}Ar diffusing in 3 mm thick foils composed of 1 µm graphite grains). The corresponding diffusion coefficient has been found to be 4.0 x10^{-9} cm^2.s^{-1}. It was then used to calculate mean release times and the release efficiencies as presented in Figure 80, Figure *81* and Figure *82*. Going from 0.5 µm to 8 µm radii, the experimental release efficiency dropped from 0.98 to 0.22 (yellow dots in Figure 81). This efficiency is lower than the one predicted with our description, which gives a result equal to 0.5. The assumption made in our calculation, where we consider completely open porosity, can partly explain the overestimation in release efficiency.

Relation between density and porosity

Porosity is defined to be the ratio of the volume of the voids, or pore space, divided by the total volume of the matter.

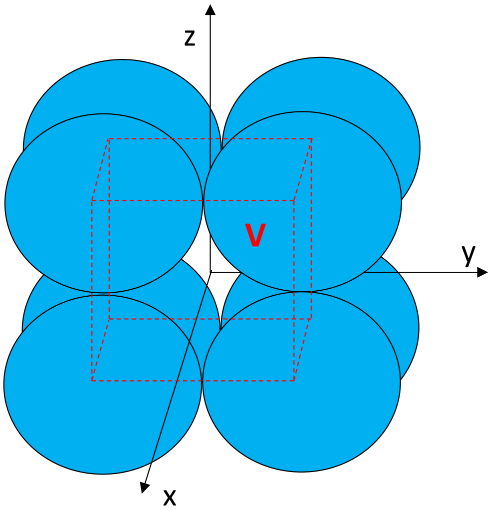

Figure 78: Representation of the elementary cube.

The porosity for an elementary volume, as represented in Figure 78, is the volume of one sphere minus the volume of six overlapping caps divided by the volume of the cube.

$$porosity\ (\%) = 100 - 100 * \left(\frac{V_m}{V_c}\right)$$

"V_m" is the volume occupied by the sphere, and is written:

$$V_m = \frac{4\pi R_s^3}{3} - 6 * \left[\frac{\pi h^2}{3}(3R_s - h)\right] = \frac{2\pi R^3}{3}[-4\alpha^3 + 9\alpha^2 - 3]$$

"V_c" is the total volume of the cube:

$$V_c = 8R^3$$

Hence, the porosity is written:

$$porosity\ (\%) = 100 - 100 * \left(\frac{\pi}{12}[-4\alpha^3 + 9\alpha^2 - 3]\right)$$

"α" is a geometrical parameter related to the grain density and size. The variation of the porosity as a function of the density is shown in Figure 79.

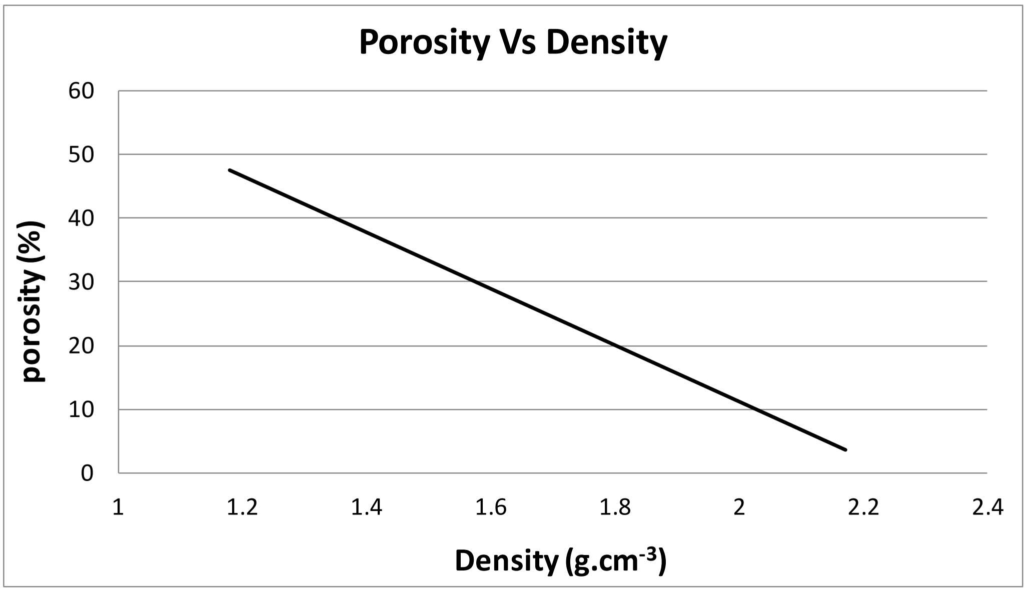

Figure 79: The porosity as a function of density.

Calculation of the optimum grain size

The optimum grain size is defined by the size corresponding to the minimum value of the mean release time. The mean release time is necessarily limited by the half-life of the isotope considered, but the minimum mean release time depends only on a balance between the diffusion and effusion processes. Figure 80 shows the optimum grain size of a material in which ^{35}Ar isotopes diffuse and effuse. The mean release time has been calculated for the same work conditions as in a previous PhD thesis [8]. The grain size was 1 µm, the density 1.8 g/cm^3 and the temperature was 2100 K. As shown in the previous paragraphs, these three parameters were sufficient to calculate the effusion coefficient used in the expression of the mean release time.

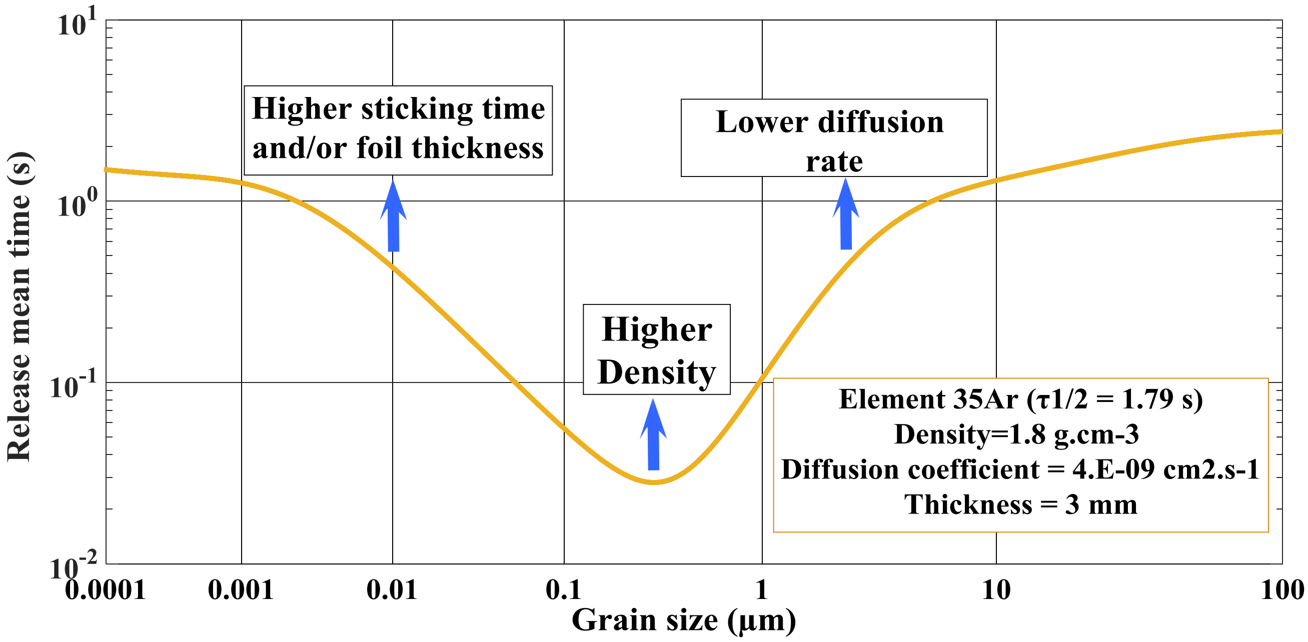

Figure 80 : The influence of grain size on the mean release time of target.

For large grains, the diffusion process dominates and release times increase. For small grains, the diffusion process becomes negligible compared to the effusion process.

According to our calculation, the mean release time drops to approximately 25 ms for an optimum grain radius of 0.3 µm.

Describing matter this way shows that an optimum grain size exists for each radioactive element and is not simply the smallest. Seeking target materials made of systematically smaller grain size does not appear to be justified if the decrease is made at constant density.

Effect of grain radius and density on release efficiencies

The efficiency of the release out of the target materials results from both the diffusion of the atoms out of the grains and the effusion through the inter-grain volumes. As the processes are considered consecutive, the release efficiency can be calculated by the multiplication of the diffusion efficiency ε_{diff} by the effusion efficiency ε_{eff}.

$$\boldsymbol{\varepsilon = \varepsilon_{diff} \times \varepsilon_{eff}} \qquad \text{Equation 29}$$

According to Fujioka, for a spherical grain, the diffusion efficiency is written:

$$\boldsymbol{\varepsilon_{diff} = 3\frac{\sqrt{\frac{\lambda}{\lambda_D}}.coth\sqrt{\frac{\lambda}{\lambda_D}}-1}{\frac{\lambda}{\lambda_D}}} \qquad \text{Equation 30}$$

And the effusion efficiency out of a foil is written:

$$\boldsymbol{\varepsilon_{eff} = 2\sqrt{\frac{\lambda_E}{\lambda}}.tanh\left[\frac{1}{2}\sqrt{\frac{\lambda}{\lambda_E}}\right]} \qquad \text{Equation 31}$$

In Figure 81 the release efficiency of the target is shown as a function of grain size, R.

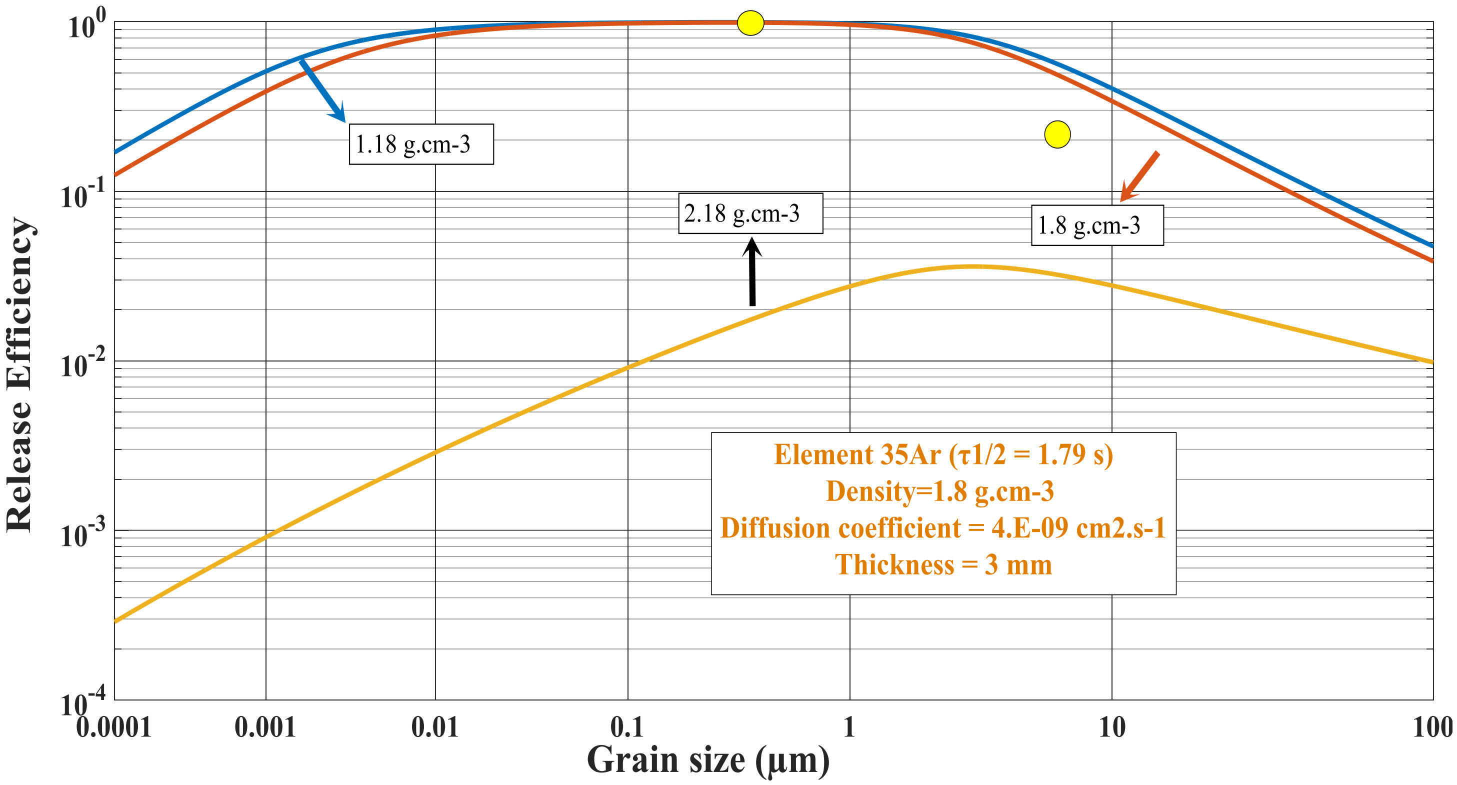

Figure 81 : The release efficiency versus grain size for three different densities. Values shown as yellow dots are experimental results.

A density of 1.18 g/cm^3 implies no overlap between grains. A density of 1.8 g/cm^3 corresponds to a material previously tested and assumes overlapping grains. A density of 2.18 g/cm^3 is a value close to the maximum.

For grain sizes ranging from 50 nm to 1 µm and a density of 1.18 g/cm^3, the release efficiency is close to 100%. In this range, the efficiency difference between 1.8 g/cm^3 and 1.18 g/cm^3 densities is not significant. So, there would be no point in looking for too low density materials, which are often more difficult to synthesis and which lead to larger target volumes. The energy deposited by the primary beam is also more difficult to evacuate in this case.

As shown in Figure 81, decreasing the density from 2.18 g/cm^3 to 1.18 g/cm^3 leads to a two orders of magnitude increase in release efficiency for 1 µm grains. The effect of the density is more important on the effusion process than that of diffusion, as the difference in efficiency is more important for small grain regions, where effusion dominates the release time.

Figure 82 shows the release efficiency as a function of grain size for different half-lives, assuming a non-sticking element of mass 40 and a material temperature of 1800 °C. For the optimum grain size (approx. 0.3 µm) and for a half-life of 10 ms, the release efficiency is close to 50%.

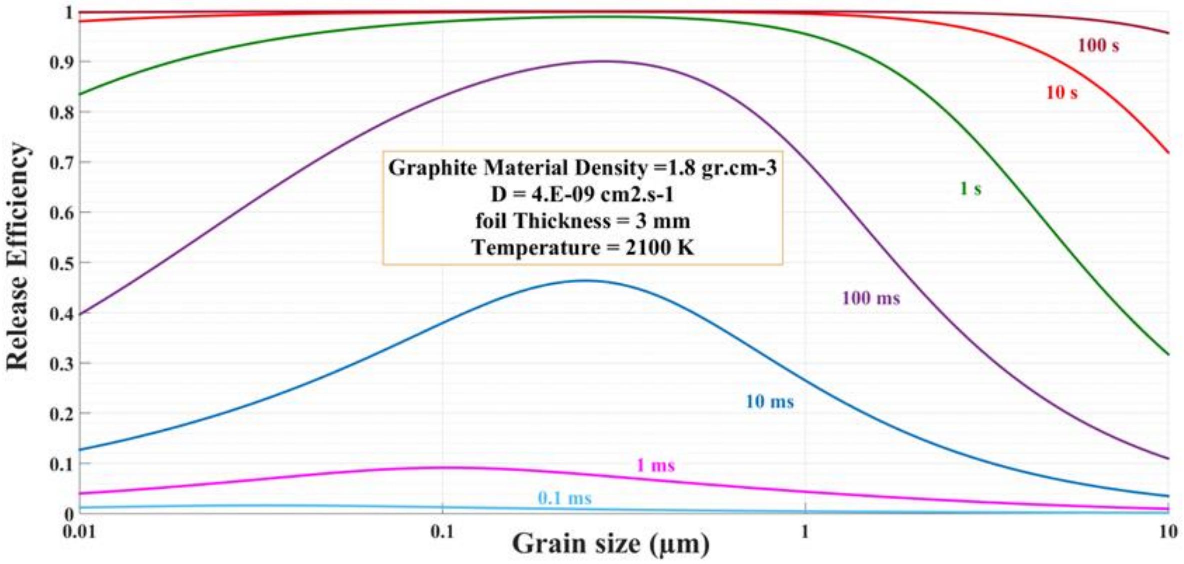

Figure 82: The release efficiency as a function of grain size for different half-lives, assuming a non-sticking element of mass 40 and a material temperature of 1800 °C.

Conclusions

One conclusion from this study is that it is important to develop target structures made of very small parts of matter, separated by sufficiently large and open spaces which, in principle, corresponds to a large open porosity.

Using large open porosity target materials has consequences on other target features. The ability to evacuate the primary beam power is reduced and makes the target more liable to local over-heating. Decreasing the number of target nuclei per unit surface will also lead to lower interaction rates. Maintaining constant in-target production rates would then require thicker targets, leading to longer atomic release times. These aspects have not been considered here.

The study shows that the optimum grain size depends on the half-life of the radioactive element, and that the optimum grain size is not the smallest one. For ^{35}Ar, the optimum size seems to be of the order of 0.3 µm at 2100 K. Our description seems to reproduce previous observations but this agreement must be confirmed, or the description improved, by additional comparison to experimental results.

This approach has the advantage of describing release rates without adjustable parameters. It is thus easy to apply to any other micro-structured ISOL target material. Substituting in equation 5 the expression of the flux released by grains with the expression of the flux released by fibers is possible and simple.

Sticking time issues and the propagation mechanism of atoms within matter have not been treated in this study. They will have to be in future, to extend the application of this approach to a wider range of atoms.

"The smaller the target density, the shorter the release time from the target". This widely spread statement is inexact as it only considers the optimization of the release and not the first requirement of ISOL targets, which is to produce a maximum in-target rate of radioactive atoms. Minimizing the density to optimize the release from the target material has been considered for many years in ISOL target material design. However, its consequence on the macroscopic target geometry must also be taken into account if one wants to optimize the whole atom-to-ion transformation efficiency. To conserve the same in-target production rates, the number of target atoms along the path of the impinging ions must also be conserved. The target must be lengthened if lower density materials are used. The total volume of the target will then be greater and will increase the radioactive atom release times. The effect of grain size is opposite on diffusion and effusion processes, and so the density of the target material has to be adjusted to simultaneously optimize these processes.

All processes involved in the atom-to-ion transformation are related; none of them can be optimized independently. A global optimization is not presented in this study, but is essential in the design of TISS aiming to produce short lived-elements. Release times from target material is presented here, and is generally identified as being one of the most important processes influencing the atom-to-ion transformation efficiency.

Appendix 3.1

Properties of materials used to develop the TISS.

This appendix presents some materials chosen for the cavity walls, the catcher and, the target. The properties of some materials intended for use in the development of the target ion source system (TISS) are studied. Two different types of graphite were used. The catcher, used to stop the fusion-evaporation residual ions, is a thin layer of graphite paper, with the commercial name "PAPYEX". The second is used to build the container. Nickel is used as the target material for ^{74}Rb production.

Materials used to develop the TISS.

- Rigid graphite: Toyo Tanso [95], IG-19 type.
- Graphite paper: Mersen [118] , PAPYEX type, thickness of the foil : 0.2 mm.
- ^{58}Ni foils: Good fellow (USA), thickness: 3 µm.

Some material properties are presented in the following paragraphs.

Common requirements were:

- A fusion temperature above 1600°C
- High thermal emissivity to efficiently evacuate heat from the cavity
- A work function higher than the first ionization potential of Rb, to maximize the ionization probability per contact
- Suitable mechanical features allowing for machining and mounting
- High electrical resistance of the cavity body to maximize the potential difference between the cavity extremities. The desired electric field was 1 V/cm, over 5 cm in length. The maximum current available is 300 A. The minimum value of the global cavity resistance is then 17 mΩ.
- Thin materials to increase the electrical resistance

Ni target

A 3 µm thick ^{58}Ni target was chosen to optimize production yields of the desired ^{74}Rb radioactive nuclei. The detailed properties of Nickel are presented in Table 9. This material is a relatively good conductor compared to graphite. As Nickel and Papyex foils are electrically connected in parallel, the potential between the extremities of the cavity is determined by the parts having the lowest resistance. Since the thickness of the Ni foil is 3µm, its resistance is significantly higher than the resistance of the graphite components, despite a lower resistivity. The cavity potential is therefore mainly dictated by the graphite parts.

Properties at ambient temperature	Nickel foil
The thickness of the foil	3 µm
Melting point	1455 °C
Work function	5- 5.35 eV
Density	8.9 g/cm^3
Thermal expansion coefficient	13x10^{-6} K^{-1}
Thermal Conductivity	80.4 W.m^{-1}.C^{-1}
Electrical Resistivity	59 µΩ.cm [119]
Emissivity	0.3

Table 9: Some properties of the nickel foil target.

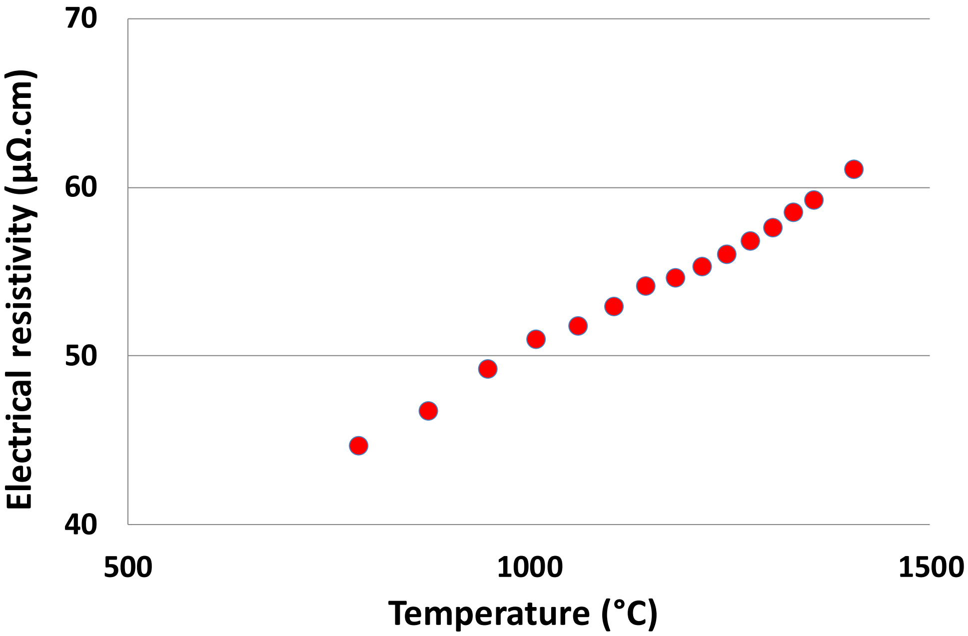

Figure 83: The measured electrical resistivity of nickel as a function of temperature.

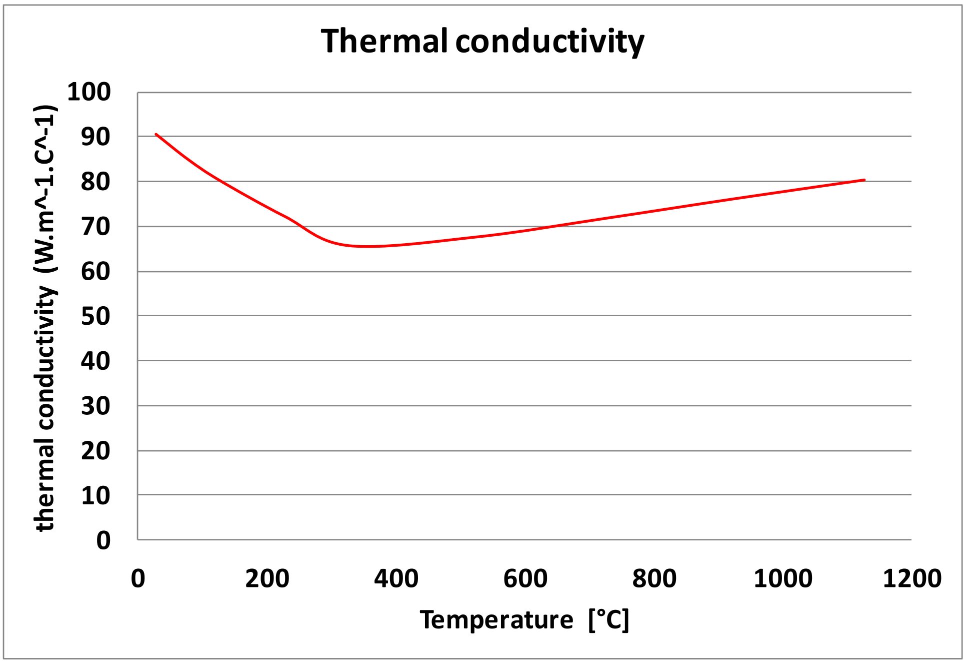

Figure 84: The thermal conductivity of nickel as a function of temperature.

The catcher

The catcher must release of radioactive isotopes quickly and efficiently. As discussed in chapter 2 and appendix 2.3, low density materials favor the release when associated with non-negligible open porosity. The minimum thickness of a catcher made of Papyex must be around 13 µm to stop the ^{74}Rb recoils (see appendix 2.2). A minimum thickness of 25 µm was chosen to favor the release of the ^{74}Rb towards the target cavity. Given the minimum commercially available thickness was 200 µm, this thickness was used and the other parts of the TISS have been designed to cope with this constraint.

Properties at ambient temperature	Toyo Tanso IG-19 [95]	PAPYEX [13] in-plane direction
The thickness of the foil (mm)	3	0.2
Density (g/cm^3)	1.75	1
Coefficient of thermal expansion (K^{-1})	4.6×10^{-6}	25×10^{-6}
Electrical resistivity (µΩ.cm)	1700	1070
Emissivity	0.8	0.45
Thermal Conductivity W/(m.K)	80	60

Table 10: Properties of Papyex graphite and comparison with the properties of isotropic solid graphite.

The container

The container defines the volume in which atoms effuse. It is made of the Ni target on one side, placed parallel to the graphite catcher on the other side, separated by a distance of 12 mm. A circular wall allows to fix the target and the catcher in position.

The container is made of Toyo Tanso graphite (IG-19 type). Its characteristics are compared to that of POCO graphite (ZXF 5Q type). The Toyo Tanso material was chosen mainly due to its higher thermal conductivity, but also a better commercial offer for machining.

Properties at ambient temperature	Toyo Tansu IG-19 [95]	ZXF 5Q POCO
Density (g/cm^3)	1.75	1.78
Coefficient of thermal expansion (K^{-1})	4.6×10^{-6}	2.9×10^{-8}
Electrical resistivity (µΩ.cm)	1700	1950
Thermal Conductivity W/(m.K)	80	70

Table 11: Properties at room temperature of Toyo-Tanso IG 19 and POCO ZXF 5Q graphites.

The work function of graphite is 4.5 eV, which is high enough to give an ionization probability per contact close to 100% for rubidium isotopes.

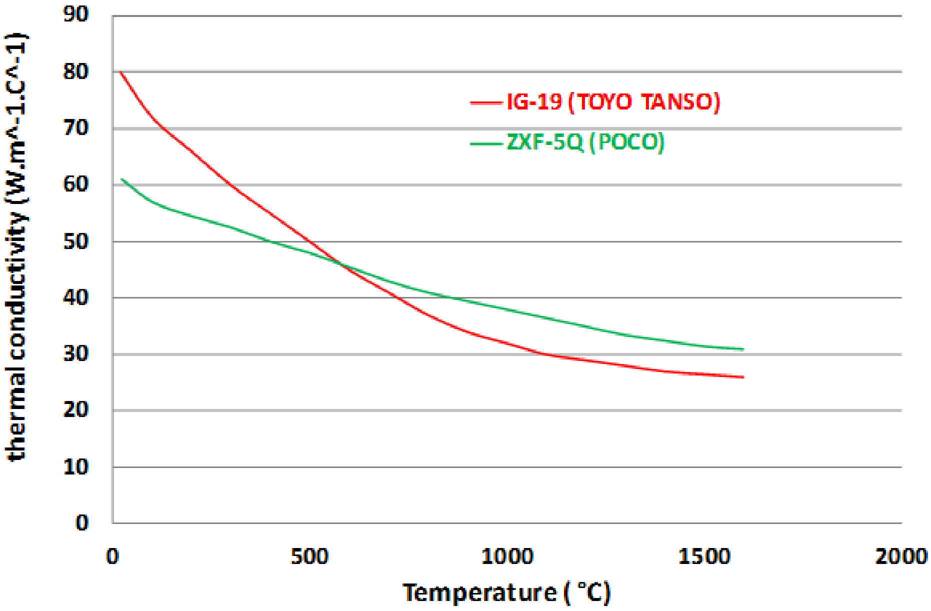

Figure 85: Thermal conductivities of two different types of graphite often used at GANIL for TISS construction as a function of temperature.

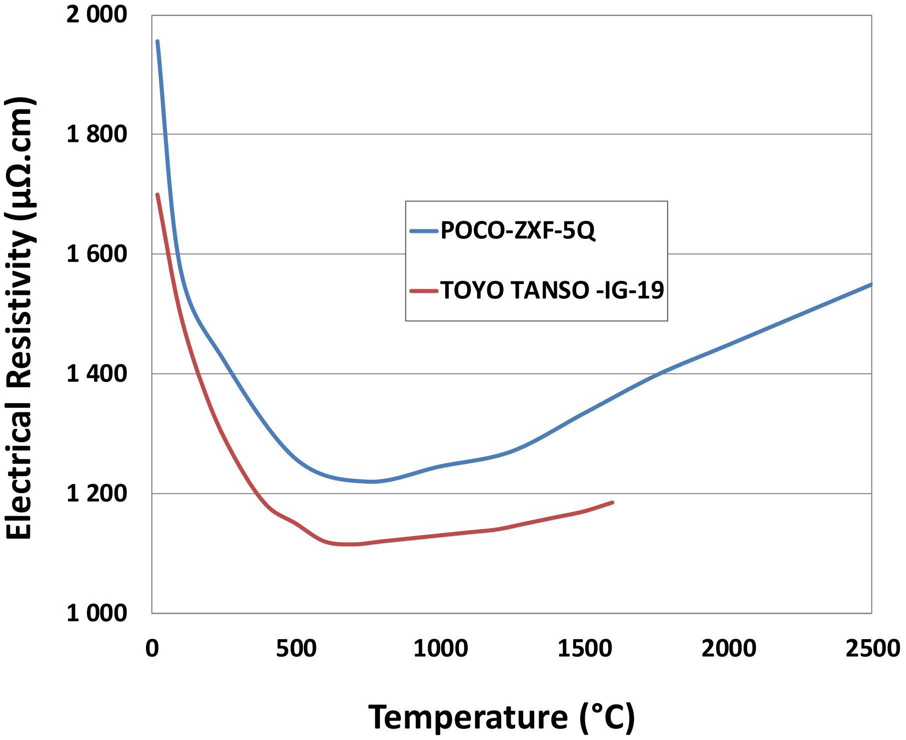

Figure 86: Electrical resistivity of Poco-ZXF-5Q and Toyo Tanso-IG-19 graphite types as a function of temperature.

Characteristics presented here led to choosing thicknesses of 0.2 mm for the catcher and 0.8 mm for the cavity. These thicknesses are the lowest limit acceptable by experts as regards the machining process and the mechanical risks during mounting.

Appendix 3.2

Characterization of resistivity and emissivity of materials

Introduction

Radioactive ion beam production using the Isotope Separator on Line method (ISOL) involves the bombarding of solid target material by intense beams of stable nuclei. Radioactive nuclei produced during the collisions are stopped within the target material, then diffuse and effuse out of the target. Generally, the target is operated at high temperatures to accelerate diffusion and effusion processes, leading to faster extraction times. The target must therefore be able to sustain the working temperature.

The target dissipates heat by thermal conduction through the contact with colder parts of the chamber, and by radiation. Thermal radiation becomes important in the heat transfer mechanisms at high temperature. Temperature and emissivity are key parameters which determine the amount of radiation power emitted by the material. The emissivity depends on the material, its temperature, the characteristic wavelength emission and its surface structure. Metals with clean smooth surfaces have lower emissivity than metals with a roughened surface.

A comprehensive understanding of thermal and physical-chemistry properties materials employed is important if heat transfer, thermal and electrical calculations are to be accurate. Quite often little data is available in the literature, or when some is found, values have been obtained in experimental conditions too far from the present case for comparisons to be valid. Data are essential for TISS designing since ISOL systems generally operate at high temperatures. A systematic study of material resistivity and emissivity was carried for the present TISS materials.

The most widely applied method for temperature measurements make use of physical probes, such as thermocouples. One disadvantage is the intrusive nature of the probe. Thermocouples provide only single point measurements and are difficult to use for measuring temperature distributions. Several non-intrusive techniques have been developed to measure the radiation emission namely, the infrared monochromatic and multi-wavelength pyrometer [1]–[9].

In this work, a multi-wavelength pyrometer was used to measure temperatures ranging from 750°C to more than 2000°C. Several commonly used refractory materials were studied (Ni, W, Ta, Mo, Nb, V, Hf, Ti, Pt, Co, Fe and stainless steel). All the foils were supplied by Goodfellow [10].

The bi-chromatic pyrometer principle

The multi-wavelength pyrometer provided results based on the relation between the wavelength distribution radiated by a hot body and its temperature. Two wavelengths are selected, and their intensities compared. According to the known change in intensity ratio for different temperatures, the temperature is deduced from the measured intensity ratio. Compared to the monochromatic pyrometer, which requires an absolute intensity measurement, the multi-wavelength pyrometer is therefore more easy to use since only ratios are required. If a screen is placed between the hot body and the pyrometer, and if we suppose that all wavelengths are equally attenuated, then the temperature measurement is unaffected.

A drawback of the bi-chromatic pyrometer is related to the wavelength distribution of the material studied, which can be slightly different from the one taken as reference by the pyrometer (a Planck function, see below). This difference can introduce an error in the measurement. It would be interesting to compare measurements from the bi-chromatic pyrometer with those given by a thermocouple.

Theoretical background

All bodies at temperatures above absolute zero are sources of thermal radiation. The radiated intensity increases as the body temperature increases. The black body intensity spectrum $I_b\ (T, \lambda)$ at wavelength λ and at temperature T is determined by the Planck function [11]:

$$\boldsymbol{I_b\ (T, \lambda) = \frac{2.h.c^2}{\lambda^5.\left[exp\left(\frac{hc}{\lambda kT}\right) - 1\right]}} \qquad \textbf{Equation 32}$$

Where h and k are the Plank and Boltzmann constants respectively, and c the speed of light.

Note: The two wavelengths considered in this study are 0.75 to 1.1 µm over a temperature range 750 °C to more than 2200 °C.

When $\exp\left(\frac{hc}{\lambda kT}\right) \gg 1$, the Plank formula can be simplified to:

$$\boldsymbol{I_b(T, \lambda) = \frac{2.h.c^2}{\lambda^5}\ .exp\left(-\left(\frac{hc}{\lambda kT}\right)\right)} \qquad \textbf{Equation 33}$$

For real surfaces, the radiation intensity $I_r(T, \lambda)$ emitted at the surface at temperature T is always lower than the intensity $I_b(T, \lambda)$ emitted by a perfect black body. The ratio of the two intensities is called the monochromatic emissivity

$$\boldsymbol{\varepsilon(T, \lambda) = \frac{I_r(T,\lambda)}{I_b(T,\lambda)}} \qquad \textbf{Equation 34}$$

The radiation intensity $I_r(T, \lambda)$ emitted at wavelength λ at temperature T in direction θ is:

$$\boldsymbol{I_r(T, \lambda) = \ \varepsilon(T, \lambda, \theta).I_b(T, \lambda)} \qquad \textbf{Equation 35}$$

To eliminate inaccuracies affecting absolute radiation intensity measurements, it is possible to measure the ratio of intensities emitted at two wavelengths λ_1 and λ_2 (0.75 to 1.1 µm in the present study). The ratio of the intensities is then written:

$$\boldsymbol{\frac{I_{\lambda_1,r}}{I_{\lambda_2,r}} = \frac{\varepsilon(\lambda_1,\theta)}{\varepsilon(\lambda_2,\theta)} \cdot \frac{I_{\lambda_1,b}}{I_{\lambda_2,b}}} \qquad \textbf{Equation 36}$$

Rearranging Equations 2 and 5, the temperature for a given emissivity ratio and wavelength is then:

$$T = \frac{\frac{hc}{k} \cdot \left(\frac{\lambda_1 - \lambda_2}{\lambda_1 . \lambda_2}\right)}{ln\left(\frac{I_{\lambda_1,r}}{I_{\lambda_2,r}}\right) + ln\left(\frac{\varepsilon\,(\lambda_{2,\theta})}{\varepsilon\,(\lambda_{1,\theta})}\right) + ln\left(\frac{\lambda_1^5}{\lambda_2^5}\right)} \qquad \textbf{Equation 37}$$

Equation 6 describes the relation used in the bi-chromatic pyrometer to determine the temperature of a real emitting surface. If the emissivity depends on the wavelength, the emissivity difference must be known and this ratio must be included in the measurement procedure.

Temperature measurement process

Once the temperature and electrical resistivity measured using the bi-chromatic pyrometer, the emissivity is determined by adjusting the instrument emissivity values until it matches the measured electrical resistivity for this temperature. As a cross-check of the measured temperature in bi-chromatic mode, the disappearing filament pyrometer is used to establish an absolute scale, in the same experimental conditions.

Experimental set-up

An experimental set-up was developed and built at GANIL during this PhD study. The principle is presented in *Figure 87*. The goal was to simultaneously measure the emissivity and resistivity of refractory materials and their variation with temperature, in the range 750 °C to 2200 °C. The experiment was repeated for several refractory materials.

The set-up is made of:

- A large cooled vacuum chamber (600 mm x 600 mm x 600 mm);
- A pumping system to maintain a pressure lower than 10^{-6} mbar;
- Vacuum gauges to control pressure levels;
- An upper flange supporting water cooled feedthroughs for high current and low voltage feedthroughs;
- Two clamps, separated by 100 mm and used to fix the strip of refractory material: each strip is 110 mm long and 10 mm wide. Clamps are cooled by water circulating in the feedthroughs.
- Two Ta wires inside the chamber are used to measure the voltage on the central part of the strip. The wires are connected on the strip at two points, separated by 30 mm.
- A window, allowing to observe the strip with the pyrometers.

Outside the chamber, there are:

- A power supply to heat the strip of material (I_{max} = 500 A and V_{max}= 30 V);
- A voltmeter to measure the voltage difference on the strip;
- Two pyrometers (one bi-chromatic and one using a hot filament);
- A computer to record the experimental parameters (temperature, emissivity ratio, and emissivity).

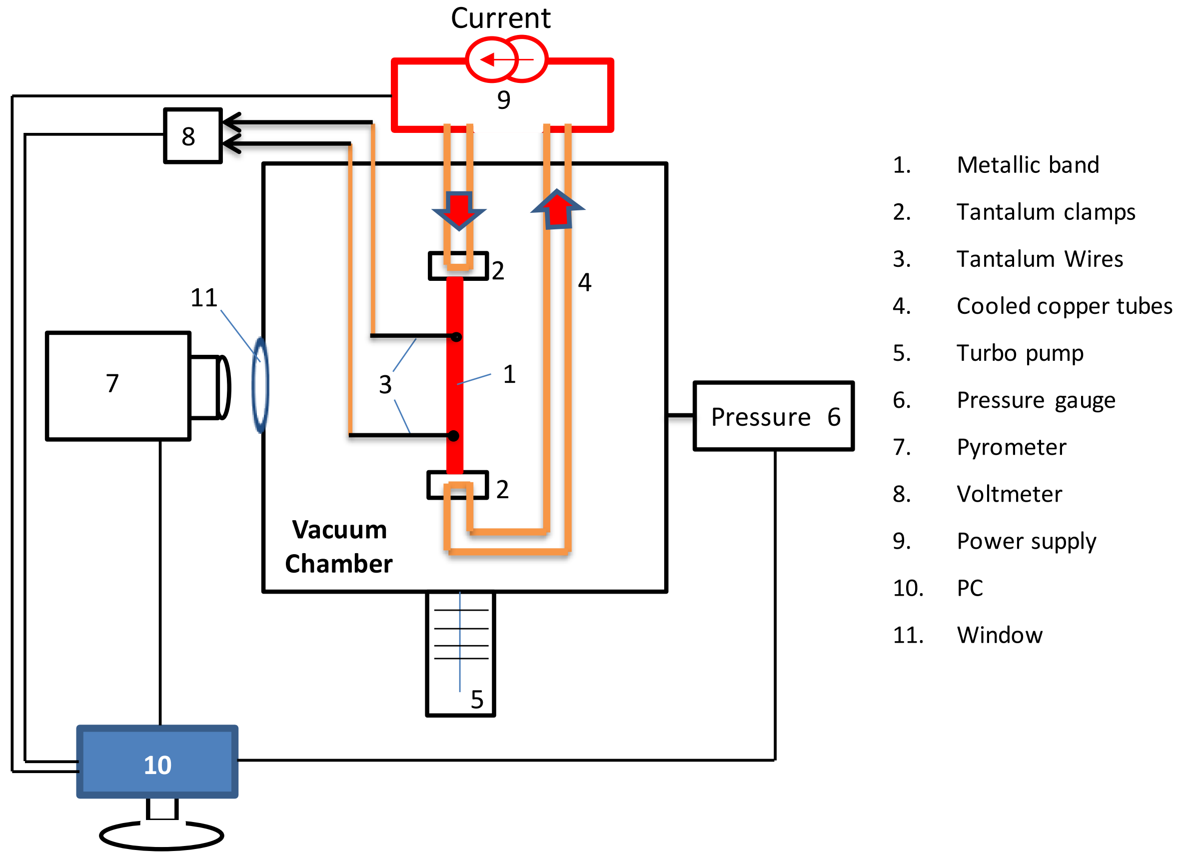

Figure 87: An overview of the experimental set-up.

Measurement procedure

The emissivity and temperature measurements were carried out by increasing the heating power in 10 W steps, starting from 0 W up to maximum of 1500 W, in this case, for each material sample in turn (Ni, PAPYEX, Ta, Mo, Nb, V, Ti, Co and Fe). The DC electrical current was kept constant for about 15 min at each step to allow the temperature to stabilize, and then steady state temperature measurements could be perfomed. The resistivity is deduced by measuring the voltage on the sample, using the two tantalum wires spaced by 3 cm in the center of the sample strip, and the current measured in an ammeter.

Window transmission measurement

Understanding losses induced by the media between the radiation source and the pyrometer is essential to correct, a posteriori and if necessary, the temperature measurement. Within the wavelength range considered (0.75 to 1.1 µm), the transmission in air is considered to be 100%. The window material transmission is proportional to its thickness and can vary with the wavelength. In order to minimize eventual temperature corrections, three windows were selected: sapphire (Al2O3), CaF2, BaF2, and zinc selenide (ZnSe), and the one with the lowest impact on transmission was chosen for the experiment. The transmission efficiency of each window, within the pyrometer wavelength range of 0.75 µm to 1.1 µm, is presented in *Figure 88*.

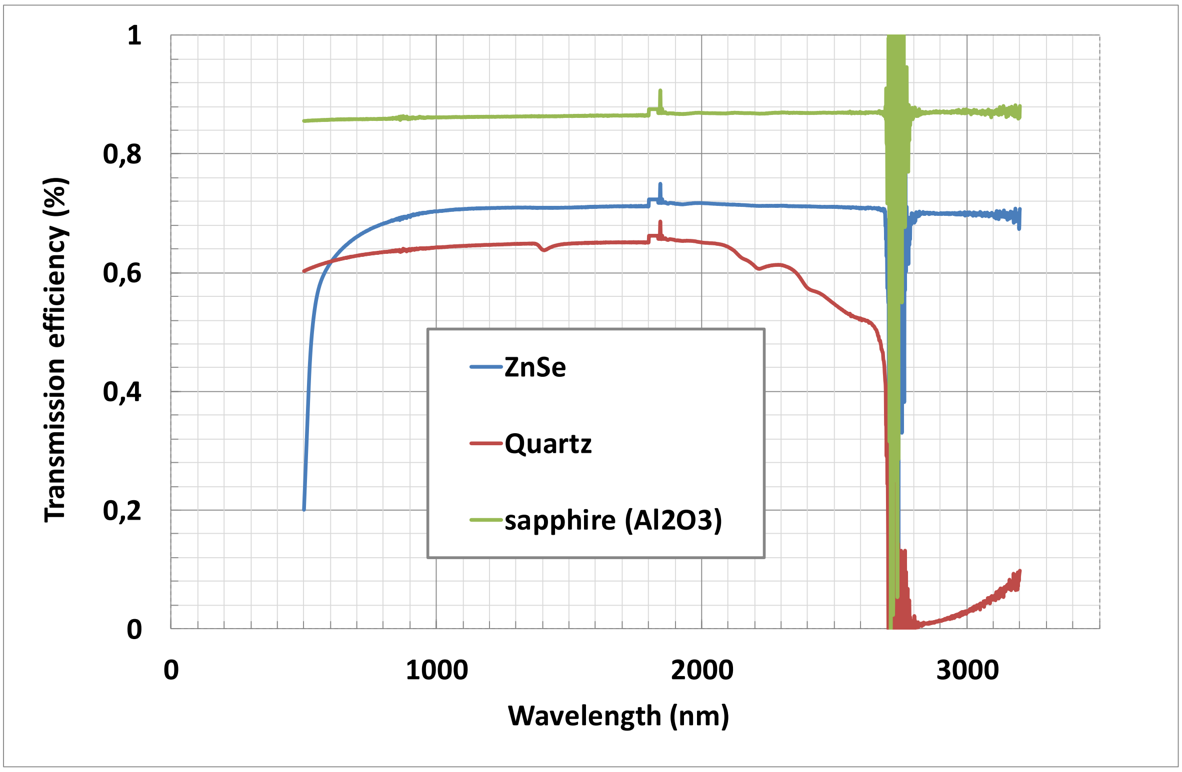

Figure 88: The transmission efficiency of selected windows as a function of wavelength.

The window transmission efficiencies were measured with a PerkinElmer apparatus LAMBDA 950 UV/V spectrophotometer [12]. From *Figure 88*, it can be seen that a sapphire (Al_2O_3) window gives the best transmission efficiency over the full pyrometer range.

Experimental Results

Results were obtained for the different samples (Ni, PAPYEX, Ta, Mo, Nb, V, Ti, Co and Fe), and compared to experimental values extracted from literature [13]–[15] [16]. They are summarized in the following.

Characteristics of the different materials tested, as provided by suppliers, are reported in Table 12. The roughness, which can play an important role on the emissivity, was measured at GANIL.

					Roughness Ra (µm)			
Material	**Thickness (mm)**	**Purity (%)**	**State**	**Weight (g)**	**Measure 1**	**Measure 2**	**Average value**	**Goodfellow ref.**
Stainless steel	0,1		Annealed	7,9	0,11	0,12	0,115	FE240265/4
Hafnium	0,14	97	Annealed	18,3	0,154	0,151	0,1525	HF000214/1
Platinum	0,0125	99,95	Rolled	2.68	0,55	0,53	0,54	PT000220/103
Iron	0,1	99,5	Dur	7,87	0,2	0,22	0,21	FE000320/21
Titane	0,1	99,6	Annealed	4.81	0,14	0,14	0,14	TI000370/12
Vanadium	0,04	99,8	Rolled	2.38	0,188	0,191	0,1895	V0003000/6
Niobium	0,1	99,9	Annealed	8,14	0,137	0,14	0,1385	NB000330/5
Molybdenum	0,1	99,9	Annealed	10,2	0,21	0,2	0,205	MO000310/38
Tantale	0,1	99,9	Annealed	16.6	0,132	0,125	0,1285	TA000410/51
Tungsten	0,1	99,95	Rolled	19,3	0,354	0,344	0,349	W000270/56
Cobalt	0,5	99,9	Annealed	45,2	0,208	0,213	0,2105	CO000282/3
Nickel	0,1	99	Annealed	8,9	0,192	0,195	0,1935	NI000480/24
Nickel	0.01	99,95	Electro-deposited	< 1	0,304	0,297	0,3005	NI000270/13

Table 12 : Characteristics of the materials tested and commercial references.

Uncertainty calculation in the measurement

The sample thicknesses were measured for each strip of material before placing it in the vacuum chamber. The thickness was measured at three different points and the mean value was used to calculate the relative uncertainty of the geometrical cross section. Measured values are presented in Table 13.

Material	Supplier's thickness (mm)	Measurements			Mean value (mm)	Relative error (%)
		Point1 (mm)	Point2 (mm)	Point3 (mm)		
Stainless steel	0.1	0.105	0.103	0.102	0.1033	1.2
Pt	0.0125	0.098	0.099	0.098	0.0983	0.48
Fe	0.1	0.103	0.099	0.098	0.1	2.1
Ti	0.1	0.104	0.103	0.102	0.103	0.8
V	0.04	0.039	0.04	0.039	0.0393	1.2
Nb	0.1	0.103	0.102	0.103	0.1027	0.46
Mo	0.1	0.101	0.103	0.102	0.1020	0.8
Ta	0.1	0.102	0.102	0.101	0.1017	0.46
W	0.1	0.099	0.099	0.1	0.0993	0.47
Co	0.5	0.5	0.499	0.499	0.4993	0.09
Ni	0.1	0.103	0.102	0.1	0.1017	1.22

Table 13: Relative error in the material thickness determination.

The total relative errors in the measurement of electric resistivity and emissivity are estimated to ±5%. An error in the measurement of the temperature must also be considered but, first of all, the whole measurement process has to be improved. The measurement of the temperature for one material depends on knowing its emissivity, and to know its emissivity we need to know its resistivity which, in turn, depends on the temperature. Since these parameters are inter-dependent, an absolute value must be determined to limit the effect of this inter-dependence on the precision of the different measurements. One starting point could consist of measuring the emissivity of each material in a black-body oven. The oven temperature could be determined using a, generally pre-calibrated, thermocouple. The differences between our measurements and values extracted from literature can be partly justified by these considerations.

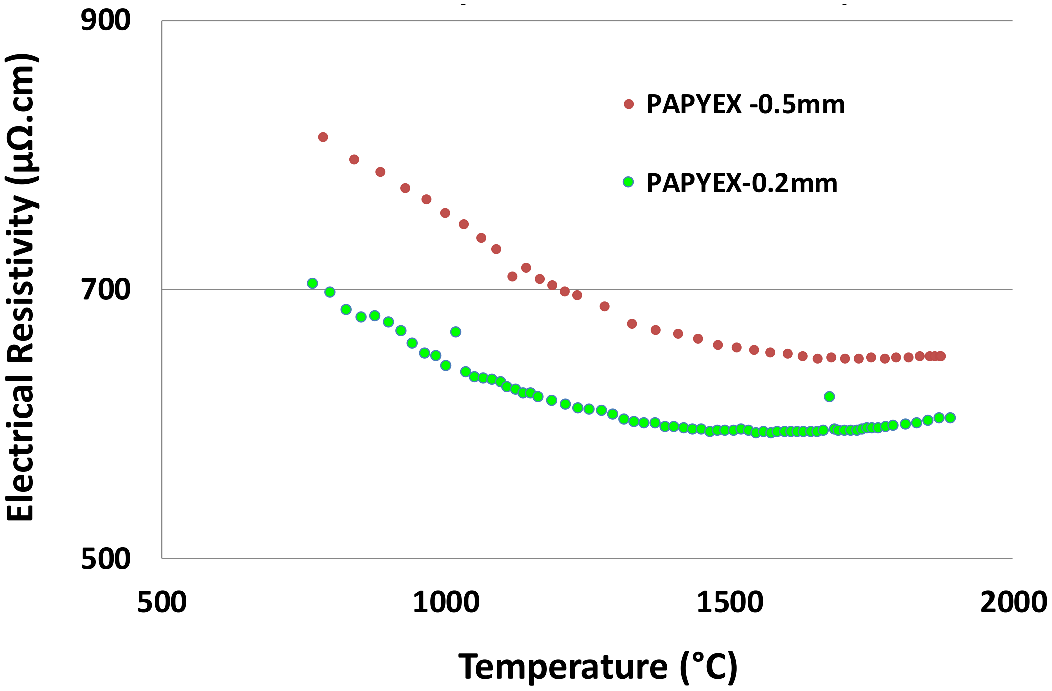

Figure 89: Electrical resistivity of PAPYEX as a function of temperature.

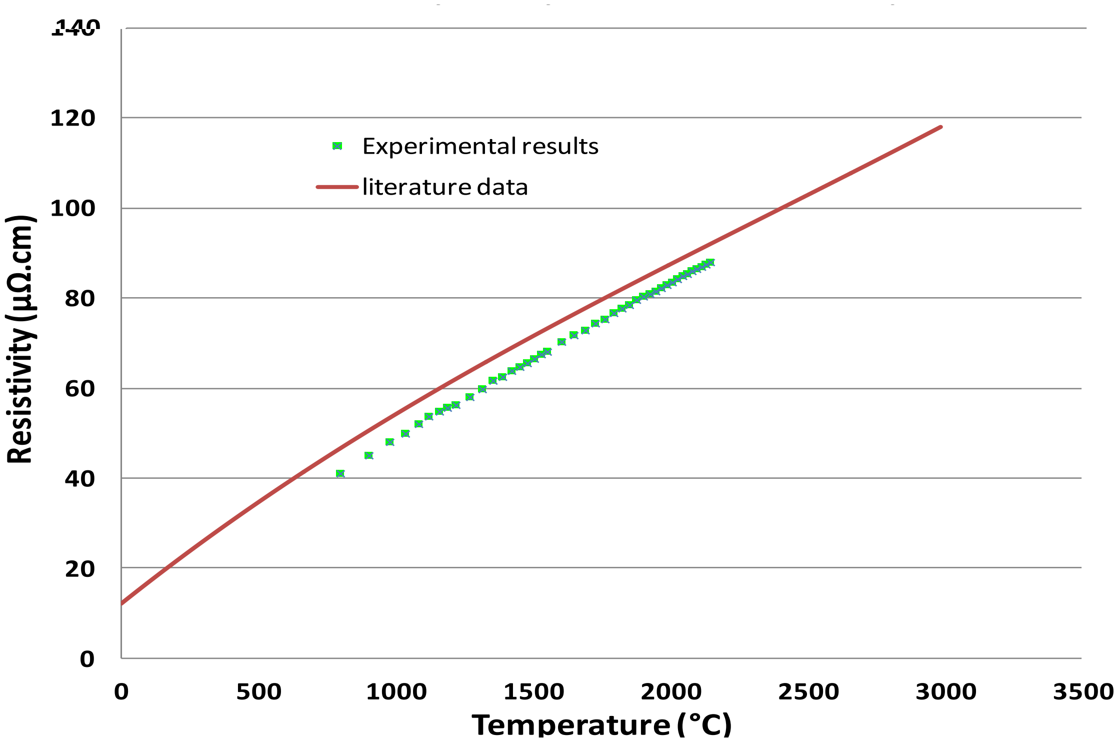

Figure 90: Electrical resistivity of Molybdenum as a function of temperature.

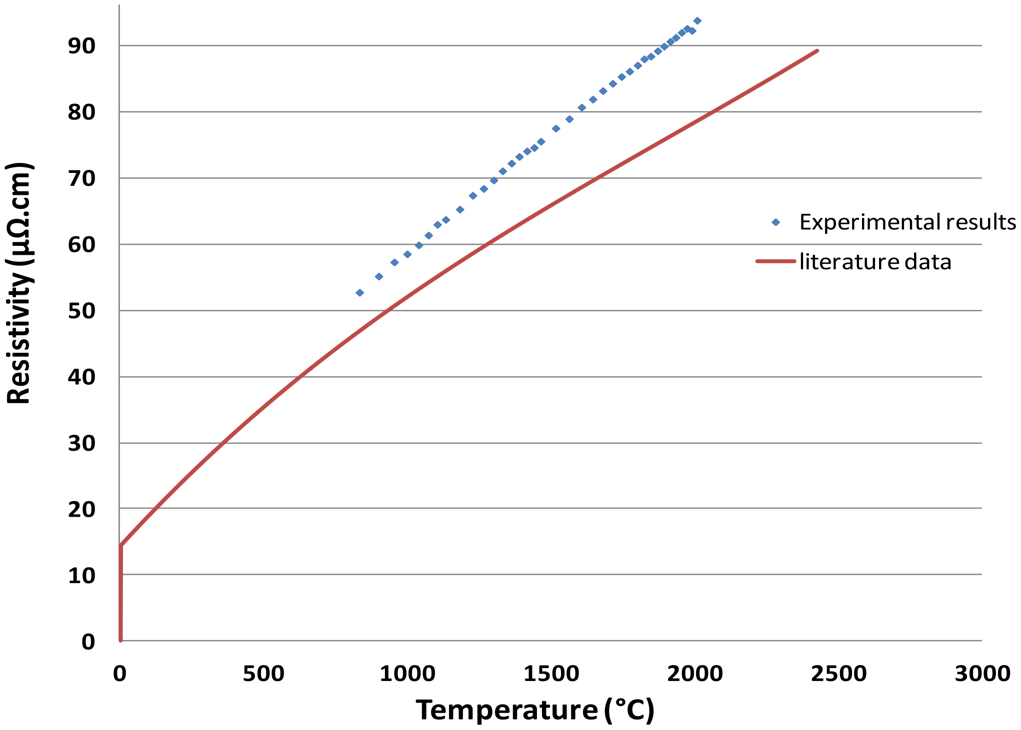

Figure 91: Comparison of Electrical resistivity of Niobium as a function of temperature

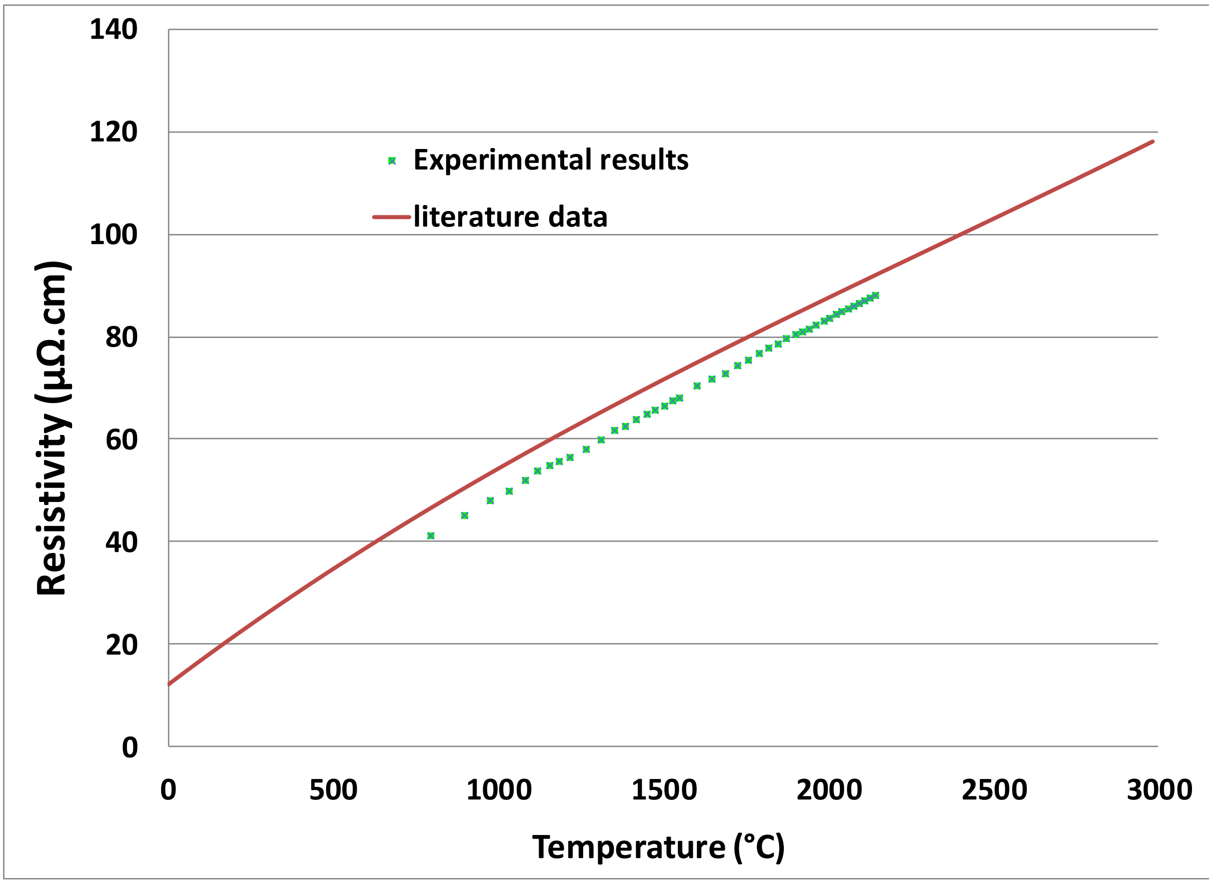

Figure 92: Comparison of Electrical resistivity of Tantalum as a function of temperature.

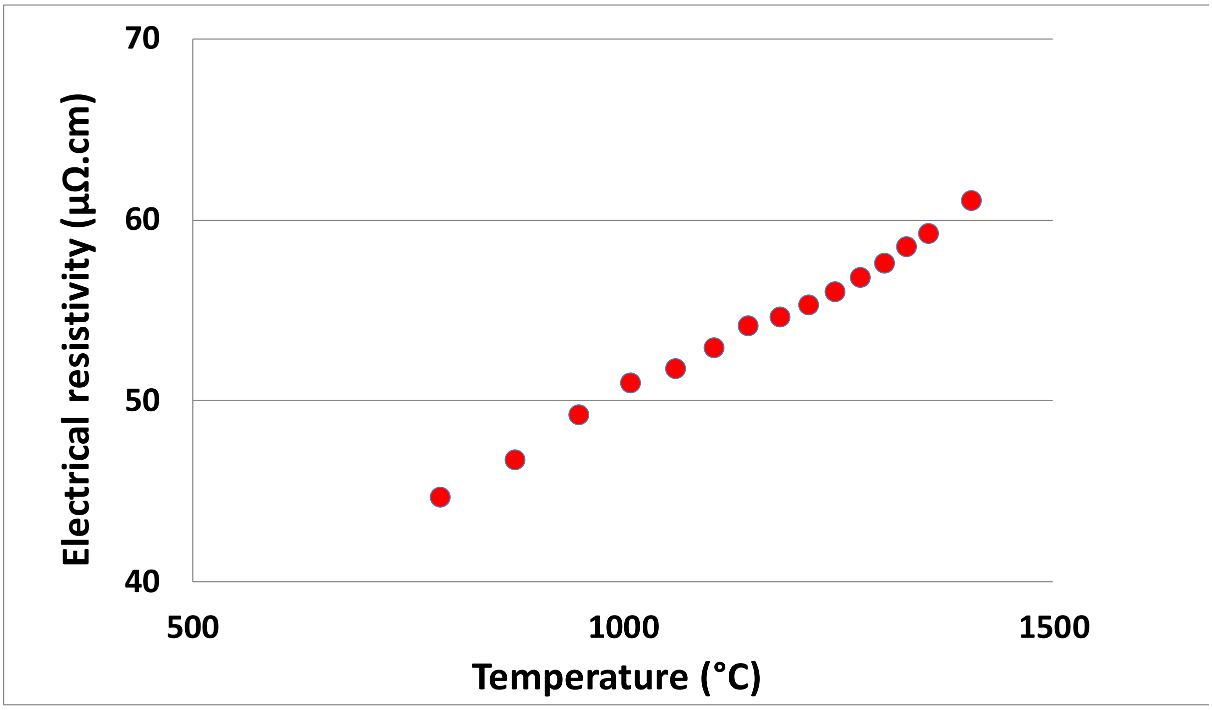

Figure 93: Comparison of Electrical resistivity of Nickel as a function of temperature.

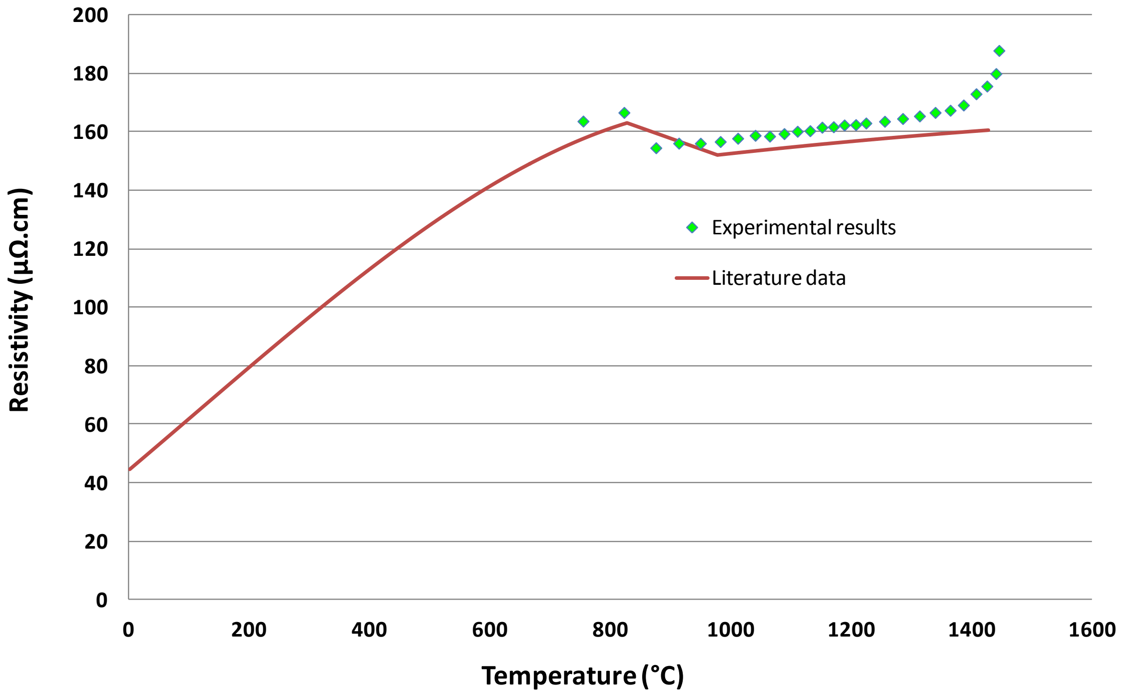

Figure 94: Electrical resistivity of Titanium as a function of temperature.

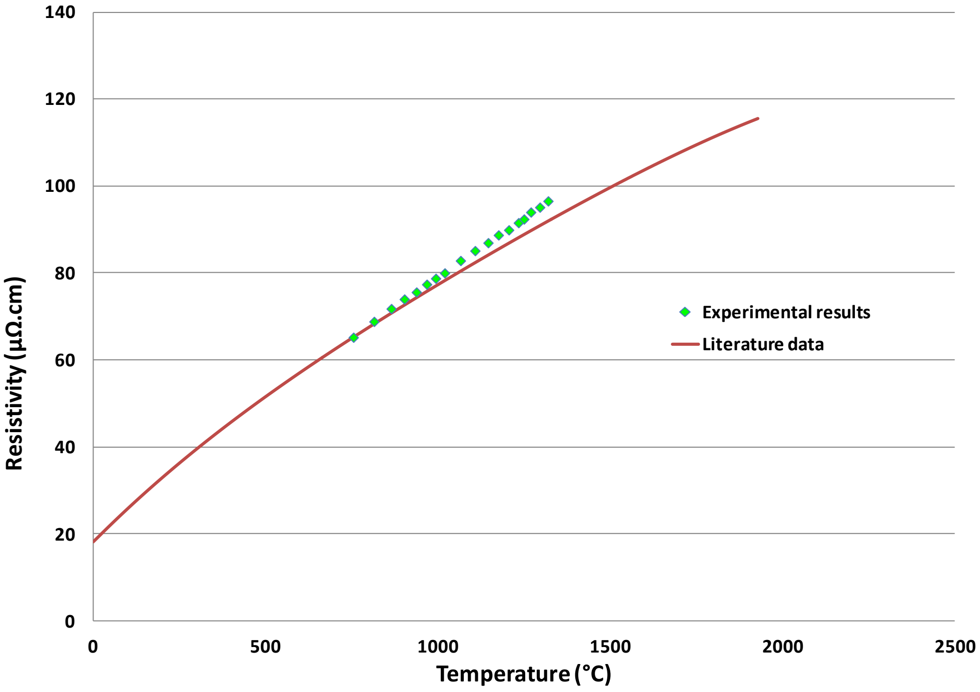

Figure 95: Electrical resistivity of Vanadium as a function of temperature.

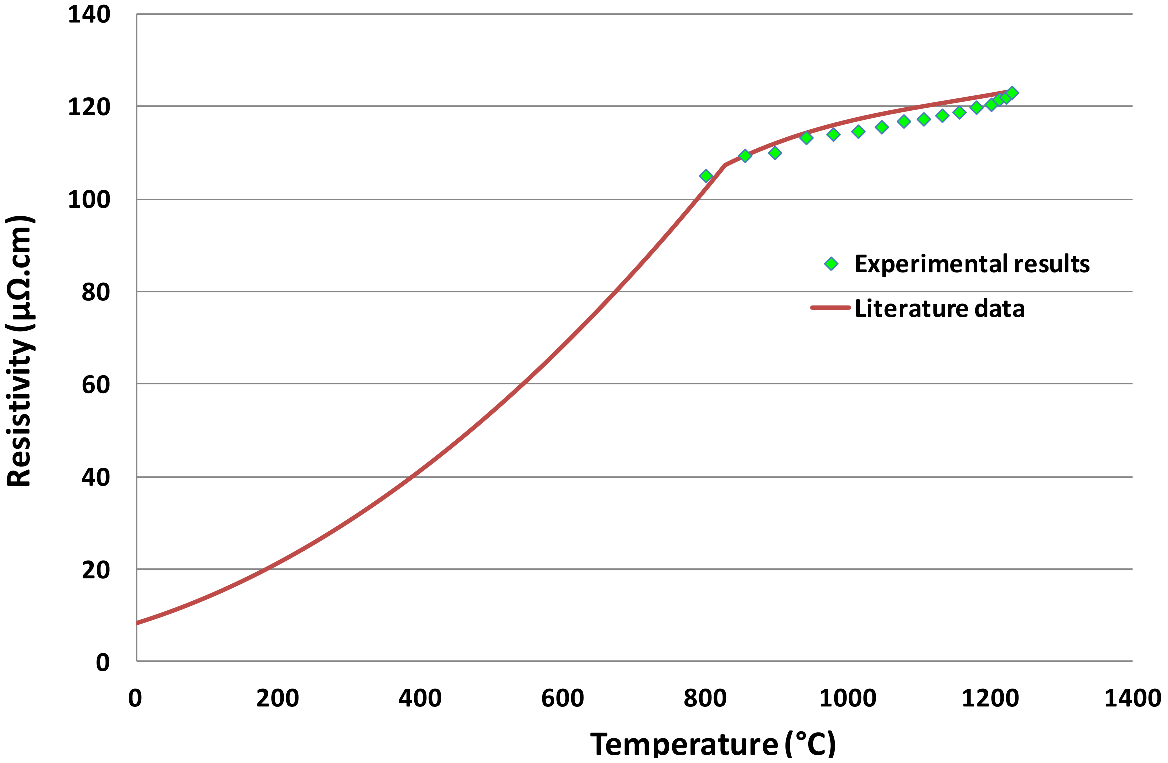

Figure 96: Comparison of Electrical resistivity of Iron as a function of temperature.

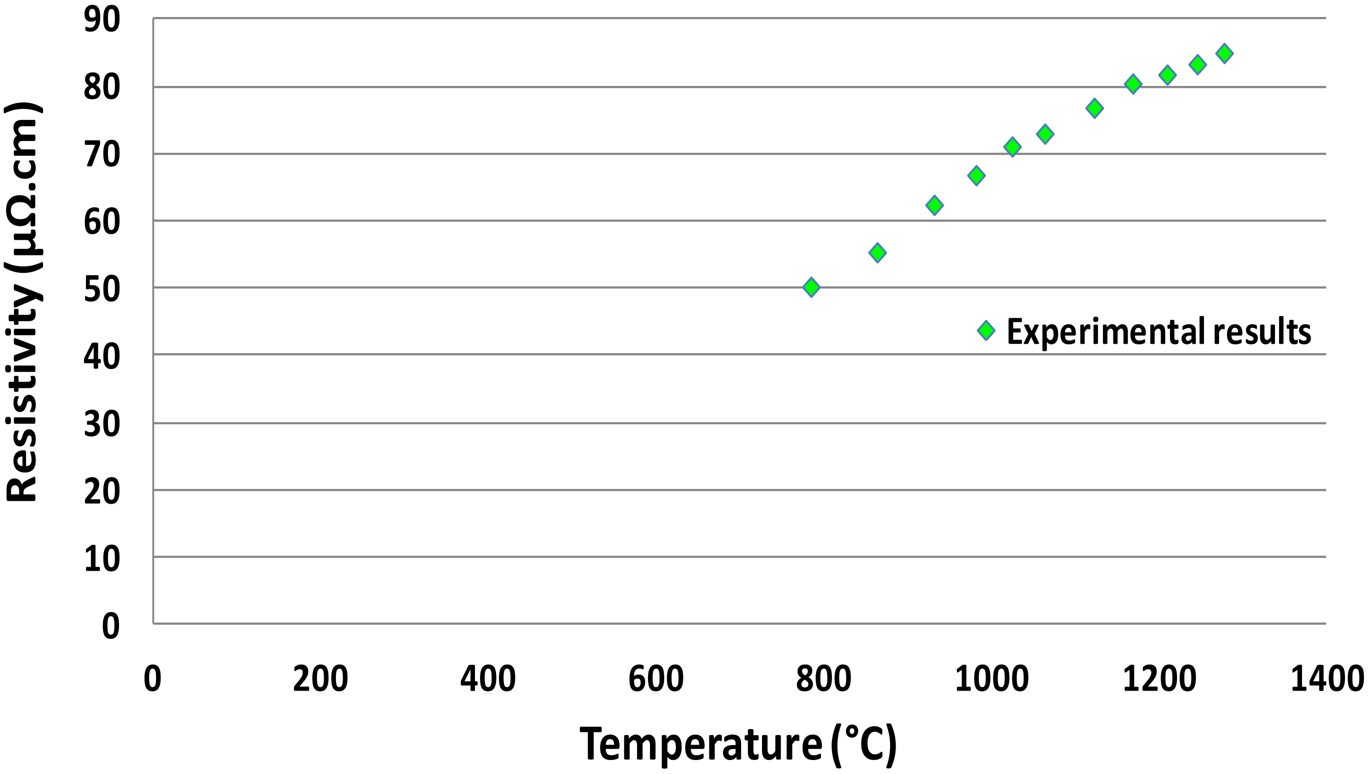

Figure 97: Electrical resistivity of cobalt as a function of temperature.

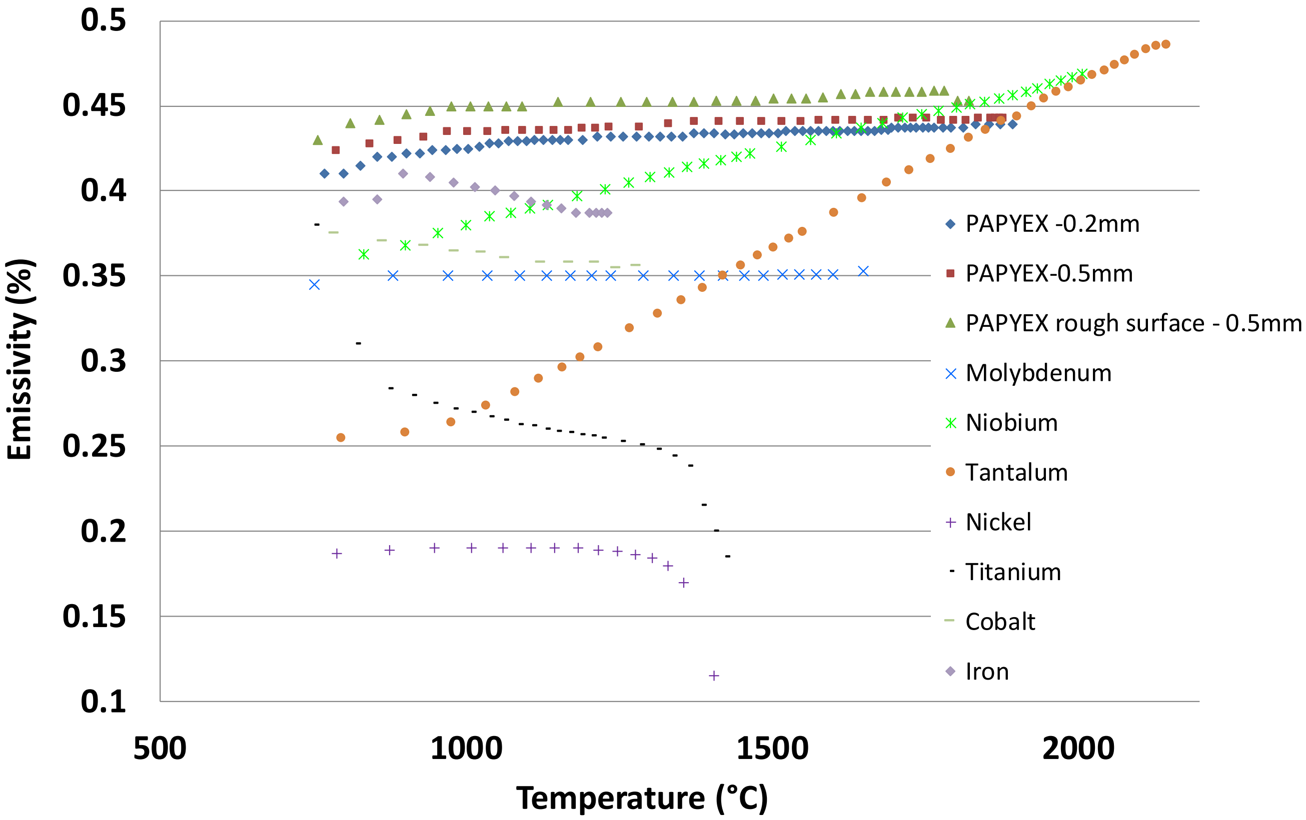

Figure 98: Emissivity as a function of temperature for sample measured with a bi-chromatic pyrometer. The estimated uncertainty is $\pm$ ***5.3 %.***

In *Figure 98*, it can be seen that the behaviour of the emissivity as a function of temperature strongly depends on the material considered, some decrease and some increase. Moreover, the roughness plays a role as shown for Papyex. Papyex of 0.2mm and 0.5 mm thicknesses had smooth surfaces, resulting from their manufacturing process. After abrasion with grade 400 sandpaper, the emissivity was seen to increase. This simple test indicates that rough surface could be used if higher emissivity is required, while conserving the same material.

Conclusions

The electrical resistivity and emissivity of different materials (Ni, PAPYEX, Ta, Mo, Nb, V, Ti, Co and Fe) were measured in conditions as similar as possible, and a set of comparable emissivity and resistivity values for different materials was obtained. The material characteristics are identical to those used to design and build the TISS, and were measured over a temperature range specific to the working conditions of the TISS. The results do not pretend to provide benchmarks since more stringent experimental conditions, not satisfied during the present measurements, are required.

The behaviour of temperature dependent resistivity is identical to the one found in literature for Mo, Ta, Ni, Ti, V, and Fe. Differences could be explained by the uncertainty on the emissivity and by a systematic shift of the temperature scale. Absolute and precise values of temperature are difficult to determine with our system. A black body oven to fix the temperature scale should be used. Nevertheless, in the case of Nb, such rescaling is insufficient to compensate for the difference between the measured resistivity and that found in the literature. Additional studies are required.

Appendix 3.3

Monte Carlo simulation of ion trajectories in a cavity including an electrostatic field.

This appendix describes the Monte Carlo program written to simulate trajectories of ions in a cavity with an electric field. This simulation allows to estimate the effusion and sticking times of the ions with, and without, an electric field. It therefore allows to appreciate the gain in time due to the presence of the electric field.

Inputs are:

- Ion masses
- Charge states (1+)
- Cavity geometry: the cavity is designed with CATIA code, and is able to handle STL format. This allows outputs from SIMION simulations to be easily imported.
- Cavity dimensions: 50 mm in diameter, 12 mm in length, aperture of 4 mm in diameter
- The electric field chart, calculated using the SIMON program (the maximum potential difference is 3.4 V)
- The temperature of the cavity
- The sticking time of the atoms/ions on the different materials

Assumptions are:

- The ionizing process is not taken into account. The atoms are considered to be permanently ionized. This assumption is justified for atoms in a cavity made of a material with a work function higher than the first ionization potential of the atoms
- The angular distribution of ions when they leave the surface (as defined in SIMION)

Outputs are:

- The total time of flight of ions in the cavity
- The number of collisions with the walls of the cavity, and the location of their last collision
- The proportion of ions exiting the cavity
- The distribution of the number of particles released from the cavity versus time

During the calculation, the initial number of atoms N_0 is 10,000, and is sufficient to get a reasonable statistical distribution of particles released from the cavity, as a function of time (the distributions are shown in the following Figures). A larger number of atoms would reduce the dispersion of the distribution but would also increase the calculation time without significantly improving the value of the mean release time extracted from the distributions.

Two types of initial conditions are considered:

- The ions are uniformly distributed within the volume of the cavity and their velocities follow a Maxwell-Boltzmann distribution.
- They are in a "molecular" vacuum regime, i.e. the ion-ion interaction probability is considered negligible when compared to the probability of an interaction with cavity walls.

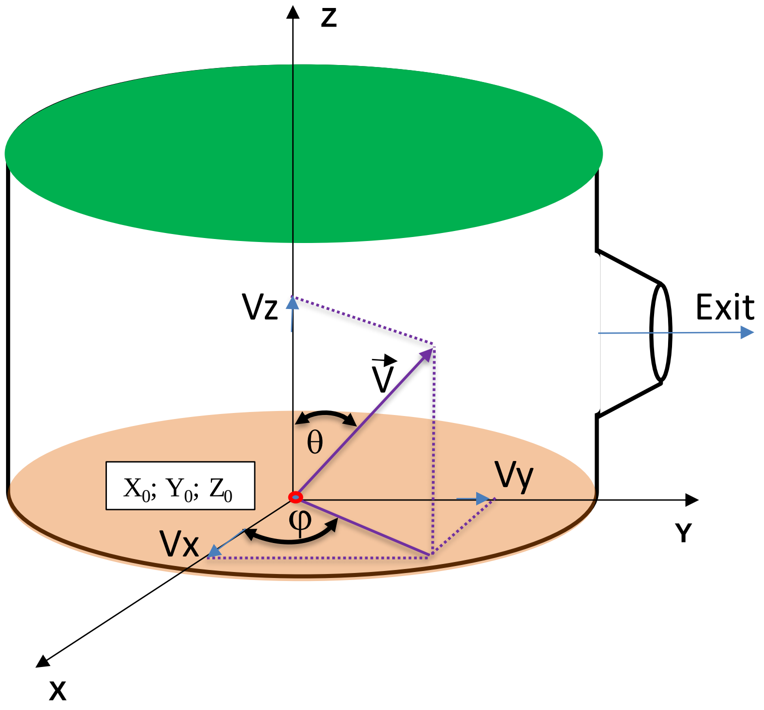

Figure 99: Diagram representing the particle distribution parameters inside the cavity.

The initial position of the ions (X_0, Y_0, Z_0) on the graphite catcher is chosen randomly. Spherical coordinates φ and θ are defined in the way shown in Figure 99. φ ranges from 0 to 2π and θ ranges from - π to + π. The components of the velocity vector V are then defined as:

$$\mathrm{V} \; = \; \left\{ \begin{array}{c} V_x = \mathrm{V}.\cos\varphi \,.\sin\theta \\ V_y = \mathrm{V}.\sin\varphi \,.\sin\theta \\ V_z = \mathrm{V}.\cos\theta \end{array} \right\}$$

The time of flight and the number of hits of the ions on the cavity wall are saved, up to their exit out of the cavity or, to their moment of radioactive decay. On each contact with the walls, a new velocity and position are assigned to the ion.

In order see the electric-field effect on a particle trajectory and on the number of hits, the simulations are carried out with, and without, an electric field.

For $^{74}\mathrm{Rb}^+$ ions, the time distribution with and without an electric field are shown in Figure 100.

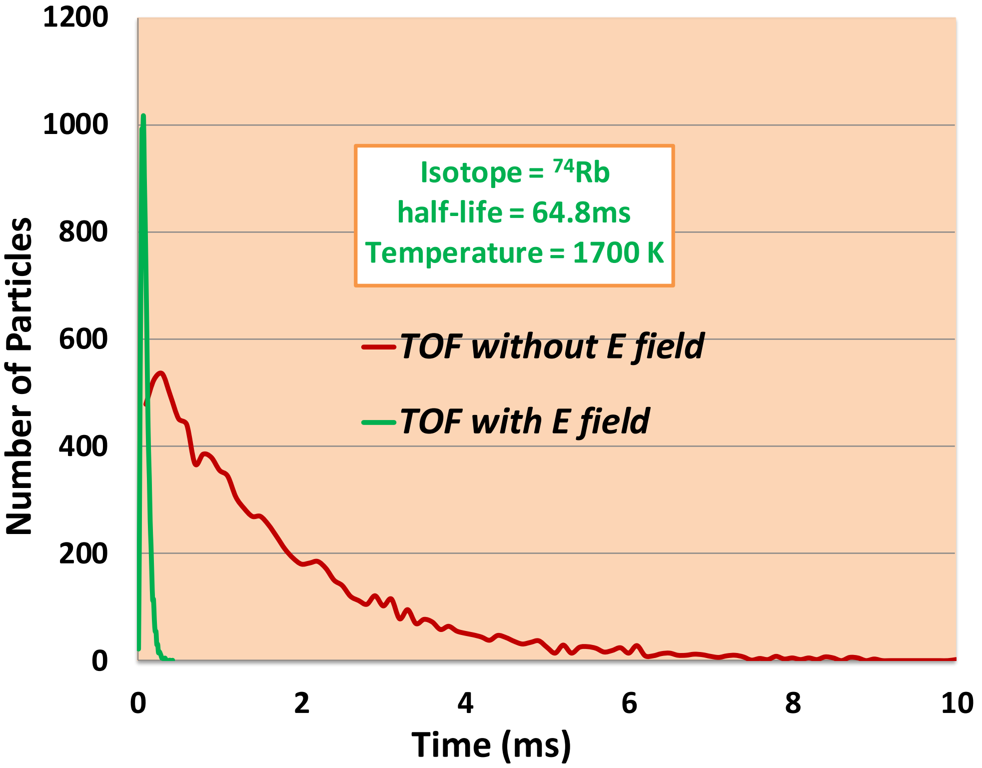

Figure 100: The effect of the electric field on the time of flight of rubidium isotopes.

With the electric field and if the sticking time is not taken into account, the time is reduced to 90 µs (with E field) and the number of hits on the walls is 25, compared to 1.7 ms and 450 hits, respectively, in the absence of an electric field. The time is thus reduced by a factor of 19 and the number of hits by a factor of 18.

The effusion time $t_{1/2}$ without the electric field can be compared to the time atoms of a noble gas need to exit the cavity of volume *V* and conductance *C*, and which can be theoretically calculated as follows:

$$t_{1/2} = \frac{V}{C} ln2 = \frac{V.ln2}{S}\sqrt{\frac{\pi M}{8kT}}$$

Where *M* is the mass of the atoms and *T* is the temperature within the volume. For atoms of mass 74, $t_{1/2}$ is found to be 2.7 ms, compared to the previous value of 1.7 ms. The order of magnitude is the same as that obtained with the Monte Carlo simulation, and lends some credibility to the results obtained with the simulation.

To evaluate the total effusion time, one also has to take into account the sticking time. According to the discussion presented in §2.4.3, the sticking time per contact of Rb on C and on Ni at 1700 K should be of the order of 0.5 ms. Once this sticking time introduced in the simulation, one obtains the time distribution shown in Figure 101. The sticking time is clearly the dominant effect.

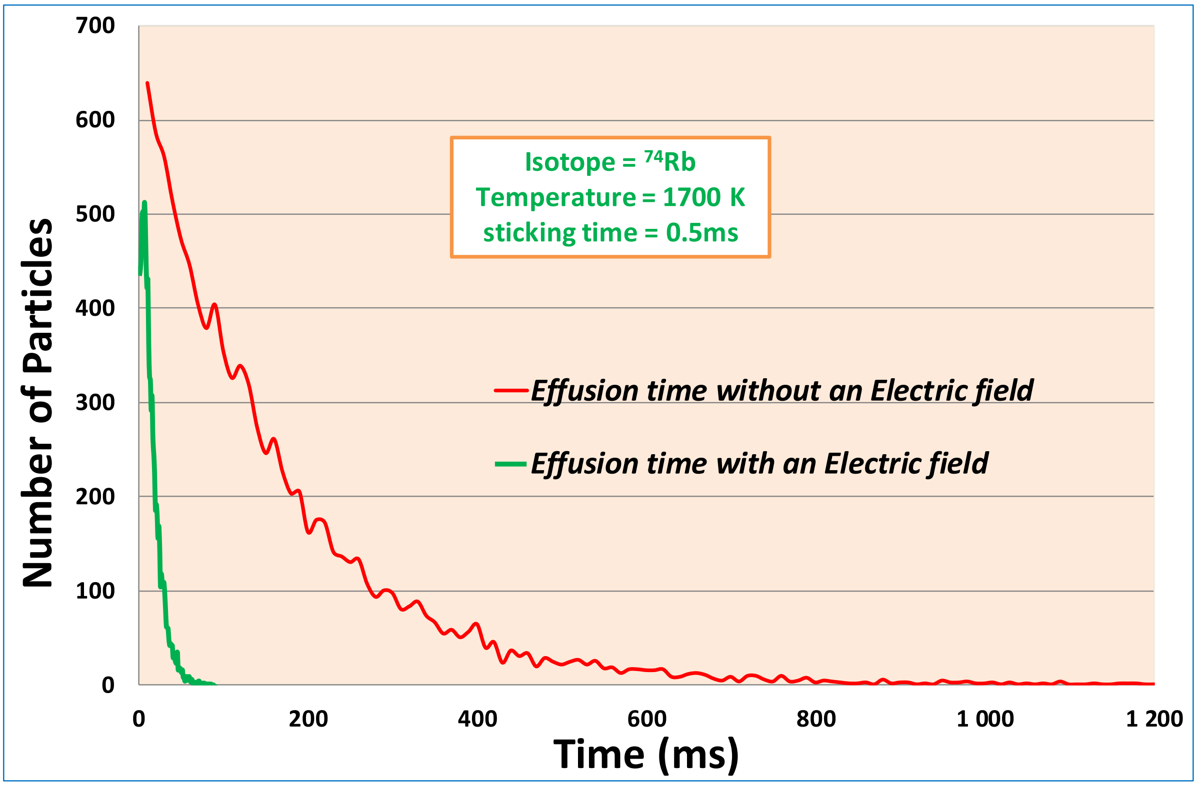

Figure 101: The effect of an electric field on the release time from the material surface for rubidium isotopes.

The release time distributions with and without electric field, for $^{74}Rb^{+}$ ions, are shown in Figure 101, *Figure 102*. The effect of the electric field on the release time is clearly visible. The electric field changes the effusion time from ~100 ms (for 50% of the population) to 12 ms, that is, 8 times faster. For radioactive ions, such as ^{74}Rb ($T_{1/2}$ 65 ms), these times lead to effusion efficiencies of 39 % and 84 % respectively.

Similar simulations were carried out for singly charged ^{114}Cs ions. The ions were uniformly distributed on the catcher, over a disk of 40 mm in diameter. The sticking time per contact considered in the calculations was 1 ms.

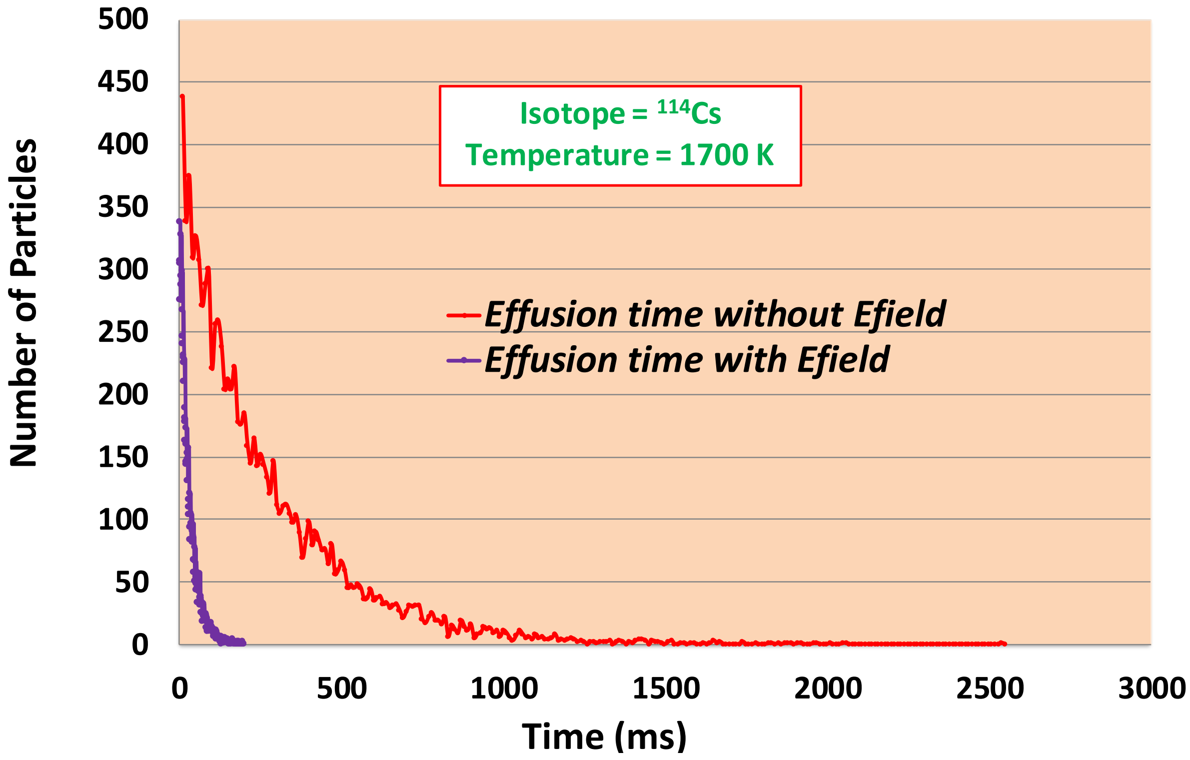

Figure 102: The effect of electric field on the effusion time. The red line represents the effusion time without an electric field and the purple line indicates the effusion time with an electric field. The sticking time per contact of 1 ms was taken into account in the calculations.

The results show that without an electric field the total effusion time is ~190 ms (for 50% of the population) and, with an electric field the total effusion time drops to 27 ms. For radioactive ^{114}Cs ($T_{1/2}$ 570 ms) these effusion times lead to extraction efficiencies of 75% and 97% respectively. Since the half-life of ^{114}Cs is longer than the half-life of ^{74}Rb, the effect of the electric field on the extraction efficiency gain is lower.

Appendix 4.1

Detailed description of the Ion Gun

Performance tests using an Ion Gun

The ion gun is used to test some performance aspects of the TISS in conditions as close as possible to online conditions. Response time measurements and atom-to-ion transformation efficiencies for stable atoms are used to predict atom-to-ion transformation efficiencies of radioactive atoms.

To measure the TISS response time, short pulses of ion beam are injected through a 5 mm diameter hole in the center of the target foil, into the cavity. The ions are stopped at the surface of the catcher, diffuse and effuse up to the catcher surface, where they are ionized and ready to leave the cavity on the internal electric field. The time between the instant where they are injected into the cavity and the instant they leave, is the cavity response time. To limit the influence of the injected pulse shape on the shape of the response time, the injected pulse must be sufficiently short, around 1ms, given typical estimated response times of a few tens of ms. The intensity of the pulse must be high enough for measurement in a Faraday cup without current integration, and low enough to avoid modification of the response time due to a modification of the ionizing feature of the cavity walls once partly covered by the atoms injected. According to previous tests, a current of the order of 1 µA is suitable. These time and current features were the main parameters to be provided by the ion gun.

By measuring the response time and knowing the intensities injected and collected at the cavity exit allows the atom-to-ion transformation efficiency to be determined. In this scenario, the diffusion of atoms out of the catcher is not accurately simulated since the energy of the ions with the ion gun, and thereby their range in the catcher material, are lower than the recoiling kinetic energies produced by fusion-evaporation reactions. Consequently, this method provides only a partial information on the TISS performance.

A compact ion gun for the production of stable alkali elements was previously developed to test target ion source systems based on surface ionization. The HV platform has been refurbished and modified to fit with the configuration of the TISS developed within this PhD study.

Technical description of the Ion Gun

The core of the ion gun consists of an anode opposite a cathode. A voltage difference is applied to accelerate ions emitted by the anode towards the cathode. A central hole in the cathode allows ions to escape. These ions are then accelerated to higher energies (around 1 kV), focused and sent to the Faraday cup for measurement.

The anode, supplied by Heat Wave Labs [114], consists in a layer of tungsten powder deposited on the extremity of a 6 mm diameter pellet.

A heating filament, inserted in a ceramic electrical insulator, fills the volume of the pellet. The temperature reached by the tungsten powder and the contact of alkali atoms with tungsten forces their evaporation in the form of ions.

According to the supplier, for a power of approximately 10 W, the temperature is raised to 1100°C, and a current of some mA/cm^2 can be obtained for ~100 hours. Nevertheless, the extraction current strongly depends on the potential difference between the anode and cathode.

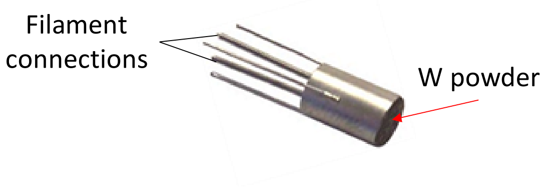

Figure 103: Anode used for alkali ion production

Before using the ion gun, it was necessary to characterize it on a test bench. The vacuum chamber used for the tests is shown *Figure 104*.

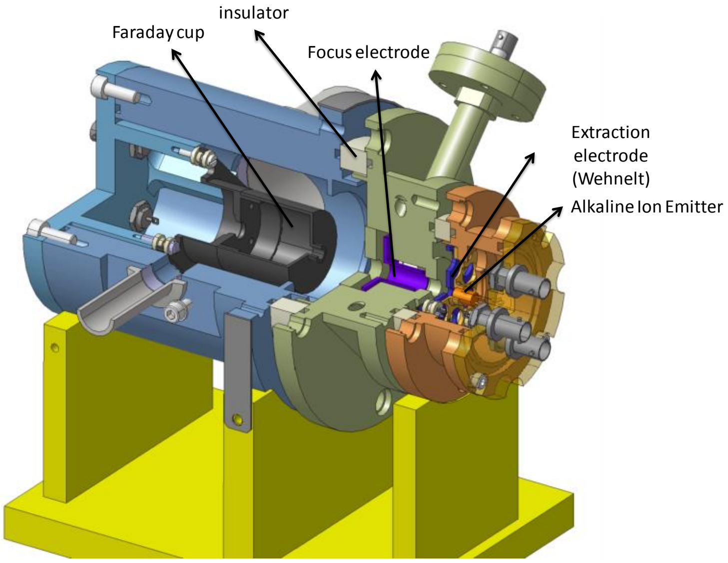

Figure 104: Sectional view of the ion gun, showing the different parts.

The system consists of three flanges, electrically insulated from each other. The first flange holds an alkaline ion emitter (anode) and its extraction electrode (cathode). The potential difference with the anode determines the ion current. Applying a positive voltage to the cathode allows to fix the zero current. When the current is pulsed, a short negative voltage pulse is first applied to the cathode and thereby enabling ion extraction from the anode. Then the cathode voltage is raised to a positive value, and so disabling the ion extraction. The electrical logic is shown in Figure 105.

The second flange is at a potential close to ground, and determines the final ion energy. The flange contains an electrostatic cylindrical lens which is used to focus the beam at the entrance of the Faraday cup. Its hole is 5 mm in diameter, the same as the hole pierced in the TISS target foil center.

The third flange houses the Faraday cup and provides vacuum pump connections. The Faraday cup is electrically insulated from the chamber.

To make the tests as straightforward as possible and the measurement as reliable as possible, the test bench should ideally be as simple as possible. Therefore, in steady state, all currents and voltages are measured using portable ammeters and voltmeters. During the pulsed regime, the signals were recorded using an oscilloscope. When the signals were collected at high voltage, they were converted and transmitted to measuring apparatus placed at ground level using optical fibers (with analogue-to-optical and optical-to-analogue conversion). The linearity of the conversion chains were checked prior to the measurements.

Currents leaving -or deposited on- all the electrodes are measured to check the global current balance and ensure that all the current emerging from the ion gun is injected into the Faraday cup.

The currents are measured using resistances placed in series with each electrode. Since the currents are all in the range of 10 nA to 1 µA, resistances of 10 kΩ to 1 MΩ were used, and are sufficient given the resolution of the measuring apparatus is around 1 mV.

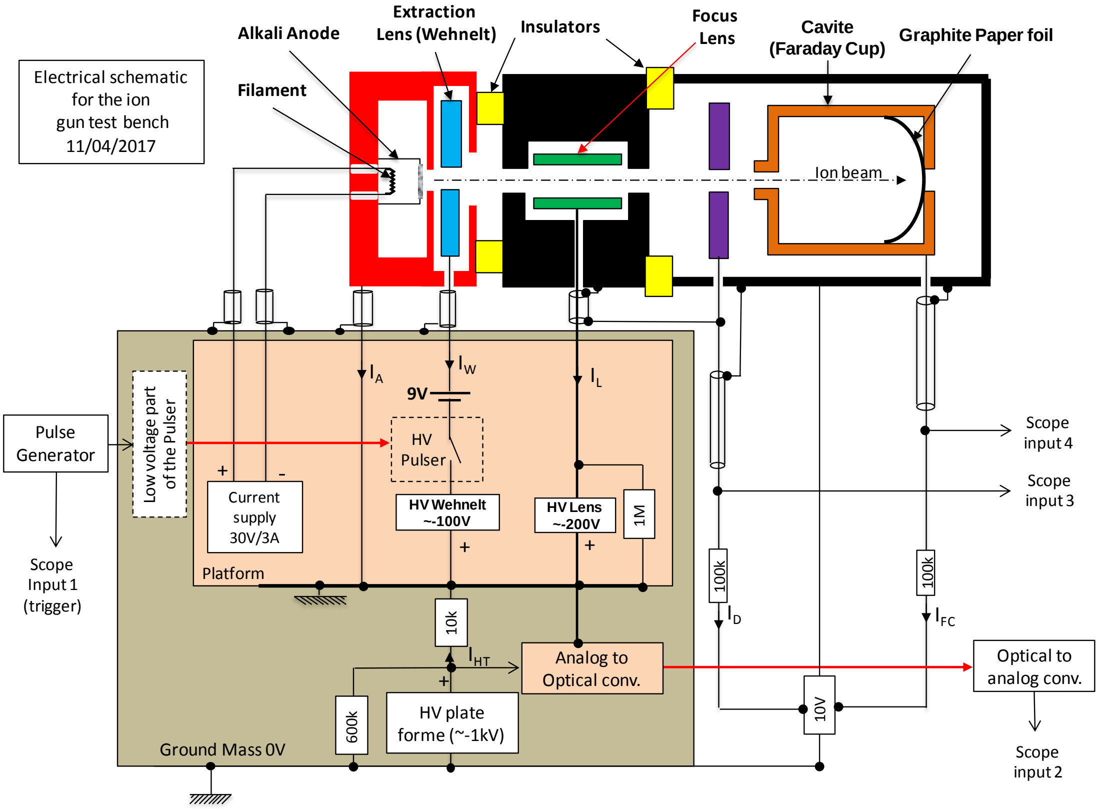

Figure 105: Details of the electrical layout of the ion gun (upper part) and HV platform (lower grey shaded part).

The diaphragm and the Faraday cup were polarized in order to limit undesirable parasitic currents due to electrons sputtered at the surface of materials by ion impact. It is possible for such parasitic electrons to be accelerated to positive electrodes and result in incorrect current measurements.

Most of the tests were performed at an acceleration voltage of 1 kV as for lower values the transport efficiency rapidly decreases. Thus an acceleration voltage equal or higher than 1 kV should be preferably used during the TISS tests.

During the TISS tests, the ion gun and its platform will be installed on the high voltage platform of the TISS, which operated up to 20 kV.

7. Bibliography

[1] S. Koscielniak, P. Bricault, B. Davids, and et al., “Proposal for a 1/2 MW electron linac for rare isotope and materials science,” *Proc. EPAC08*, pp. 985–987, 2008.

[2] P. Jardin, O. Bajeat, P. Delahaye, and et al., “New target ion source systems at GANIL/SPIRAL1: Prospective,” *Nucl. Inst. Methods Phys. Res. B*, vol. 376, pp. 64–67, 2016.

[3] M. Huyse, M. Facina, Yuri Kudryavtsev, and et al., “Intensity limitations of a gas cell for stopping, storing and guiding of radioactive ions,” *Nucl. Inst. Methods Phys. Res. B*, vol. 187, no. 4, pp. 535–547, 2002.

[4] R. V. Ambartsumian, A. M. Apatin, V. S. Letokhov, and E. Al., “Selective two-step ionization of rubidium by laser radiation,” *Sov. Phys. JETP*, vol. 43, no. 5, pp. 866–872, 1976.

[5] Y. Kudryavtsev, M. Facina, M. Huyse, and et al., “Beams of isotopes produced at LISOL by laser ionization after thermalization of energetic ions in a gas cell,” *Nucl. Inst. Methods Phys. Res. B*, vol. 204, pp. 336–342, 2003.

[6] D. A. Fink, S. D. Richter, K. Blaum, and et al., “On-line implementation and first operation of the Laser Ion Source and Trap at ISOLDE/CERN.,” *Nucl. Inst. Methods Phys. Res. B*, vol. 344, pp. 83–95, 2015.

[7] R. Kirchner and E. Roeckl, “Investigation of small-volume gaseous discharge ion sources for isotope separation on-line,” *Nucl. Inst. Methods Phys. Res. B*, vol. 131, no. 2, pp. 371–374, 1975.

[8] R. Kirchner, K. H. Burkard, W. Hüller, and O. Klepper, “The ion sources for the GSI on-line separator,” *Nucl. Inst. Methods Phys. Res. B*, vol. 186, no. 1–2, pp. 295–305, 1981.

[9] I. D. Moore, P. Dendooven, and J. Ärje, “The IGISOL technique-three decades of developments.,” *Hyperfine Interact.*, vol. 223, no. 1–3, pp. 17–62, 2014.

[10] A. Gavron, “Statistical model calculations in heavy ion reactions.,” *Phys. Rev. C - Nucl. Phys.*, vol. 21, 1980.

[11] J. F. Ziegler, M. D. Ziegler, and J. P. Biersack, “SRIM - The stopping and range of ions in matter (2010),” *Nucl. Inst. Methods Phys. Res. B*, vol. 268, no. 11–12, pp. 1818–1823, 2010.

[12] R. Kersevan and J.-L. Pons, “Introduction to MOLFLOW+: New graphical processing unit-based Monte Carlo code for simulating molecular flows and for calculating angular coefficients in the compute unified device architecture environment.,” *J. Vac. Sci. Technol. A Vacuum, Surfaces, Film.*, vol. 27, no. 4, pp. 1017–1023, 2009.

[13] R. A. Causey and K. L. Wilson, “Retention of deuterium and tritium in Papyex graphite,” *J. Nucl. Mater.*, vol. 138, no. 1, pp. 57–64, 1986.

[14] A. Pichard, “Développement de faisceaux d’ions radioactifs pour le projet SPIRAL 2. Physique Nucléaire Expérimentale [nucl-ex],” *Univ. Caen*, pp. 1–292, 2010.

[15] “ANSYS Academic Research Mechanical Release 18.1:,” *http://www.ansys.com/products.*

[16] A. Osa, M. Matsuda, T. K. Sato, and et al., “Release and efficiencies of radioactive ion beams from the JAEA-ISOL target/ion source systems,” *Nucl. Inst. Methods Phys. Res. B*, vol. 266, no. 19–20, pp. 4373–4377, 2008.

[17] B. Roussière, O. Bajeat, N. Barré, and et al., “Release of Kr, Ag, Sn, I and Xe from UCx targets,” *Nucl. Inst. Methods Phys. Res. B*, vol. 246, no. 2, pp. 288–296, 2006.

[18] G. D. Alton and J. Dellwo, “Selection of RIB targets using ion implantation at the Holifield Radioactive Ion Beam Facility.,” *Nucl. Inst. Methods Phys. Res. A*, vol. 382, pp. 225–231, 1996.

[19] G. J. Beyer, E. Hagebø, A. F. Novgorodov, and et al., “The role of diffusion in ISOL targets for the production of radioactive ion beams,” *Nucl. Inst. Methods Phys. Res. B*, vol. 204, pp. 225–234, 2003.

[20] J. R. J. Bennett, “Targets for the production of high intensity radioactive ion beams,” *Nucl. Inst. Methods Phys. Res. B*, vol. 126, no. 1–4, pp. 105–112, 1997.

[21] R. Kirchner, “On the release and ionization efficiency of catcher-ion-source systems in isotope separation on-line,” *Nucl. Inst. Methods Phys. Res. B*, vol. 70, no. 1–4, pp. 186–199, 1992.

[22] F. Landré-Pellemoine, “Production de faisceaux d’ions radioactifs par la méthode ISOL pour SPIRAL. Physique Nucléaire Expérimentale [nucl-ex],” *Univ. Caen*, p. 212, 2001.

[23] Mr Cyrille ELEON, “Recherche et développement concernant la production d ’ ions radioactifs dans le cadre de SPIRAL. Physique Nucléaire Expérimentale [nucl-ex].,” *Univ. Caen*, 2007.

[24] M. Fujioka and Y. Arai., “Diffusion of radioisotopes from solids in the form of foils, fibers and particles,” *Nucl. Inst. Methods*, vol. 186, pp. 409–412, 1981.

[25] V. Kuchi and P. Jardin, “Grain size influence on the release of radioactive isotopes out of target materials made of powder,” *Open-Access J. Basic Princ. Diffus. Theory*, vol. 30, pp. 4–11, 2017.

[26] B. Eichler and H. RoBbach, “Adsorption von Metallen auf metallische oberflächen und Mögliahkeiten ihrer Nutzung in der Kernchemie,” vol. 527, 1984.

[27] V. J. F. Leningrad, “Theorie der Adsorption und verwandter Erscheinungen,” pp. 117–138, 1924.

[28] M. Thoennessen, “Current status and future potential of nuclide discoveries,” *Reports Prog. Phys.*, vol. 76, no. 5, 2013.

[29] R. Kirchner, “Progress in ion source development for on-line separators.,” *Nucl. Inst. Methods Phys. Res. B*, vol. 186, no. 1–2, pp. 275–293, 1981.

[30] D. G. Truhlar and J. T. Muckerman, *Reactive Scattering Cross Sections: Quasiclassical and Semiclassical Methods*, no. January. 1979.

[31] M. Samuel and U. Smilansky, “Coulomb excitation near the coulomb barrier,” *phy. Lett.*, vol. 28, no. 5, pp. 3–5, 1968.

[32] A. Krása, “Spallation Reaction Physics,” 2010.

[33] H. L. Ravn, T. Bjørnstad, P. Hoff, and et al., “Use of refractory oxides, carbides and borides as targets for on-line mass separation,” *Nucl. Inst. Methods Phys. Res. B*, vol. 26, no. 1–3, pp. 183–189, 1987.

[34] M. V. Ricciardi, S. Lukić, A. Kelić, and et al., “Secondary-beam production: Protons versus heavy ions,” *Eur. Phys. J. Spec. Top.*, vol. 150, no. 1, pp. 321–324, 2007.

[35] TENDL nuclear data Base, “https://tendl.web.psi.ch/tendl_2017/proton_html/Nb/ProtonNb93residual.html.”

[36] Y. Blumenfeld, T. Nilsson, and P. Van Duppen, “Facilities and methods for radioactive ion beam production,” *Phys. Scr.*, vol. 2013, no. T152, p. 14023, 2013.

[37] P. Van Duppen, *The Euroschool Lectures on Physics With Exotic Beams, Vol. II: Isotope Separation On Line and Post Acceleration*, vol. 700. 2006.

[38] “NSCL,” *https://nscl.msu.edu/*. [Online]. Available: https://nscl.msu.edu/.

[39] “GANIL,” *https://www.ganil-spiral2.eu/*.

[40] “RIKEN,” *http://www.riken.jp/en/*.

[41] “FRIB,” *https://frib.msu.edu/*.

[42] “FAIR,” *https://fair-center.eu/*.

[43] “ISOLDE,” *http://isolde.web.cern.ch/.*

[44] E. Petit, “Status report on the SPIRAL 2 facility at Ganil,” *Proc. NAPAC2016*, pp. 240–245, 2016.

[45] “TRUMF,” *http://www.triumf.ca/.*

[46] “INFN,” *http://home.infn.it/en/*.

[47] “IPNO,” *http://ipnwww.in2p3.fr/ALTO-facility*.

[48] “List of intensities predicted from the SPIRAL upgrade.”

[49] O. B. Tarasov and D. Bazin, “Development of the program LISE: Application to fusion-evaporation,” *Nucl. Inst. Methods Phys. Res. B*, vol. 204, pp. 174–178, 2003.

[50] E. Baron, “Les cyclotrons,” *GANIL Rep. la source à la cible*, pp. 1–18, 2004.

[51] L. Penescu, R. Catherall, J. Lettry, and T. Stora, “Development of high efficiency Versatile Arc Discharge Ion Source at CERN ISOLDE,” *Rev. Sci. Instrum.*, vol. 81, no. 2, pp. 2–6, 2010.

[52] P. Chauveau, P. Delahaye, M. Babo, and et al., “A new FEBIAD-type ion source for the upgrade of SPIRAL1 at GANIL,” *Nucl. Inst. Methods Phys. Res. B*, vol. 376, pp. 35–38, 2016.

[53] P. Chauveau, “Design, simulations and test of a Time-of-Flight spectrometer for mass measurement of exotic beams from SPIRAL1/SPIRAL2 and -ray spectroscopy of N=Z nuclei close to 100Sn. Nuclear Experiment [nucl-ex].,” *Univ. Caen Normandie*, 2016.

[54] K. Pyszniak, A. Droz, M. Turek, D. Ma, and J. Meldizon, “Atom ionization process in the thermoionization ion source,” *Vac. Surf. Eng. Surf. Instrum. Vac. Technol.*, vol. 81, pp. 1150–1153, 2007.

[55] M. HUYSE, “Ionization in a hot cavity and the temperature.,” *Nucl. Inst. Methods*, vol. 215, pp. 1–5, 1983.

[56] J. M. D’AURIA, L. C. CARRAZ, and H. L. Ravn, “THE N = Z NUCLIDE 74Rb.,” *phy. Lett.*, vol. 66, no. 3, pp. 233–235, 1977.

[57] M. Dombsky, P. Bricault, P. Schmor, and M. Lane, “ISAC target operation with high proton currents,” *Nucl. Inst. Methods Phys. Res. B*, vol. 204, pp. 191–196, 2003.

[58] R. Kirchner and A. Piotrowski, “Thermal ionization in a hot cavity,” *Nucl. Inst. Methods Phys. Res. B*, vol. 153, no. 2, pp. 291–292, 1978.

[59] K.H. Kingdon and I. Langmuir, “The removal of thorium from the surface of a thoriated tungsten filament by positive ion bombardment.,” pp. 148–160, 1921.

[60] T. K. Sato, N. Sato, M. Asai, and et al., “First successful ionization of Lr (Z = 103) by a surface-ionization technique,” *Rev. Sci. Instrum.*, vol. 84, pp. 1–6, 2013.

[61] A. Latuszyn and D. Maczka, “High temperature cavity thermo-ionizer,” vol. 51, no. 2, pp. 109–112, 1998.

[62] F. Pühlhofer, “On the interpretation of evaporation residue mass distributions in heavy-ion induced fusion reactions,” *Nucl. Phys. A*, vol. 280, pp. 267–284, 1977.

[63] K. Hagino, N. Rowley, and A. T. Kruppa, “A program for coupled-channels calculations with all order couplings for heavy-ion fusion reactions,” *Comput. Phys. Commun.*, vol. 123, pp. 143–152, 1999.

[64] W. Reisdorf, “Analysis of fissionability data at high excitation energies,” *J. Phys. A Hadron. Nucl.*, vol. 300, no. 227, 1981.

[65] J. J. Gaimard and K. H. Schmidt, “A reexamination of the abrasion-ablation model for the description of the nuclear fragmentation reaction,” *Nucl. Physics, Sect. A*, vol. 531, no. 3–4, pp. 709–745, 1991.

[66] B. Blank, G. Canchel, F. Seis, and P. Delahaye, “Evaluation of fusion-evaporation cross-section calculations,” *Nucl. Inst. Methods Phys. Res. B*, vol. 416, no. September 2017, pp. 41–49, 2018.

[67] S. G. BRUSH, “Development of Kinetic Theory of Gases VII. Heat Conduction and the Stffan-Boltzmann Law.,” *Arch. Hist. Exact Sci.*, vol. 11, no. 1, pp. 38–96, 1973.

[68] O. Alyakrinskiy, K. Gubin, P. Martyshkin, and L. Tecchio, “Influence of grain size and porosity on the release of radioactive isotopes from target materials with high open porosity,” *Nucl. Inst. Methods Phys. Res. B*, vol. 267, no. 15, pp. 2554–2558, 2009.

[69] P. G. Bricault, “Thick target for high-power ISOL facilities,” *Nucl. Inst. Methods Phys. Res. B*, vol. 376, pp. 3–7, 2016.

[70] M. Dombsky, L. Buchmann, J. M. D’Auria, and et al., “Targets and ion sources at the TISOL facility,” *Nucl. Inst. Methods Phys. Res. B*, vol. 70, no. 1–4, pp. 125–130, 1992.

[71] U. Köster, U. C. Bergmann, D. Carminati, R. Catherall, and et al., “Oxide fiber targets at ISOLDE,” *Nucl. Inst. Methods Phys. Res. B*, vol. 204, pp. 303–313, 2003.

[72] L. C. Carraz, S. Sundell, H. L. Ravn, and et al., “High-temperature carbide targets for fast on-line mass separation of alkali and noble gas elements,” *Nucl. Inst. Methods Phys. Res. B*, vol. 158, pp. 69–80, 2000.

[73] N. Ikedla, Y. Shirakabe, J. Tanaka, and et al, “Study of a thick target surface ionizer at INS,” *Nucl. Inst. Methods Phys. Res. B*, vol. 70, pp. 150–155, 1992.

[74] L. C. Carraz, I. R. Iialdorsen, H. L. Ravn, and et al., “Fast release of nuclear reaction products from refractory matrices,” *Nucl. Inst. Methods Phys. Res. B*, vol. 148, pp. 217–230, 1978.

[75] J. P. Ramos, A. Gottberg, T. M. Mendonça, and et al., “Intense 31–35Ar beams produced with a nanostructured CaO target at ISOLDE.,” *Nucl. Inst. Methods Phys. Res. B*, vol. 320, no. 2014, pp. 83–88, 2015.

[76] F. Pellemoine, “High power density targets,” *Nucl. Inst. Methods Phys. Res. B*, vol. 317, pp. 369–372, 2013.

[77] Pierre G. Bricault, Friedhelm Ames, and Marik Dombsky, “Development of a NiO target for the production of 11C at ISAC/TRIUMF.,” *Nucl. Inst. Methods Phys. Res. B*, vol. 366, pp. 34–39, 2016.

[78] M. Czapski, T. Stora, C. Tardivat, and et al., “Porous silicon carbide and aluminum oxide with unidirectional open porosity as model target materials for radioisotope beam production.,” *Nucl. Inst. Methods Phys. Res. B*, vol. 317, pp. 385–388, 2013.

[79] A. Gottberg, “Target materials for exotic ISOL beams,” *Nucl. Inst. Methods Phys. Res. B*, vol. 376, pp. 8–15, 2016.

[80] G. J. Beyer, E. Hagebø, A. F. Novgorodov, and et al., “The role of diffusion in ISOL targets for the production of radioactive ion beams,” *Nucl. Inst. Methods Phys. Res. B*, vol. 204, pp. 225–234, 2003.

[81] J. Maassen and M. Lundstrom, “Steady-state heat transport: Ballistic-to-diffusive with Fourier’s law,” *J. Appl. Phys.*, vol. 117, no. 3, pp. 1–9, 2015.

[82] J. Crank, “the Mathematics of Diffusion,” *2nd Ed. Oxford Univ. Press. UK*, 1975.

[83] A. Magerl, “Diffusion and melting in two dimensions: A quasielastic neutron scattering study of alkali metals in graphite,” *Phys. Rev. B*, vol. 40, no. 11, pp. 7616–7632, 1989.

[84] R. I. MASEL, *Principles of Adsorption and Reaction on Solid Surfaces*. A WILEY-INTERSCIENCE PUBLICATION, 1951.

[85] R. G. Wilmoth, “Measurement of surface stay times for physical adsorption of gases,” in *University of Virginia*, 1973.

[86] F. Besenbacher, “Chemisorption on metal surfaces,” *Rep. Prog. Phys.*, vol. 53, pp. 1253–1295, 1990.

[87] I. Langmuir, “The evaporation, condesation and reflection of molecules and the mechanism of adsorption,” vol. 76, pp. 1–2, 1916.

[88] W. F. Gale, C. J. Smithells, and T. C. Totemeier, “smithells metals reference book,” *Butterworth-Heinemann*, 2004.

[89] D.R. Lide, “CRC handbook of chemistry and physics,” *CRC Press*, 2004.

[90] F. Cardarelli, “Materials handbook,” *Springer Int. Publ.*, 2007.

[91] Mario Santana Leitner, “Radioactive ion beam optimiser, RIBO.,” 2005.

[92] P. V. Cuong, “Development of a new surface ion-source and ion guide in the ALTO project. Physique Nucléaire Théorique [nucl-th],” *Univ. Paris Sud*, 2010.

[93] E. Traykov, U. Dammalapati, O. C. Dermois, and et al., “Development of a thermal ionizer as ion catcher,” *Nucl. Inst. Methods Phys. Res. B*, vol. 266, no. 19–20, pp. 4478–4482, 2008.

[94] M. Turek and K. Pyszniak, “Simulations of ionization in a hot cavity surface ion source,” *Rev. Sci. Instrum.*, vol. 83, pp. 1–10, 2012.

[95] “Toyo tanso: http://www.toyotansofrance.com/.” .

[96] T. Kuphaldt, “Lessons In Electric Circuits,” *October*, vol. 8, p. 299, 2006.

[97] G. Teodorescu, “Radiative emissivity of metals and oxidized metals at high temperature,” *Auburn Univ.*, p. 176, 2007.

[98] C. Purpura, E. Trifoni, M. Musto, G. Rotondo, and R. Della Ragione, “Methodology for spectral emissivity measurement by means of single color pyrometer,” *Meas. J. Int. Meas. Confed.*, vol. 82, pp. 403–409, 2016.

[99] K. Dieter Gruner, “Principles of Non-contact Temperature Measurement,” *J. Sol. Energy Eng.*, vol. 3, no. February, p. 1397, 2003.

[100] J. S. Redgrove, “Measurement of the spectral emissivity of solid materials,” *Meas. J. Int. Meas. Confed.*, vol. 8, no. 2, pp. 90–95, 1990.

[101] O. Riou, V. Guiheneuf, F. Delaleux, P. O. Logerais, and J. F. Durastanti, “Accurate methods for single-band apparent emissivity measurement of opaque materials,” *Meas. J. Int. Meas. Confed.*, vol. 89, pp. 239–251, 2016.

[102] A. Book, “Principle , advantages , limitations and applications of two-colour pyrometers in thermal processes,” *Infrared Thermom. Solut.*, pp. 1–8, 2010.

[103] A. Krell, T. Hutzler, and J. Klimke, “Physics and Technology of Transparent Ceramic Armor : Sintered Al2O3 vs Cubic Materials,” pp. 1–10, 2005.

[104] Sergei N. Magonov and D. H. Reneker, “characterization of polymer surfaces with atomic force microscopy.,” *Annu. Rev. Mater. Sci.*, vol. 27, no. 1, pp. 175–222, 1997.

[105] R. E. Taylor and H. Groot, “Thermophysical properties of POCO graphite,” *High Temp. - High Press.*, vol. 11, no. 22, pp. 147–160, 1980.

[106] D. A. Dahl, “SIMION for the personal computer in reflection,” *Int. J. Mass Spectrom.*, vol. 200, no. 1–3, pp. 3–25, 2000.

[107] “CATIA,” *https://www.3ds.com/fr/produits-et-services/catia/*.

[108] “LUA : https://www.lua.org/.”

[109] M. Knudsen, “The Cosine law in the kinetic theory of gases,” *Ann. Phys.*, vol. 48, pp. 1113–1121, 1915.

[110] Th. Keutgen, J. Cabrera, and et al., “Thermal and dynamical properties of fusion-fission and fusion-evaporation processes in 20Ne +159 Tb and 20Ne +169 Tm reactions between 8 and 16 MeV/nucleon.,” *Nucl. Phys. A*, vol. 654, pp. 878–881, 1999.

[111] Hervé Savajols, “Technical Proposal for the SPIRAL 2 instrumentation,” *GANIL Rep.*, pp. 1–48.

[112] W. J. Frederick, M. Hupa, J. Stenberg, and R. Hernberg, “Optical pyrometric measurements of surface temperatures during black liquor char burning and gasification,” *Fuel*, vol. 73, no. 12, pp. 1889–1893, 1994.

[113] M. Gaelens, M. Huyse, M. Loiselet, G. Ryckewaert, and P. Vanduppen, “Development of radioactive ion beams of light elements at ARENAS3,” *Nucl. Inst. Methods Phys. Res. B*, vol. 126, no. 1–4, pp. 125–129, 1997.

[114] “Heat Wave Labs : http://www.cathode.com/.”

[115] P. Jardin, C. Eleon, W. Farabolini, and et al., “Total efficiency of an isotope-separator-on-line production system based on an electron cyclotron resonance ion source associated with a carbon target: The case of SPIRAL 1,” *Rev. Sci. Instrum.*, vol. 77, no. 3, pp. 1–5, 2006.

[116] P. Jardin, O. Bajeat, C. Couratin, and et al., “Status of the SPIRAL i upgrade at GANIL,” *Rev. Sci. Instrum.*, vol. 83, no. 2, 2012.

[117] C. Eléon, P. Jardin, J. C. Thomas, M. G. Saint-Laurent, C. Huet-Equilbec, R. Alvès Condé, J. C. Angélique, D. Boilley, J. Cornell, M. Dubois, H. Franberg, G. Gaubert, B. Jacquot, U. Köster, R. Leroy, L. Maunoury, N. Orr, J. Y. Pacquet, F. Pellemoine, C. Stodel, and M. Turrion, “Measurement of the Ar diffusion coefficient in graphite at high temperature by the ISOL method,” *Nucl. Instruments Methods Phys. Res. Sect. B Beam Interact. with Mater. Atoms*, vol. 266, no. 19–20, pp. 4284–4288, 2008.

[118] “Mersen: https://www.mersen.com/produits.html.” .

[119] A. Cezairliyan and A. P. Miiller, “Heat Capacity and Electrical Resistivity of Nickel in the Range 1300-1700 K Measured with a Pulse Heating Technique,” *Int. J. Thermophys.*, vol. 4, no. 4, 1983.

[120] H. Jo, J. L. King, K. Blomstrand, and K. Sridharan, “Spectral emissivity of oxidized and roughened metal surfaces,” *Int. J. Heat Mass Transf.*, vol. 115, pp. 1065–1071, 2017.

[121] D. Ren, H. Tan, Y. Xuan, Y. Han, and Q. Li, “Apparatus for Measuring Spectral Emissivity of Solid Materials at Elevated Temperatures,” *Int. J. Thermophys.*, vol. 37, no. 5, pp. 1–20, 2016.

[122] V. C. Raj and S. V. Prabhu, “Measurement of surface temperature and emissivity of different materials by two-colour pyrometry,” *Rev. Sci. Instrum.*, vol. 84, no. 12, pp. 1–11, 2013.

[123] H. Herne, “The theoretical characteristics of bichromatic pyrometers.,” pp. 374–377, 1953.

[124] "Goodfellow : http://www.goodfellow.com/fr/."

[125] M. Planck, "The Theory of Heat Radiation," *Search*, vol. 30, pp. 85–94, 1914.

[126] N. Levati, L. Vitali, D. Fustinoni, and A. Niro, "Spectrophotometric evaluation of optical performances of polarizing technologies for smart window applications," *J. Phys. Conf. Ser.*, vol. 547, no. 1, 2014.

[127] T. Hüpf, C. Cagran, and G. Pottlacher, "Thermophysical properties of 22 pure metals in the solid and liquid state – The pulse-heating data collection," *EPJ Web Conf.*, vol. 15, p. 1018, 2011.

[128] N. D. Milosevic and K.D. Magi, "Thermophysical properties of solid phase Ti in a wide temperature range.," *High Temp. - High Press.*, vol. 37, pp. 187–204, 2008.

[129] S.L. Ames. and A.D. Mcquillan., "The resistivity temperature concentration relationships in the system Niobium-Titanium.," *Acta Metall.*, vol. 2, no. 6, 1954.

[130] P.D. Desai, T.K. Chu, H.M. James, and C.Y. Ho, *elecrical resistivity of Ta, Mo, Hf, W, and Zn.*, vol. 13. 1954, p. 1069.

Title: Development of an innovative ISOL system for the production of short-lived neutron-deficient ions.

Keywords: ISOL technique, fusion-evaporation reaction, neutron-deficient alkali isotopes, diffusion, effusion, sticking process.

In the frame of GANIL/SPIRAL-1 facility, an innovative target ion source system (TISS) has been designed in order to produce new competitive radioactive ion beams, and to determine to which extent it is possible to improve the production performances by optimizing a target ion source system dedicated to the production of a specific radioactive ion beam.

The short-lived alkali isotope of ^{74}Rb ($\tau_{1/2}$ = 64.8 ms) has been chosen as a challenging case study.

By studying and improving the processes involved in the TISS designed, *i.e.* in-target production by fusion-evaporation, implantation in and release out of graphite, effusion, and ionization, an atom-to-ion transformation efficiency of 75% was predicted, leading to an ion rate of the order of 10^4 pps at the exit of the TISS.

The estimated performances would allow the GANIL / SPIRAL1 installation to deliver beams of ^{74}Rb and ^{114}Cs with competitive intensities never reached in other installations.

The production device was developed based on my work, to cope with physics objectives and with the conditions of the SPIRAL1 operation. Efficiency, reliability and thus simplicity were essential. The system meets these requirements.

The instrumentation needed for tests existed or have been specifically designed. The TISS has been built, assembled and partly tested.

In parallel, issues have been addressed to answer related questions about sticking times, resistivity, and emissivity, to get inputs for the design of the TISS.

Expected results with alkali isotopes encouraged us to apply the same principle to the production of neutron-deficient short-lived isotopes of noble gases and eventually to metals.

Titre: Développement d'un système ISOL innovant pour la production d'ions déficitaires en neutrons de courte durée.

Mots clés: Technique ISOL, réaction de fusion-évaporation, isotopes alcalins déficients en neutrons, diffusion, effusion, collage.

Dans le cadre de l'installation GANIL / SPIRAL-1, un système innovant de source d'ions cible (TISS) a été conçu pour produire des nouveaux faisceaux d'ions radioactifs compétitifs et déterminer dans quelle mesure il est possible d'améliorer les performances de production par l’optimisation de l’ensemble cible-source (ECS) d’ions dédié à la production d'un faisceau d'ions radioactifs spécifique.

L'isotope d'alcalin de courte durée de ^{74}Rb ($\tau_{1/2}$ = 64.8 ms) a été choisi comme cas d’école.

En étudiant et en améliorant l’efficacité des processus impliqués dans le fonctionnement de l’ECS, *i.e.* production dans la cible par réaction fusion-évaporation, implantation dans- et sortie du graphite, effusion et ionisation, une efficacité de transformation atome-ion de 75% est attendue, menant à un taux d'ions de l'ordre de 10^4 pps à la sortie de l’ECS.

Les performances estimées permettraient à l'installation GANIL / SPIRAL1 de délivrer des faisceaux de ^{74}Rb et ^{114}Cs avec des intensités compétitives, jamais atteintes dans d'autres installations.

Le dispositif de production a été développé sur la base de mon travail, pour répondre aux objectifs de physique et aux conditions d'opération de SPIRAL1. L'efficacité, la fiabilité et donc la simplicité étaient essentielles. Le système répond à ces exigences.

L'instrumentation nécessaire pour les tests existait ou a été spécialement conçue. L’ECS a été construit, assemblé et partiellement testé.

En parallèle, des questions ont été abordées pour répondre à des besoins connexes sur les temps de collage, la résistivité et l'émissivité, afin d'obtenir des informations pour la conception de l’ECS.

Les résultats attendus avec les isotopes d’alcalins nous encouragent à appliquer le même principe à la production d’isotopes déficients en neutrons de courte durée de gaz nobles et éventuellement de métaux.